



Terms and Conditions of Use of Digitised Theses from Trinity College Library Dublin

Copyright statement

All material supplied by Trinity College Library is protected by copyright (under the Copyright and Related Rights Act, 2000 as amended) and other relevant Intellectual Property Rights. By accessing and using a Digitised Thesis from Trinity College Library you acknowledge that all Intellectual Property Rights in any Works supplied are the sole and exclusive property of the copyright and/or other IPR holder. Specific copyright holders may not be explicitly identified. Use of materials from other sources within a thesis should not be construed as a claim over them.

A non-exclusive, non-transferable licence is hereby granted to those using or reproducing, in whole or in part, the material for valid purposes, providing the copyright owners are acknowledged using the normal conventions. Where specific permission to use material is required, this is identified and such permission must be sought from the copyright holder or agency cited.

Liability statement

By using a Digitised Thesis, I accept that Trinity College Dublin bears no legal responsibility for the accuracy, legality or comprehensiveness of materials contained within the thesis, and that Trinity College Dublin accepts no liability for indirect, consequential, or incidental, damages or losses arising from use of the thesis for whatever reason. Information located in a thesis may be subject to specific use constraints, details of which may not be explicitly described. It is the responsibility of potential and actual users to be aware of such constraints and to abide by them. By making use of material from a digitised thesis, you accept these copyright and disclaimer provisions. Where it is brought to the attention of Trinity College Library that there may be a breach of copyright or other restraint, it is the policy to withdraw or take down access to a thesis while the issue is being resolved.

Access Agreement

By using a Digitised Thesis from Trinity College Library you are bound by the following Terms & Conditions. Please read them carefully.

I have read and I understand the following statement: All material supplied via a Digitised Thesis from Trinity College Library is protected by copyright and other intellectual property rights, and duplication or sale of all or part of any of a thesis is not permitted, except that material may be duplicated by you for your research use or for educational purposes in electronic or print form providing the copyright owners are acknowledged using the normal conventions. You must obtain permission for any other use. Electronic or print copies may not be offered, whether for sale or otherwise to anyone. This copy has been supplied on the understanding that it is copyright material and that no quotation from the thesis may be published without proper acknowledgement.

Mechanisms and Size Effects of Small to Large Strain Polymer Deformation at the Molecular Scale

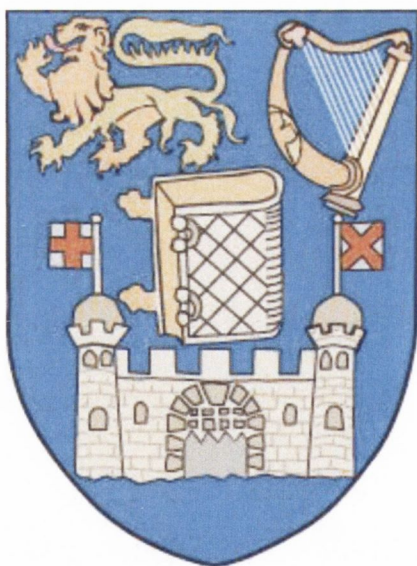
by

Roseanne Reilly

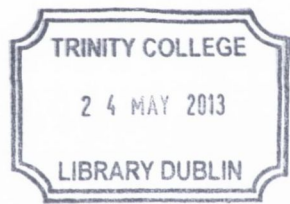
A thesis submitted to the University of Dublin for the degree of

Doctor of Philosophy

School Of Physics,
University of Dublin, Trinity College



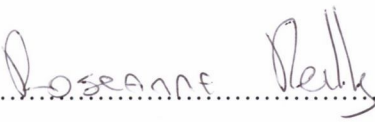
March, 2013



Thesis 9993

Declaration

This thesis has not been submitted as an exercise for a degree at any other university. Except where otherwise stated, the work described herein has been carried out by the author alone. This thesis may be borrowed or copied upon request with the permission of the Librarian, University of Dublin, Trinity College Dublin. The copyright belongs jointly to the University of Dublin and Roseanne Reilly.

Signature of Author: 

Roseanne Reilly
21st March, 2013

Summary

A core section of mechanics of materials is to understand the relationship of the mechanics to the nanoscale structure. This has been looked at in metals, ceramics, but in polymers has been virtually untouched. While micron scale polymer physics has been probed, real size effects and changes in polymer behaviour have not. This thesis attempts to remedy this by using diamond flat punch nanoindentation to probe mechanical size effects in polymer materials, from large to small strain. Additionally these findings regarding size effects in polymers are then utilised to investigate the effect of phase separation on the mechanical properties of ultra-thin block copolymers. . Block copolymers are a highly technologically relevant material that is currently being investigated for use in the semiconductor industry, meaning the mechanical properties of these ultra thin phase separated films is also technologically relevant. From a size effect point of view, phase separation also effectively adds in an additional length scale into the ultra-thin film case, with the polymers now separated into domains of individual polymers separated by polymer-polymer interfaces.

In order to be able to carry out these measurements it was necessary to start at large scale effects in these polymers and optimise the technique of flat punch nanoindentation for these materials. As nanoindentation is generally used for extremely hard materials optimising this technique for indenting into soft polymeric materials was the first challenge. In addition, designing and fabricating diamond flat punch, using focused ion beam and a scanning electron microscope, to work in the nanoindenter was another issue. Bringing the flat punch into contact with the sample in an aligned manner is also a non-trivial problem and requires careful use of a tilt stage and atomic force microscopy. These issues are all addressed in chapter four, the experimental method chapter.

Chapter five deals with effects of aspect ratio, friction and geometry on the measurements obtained by flat punch nanoindentation. Here aspect ratio is the ratio of the diameter of the flat punch to the film thickness. In this section it was important to be able to extract a yield stress and an elastic modulus, taken into consideration aspect ratio, friction and geometry,

from the forming stress and contact modulus calculated for the material by the nanoindenter. Chapter 5 continues on to probe mechanical size effects in polystyrene and poly(methyl metha) acrylate. Both polystyrene and poly(methyl metha) acrylate homopolymer supported films were found to show a dramatic mechanical weakening under indentation at reduced film thickness, of order five-fold for polystyrene and four-fold for poly(methyl metha) acrylate. For polystyrene the observed weakening with film thickness is consistent with previous results. For poly(methyl metha) acrylate, the results are new. Additionally, for polystyrene this was shown to be independent of molecular weights greater than the entanglement threshold. Below 100 nm film thickness there was also a clear decrease in elastic modulus with an eightfold decrease for polystyrene and a 3.5 fold decrease for poly(methyl metha) acrylate. This was independent of molecular weight in polystyrene, and independent of aspect ratio in polystyrene and poly(methyl metha) acrylate.

Chapter 6 uses the results from chapter 5 and flat punch nanoindentation to probe the mechanical properties of ultra-thin films of a highly technologically relevant polymer material, namely block copolymers. Here polystyrene-poly(methyl metha) acrylate diblock copolymers were chosen for investigation due to the body of knowledge that had already been built up for these polymers using flat punch nanoindentation. Additionally, the structure of the phase separated block copolymers was chosen to be in a lamellae phase of equal sized domains of polystyrene poly(methyl metha) acrylate. Flat punch nanoindentation was used to measure the effect of microphase separation on mechanical deformation of single-lamellar domain thickness block copolymer films. When compared to polystyrene and poly(methyl metha) acrylate homopolymer thin films of similar thickness and molecular weight, a strict interpolation of the room temperature stress vs. strain curve was found to high strain. This was true for polystyrene - poly(methyl metha) acrylate films in both the as-prepared spin-cast state and following microphase separation into 20 nm lamellar fingerprint domains induced by thermal annealing. Overall, the thin film stress-vs-strain curves corresponding to the ultra-thin block copolymer films showed a pronounced softening compared to measured >100 nm film response, consistent with results from chapter 6. The block copolymer pre and post phase separated states had identical small strain elastic and

yield response, while the phase separated state demonstrated an effective strain hardening effect above 0.5 strain, to a value of 40% excess stress at 0.9 strain.

Using pre and post phase separated block co polymer films also allowed us to investigate to additional questions that have arisen in the literature. Firstly, questions have been asked as to whether lack of sufficient annealing is responsible for the size effects measured in thin films of polymers. Annealing leading to microphase separation implies diffusive relaxation of the polymer chain blocks by displacement on order of the bulk radius of gyration. This leaves the anomalous thin film mechanical weakening effects observed here and elsewhere in spin-cast supported thin films difficult to attribute to sample preparation history effects such as residual stress, local structural gradients and unreleased solvent.

The second question that this addresses is the effect of the microphase separation of the polymers into separate domains and whether the addition of lateral interfaces within the block co polymer film has any effect on the mechanical properties of the ultra-thin film. It is found that the effect of reducing the film thickness, as seen in chapter 6, seems to be dominant. The introduction of lateral confinement at the 20 nm scale by creating glassy block copolymer segregation walls has a limited influence on the overall mechanics, manifesting only at high strain. For polymer nanostructures formed by block copolymer lithograph, a significant loss in mechanical strength (compared to bulk polymer) occurs by the initial creation of the supported thin film, but no further penalty is incurred by in-film structuring.

Chapter 7 attempts to push the boundaries of what nanoindentation can currently accomplish. In clean crystalline surfaces incipient plasticity is studied through the examination of indentation load-displacement curves acquired by a load controlled nanoindenter or atomistic simulations for indentation of perfect metals. However the study of incipient plasticity, or the point where the plastic deformation is just beginning to form, has not been addressed in glassy polymers. The main reason for this is the time dependency of deformation in polymer materials. One property of this time dependency can be seen in nanoindentation by increasing the strain rate which results in an increase in the yield stress.

However, so far it has not been possible to measure strain softening in polymer material, which is key to be able to access incipient plasticity in polymers. With this in mind a controlled displacement rate method of indentation was designed for use in the nanoindenter with flat punch nanoindentation. Using this method clear steps became obvious in the stress strain indentation curve which it is hypothesised to correspond to the nucleation and propagation dynamics of individual shear bands in the material. However, limitations with feedback frequency the nanoindenter can attain restricted the control with which displacement control could be carried out. Therefore these displacement controlled are preliminary results for what may be nucleation and propagation of individual shear bands in polymer materials.

Chapter 8 concludes the thesis by clearly summarising the results within the thesis, placing them in context, and suggesting the design of future experiments.

Acknowledgements

I wish to thank all the people who helped me during this long process of completing my PhD, and also helped make it an enjoyable experience. I want to thank the other members of the Cross group, in particular James Annett, Dr. Evelyn Doherty, Dr. Iratxe Mijangos and Laetitia West for very useful discussions, for passing on their insights and experiences to me and for very kindly always helping me out whenever I needed it. In addition the support network around CRANN and the tcd physics department has been invaluable to me over the years with extremely useful advice and expertise coming from all sections, including the AML where Cathal McAuley, Colm Faulkner and Tarek Lutz in particular have always enthusiastically helped me out with any questions I have and training I needed, and Peter Gleeson who helped me out many times in the cleanroom. Without these people enthusiastic help and support my experience in CRANN would have been undeniably much tougher.

I also wish to thank my friends, both long term friends, Amy Conlon, Michele Keyes, Ciara Kelly, Teresa Wurm, Ann-Marie O Regan and Cormac O Coileann and more recent friends, Evelyn Doherty, Iratxe Mijangos, Hye Young Kim, Kangho Lee, Ciaran Smyth and James Annett for their support, patience, many cups of coffee, emails, proofreading my thesis, shopping trips and nights out which helped me in an immeasurable way. Please note, not all indulged in the shopping trips, but most indulged in the nights out.

Finally I wish to thank my parents, Ollie and Helen Reilly for encouraging and supporting me in whatever I wished to do ever since I can remember, including music, swimming and college and passing on to me the confidence to know that I can aim for anything I want, and if I do change my mind at any stage that that's ok too. Also I appreciate the support my siblings Oliver, Philip, Sean, Patrick and Helena have given me while we were growing up together and now that we have to make more of an effort to stay in touch. Lastly, and far from least, I wish to thank ,my other half, Alan Byrne for his unwavering support, help, advice, patience and friendship over the past 6 year

Contents

Nomenclature	xiii
Preface	xv
1 Introduction	1
1.1 Background	1
1.2 Thesis Outline	3
1.3 References	4
2 Theory; Mechanics of Materials and Contact Mechanics	6
2.1 Strength of Materials	6
2.2 Elements of material mechanics: Stress and strain	6
2.3 Elastic to Plastic Deformation	8
2.4 Yielding Criteria	9
2.4.1 Von Mises Criteria	10
2.5 Introduction to Contact Mechanics	11
2.5.1 Hertz Theory	12
2.5.2 Indentation by a Rigid Flat Punch	12
2.5.3 Introduction to Finite Element Modelling	13
2.5.4 Effect of Stress Singularities', Aspect Ratio and Contact Geometry in Thin film Flat Punch Nanoindentation	14
2.6 Yielding of Polymers	19
2.6.1 Conventional (Bulk Scale) mechanical testing of polymer glasses	19

2.7	Advantages of Flat Punch Nanoindentation for Mechanical Testing of Polymers	21
2.8	References	24
3	Theory: Polymer Physics	26
3.1	Polymer Materials	26
3.2	Block Copolymers	27
3.3	Amorphous Polymer Glasses	28
3.4	The Glass Transition	29
3.5	Relevant Length Scales in Polymers	29
	3.5.1 Relevant Length Scales: The Random Coil Model	30
	3.5.1 The Random Coil Model	30
	3.5.2 de Gennes' Reptation Theory; How Polymers Move	33
3.6	Relaxation in Glassy Polymers	31
	3.6.1 The Effect of Hydrostatic Pressure yielding in Polymers	32
	3.6.2 Relaxations Modes in Polymers	33
	3.6.3 Effect of Pressure on Relaxation modes in Polymers	38
3.7	Effects of Confining Polymers to Nanoscale Dimensions	35
3.8	Small Size Effects: Enhanced Surface Relaxation	39
	3.9.1 de Gennes' Tentative Model for Thin Films	40
3.9	Models for Theory of Elastic to Plastic Transition in Polymer Glasses	41

3.9.1	The Eyring Model	42
3.9.2	Recent Models of Polymer Deformation	43
3.10	Yield processes in Thin Polymer Films`	45
3.11	Relevant Length Scales	46
3.12	Shear Banding in Polymer Glasses	47`
3.13	References	47
4	Experimental Methods	51
4.1	Nanoindentation	51
4.1.1	Nanoindentation Set up	53
4.1.2	Continuous Stiffness Mode of Nanoindentation	56
4.1.3	Raw data: Nanoindentation	59
4.2	Custom Tip Manufactory Process	62
4.2.1:	Initial Alignment and Planarization of Diamond	
Flat Punches		62
4.2.2:	Direct top-down FIB Milling of Diamond Flat Punches	67
4.2.3:	FIB Masking and Plasma Etching of DFPs	68
4.3	Alignment of Flat punch in Nanoindenter	69
4.3.1	Method of Alignment of Flat punch in Nanoindenter	70
4.3.2	Mounting and Alignment of Multiple Polymer	
Samples on Same Test Stub		74
4.4	Sample Preparation	75
4.4.1	Homopolymer Preparation	75
4.4.2	Block Copolymers Preparation	76
4.5	References	77

5	Flat punch Nanoindentation as a Method to Investigate Mechanical Properties of Size Effects in Polymer Thin Films	79
5.1	Introduction	79
5.2	Experimental Set-up	80
5.3	Results and Discussion	81
5.3.1	Analysis of Forming Stress and Contact Geometry	85
5.3.2	Analysis and Discussion: Effect of Hydrostatic Pressure on Deformation in Polymers	89
5.3.3	Analysis and Discussion: Effect of Contact Geometry, Aspect Ratio and Pressure on Modulus	91
5.3.4	Results and Analysis: FP Nanoindentation into sub 100 nm Films of PS and PMMA	101
5.3.5	Results and Analysis: Elastic Modulus for sub-100 nm Films of PS and PMMA	103
5.3.6	Results and Analysis: Stress Normalised by FS for Films Above and Below Size Effect	104
5.4	Conclusion	107
5.6	References	109
6	Size Effects in Polymers; From Large Scale to Small Scale FP Nanoindentation	112
6.1	Introduction	113
6.2	Review of BCP Phase Separation and Mechanical Studies	116

6.3	Experimental Set up	116
6.4	Results and Discussion	117
6.4.1	Small strain discussion – interfacial influence on relaxation	119
6.4.2	The Effect of Phase Separation	123
6.5	Implications for BCP Lithography	125
6.6	Conclusions	126
6.7	References	127
7	Displacement Controlled Indentation into Polymer Films	130
7.1	Introduction	130
7.2	Experimental Set up	132
7.3	Results and Analysis	134
7.4	Discussion and Conclusion	139
7.5	References	140
8	Conclusions and Future Work	142
8.1	Conclusions	142
8.2	Future work	148
8.3	References	150

Appendix

List of Figures

Figure 2.1: <i>Idealized classification for elastic plastic and elastic plastic indentations</i>	8
Figure 2.2: <i>Schematic of three principal stresses acting on a cube.</i>	9
Figure 2.3: <i>Schematic of Flat Punch nanoindentation.</i>	13
Figure 2.4: <i>Schematic of pressure (P) versus x/a</i>	16
Figure 2.5: <i>Schematic of cylindrical billet upsetting.</i>	17
Figure 2.6: <i>Two dimensional schematic of material flow in TFFPN vs. cylindrical billet upsetting.</i>	18
Figure 2.7 <i>A schematic diagram of nominal stress vs. nominal strain of a conventional tensile test when the sample necks.</i>	20
Figure 2.8 a) <i>shows tensile stress vs. strain behaviour of polycarbonate (PC) at a constant strain rate at various temperatures from 25°C to 150°C.</i>	20
Figure 2.9: a) <i>Intense shear bands in slowly cooled PS deformed at room temperature.</i> b) <i>Shear bands formed in quenched PS deformed in the same manner.</i>	21
Figure 2.10: <i>A characteristic graph of flat punch indentation into an ultra-thin film of Polystyrene.</i>	23
Figure 3.1: <i>an example of a polymer chain; polyethylene</i>	27
Figure 3.2: <i>Block Copolymer representation.</i>	28
Figure 3.3: <i>Typical data from an ellipsometric scan.</i>	35
Figure 3.4: <i>EM/bulk EM versus film thickness for various polymers</i>	38
Figure 3.5: <i>presents FS over Bulk FS against film thickness for PS.</i>	39

<i>Figure 3.6: Representation of kink in a polymer molecule when shear stress applied</i>	
<i>H represents energy.</i>	43
<i>Figure 3.7: Image of molecular dynamics simulations from Capaldi et al.</i>	44
<i>Figure 3.8. Glassy elastic-to-plastic transition behaviour for low polydispersity 9000K, 900K, and 44K Mw polystyrene at 170 nm film thickness.</i>	46
<i>Figure 4.1: Simple Schematic of nanoindenter set up.</i>	54
<i>Figure 4.2: Schematic of configuration of AC modulation.</i>	55
<i>Figure 4.3: Raw nanoindenter data.</i>	59
<i>Figure 4.4: Raw nanoindenter data.</i>	59
<i>Figure 4.5: Raw nanoindenter data.</i>	61
<i>Figure 4.6: Initial FIB set up for manufacturing diamond flat punches.</i>	63
<i>Figure 4.7: Ultra high resolution images of diamond nanoindentation tip</i>	64
<i>Figure 4.8: FIB images of a well aligned tip in the FEI FIB system.</i>	64
<i>Figure 4.9: UHR resolution ebeam of indenter tip</i>	65
<i>Figure 4.10 : FIB set up for top down milling of diamond flat punches.</i>	66
<i>Figure 4.11 : Images of indenter tip adter milling</i>	67
<i>Figure 4.12: a) FIB side view of finished flat punch. b) E beam tilted view of finished flat punch.</i>	68
<i>Figure 4.13: 400 nm diamond flat punch.</i>	68
<i>Figure 4.14: Characteristic measurement of DFP into polymer film.</i>	68
<i>Figure 4.15: Schematic of aligned flat punch indentation.</i>	70

<i>Figure 4.16: Schematic of misaligned flat punch indentation.</i>	70
<i>Figure 4.17: Nanoindenter x and y plane, top down alignment with AFM.</i>	71
<i>Figure 4.18: 700 nm DFP indents into 150 nm film of PMMA.</i>	72
<i>Figure 4.19: AFM images to 20 nm depth and corresponding profiles.</i>	72
<i>Figure 4.20: AFM and profile image after adjusting x and y plane.</i>	73
<i>Figure 4.21: 400 nm punch into 30 nm film aligned.</i>	73
<i>Figure 4.22: Schematic to illustrate the alignment process in indenter.</i>	75
<i>Figure 4.23: AFM phase image of 37-37 K block copolymers.</i>	87
<i>Figure 5.1: DFP's used in experiments</i>	81
<i>Figure 5.2: Stress strain curves; 320 nm DFP into 52 nm 9000 K PS.</i>	83
<i>Figure 5.3: Stress strain curves; DFPs into various films.</i>	84
<i>Figure 5.4: a) FS against film thickness into PMMA and PS.</i>	85
<i>Figure 5.5: FS against punch radius into PMMA and PS.</i>	86
<i>Figure 5.6: Forming stresses for 400 nm DFP, 650 nm DFP and 800 nm DFP against aspect ratio for various film thicknesses of PMMA.</i>	87
<i>Figure 5.7: Forming Stress against a/h in PS for 900 nm DFP and 650 nm DFP.</i>	88
<i>Figure 5.8: Hydrostatic pressure divided by von Mises stress vs. Poisson ratio in thin film flat punch contact.</i>	90
<i>Figure 5.9: Elastic modulus versus hydrostatic pressure for PMMA.</i>	93
<i>Figure 5.10: Elastic modulus versus hydrostatic pressure for PS.</i>	95
<i>Figure 5.11: Elastic modulus versus strain for PMMA.</i>	95

Figure 5.12: Elastic modulus versus strain for PS.	95
Figure 5.13 : 900 nm DFP into a) 168 nm film of 9000 K PS and b) 84 nm film of 9000 K PS.	97
Figure 5.14: CM plotted against original film thickness for PMMA and PS.	98
Figure 5.15: Contact Modulus plotted against radius of diamond flat punch for several punches indenting into a) PMMA and b) PS.	98
Figure 5.16: 400 nm DFP, 650 nm DFP and 800 nm DFP into PMMA.	99
Figure 5.17: Contact modulus against a/h in PS.	99
Figure 5.18: Stress versus strain for large scale 10 to 1 aspect ratio and small scale 10 to 1 aspect ratio indentation of PS and PMMA	102
Figure 5.19 FS against aspect ratio for 400 nm plasma etched DFP indented into film thicknesses of PMMA varying from 28 nm to 200 nm.	102
Figure 5.20: E versus hydrostatic pressure for 900 nm DFP and 650 nm DFP into film thicknesses of PS 9000 K, 900 K and 44 K varying from 168 nm to 40 nm.	103
Figure 5.21: Elastic modulus versus hydrostatic pressure for 800 nm DFP and 650 nm DFP into film thicknesses of 48 K PMMA varying from 150 nm to 40 nm.	104
Figure 5.22: PS homopolymer stress vs. strain curves normalized by their own forming stress value for 10 to 1 aspect ratio.	105
Figure 5.23: PMMA homopolymer stress vs. strain curves normalized by their own forming stress value for 10 to 1 aspect ratio.	106
Figure 5.24: PS and PMMA homopolymer stress vs. strain curves normalized by their own forming stress value for 10 to 1 aspect ratio .	106

Figure 6.1: The effect of microphase separation on the mechanical stress vs. strain curve of an ultrathin block copolymer film	117
Figure 6.2: SEM image of the strongly segregated state of the PS-b-PMMA	118
Figure 6.3: Stress versus strain response for thin film systems	120
Figure 6.4: Stress versus strain response for thin film systems of 28 nm thin film PS, 26 nm thin film PMMA and 33 nm BCP film.	120
Figure 6.5: Low strain zoom of average stress versus strain response for thin film systems of 28 nm thin film PS, 26 nm thin film PMMA and 33 nm BCP film.	121
Figure 6.6: Weight average homopolymer response compared to the BCP pre and post phase separated response.	122
Figure 6.6: Weight average homopolymer response compared to the BCP pre and post phase separated response.	
Figure 6.7: Expected BCP system chain packing and entanglement state pre and post phase separation.	125
Figure 7.1: A "pop in" event occurring in silicon	131
Figure 7.2: Figure adapted Schuh et al showing a "staircase" response of indenting under load control into bulk metallic glass.	132
Figure 7.3: Stress strain curves for 8 indents to different depths in a 700 nm PS film.	134
Figure 7.4: a) Graph showing raw data of 2 6200 nm DFP indents to 600 nm into an 800 nm film of Polystyrene, one under load control and the other under displacement control.	135
Figure 7.5: Displacement controlled indentation carried out by 6200 nm DFP into 800 nm PS.	136

<i>Figure 7.6: Graph of circumferential cracks versus number of steps for 6200 nm DFP indenting under displacement control into 800 nm PS.</i>	137
<i>Figure 7.7: AFM image's corresponding to 3 of the indents shown in figure 8.3.</i>	137
<i>Figure 7.8: load versus displacement curve for the 6200 nm DFP into 800 nm 382 K PS.</i>	139

Appendix A	A
<i>Figure A.1: 900 nm DFP indenting into 168 nm 9000 K PS</i>	A
<i>Figure A.2 : 900 nm DFP into 84 nm 9000 K PS</i>	A
<i>Figure A.3: 900 nm DFP into 63 nm 9000 K PS</i>	B
<i>Figure A.4 :900 nm DFP in 52 nm 9000 K PS.</i>	B
<i>Figure A.5: 900 nm DFP into 42 nm 9000 K PS</i>	C
<i>Figure A.6: 900 nm DFP into 168 nm 44 K PS</i>	C
<i>Figure A.7: 900 nm DFP into 80 nm 44 K PS.</i>	D
<i>Figure A.8: 900 nm DFP into 150 nm 48 K PMMA</i>	D
<i>Figure A.9: 800 nm DFP into 150 nm 48 K PMMA</i>	E
<i>Figure A.10: 800 nm DFP into 100 nm 48 K PMMA</i>	E
<i>Figure A.11: 800 nm DFP into 48 K PMMA</i>	F
<i>Figure A.12: 650 nm DFP into 160 nm 900 K PS</i>	F
<i>Figure A.13: 650 nm DFP into 64 nm 900 K PS</i>	G
<i>Figure A.14: 650 nm DFP into 52 nm 9000 K PS</i>	G
<i>Figure A.15: 400 nm DFP into 200 nm 48 K PMMA</i>	H
<i>Figure A.16: 400 nm DFP into 90 nm 48 K PMMA</i>	H

<i>Figure A.17: 400 nm DFP into 60 nm 48 K PMMA</i>	<i>I</i>
<i>Figure A.18: 400 nm DFP into 26 nm 44 K PMMA</i>	<i>I</i>
<i>Figure A.19: 400 nm DFP into 52 nm 9000 K PS</i>	<i>J</i>
<i>Figure A.20: 400 nm DFP into 31 nm 9000 K PS</i>	<i>J</i>
<i>Figure A.21 : 320 nm DFP into 52 nm 9000 K PS</i>	<i>K</i>
<i>Figure A.22: 320 nm DFP into 28 nm 44 K PS</i>	<i>K</i>
<i>Figure A.23 : 320 nm DFP into 26 nm 48 K PMMA</i>	<i>L</i>

Nomenclature

ω	Angular frequency
σ	Applied Stress
AFM	Atomic Force Microscopy
BCP	Block Copolymer
BDS	Broadband Dielectric Spectroscopy
CM	Contact Modulus
CSM	Continuous Stiffness Measurement
A_0	Cross Sectional Area
C_i	Damping Coefficient
DFP	Diamond Flat Punch
δ	Displacement
E	Elastic Modulus
ε	Engineering Strain
FIB	Focused Ion Beam
FS	Forming Stress
T_g	Glass Transition Temperature
h	Film Thickness
FE	Finite Element
ν	Frequency
H	Hardness
τ_i	Intrinsic shear stress yield
σ_0	Intrinsic Yield
b_0	Kuhn Segment Length
l	Length
L	Load

σ_m	Mean pressure
\bar{p}	Mean pressure under punch
M_w	Molecular weight
NIL	Nano-Imprint Lithography
L_0	Original Length
ν	Poisson's Ratio
PC	Polycarbonate
PE	Polyethylene
PS	Polystyrene
PMMA	Poly (Metha Methyl) acrylate
ΔH	Potential Energy Barrier
P	Pressure
n	Pressure coefficient
a	Punch Radius
R_g	Radius of Gyration
SEM	Scanning Electron Microscopy
G	Shear Modulus
τ	Shear Stress
m	slope
K	Spring Constant
S	Stiffness
ε	Strain
$\dot{\varepsilon}$	Strain rate
G_r	Strain hardening
YS	Yield Stress
k	Yield stress in shear
uhb	Ultra High Beam

Preface

The bulk of the material presented here is my own work and is, to the best of my knowledge, novel. I have, of course, presented some background material by way of introduction and in general I use standard terminology and notation. Where I use the work of others I have referenced it carefully.

Chapter 1 Introduction

1.1: Background

Ever since Drexler coined the unfortunate phrase “grey goo” nanoscience has captured the imagination of the world[1]. Self-replicating nanomachines may remain out of reach[2], but many aspects of nanoscience have already yielded enormous benefits. Nanoscale technology has the potential to improve the performance and efficiency of materials, sensors and devices by tailoring the required properties of even macro-scale materials at the nanometre length scale. With this in mind, nanoscale manipulation of matter by mechanical means has become a major sub-discipline of nanoscience in the past decade. The interest in this area stems from the technologically advantageous promise of novel properties in a wide variety of materials which could be assembled on the nanoscale, while simultaneously realising successful integration to macroscopic dimensions. Mechanical nanostructure forming techniques have emerged as a success story in nanotechnology [3] due to the arrival of high resolution, techniques such as nanoimprint lithography (NIL), which can be done in parallel over large areas.

NIL is a method of fabricating nanometer scale patterns. It is, in principle, a simple low cost, high throughput and high resolution nanolithography process. It creates patterns by mechanical deformation of imprint resist and subsequent processing. During NIL of polymers, a rigid, patterned die squeezes a supported polymer thin film to dimensions comparable to the size of the polymer molecule. The squeeze flow between protruding die regions and the supporting substrate governs the dynamics of NI [3]. The polymer properties, film thickness, and the distribution of cavity sizes and shapes significantly affect the processing conditions required for NIL and ultimate replication fidelity. This means that investigations of the dynamics of amorphous polymer systems during squeeze flow are of crucial importance.

Despite its apparent simplicity, nanoimprint lithography faces major challenges, including limited scientific understanding of the mechanical processes and interfacial phenomena that govern fabrication on the nanoscale [4, 5]. This shortcoming in fundamental scientific knowledge leads to a loss of production fidelity in functional design. This stems from a

lack of predictive capability for materials and their properties on the nanoscale. Hence, the aim of this thesis is to address fundamental issues in the nanoscale deformation of polymer materials. At the bulk (*i.e.* macroscopic) scale, polymers in the glassy and melt state are thought of as amorphous materials. However this cannot be assumed when they are investigated at the nanoscale where the inherent length scales of the polymers become important. At these scales, for instance where films are prepared with a thickness approaching the size of the polymer macromolecule, we can learn directly about the collective motion of small groups of polymers. This is why the nanoscale mechanics of polymers are especially interesting.

Methods for the characterization of thin film polymer mechanical properties date back to the copper grid extension method introduced by Kramer[6]. Modern studies include variations of this technique and a surface buckling technique developed by Stafford *et al* [7-9] which are used in conjunction with either AFM, laser diffraction or reflectance optical microscopy to allow the elastic modulus of thin films to be measured. Dewetting tests of supported thin polymer films [10-12] (< 100 nm) conducted above and below the polymer glass transition temperature T are used to investigate the rate of hole formation as a function of film thickness, molecular weight MW , temperature T , and thermal history. However, none of these techniques can access the yielding point of thin polymer films, in addition to measuring the mechanical properties of the films from low to high strain. This is where flat punch nanoindentation comes into its own as an exceptionally useful and unique technique that allows access to the dynamics of polymer materials which is vitally important to areas such as nanoimprint lithography.

This work represents a challenge to conventional testing techniques and is carried out via an experimental program comprising new generations of nanoindentation techniques used in conjunction with cutting edge microscopy methods. The focus is on scalable mechanical manipulation at the nanoscale. Small to large strain deformation processes in nanoscopic volumes are be probed using flat punch nanoindentation and thin film systems [13, 14]. The materials under investigation are primarily disordered soft matter systems in particular amorphous polymer glasses and block copolymers. These materials are highly

technologically relevant, with uses as an industrial structural material and adhesives, as well as a functional biological materials.[15] In addition, understanding the small scale mechanics of polymer based materials and composites is also important for future applications in areas such as pressure sensitive adhesives[16], lubricants and interlayer dielectrics in microelectronics[17-19], thus how they behave on the nanoscale is an issue of critical importance.

1.2 Thesis Outline

In chapter 2 the mechanics of materials with the relevant basics in stress, strain, elastic and plastic behaviour and yielding criteria are introduced. Contact mechanics is then discussed with emphasis on flat punch nanoindentation. Finally the conventional mechanical testing of polymers is presented with a discussion of the confinement of polymers to nanoscale dimensions and why flat punch nanoindentation is advantageous for these type of measurements.

Chapter 3 introduces polymer materials and block copolymers. How polymers move, conform and relax is discussed in some detail with various models and a comparison with some of the vast experimental work which has been carried out on polymer materials. The effect nanoscale confinement on polymers is once again discussed, but from a polymer physics point of view. Several of the leading theories of how polymers yield, on large and small scales are also presented.

Chapter 4 focuses on the experimental techniques which are utilised in this thesis with an emphasis on the nanoindenter, fabrication of flat punches, how flat punches are aligned and the preparation of process of homopolymer films and block copolymer films. In chapter 5 the consequences of aspect ratio, friction and hydrostatic pressure on flat punch nanoindentation are discussed, and experiments and results analysed to endeavour to quantify the effects of these on the forming stress and contact modulus. Chapter 5 then discusses size effects in polymer physics, results are presented from flat punch nanoindentation into thick and ultra-thin polymers. The characteristic signature of flat punch nanoindentation, which if scaled with forming stress is consistent for large and small scale indentations even allowing for size effects in polymers, is presented and the

physical consequences are discussed. Experimental results of yielding in ultrathin polymer films using a velocity controlled technique, which appears to generate a different type of yielding in the material than is generally seen using nanoindentation, are presented. Here the challenge of developing reliable strain-rate control of flat punch indentation is also discussed.

Chapter 6 presents mechanical testing of ultrathin block copolymer (BCP) films. BCPs are very interesting nanocomposite materials which are of huge interest to the lithographic community. An investigation was carried out into the effect of phase separated domains on the deformation mechanics of block copolymers (BCPs). Experiments were carried out on the unordered and ordered block copolymers, allowing the data before and after the BCPS had phase separated to be assessed, and hence before and after an additional length scale of $\sim 30\text{-}40$ nms has been imposed on the system of already ultra-thin films. The results from the block copolymers are compared and contrasted with homopolymer films and the implications for BCP lithography discussed. Finally chapter 8 concludes the thesis and some future experiments are suggested.

1.3 References

- [1] K. E. Drexler, *Engines of creation* Garden City, N.Y. : Anchor Press/Doubleday, 1986.
- [2] C. Phoenix and E. Drexler, "Safe exponential manufacturing," *2004* vol. 15, 2004
- [3] G. L. W. Cross, "The production of nanostructures by mechanical forming," *Journal of Physics D: Applied Physics*, p. R363, 2006.
- [4] G. L. W. Cross, B. S. O'Connell, J. B. Pethica, and W. C. Oliver, "Some Issues in the Mechanical Forming of Nanoimprint Structures," *Journal of Photopolymer Science and Technology*, vol. 18, pp. 559-562, 2005.
- [5] G. L. W. Cross, B. S. O'Connell, J. B. Pethica, H. Schulz, and H. C. Scheer, "Instrumented indentation testing for local characterisation of polymer properties after nanoimprint," *Microelectronic Engineering*, vol. 78-79, pp. 618-624, 2005.
- [6] A. M. Donald and E. J. Kramer, "Effect of molecular entanglements on craze microstructure in glassy polymers," *Journal of Polymer Science: Polymer Physics Edition*, vol. 20, pp. 899-909, 1982.
- [7] C. M. Stafford, C. Harrison, K. L. Beers, A. Karim, E. J. Amis, M. R. VanLandingham, H.-C. Kim, W. Volksen, R. D. Miller, and E. E. Simonyi, "A buckling-based metrology for measuring the elastic moduli of polymeric thin films," *Nat Mater*, vol. 3, pp. 545-550, 2004.
- [8] J. M. Torres, C. M. Stafford, and B. D. Vogt, "Elastic Modulus of Amorphous Polymer Thin Films: Relationship to the Glass Transition Temperature," *ACS Nano*, vol. 3, pp. 2677-2685, 2009.

- [9] J. M. Torres, C. Wang, E. B. Coughlin, J. P. Bishop, R. A. Register, R. A. Riggelman, C. M. Stafford, and B. D. Vogt, "Influence of Chain Stiffness on Thermal and Mechanical Properties of Polymer Thin Films," *Macromolecules*, 2011/11/03.
- [10] G. Reiter, uuml, and nter, "Dewetting of thin polymer films," *Physical Review Letters*, vol. 68, p. 75, 1992.
- [11] G. Reiter, M. Hamieh, P. Damman, S. Slavovs, S. Gabriele, T. Vilmin, and E. Raphael, "Residual stresses in thin polymer films cause rupture and dominate early stages of dewetting," *Nat Mater*, vol. 4, pp. 754-758, 2005.
- [12] H. Bodiguel and C. Fretigny, "Viscoelastic Properties of Ultrathin Polystyrene Films," *Macromolecules*, vol. 40, pp. 7291-7298, 2007.
- [13] H. D. Rowland, W. P. King, G. L. W. Cross, and J. B. Pethica, "Measuring Glassy and Viscoelastic Polymer Flow in Molecular-Scale Gaps Using a Flat Punch Mechanical Probe," *ACS Nano*, vol. 2, pp. 419-428, 2008.
- [14] G. L. W. Cross, B. S. O'connell, J. B. Pethica, H. Rowland, and W. P. King, "Variable temperature thin film indentation with a flat punch," *Review of Scientific Instruments*, vol. 79, pp. 013904-13, 2008.
- [15] C. A. Tweedie, G. Constantinides, K. E. Lehman, D. J. Brill, G. S. Blackman, and K. J. Van Vliet, "Enhanced stiffness of amorphous polymer surfaces under confinement of localized contact loads," *Adv. Mater.*, vol. 19, p. 2540, 2007.
- [16] H. R. Brown, "Effect of a diblock copolymer on the adhesion between incompatible polymers," *Macromolecules*, vol. 22, pp. 2859-2860, 1989.
- [17] V. Gowrishankar, N. Miller, M. D. McGehee, M. J. Misner, D. Y. Ryu, T. P. Russell, E. Drockenmuller, and C. J. Hawker, "Fabrication of densely packed, well-ordered, high-aspect-ratio silicon nanopillars over large areas using block copolymer lithography," *Thin Solid Films*, vol. 513, pp. 289-294, 2006.
- [18] R. Ruiz, H. Kang, F. A. Detcheverry, E. Dobisz, D. S. Kercher, T. R. Albrecht, J. J. de Pablo, and P. F. Nealey, "Density Multiplication and Improved Lithography by Directed Block Copolymer Assembly," *Science*, vol. 321, pp. 936-939, August 15, 2008 2008.
- [19] H. W. Li and W. T. S. Huck, "Ordered Block-Copolymer Assembly Using Nanoimprint Lithography," *Nano Lett.*, vol. 4, pp. 1633-1636, 2004.

Chapter 2: Mechanics of Materials and Nanoindentation

In this chapter, the work focuses on the mechanics of materials, specifically polymer materials, with focus on flat punch (FP) nanoindentation. The next chapter focuses specifically on polymer physics. In this section, a brief introduction to basic concepts of stress and strain is presented before further describing various characteristic phenomena in the deformation of polymeric matter using nanoindentation.

2.1 Strength of Materials

The body of knowledge known as the “Strength of Materials” deals with the relation between internal forces, deformation and external loads of matter [1, 2]. In the conventional method of analysis, the initial assumption is that the material is in its equilibrium state. Other primary assumptions include that the sample being analysed is continuous, homogeneous and isotropic. In this case “continuous” is defined as that which does not contain voids or empty spaces, homogeneous implies identical properties at all points and across all length scales and isotropic condition ensures that properties do not vary with direction or orientation.

While materials such as metals, ceramics and polymers meet these conditions on a broad scale, it becomes apparent that when viewed on a nanoscale or even microscale these assumptions break down; they may not be homogeneous and isotropic; there exists rather a rich “sub-continuum” structure. Furthermore, unlike ceramics and metals, in the case of polymers in a solid, which is a glass-like state, the assumption of equilibrium is also often invalid.

2.2 Elements of material mechanics: Stress and strain

There are two kinds of external forces which may act on a body, surface forces and body forces. Forces distributed over the surface of a body, such as hydrostatic pressure or forces exerted by one body on another are called surface forces or tractions. Forces distributed over the volume of a body, such as gravitational forces, magnetic forces or inertia forces are called body forces.

In general the force can be distributed over any cross-section of the body (cross section of two planes meeting is a line not an area - thus body singular?). Stress is defined as force (P) per unit area (A)

$$\sigma = \frac{P}{A} \quad (\text{Equation 2.1})$$

Total stress is normally resolved into two components, firstly a normal stress (σ) which is perpendicular to the plane. Tension and compression are both examples of normal stresses, where the stress occurs perpendicular to the plane under consideration. There exists also a shearing stress (τ) in the plane of the material. Shear stress occurs when the force acts parallel to the plane. Linear strain, also known as engineering strain, is the ratio of change in length to the original length (L_0) in the same dimension.

$$\varepsilon = \frac{L-L_0}{L_0} \quad (\text{Equation 2.2})$$

In general, when any solid material is subjected to an external load, it experiences a deformation. However up to a certain limiting stress, a solid can recover its original dimensions upon removal of the load. This is known as elastic behaviour. The load beyond which the material no longer behaves elastically is known as the elastic limit. For most materials, if the elastic limit of a few percent deformation strain is not exceeded, the stress (σ) strain (ε) relationship is linear.

$$\frac{\sigma}{\varepsilon} = E = \text{constant} \quad (\text{Equation 2.3})$$

The constant E is the elastic modulus of the material, sometimes known as Young's modulus. Rubber is an example of an elastic material with a nonlinear load deformation relationship but which still satisfies the criteria for an elastic material.

Another, but equivalent, way to consider elastic materials is that the application of a force (F) resulting in a small deflection, dx , of an element from its equilibrium position as described by Hooke's law

$$dF = k dx \quad (\text{Equation 2.4})$$

where k is a constant of proportionality known as the spring constant.

2.3 Elastic to Plastic Deformation

If, for ductile materials, the elastic limit is exceeded, the body will experience permanent deformation when the load is removed. The body is then said to have undergone plastic deformation through a process of yield. If the material is brittle the material will fracture before it begins to yield.

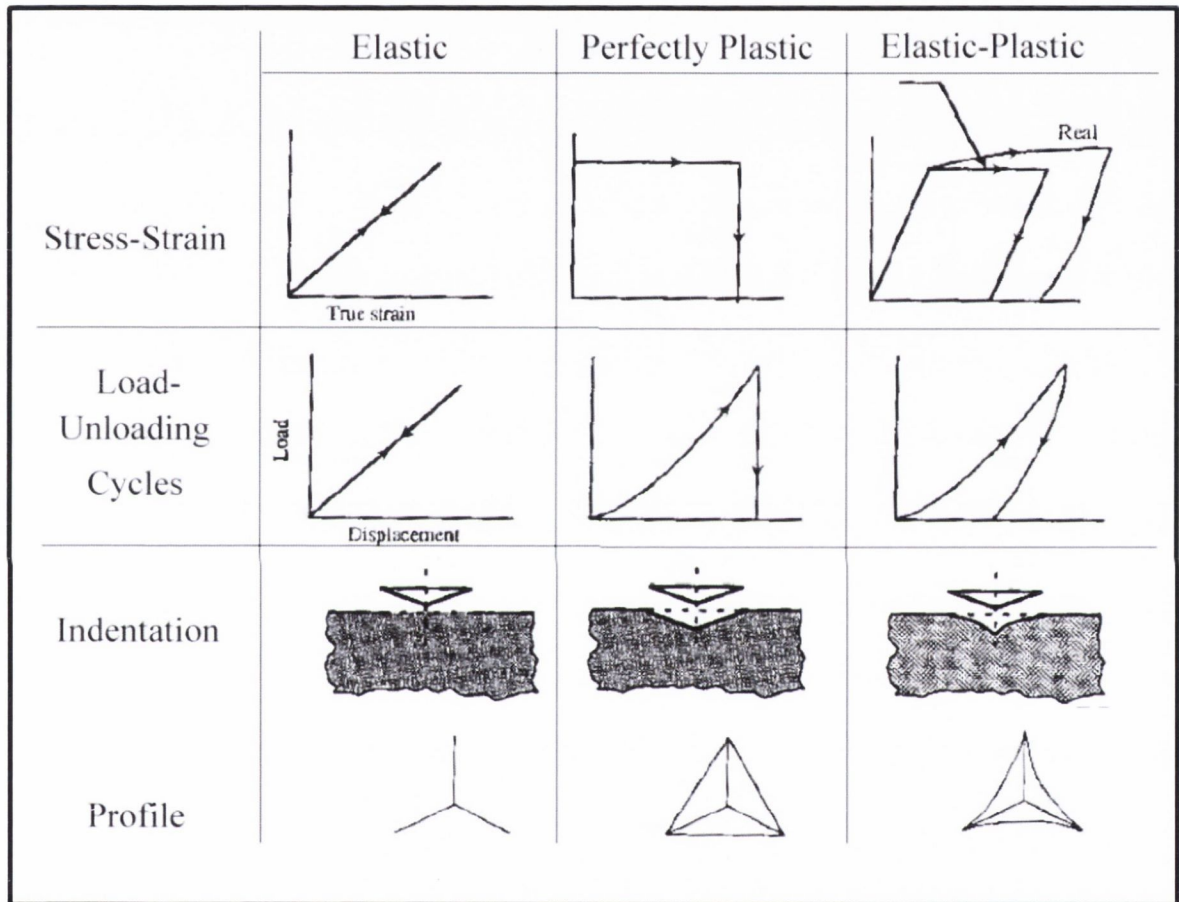


Figure 2.1: Idealized classification for elastic, perfectly plastic and elastic plastic indentations showing the associated idealised stress strain and load-unloading cycles along with side and top down views as resulting indents. Adapted from Bhusan [3].

Deformation due to indentation can be classified in the simplest terms as elastic, plastic or elastic plastic. Figure 2.1 shows an example of a stress vs. strain curve for a complete load-unloading cycle and what the indentation profile would look like for each of the three cases. A simple elastic model completely neglects plasticity and upon removal of the load there is complete recovery of the material. In contrast, a simple plastic model completely

disregards elasticity and strain hardening and upon application of a stress the material begins to deform instantaneously. It then linearly deforms and there is no recovery upon removal of the load. An elastic-plastic indentation is the most common and in this case there is first elastic deformation of the material before plastic deformation begins. The elastic-plastic transition is an idealization of ductile material behaviour characterized by the yield stress at which a material begins to deform plastically. Prior to the yield point, the material will deform elastically and will return to its original shape when the applied stress is removed. Once the yield point is passed some fraction of the deformation will be permanent and non-reversible. A general picture is that applied stress converts the structure of the material from one metastable state to another, which persists after the stress is gone [4].

2.4: Yielding Criteria

The problem of predicting the conditions at which plastic yielding begins, when a ductile material is subjected to a combination of stresses, is central to the field of plasticity. For uniaxial-compression plastic flow begins at a yield stress (σ_0). It is expected that this yielding can be related to some combination of principal stresses on the body. However, yielding criteria are essentially empirical relationships and thus must be consistent with a number of experimental observations, amongst them that pure hydrostatic pressure does not cause yielding in a continuous solid. Consider a cube which has three yield stresses acting on it on along the three principal axes σ_x , σ_y and σ_z .

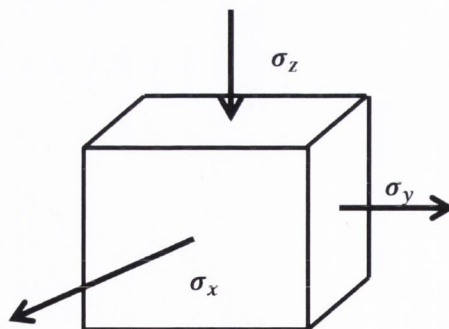


Figure 2.2: Schematic of three principal yield stresses acting on a cube.

The average of these three stresses acting in all three directions causes the cube to change volume. This average stress is also called Hydrostatic stress (σ_m) and is calculated by

$$\sigma_m = \frac{1}{3}(\sigma_x + \sigma_y + \sigma_z). \quad (\text{Equation 2.5})$$

This stress does not cause the material to begin to yield, rather it's the difference between the average and individual stresses acting on it that causes an angular distortion, which ultimately leads to its failure. Thus it is shear stress that is the cause of failure every time as it produces angular distortion. However, as this thesis focuses on polymer deformation the hydrostatic pressure will be discussed in a later chapter. Unlike metals, where deformation is normally considered independent of hydrostatic pressure, in polymers, due to a reduced free volume associated with hydrostatic pressure, hydrostatic pressure effects mechanisms by which yielding can occur.

If we consider that the total stress tensor which is:

$$\sigma = \begin{pmatrix} \sigma_{xx} & \sigma_{xy} & \sigma_{xz} \\ \sigma_{xy} & \sigma_{yy} & \sigma_{yz} \\ \sigma_{xz} & \sigma_{yz} & \sigma_{zz} \end{pmatrix} \quad (\text{Equation 2.6})$$

It can be divided into a hydrostatic stress which involves only pure tension or compression (σ_m) as in equation 2.5 and a deviator stress tensor (I_2) which represents the shear stresses in the total state of stress. It is the postulate of most theories of plasticity that shear stresses which cause permanent shape change (*i.e.* yielding) in ductile materials.

$$I_2 = \frac{1}{6} \left[(\sigma_x - \sigma_y)^2 + (\sigma_y - \sigma_z)^2 + (\sigma_z - \sigma_x)^2 \right] \quad (\text{Equation 2.7})$$

2.4.1 Von Mises Criteria

Prior to yield, material response is assumed to be elastic. The von Mises criterion states that failure occurs when the energy of distortion, or the elastic strain energy "density" (I_2), reaches the same energy for yield/failure in uniaxial tension or compression. Thus the von Mises criterion also satisfies the property that two stress states with equal distortion energy have equal von Mises stress. In 1913, Von Mises proposed that yielding would occur when the deviator stress tensor (I_2) exceeded some critical value [1]. If we let that value be k^2 then

$$I_2 = k^2 \quad (\text{Equation 2.8})$$

We can work out the value at which yielding will occur. To evaluate the constant k we hold that at yielding in a uniaxial or compression tests that $\sigma_x = \sigma_0$, and $\sigma_y = \sigma_z = 0$. For uniaxial tension, σ_0 is positive and negative in compression. However since we are concerned k squared we don't need to consider this in the Von Mises criteria. So:

$$\frac{1}{6} \left[(\sigma_x - \sigma_y)^2 + (\sigma_y - \sigma_z)^2 + (\sigma_z - \sigma_x)^2 \right] = k^2 \quad (\text{Equation 2.9})$$

$$\Rightarrow \frac{1}{6} [(\sigma_0 - 0)^2 + (0 - 0)^2 + (0 - \sigma_0)^2] = \frac{1}{3} (\sigma_0^2) = k^2 \quad (\text{Equation 2.10})$$

$$\Rightarrow \frac{1}{\sqrt{3}} \sigma_0 = k \quad (\text{Equation 2.11})$$

$$\Rightarrow \sigma_0 = \sqrt{3}k \quad (\text{Equation 2.12})$$

Where σ_0 is the intrinsic yield stress of the material. This can also be written as:

$$\frac{1}{\sqrt{2}} \left[(\sigma_x - \sigma_y)^2 + (\sigma_y - \sigma_z)^2 + (\sigma_z - \sigma_x)^2 \right]^{1/2} = \sigma_0 \quad (\text{Equation 2.13})$$

2.5 Introduction to Contact Mechanics

For contact mechanics it is necessary to distinguish between two types of contact, conforming and non-conforming. A contact is said to be conforming if the two bodies "fit" exactly or even closely together without deformation. Bodies which are dissimilar are said to be non-conforming. When brought into contact without deformation they will touch first at some point - a point contact, or along a line - a line contact. Line contact occurs when the profiles of the bodies are conforming in one planer direction and non-conforming in the perpendicular direction. Experiments in this area generally take the form of a body, normally called an indenter, to which a loading force is applied and a sample which undergoes some deformation of interest. This contact may be purely elastic, or it may involve some permanent deformation, or a plastic response, of the specimen, the indenter, or both. The basic theory for contact mechanics is taken from Johnson's Contact Mechanics [5]. The flat punch technique is the primary focus of this thesis and as such it is used for the bulk of the experimental work.

2.5.1 Hertz Theory

Consider the case of nonconforming elastic bodies in contact whose deformation is sufficiently small for the linear small strain theory of elasticity to be relevant. It is inevitable in this case that the area of contact is small compared to the radii of curvature of the undeformed surfaces. The contact stresses are highly concentrated close to the contact region and decreases sharply in intensity with distance from the point of contact. Therefore the region of practical interest lies close to the contact interface. This implies that provided the bodies are large themselves compared to the dimensions of the contact region, the stresses in this region are not critically dependent upon the shape of the bodies at a distance from the contact area, nor how they are supported within the body.

The stresses may be calculated to a good approximation by considering each body as a semi-infinite elastic body bounded by a surface plane. This allows the use of the theory of elasticity which has been developed for the elastic half space.

2.5.2 Indentation by a Rigid Flat Punch

To do this consider the stresses produced in an elastic half space by the dynamic action of a rigid flat punch pushing into the sample [5], as shown in figure 2.3. The punch has a circular flat base of diameter $2a$ and sharp square corners. The base of the punch is aligned with the sample which allows us to simplify the conditions to be plane strain. As the punch is assumed to be perfectly rigid, the surface of the elastic solid must remain flat where it contacts the punch. We assume a perfectly aligned tip so that the punch face remains parallel to the undeformed surface of the solid. Thus the first boundary condition to be identified is one of specific normal displacement. So that the displacement by the tip as it is moved into sample (δ) equals the displacement into the sample (x).

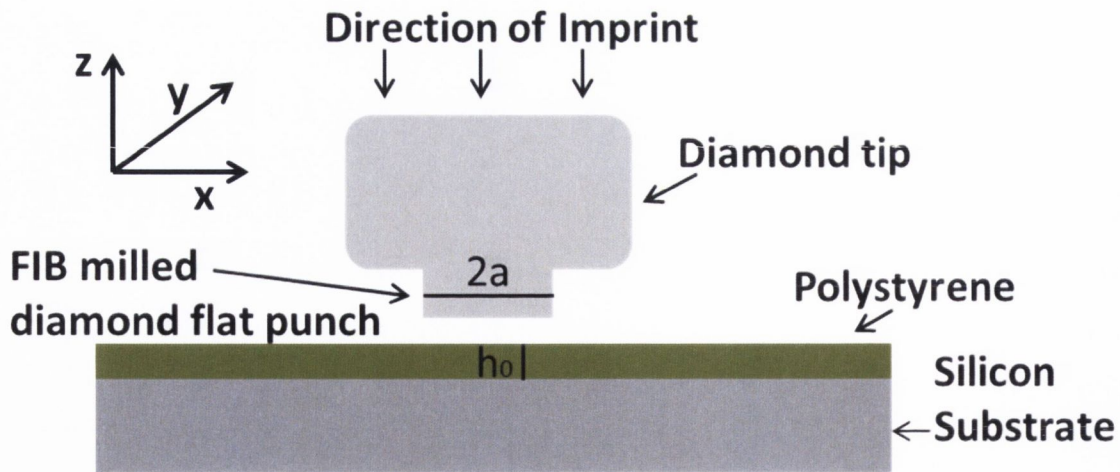


Figure 2.3: Schematic of Flat Punch nanoindentation.

This allows a very simple calculation of engineering strain using equation 2.14. As the area in contact remains constant throughout the indentation, engineering stress can also be calculated in a straightforward manner (equation 2.14). Therefore $\frac{P}{\pi a^2}$ is once again the indentation stress and $\frac{L-L_0}{L_0}$ is taken as the indentation engineering strain.

Therefore the equation for the stress strain curve in flat punch indentation is

$$\sigma = E \left(\frac{L-L_0}{L_0} \right) = \frac{P}{\pi a^2} \quad (\text{Equation 2.14})$$

Geometrically, there is an additional complication at the square edges of the flat punch that leads to Cauchy stress singularities as soon as the punch is in contact with the material.[5].

2.5.3 Introduction to Finite Element Modelling

In recent years nanoindentation has become a standard test for investigating the mechanical properties of materials [2]. This has thus caused increased interest in the analytical understanding of flat punch nanoindentation. To calculate most mechanical properties the stress field must be known. In many cases the subsurface stresses are the most dominant when wishing to understand mechanical behaviour. In the absence of any direct experimental method for measuring these stress fields it is necessary to use numerical techniques. One such technique is Finite Element (FE) Modelling. Since the late eighties this technique has been used, in conjunction with experimental work, to extract E and H from load displacement curves; for example by Doerner and Nix [6] and Oliver and

Pharr [7]. For instance, E can be calculated from the initial slope of the unloading curves using the method of Oliver and Pharr. The FE Method is a numerical technique for finding approximate solutions to partial differential equations, integral equations and their systems. In simplest terms, FE modelling is a method for dividing up a complicated problem into small elements that can be solved in relation to each other. It has proved to be a useful technique, in conjunction with simple material models, for extracting both E and H from the unload section of the nanoindentation curve [6], although the effect of the substrate must be taken into consideration. A general rule of thumb for indentation is that that indent depth should be a maximum of 10% of the original film thickness. After this the substrate begins to have an effect on the mechanical properties measured. While this is sufficient for bulk uniform samples, this becomes an issue when considering compound, or layered structures, particularly in thin layered films. In this situation FE modelling is a particularly effective tool where FE techniques are utilised by matching the simulated loading and unloading curves with the experimental ones. Even as the sample thickness is reduced, these techniques yield useful results, as shown by Bhattacharya and Nix [8] down to a sub micrometre scale. Also, as contact depths are reduced below 50 nm the tip radius does become more important, although work by Yu et al, once again utilising a mix of experimental and FE modelling, has shown that as long as the tip geometry/radius is well known it is possible to use FE modelling to extract E and H from these contact depths [9]. Knapp et al [10] have also shown that FE modelling, in conjunction with nanoindentation, can be used to extract the yield strength, E and H of even ion-beam-modified ultrathin layers of materials independently of the properties of the underlying substrates.

FE modelling has also been utilised for flat punch nanoindentation where it is possible to carry out 2 dimensional rectangular punch indentations or 3 dimensional cylindrical flat punch indentations. 3 dimensional simulations are more detailed and accurate, although there is a time cost to running these simulations.

Yang has found analytical solutions for cylindrical flat punch indentation using FEA in conjunction with perturbation theory that describe the stress state under the flat punch for indentations into compressible elastic thin films bonded to a rigid substrate as aspect ratio tends towards infinity.[11] He found that both the normal stress and the shear stress are inversely proportional to the thickness of the thin film and proportional to the indentation

depth, and are shown in equations 2.15 - 2.17. Here cylindrical polar coordinates (r, θ, z) are used such that the z -axis coincides with the axis of the indenter, the r -axis is perpendicular to the z -axis, and θ is the angular distance between a reference line and the r -axis.

$$\sigma_{zz} = -(\gamma + 2G) \frac{\delta}{h} \quad \text{Equation 2.25}$$

$$\sigma_{rr} = -\frac{\gamma\delta}{h} \quad \text{Equation 2.16}$$

$$\sigma_{rz} = -\mu(\gamma + 2G) \frac{\delta}{h} \quad \text{Equation 2.17}$$

where σ refers to stress, h is the film thickness, G is the shear modulus of the material, γ is the Lamé constant and δ is the indentation depth. What is interesting to notice here is the lack of dependence on friction in these equations, even though it was originally included in the model. This analysis, which also utilises perturbation theory in conjunction with FE modelling, provides an extremely useful approach to evaluate the mechanical properties of ultra-thin films using nanoindentation.

2.5.4 Effect of Stress Singularities', Aspect Ratio and Contact Geometry in Thin film Flat Punch Nanoindentation

Figure 2.4 shows the case of pressure (P) under a flat punch plotted against distance from centre of punch. A represents the frictionless case and B the case of full stick. This schematic is adapted from chapter two of Johnson's Contact Mechanics where full conditions and calculations used in calculating $P(x)$ can also be found [5]. What is significant to notice here is that as x/a approaches 1 the pressure under the punch increases sharply. According to Johnson the pressure reaches a theoretically infinite value at the edges of the punch ($x = \pm a$). The stresses within the material in the vicinity of the corners of the punch were found in 1963 [12] who found that the principal shear stress reaches a theoretical infinite value as x approaches a . Therefore one would expect a real material to yield plastically close to the corners of the punch at even the lightest loads[5].

The second boundary condition in the loaded region depends on the frictional conditions at the interface, but what is shown in figure 2.4 is that by Johnson's analysis the influence of friction on the pressure under the punch is relatively small. This is consistent with findings by Yang who used FE analysis to show that friction under a flat punch has no

effect on the pressure under the punch required to cause deformation for a compressible material at low strain. [11, 13].

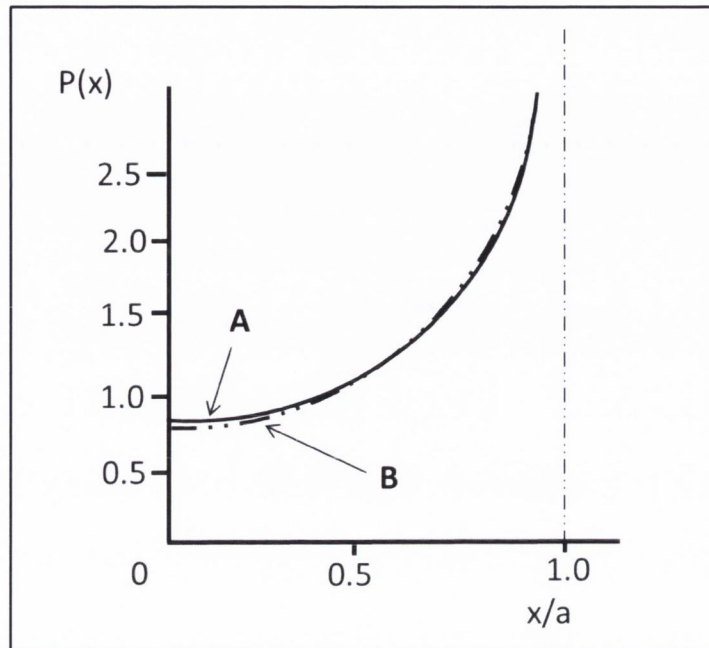


Figure 2.4: Schematic of pressure (P) versus x/a , where x is distance from centre of punch and a is the punch diameter, under a flat punch where Poisson's ratio is taken to be 0.3. A represents the frictionless case and B represents the case of full stick. Adapted from Johnson's Contact Mechanics [5].

However, to expand upon this consider thin film flat punch nanoindentation (TFFPN) in more detail. TFFPN consists of a rigid (diamond in the case of this thesis) flat punch coming in contact with polymer thin film. The polymer thin film is assumed to be rigidly bound to a silicon substrate. Aspect ratio and contact geometry will be dealt with concurrently here.[1]

The effect of changing aspect ratios for indenting flat punches into thin films is expected to have an effect on the pressure required to cause deformation in the materials due to a fundamental change in the flow field. However, in the past carrying out experimental work to test these theories and numerical simulation however has been extremely difficult to do due to difficulties with aligning flat punches and samples. Additionally in other experimental setups, for example cylindrical billet upsetting of metals, friction has been

shown to have a large effect on the mean pressure required for deformation. [1] While this model is different from flat punch indentation it does serve as an experimental comparative starting point for the effect of aspect ratio and friction in TFFPN. This technique of cylindrical billet (Figure 2.5) upsetting whereby a cylindrical sample (billet) is placed between two platens and compressed is in widespread use for measuring the mechanical properties of billets/pillars of various metals. [1, 14-17]

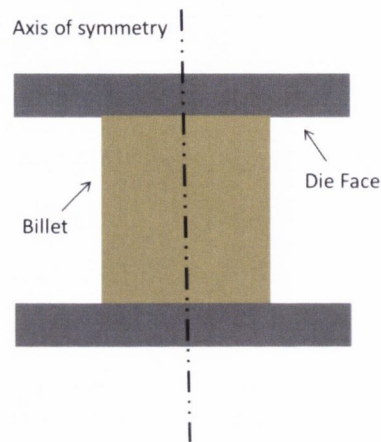


Figure 2.5: Schematic of cylindrical billet upsetting.

However, the question then arises of how similar cylindrical billet upsetting is to TFFPN. It is possible to make an argument that these two geometries can be compared, but as the flow field does change between the two systems this must be taken into consideration. To accomplish this a simple 2 dimensional system is considered (Figure 2.6) which focuses on the movement of the material at the side of the punches. Geometrically, the difference between these two systems is dominated by the infinite film which acts to confine the polymer thin film at the edge of TFFPN (Figure 2.6 a). In cylindrical billet upsetting the material is able to move outwards (Figure 2.6 b) whereas the material in the TFFPN case must move up and around the flat punch.

Analysis comparing these two systems under 2D plane strain conditions has been done by Johnson and Kudo where they considered 2 punches, one above and one below a material that they wished to deform. [18] They used slip line theory to analyse the flow stress in this system where the width of the lower punch was varied to from equivalent to much larger than the upper punch. TFFPN corresponds to the case where there is, effectively, an infinitely wide punch on the bottom with material bonded to the punch, while on top there

is a smaller punch. This means material is able to flow up and around the punch in a similar manner to TFFPN. They assumed that there is a full stick condition between the substrate and the film, similar to Yang's assumption.[19] Their findings show that the difference between a cylindrical billet upsetting experiment and TFFPN experiment is a factor of 2.5 in pressure required for plastic deformation, due to constraining effects of the surrounding material. Therefore in TFFPN yield will appear to occur at 2.5 times the value required in cylindrical billet upsetting and this can be considered to be due to geometrical differences between the two set ups. This is closely related to the constraint correction factor connecting indentation hardness to tensile yield stress discovered by Tabor for indentation using various tip geometries, [20] and well predicted by slip-line field analysis.[1] The Tabor factor, which arises from the constraining elastic hinterland that surrounds all indents, was found to be close to 3 for metals and to range from 1.5 to 2 for polymers.

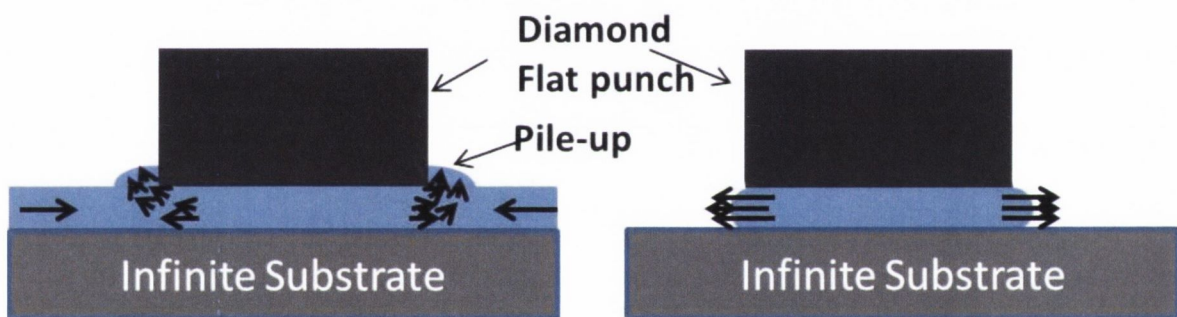


Figure 2.6 a) 2 dimensional schematic of material flow in TFFPN. Note the pile up at the side of the punch, and the way the material must move up and around the punch due to the material confinement as a result of the infinite film (represented by the arrows pointing in towards the flat punch). b) 2 dimensional schematic of material flow in cylindrical billet upsetting. Here the material is not confined and simple moves outwards.

A simple linear model to explore the effect of aspect ratio and geometry, inspired by a cylindrical billet upsetting model,[1] will be used in this thesis. The stress at which the material begins to yield in TFFPN, which is known as the forming stress (FS) throughout this thesis will be plotted against the aspect ratio, where aspect ratio is defined as the radius of the punch (a) over the original film thickness (h).

At this stage we can refer to Johnson and Kudo's analysis that shows that for TFFPN the stress required for plastic flow will be 2.5 times higher due to the confining effect of the surrounding material (Figure 2.6). As this result arises from a rigid plastic analysis more akin to metal deformation, we expect, following the Tabor parameter scaling, a value of about half to two-thirds of this for polymer systems. [2]

2.6 Yielding of Polymers

When solid polymers are subjected to a stress of sufficient magnitude they virtually all undergo a permanent shape change. Here, we are interested in the onset of this irreversible deformation, or the transition from elastic to plastic behaviour in glassy polymers. The area of mechanics of bulk glassy polymers has been addressed extensively over the past 40 years [4, 21-23], with a lot of research been carried out on the mechanisms through which these materials deform.

2.6.1 Conventional (Bulk Scale) mechanical testing of polymer glasses

In macroscopic mechanical testing of bulk polymer glasses, uniaxial tensile deformation is the most commonly used test. Specimens such as those shown in figure 2.7, with rectangular gauge sections of initial length (l_0) and cross-sectional area (A_0) are clamped at the larger gripping portions and extended at a constant rate. The stretching force (F) is recorded as a function of increasing length (l) of the gauge section. Within the uniaxial gauge section the uniaxial stress is calculated as in equation 2.1. Where the area $A \leq A_0$, as during elastic extension along the y -axis A decreases.

A schematic diagram of engineering stress versus engineering strain is shown in figure 2.7. Initially the material deforms elastically, before a collection of shear zones occur at the peak load or nominal yield stress. The neck evolves during the load drop after which the stable neck propagates along the gauge section. Stress then rises when the neck advances into the clamping region.

Other tests that are uniformly carried out involve repeating these tests while varying the temperature and strain rate as polymers are a time and temperature dependent materials. The theory regarding this rate dependence is presented in Chapter 3, but here it should be noted that as one would expect from temperature and time dependent polymers, that the

strain rate ($\dot{\epsilon}$) increases as σ increases, and as temperature (T) increases σ decreases. This is shown below in figure 2.8 for conventional tensile testing of polycarbonate PC [4].

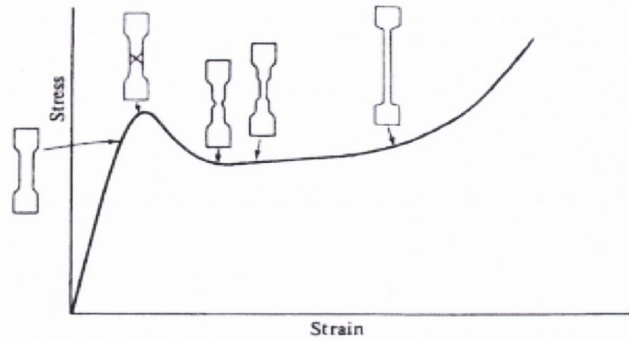


Figure 2.7: A schematic diagram of nominal stress vs. nominal strain of a conventional tensile test when the sample necks. Initially the material deforms elastically, before localised shear bands form just before or at the load maximum. The neck then evolves during the following load drop after which the stable neck propagates along the gauge section. Stress then rises when the neck extends towards the clamping region. This graph is adapted from page 163 of *The Physics of Glassy Polymers* [4].

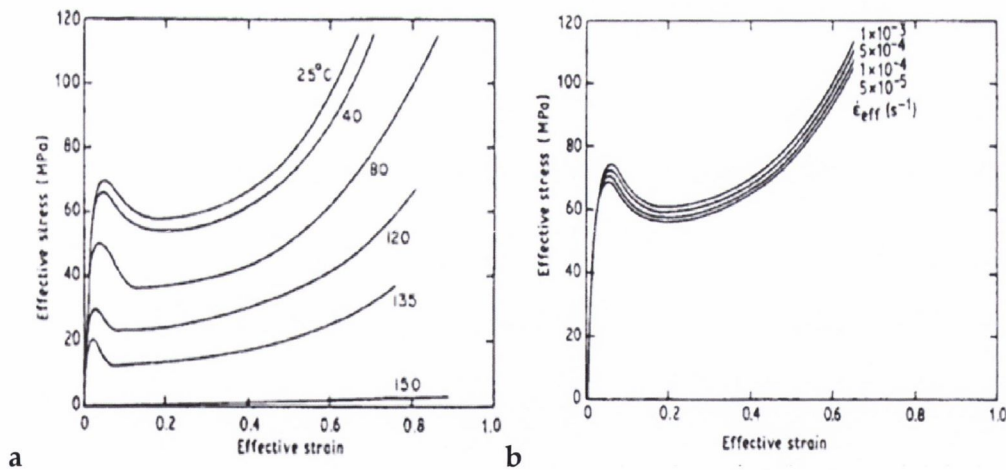


Figure 2.8: a) shows tensile stress vs. strain behaviour of polycarbonate (PC) at a constant strain rate at various temperatures from 25° C to 150° C. Yield stress and yield strain increase as temperature is lowered. b) shows tensile stress vs. strain behaviour of PC at constant temperature but with strain rate dependence varying between 1×10^{-3} to 5×10^{-5} . As the strain rate decreases the yield stress and yield strain decrease also. Both once again adapted from *The Physics of Polymer Glasses*. [4]

Another characteristic of glassy polymers is the sample preparation history dependence *i.e.*, whether samples are quenched from the liquid state or annealed (slowly cooled). The yield point is much higher for annealed samples than for quenched, although the yield strain point occurs at the same point [4, 24]. Pressure also has an effect on the yield point in glassy polymers. In conventional tensile stress strain tests the yield stress and yield strain increase with increasing pressure. Strain softening is another characteristic of complex soft matter systems such as polymers. It takes place in such materials after the yield point has been reached; deformation continues to occur at loads lower than the yield point. Strain softening is demonstrated in figure 2.8, where after the yield point is reached there is a drop in effective stress as effective strain increases.

Another important consideration to understand polymer deformation is the uniformity of the plastic flow field. In macroscopic deformation, shear bands can develop, the nature of which depends on the thermal history of the sample [25]. Shear bands are localised regions of plastic flow where the material has undergone high strain deformation. Under simple compression and tension, these tend to nucleate at an angle of 45 degrees to the loading direction. Other non-elastic responses include crazing but these are not the focus of discussion in this thesis. Optical micrographs of shear bands in a bulk sample are shown in figure 2.9, where intense shear bands in slowly cooled PS and quenched PS are shown, where both bulk samples were deformed in the same manner [4]. The slowly cooled sample shows localised deformation which can be seen by the thin shear bands throughout the sample (figure 2.9 a).

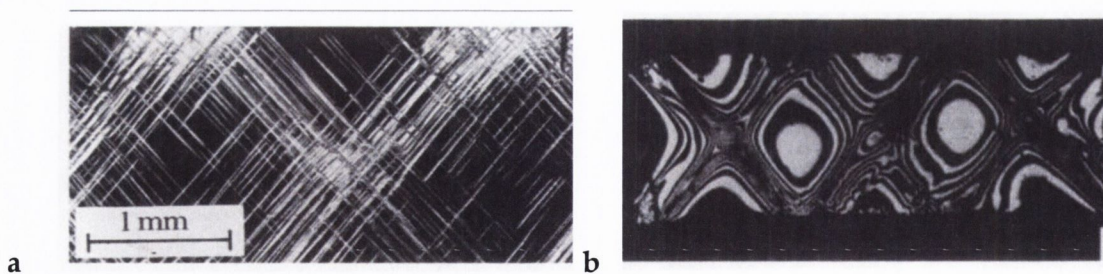


Figure 2.9: a) Intense shear bands in slowly cooled PS deformed at room temperature. b) Shear bands formed in quenched PS deformed in the same manner. These images are adapted from reference [4].

The quenched sample deformed in a uniform manner which can be seen by the thick shear bands throughout the deformed sample (figure 2.9 b). This is shown for bulk samples, but how materials deform on the nanoscale in terms of the plastic flow field is not as clear-cut where flow field visualization techniques are incredibly difficult.

2.7 Advantages of Flat Punch Nanoindentation for Mechanical Testing of Polymers

A well aligned, high aspect ratio of the punch to film thickness allows measurement of soft material film properties to dimensions much smaller than conventional nanoindentation [26]. This experimental approach has yielded access to the mechanical properties of both thick [27] to thin polymer films from the glassy to the melt state [28]. Using this technique there is a clear distinction between elastic and plastic deformation within a material. For a polymer in the glassy state a step like feature corresponding to the yield point of the material is clearly identified, while in the melt state this step is quenched. It has also been shown by this flat punch indentation method the yield point in the stress strain curves can be suppressed by increasing the temperature, while increasing the strain rate has the effect of reducing the yield point; proving the validity of this method for accessing material properties of ultra-thin polymer films.

With flat punch indentation a certain characteristic signature of indentation for a film of elastic-plastic material (figure 2.10) is expected. From this we infer with increasing strain, successive regimes of elastic deformation and an elastic to plastic transition at a specific yield point followed by a post yield elastoplastic flow. After the elastoplastic flow the effect of the substrate elasticity when the film has become very thin can be seen, followed by a hold section where creep is calculated. After creep is calculated the unload process is carried out. Figure 2.10 shows this characteristic graph for a 52 nm thin film of PS ($M_w = 9000K$ and $R_g = 84$ nm). The punch used was a 400 nm diamond flat punch with a punch face roughness of 2-3 nm. This punch face roughness and any misalignment of the flat punch leads to contacting defects in the contacting zone. The strain at the yield point appears to be high due to these contacting defects and also the effect of hydrostatic pressure.

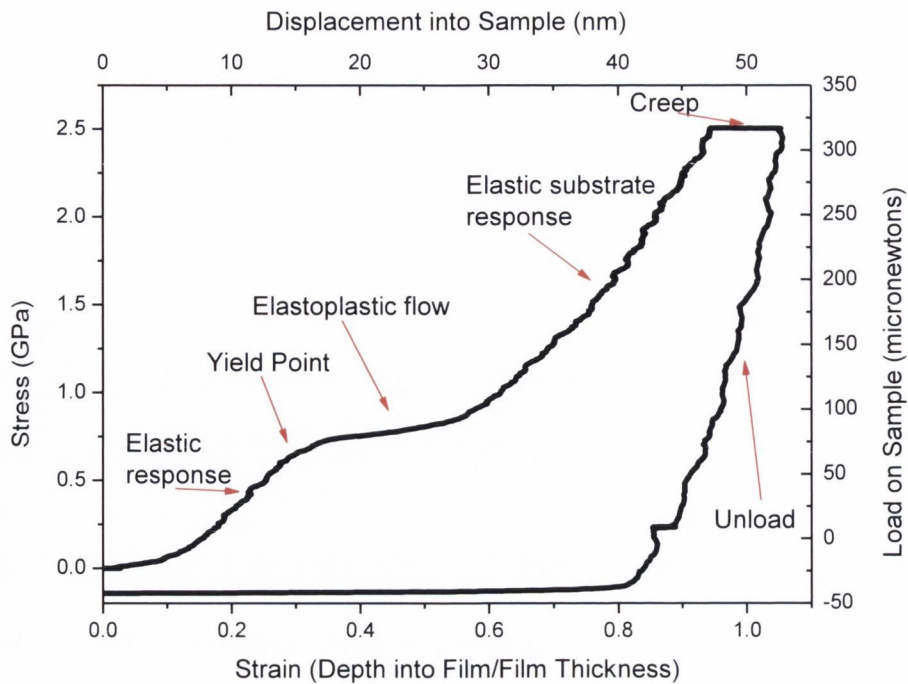


Figure 2.10: A characteristic graph of flat punch indentation into an ultra-thin film of Polystyrene. The punch used was a 400 nm diamond flat punch and the film thickness was 52 nm. Full contact was established at 6 nm and the strain at yield point appears to be high due to contacting defects.

What is very important to note here is the similarity figure 2.10 has with figure 2.7. Both graphs show clear elastic regions and yielding regions simply from carrying out either the tensile test or the flat punch nanoindentation. Therefore there is a clear correlation between macroscopic conventional mechanical testing and flat punch nanoindentation, which allows identification of the yield point in a material.

Thin film flat punch indentation specifically allows the measurement of mean stress vs. engineering strain signals in an experiment. The question addressed in this thesis is how well can these curves can be used to extract the intrinsic elastic modulus (E) and yield stress (YS) material parameters, for instance in a simple picture where one assumes behaviour can be adequately captured by an elastic-plastic constitutive law. With this in mind two terms are introduced, contact modulus (CM) and forming stress (FS). CM is related to E in that it corresponds to the slope of the initial linear section of the stress strain curve in flat punch nanoindentation which is associated with the elastic section of the indent. FS is related to YS in that it corresponds to the “knee” in the stress strain curve that

corresponds to the transition from elastic to plastic behaviour in flat punch nanoindentation. This can be seen in figure 2.10 as the region of the nanoindentation curve which is highlighted as the point where the material begins to yield. However, CM and FS are not directly equivalent to E and YS as aspect ratio, friction and hydrostatic pressure may cause CM and FS to vary from the intrinsic material values calculated using other techniques.

2.8 References

- [1] G. E. Dieter, *Mechanical Metallurgy*, 3rd ed.: McGraw-Hill Book Company (UK) Limited, 1988.
- [2] A. C. Fischer-Cripps, *Nanoindentation*, 2nd Edition ed. New York Springer-Verlag, 2004.
- [3] B. Bhushan, *Handbook of Micro/Nano Tribology, Second Edition*: Taylor and Francis, 1998.
- [4] R. N. Haward and R. J. Young, *The Physics of Glassy Polymers*. London: Chapman And Hall, 1997.
- [5] K. L. Johnson, *Contact Mechanics*, 1 ed. Cambridge: Cambridge University Press, 1985.
- [6] M. F. Doerner and W. D. Nix, "A method for interpreting the data from depth-sensing indentation instruments," *Journal of Materials Research*, vol. 1, pp. 601-609, 1986.
- [7] W. C. Oliver and G. M. Pharr, "An improved technique for determining hardness and elastic modulus using load and displacement sensing indentation experiments," *Journal of Material Research*, vol. 7, 1992.
- [8] A. K. Bhattacharya and W. D. Nix, "Finite element simulation of indentation experiments," *International Journal of Solids and Structures*, vol. 24, pp. 881-891, 1988.
- [9] N. Yu, A. A. Polycarpou, and T. F. Conry, "Tip-radius effect in finite element modeling of sub-50 nm shallow nanoindentation," *Thin Solid Films*, vol. 450, pp. 295-303, 2004.
- [10] J. A. Knapp, D. M. Follstaedt, S. M. Myers, J. C. Barbour, and T. A. Friedmann, "Finite-element modeling of nanoindentation," *Journal of Applied Physics*, vol. 85, pp. 1460-1474, 1999.
- [11] Y. Fuqian, "Axisymmetric indentation of an incompressible elastic thin film," *Journal of Physics D: Applied Physics*, vol. 36, p. 50, 2003.
- [12] A. Nadai, *Theory of Flow and Fracture of Solids* vol. 2. New York: McGraw-Hill, 1963.
- [13] F. Yang, "Asymptotic solution to axisymmetric indentation of a compressible elastic thin film," *Thin Solid Films*, vol. 515, pp. 2274-2283, 2006.
- [14] H. Zhang, B. E. Schuster, Q. Wei, and K. T. Ramesh, "The design of accurate micro-compression experiments," *Scripta Materialia*, vol. 54, pp. 181-186, 2006.
- [15] J. Greer and W. Nix, "Nanoscale gold pillars strengthened through dislocation starvation," *Physical Review B*, vol. 73, 2006.
- [16] G. Lee, J.-Y. Kim, M. J. Burek, J. R. Greer, and T. Y. Tsui, "Plastic deformation of indium nanostructures," *Materials Science and Engineering: A*, vol. 528, pp. 6112-6120.
- [17] W. D. Nix, J. R. Greer, G. Feng, and E. T. Lilleodden, "Deformation at the nanometer and micrometer length scales: Effects of strain gradients and dislocation starvation," *Thin Solid Films*, vol. 515, pp. 3152-3157, 2007.
- [18] W. Johnson and H. Kudo, "The compression of rigid-perfectly-plastic material between rough parallel dies of unequal width," *International Journal of Mechanical Sciences*, vol. 1, pp. 336-341, 1960.

- [19] F. Q. Yang, "Asymptotic solution to axisymmetric indentation of a compressible elastic thin film," *Thin Solid Films*, vol. 515, pp. 2274-2283, Dec 2006.
- [20] D. Tabor, *The Hardness of Metals* Oxford University Press., 1951.
- [21] C. A. Schuh, T. C. Hufnagel, and U. Ramamurty, "Mechanical behavior of amorphous alloys," *Acta Materialia*, vol. 55, pp. 4067-4109, 2007.
- [22] A. M. Mayes, "Glass Transition of Amorphous Polymer Surfaces," *Macromolecules*, vol. 27, pp. 3114-3115, 1994.
- [23] G. F. Meyers, B. M. DeKoven, and J. T. Seitz, "Is the molecular surface of polystyrene really glassy?," *Langmuir*, vol. 8, pp. 2330-2335, 1992.
- [24] O. A. Hasan and M. C. Boyce, "Energy storage during inelastic deformation of glassy polymers," *Polymer*, vol. 34, pp. 5085-5092, 1993.
- [25] J. C. M. Li, "Behavior and properties of shear bands," *Polymer Engineering & Science*, vol. 24, pp. 750-760, 1984.
- [26] G. L. W. Cross, B. S. O'connell, J. B. Pethica, H. Rowland, and W. P. King, "Variable temperature thin film indentation with a flat punch," *Review of Scientific Instruments*, vol. 79, pp. 013904-13, 2008.
- [27] H. G. H. van Melick, O. F. J. T. Bressers, J. M. J. den Toonder, L. E. Govaert, and H. E. H. Meijer, "A micro-indentation method for probing the craze-initiation stress in glassy polymers," *Polymer*, vol. 44, pp. 2481-2491, 2003.
- [28] H. D. Rowland, W. P. King, J. B. Pethica, and G. L. W. Cross, "Molecular Confinement Accelerates Deformation of Entangled Polymers During Squeeze Flow," *Science*, vol. 322, pp. 720-724, October 31, 2008 2008.

Chapter 3 Theory: Polymer Physics

This section introduces the basics of polymer materials and some of their key structural and mechanical features. Amorphous polymers and what constitutes the glassy state are then discussed and block copolymers (BCPs) introduced. This is followed by a discussion on plastic deformation in bulk glassy polymers and an introduction to some of the key models that deal with the elastic to plastic transition in polymer glasses. Key results of conventional mechanical testing of bulk polymers are presented before the effect of pressure on the deformation behaviour of polymers are discussed. Hydrostatic pressure is an important side effect of flat punch nanoindentation and so must not be neglected. The motivation for scaling right down to nanoscale and nanoindentation are presented. Yield processes in thin films and results to date are also discussed and expanded upon.

3.1 Polymer Materials

Polymers, also known as macromolecules, are made up of a large number of molecular units. They are often measured in the hundreds of thousands of atomic mass units and are linked together by covalent bonds. The first polymers used were natural products like cotton, starch proteins and wool. Artificial polymers first began to be synthesised in the twentieth century. Bakelite and nylon were amongst the most important polymers synthesised, although the scientists of the day did not understand many of the chemical structures and physical properties that resulted. Key aspects of polymer science include molecular weight, molecular weight distribution and the organisation of the atoms in the polymer chain. These aspects affect the relationships between polymer structure, morphology and physical and mechanical behaviour.

A polymer is essentially made up of many (poly) short structures which repeat, called mers, which are the building blocks of the chain. For example polyethylene is a particularly simple structure and is made up of many (poly) ethylene structures (mers) (Figure 3.1).

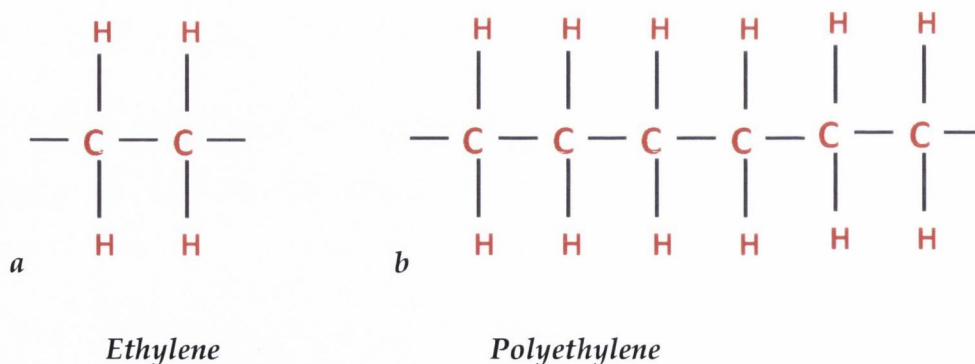


Figure 3.1: an example of a polymer chain; polyethylene

Many polymers crystallise, and the size, shape and organisation of the crystallites depend on how the polymer was crystallised. Effects like annealing are very important as they have a strong influence on the final state of the molecular organisation. Other polymers are amorphous as their chains are too irregular to allow regular packing. These polymers will appear to be in a glassy state, although when heat is applied they will pass from this glassy state to the rubbery state with the onset of chain molecular motion. Entanglement is another important aspect of polymers. This is when long chains of polymers become entangled together, which helps strengthen the material when it experiences stress. In the melt state these entanglements also cause the viscosity to be raised significantly. The mechanical properties of polymers that will be focused on in this section are elastic modulus and contact stress. In addition, the theory behind activation volumes and activation energies generated by the Eyring model will be presented, as well as additional polymer models.

3.2 Block Copolymers

Block copolymers (BCPs) consist of two or more distinct polymer chains covalently bonded together to form a more complex macromolecule. If the constituent polymers are immiscible, phase separation on the same scale as the copolymer chains can be induced, meaning thin films of BCPs can be characterised by their highly oriented domain [1].

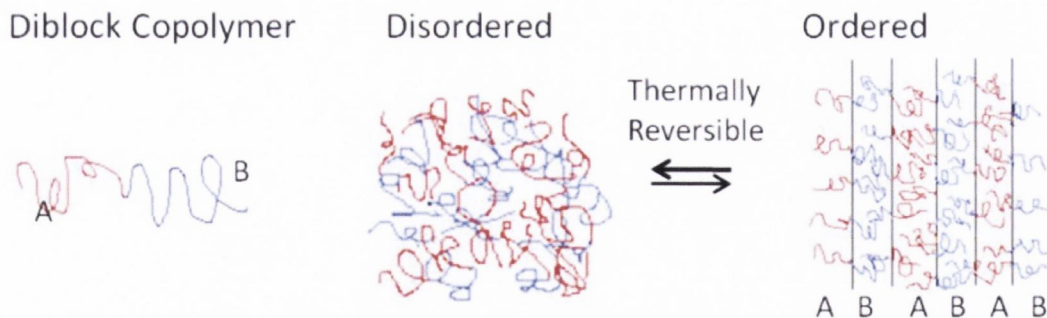


Figure 3.2: Block Copolymer representation. A and B represent the two joined polymers respectively. Image shows schematic representation of the block copolymer in disordered and ordered state.

In recent times BCPs have begun to be seriously considered for nanotechnological applications. They are ideal templates for creating nanostructures including porous membranes, arrays of quantum dots, metal dots and wires and nanocrystals which have been used in devices such as flash memory [2-4]. While these thin films of phase separated polymers can be imaged using atomic force microscopy (AFM)[5, 6] and scanning electron microscopy (SEM)[4] it is impossible to access their mechanical properties using conventional testing techniques.

3.3 Amorphous Polymer Glasses

Many materials can be found in the glassy state. The transition to the glassy state for materials can be considered via the rapid increase in viscosity that occurs when liquids are cooled and crystallization does not occur. Most simple compounds, such as metals, crystallise on cooling below their melting temperature. In more complex materials, such as polymers, the rate of crystallization may be so slow that a glass is formed before a significant proportion of the material has crystallised. In some other cases, especially with polymers that have a low level of structural symmetry, *e.g.* atactic vinyl polymers, the crystallisation of the material is not possible and the glassy state is the natural state of the polymer at low temperatures. Synthetic glassy polymers have been developed since the 1950's and were first developed for use as thermoplastics.[7]

3.4 The Glass Transition

The glassy state can be characterised from an experimental point of view through the changes that occur in the material as it is cooled at constant pressure. Once the glass forming material is cooled below its melting state a super cooled liquid is obtained. The viscosity of the liquid increases rapidly as the temperature decreases until a situation is reached where the intermolecular rearrangement is slow compared with the time scale of the experiment. At this point the material can be considered to be in the glassy state after passing through its glass transition temperature (T_g).

The glass transition temperature is a highly discussed topic, mainly due to its incredibly complex nature, whereby it is not a true second order thermodynamic transition but rather appears to be a kinetic phenomenon; there is still some debate on this matter [8, 9]. In a true first order thermodynamic transition the free energy as a function of any given state variable is a continuous function, but the first partial derivatives of the free energy with respect to the relevant state variable are discontinuous. The signature of the glass transition is a break in a property, (for example volume or enthalpy) or a sudden change in its derivative, (for example heat capacity or coefficient of thermal expansion). None of these are examples of first order thermodynamic transitions, but they are signs that some change is occurring at T_g . An alternative definition of T_g is when the time taken for a relaxation is of the order of 100 seconds. This great increase in relaxation times upon cooling a system in the neighbourhood of this glass temperature is associated with the decrease to very small values in the number of configurations available to the system in this region.[8] Most results discussed in this thesis refer to polymers below T_g , therefore this is the area of great importance.

3.5 Relevant Length Scales in Polymers

The Kuhn segment length (b_0) is the basic scale for specifying the size of a chain segment. For flexible polymers the Kuhn segment varies between 6 and 12 mers and has a value of eight mers for polystyrene (PS), corresponding to a length of 1.8 nm and 6 mers for Poly (methyl methacrylate) (PMMA) corresponding to a length of 1.7 nm.[10] The Kuhn Segment also encapsulates the idea of how far one must travel along a chain until the

memory of the starting direction is lost, that is, the segment has an orientation independent of its adjacent elements. Additionally, the Kuhn segment is also related to the persistent length of a polymer (p) with $2p = b_0$. [10]

3.5.1 Relevant Length Scales: The Random Coil Model

The random coil model, sometimes called the Gaussian coil, describes the conformation of a polymer chain in space. For a random linear polymer coil obeying Gaussian statistics the end to end distance squared depends on the molecular weight (M_w) such that a polymer of molecular weight is made up of a chain of N links, each of length b_0 , able to point in any direction independent of each other.

$$\langle R \rangle = b_0 \sqrt{N} \quad (\text{Equation 3.1})$$

This derivation can be found in Doi and Edwards. [11]

However, since all objects possess a radius of gyration this can be used to characterise the size of a polymer of any architecture. The radius of gyration of a polymer (R_g) is defined as the average square distance between monomers in a given conformation and the polymer's centre of mass [12].

$$\langle R_g^2 \rangle = \frac{b_0^2 N}{6} = \frac{\langle R \rangle^2}{6} \quad (\text{Equation 3.2})$$

The first molecular theories concerned with the motion of polymer chains were developed by Rouse and Bueche [7, 10]. This model considers a polymer chain to be made up of a series of equal submolecules each long enough to obey a Gaussian distribution function, i.e. each submolecule is a random coil in its own right. In this model every submolecule is replaced by a bead of mass M connected by springs with a Hooke's constant. The shortest relaxation time of the Rouse model is the time it takes a monomer to relax. The longest relaxation time is called the Rouse time and is the time taken for an entire chain to relax.

3.5.2 de Gennes' Reptation Theory; How Polymers Move

While the Rouse-Bueche theory was successful in establishing the idea that chain motion was responsible for creep, relaxation and viscosity, quantitative agreement with

experiment was less satisfactory. Hence de Gennes introduced his theory of reptation of polymer chains[13, 14]. His model consisted of a single polymeric chain trapped inside what can be imagined to be a three dimensional tube. The chain is not allowed to go outside the tube, but it is allowed to reptate along it. The chain is assumed to have certain “defects”, and these defects are allowed to migrate along the chain in a type of defect current. The reptation motion yields forward motion when a defect leaves the tube at an extremity, and then can assume various new conformations. Using this model de Gennes found that the self diffusion coefficient D , of a chain in one of these tubes depends on the molecular weight (M_w) as

$$D \propto M_w^{-2} \quad (\text{Equation 3.3})$$

Numerical values of the diffusion coefficient in bulk systems have a range of 10^{-12} to 10^{-6} cm/s in the melt state.

de Gennes also developed a model to try and explain why there are variations in T_g as polymer film thickness is reduced. This is presented in more detail in section 3.8.1.

3.6 Relaxation in Glassy Polymers

Below T_g large scale translational and rotational rearrangements are not energetically accessible. However the complex structure of glass forming liquids means that more localised molecular or atomic rearrangements are possible below, and often well below T_g [47]. The majority of the measurements presented here, using flat punch nanoindentation, are taken at room temperature, which for the polymers PS and PMMA is approximately 80-90 degrees below T_g . Therefore this discussion will focus on the type of relaxations that can occur in polymers in the glassy state. In addition the effect of pressure on the different types of relaxation will be discussed using results from different techniques, e.g. broadband dielectric spectroscopy and mechanical measurements. These results help shed light on the effect that hydrostatic pressure has in flat punch nanoindentation, and nanoindentation in general, for polymers below. This is a very different effect than the well known T_g hydrostatic pressure dependence which also occurs in polymers. [9]

3.6.1 The Effect of Hydrostatic Pressure yielding in Polymers

The effect of hydrostatic pressure on the glass transition temperature (T_g) has been introduced and discussed briefly above. In quantitative measurements via broadband dielectric spectroscopy (BDS), for PS and PMMA, pressure was found to have the effect of increasing T_g by 0.3° per MPa [9, 15]. T_g is commonly associated with the α relaxation, which refers to the relaxation. Such a system can be viewed as seeking a minima on an (effective) local free energy landscape[16]. Using BDS it was found that increasing hydrostatic pressure had the effect of moving the α -relaxation to lower frequencies, and due to the α -relaxation association with T_g this is where this calculation of pressure dependency on T_g originates.

The effect of hydrostatic pressure on elastic modulus and yielding in a polymer material is less studied. Quinson et. al. show an increase in pressure results in a shift of α molecular relaxations towards higher temperatures, while having a lesser but still noticeable effect on the weaker β relaxations. The separation of the α and β relaxations was done by considering the theoretical temperature dependence of the two relaxation modes. Quinson showed their results, obtained by testing via uniaxial tension and uniaxial compression, are supportive of the results obtained from BDS below T_g presented in the next section. They also showed that the cooperative molecular motions that lead to yielding are of the same nature of motion that produces α relaxation. In particular they are closely linked to the motions associated with the low temperature side of alpha relaxation. It has been postulated that pressures up to 100 MPa the yield stress depends linearly on pressure. Therefore

$$\tau_i = \tau_{\text{octo}} + nP \quad (\text{Equation 3.4})$$

here τ_i is the yielding shear stress, τ_{octo} is the octahedral shear stress related to the deviatoric stress introduced in chapter 3, P is the hydrostatic pressure and n is the pressure coefficient which quantifies the yield stress sensitivity to pressure. A value for n has been quantified by Spitzig and Richmond [17] for polyethylene (PE) and polycarbonate (PC) in very thorough experiments where the hydrostatic pressure was increased from 0.1 MPa (atmospheric pressure) to 1104 MPa in tensile and compressive testing at room

temperature. They found an observable effect that pressure moves the yield point to a higher strain (yield strain) and has the effect of increasing the yielding value by $n = 0.18$ Mpa per Mpa of pressure in Polyethylene and $n = 0.14$ in Polycarbonate. Quinson et al[18] also measured n and found it to be 0.18 for PS at 20°C and 0.23 for PMMA for 20°C, numbers which are in good agreement with Spitzig and Richmond. Pressure has also been shown to have the effect of increasing the elastic modulus in polymers.[17, 19]

3.6.2 Relaxations Modes in Polymers

Amorphous polymers exhibit multiple relaxation processes ranging from local relaxations to cooperative relaxations to end-to-end vector relaxation which gives rise to another slower dynamic referred to as normal mode. The two main modes of structural relaxation are called α -relaxations and β -relaxations.

The α transitions refers to relaxation via cooperative rearrangement of molecules which allows molecular chains to slide past each other[8] and is the main relaxation related to T_g . Hydrostatic pressure in dielectric measurements has been shown to have a large effect on α relaxation. With increasing pressure, and hence increasing densification, it becomes increasingly difficult for the polymers to find the volume to accommodate the large scale movements required for α relaxation. This has the effect of increasing T_g with increasing pressure. This has been measured to be 0.3 degrees per MPa in PS and PMMA[9, 15].

The β transitions correspond to local structural relaxations such as sub segmental relaxations, for example the reorientation of an ester side group, and are a much higher frequency dependent relaxation mode.[20] According to dielectric spectroscopy there are two types of β -relaxations, fast and slow. It is this relaxation that dominates in the glassy region.

The β -relaxation often involves a localised motion of a small segment of the chain. However it can also be as a result of a whole of a side group moving from one potential energy minimum to another, although without necessarily making a complete rotation.[7] Since in the glassy state there is less free volume for large scale cooperative motion of molecules (α relaxation), it is the β -relaxation which is more prominent. However most

techniques do not differentiate clearly between relaxation modes, therefore they tend to get clumped together and treated as a uniform topic. However as we will see, β -relaxations are affected differently by hydrostatic pressure than α -relaxations, therefore what we expect to happen at and around T_g is very different from what occurs 80 degrees below T_g .

The complex structure of glass forming liquids means that localised molecular or atomic rearrangements are possible below, and often well below T_g [21]. The effect of pressure on the α transition is not enough to warrant the expectation that at room temperature, in the glassy polymer state, pressure will have the same effect on elastic modulus or yield strength. However results from Spitzig and Richmond[17] do indicate a similar type of dependence, although on a lesser scale of approximately 0.14 MPa per MPa for PC and 0.18MPa per MPA for Polyethylene for yield as opposed to 0.3 °C (or MPa) per MPa that is seen for the T_g of PS. Quinson et al [22] have measured the pressure dependency for PS to be 0.19 MPa/MPa and for PMMA to be 0.23 MPa/ MPa.

3.6.3 Effect of Pressure on Relaxation modes in Polymers

The β relaxations correspond to local structural relaxations known as sub-segmental relaxations, for example the reorientation of an ester side group and are a much higher frequency dependent relaxation mode. [20] In PMMA, the reorientation of an ester side group is an example of a beta relaxation. [7] Since in the glassy state there is less free volume for large scale cooperative motion of molecules, it is short range relaxations which are the more prominent. Many experimental techniques are unable to differentiate clearly between relaxation modes; therefore they tend to get treated as a uniform relaxation mode. In contrast to larger scale molecular motions the shorter scale appears to be not as sensitive to pressure. [18, 22, 23] It is this relaxation mode that appears to dominate at room temperature in PS and PMMA so is of keen interest in this discussion. The measurements presented here using flat punch nanoindentation are taken at room temperature, which for both these polymers is approximately 80-90 degrees below T_g .

Below T_g large scale translational and rotational rearrangements are not energetically available. However the complex structure of glass forming liquids means that more localised molecular or atomic rearrangements are possible below, and often well below T_g

This has been measured by Quinson et al [22] who found the pressure dependency for PS to be 0.19 MPa/MPa and for PMMA to be 0.23 MPa/ MPa.

3.7 Effects of Confining Polymers to Nanoscale Dimensions

Scaling down from bulk to nanoscale experiments is not trivial. Since Keddie, Jones and Cory's pioneering paper in 1994 on the size dependent depression of T_g in polymer films this topic has been a hugely controversial topic,[24] with many conflicting results.

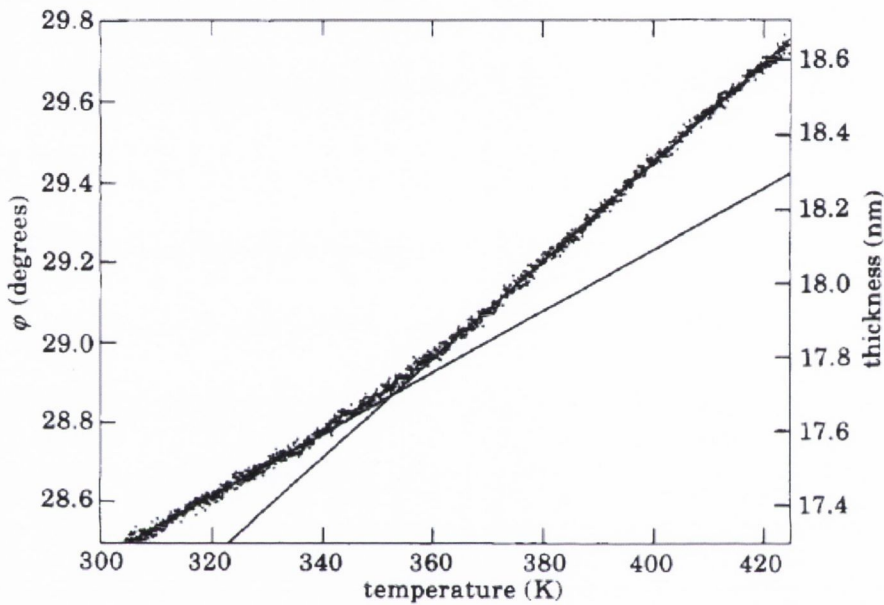


Figure 3.3: Typical data from an ellipsometric scan reproduced from Keddie et al.[24] This sample (MW = 900 000), initially 17.3 nm thick, shows a T_g of 353 K. Approximate film thickness is shown on the right axis. The scan was conducted with radiation having a wavelength of 387.5nm and an angle of incidence of 80° .

Keddie *et al.* measured the T_g of thin polystyrene films as a function of film thickness via an ellipsometry technique that calculated the discontinuity in expansivity as the films were heated at a constant rate. They found that the glass transition decreases in temperature as the thickness of the film is reduced. In addition they found the effect is not strongly molecular-weight dependent, ruling out chain confinement as the major cause; instead they suggested that at the surface of the glassy film is a liquid-like layer whose size diverges as the glass transition temperature is approached from below.

They measured values of the glass transitions for three different molecular weights of polystyrene, each measured at about 15 different thicknesses, plotted against the film thickness. They found thick films approached a constant bulk value which is close to that measured by other techniques. For the molecular weights used, the small molecular weight dependence of the T_g (bulk) temperature was found to be insignificant. When the films are thinner than a few tens of nanometres, substantial reductions in T_g are apparent. They fitted their data to the function

$$T_g(d) = T_g(\text{bulk}) \left[1 - \left(\frac{A}{d} \right)^\delta \right] \quad (\text{Equation 3.4})$$

where d is the film thickness, A is the characteristic length (3.2 nm), $\delta = 1.80$ and $T_g(\text{bulk})$ is 374 K.

However the effect on T_g of confining polymers to these nanoscale geometries is not fully understood. Indeed there are multiple reports that show that the glass transition temperature decreases, increases, remains the same, or even disappears depending upon details of the experimental conditions or molecular simulation conditions.[9] Matz *et al.*, the authors of an excellent 2005 topical review state that different behaviours have been observed for the same material depending on the experimental methods used. Importantly, they conclude that the vast majority of the experiments they discuss have been carried out carefully and the results are reproducible. They also conclude that the existing theories of T_g are unable to explain the range of behaviours seen at the nanometre size scale, in part because the glass transition phenomenon itself is not fully understood.

Recently it has been suggested that measurement of anomalous T_g values may be a result of film preparation history, with independent groups showing when some systems are sufficiently annealed, the apparent film thickness dependency of T_g disappears[25, 26]. Other researchers have found that when polymers are confined to film thickness approximately equal to the molecular chain radius of gyration R_g , the material softens[27, 28] and enhanced inelastic strain is observed for a given stress[29]. In addition, as films are reduced to less than approximately 40 nm, a thickness dependent reduction in modulus[30, 31], yield and simultaneously in modulus and yield [us] [29] has been found. The modulus effect may not be universal, but instead depend on chain flexibility[32] with

flexible polymers such as PS and PMMA showing reduction, while polymers with, for example, backbone rigidity due to bicyclic (norbornyl) units having a modulus independent of film thickness. It has further been suggested that deviant properties may be due to residual stress and/or chain morphology gradients arising from the film preparation process.

Methods leading to characterization of thin film polymer mechanical properties date back to the copper grid extension method introduced by Kramer.[33] Modern studies include variations of this technique and a surface buckling technique introduced by Stafford et al[32, 34, 35] used in conjunction with either AFM, laser diffraction or reflectance optical microscopy which allows the elastic modulus of thin films to be measured. Dewetting tests of supported thin polymer films [36-38] (< 100 nm) conducted above and below the polymer glass transition temperature T_g investigated the rate of hole formation as a function of film thickness, molecular weight MW, temperature T , and thermal history.

Lateral Force Microscopy (LFM) experiments were carried out by Dinelli et al to determine the T_g of heterogeneous polymer surfaces.[39] For confined heterogeneous system 40 nm in height and a few hundred nm in width they observed that T_g was reduced by 6 degrees to 267 degrees from the bulk glass transition due to confinement induced by the low interaction interface. A collaboration including Overney (Sills et al) [40] also measured interfacial T_g in spin cast ultra thin films of PS using shear-modulated scanning force microscopy. T_g was measured as a function of film thickness, molecular weight and crosslinking density. Across the film there were two regimes, firstly a sublayer extending approximately 10 nm from the substrate with T_g lowered by up to 10 °C below the bulk value and a second regime extending over 200 nm beyond the sublayer where T_g exceeded the bulk value by up to 10 °C. When Mw was increased it resulted in a shift in the first sublayer from the substrate interface of the order of 10 nm/Da. Crosslinking the precast films increased the absolute T_g values but had no effect on the spatial length scale of T_g . Another contact nanoindentation technique using conospherical diamond probes was carried out by Tweedie et al [16] where they loading up the probes to various loads corresponding to depths between 5 nm and 100 nm into 1 micron samples of PS, PMMA and PC. Their results showed an unexpected, but consistent, increase in the elastic

modulus of up to 200% at depths < 50 nm into the polymers. This is in contrast to what is seen in this paper, elastic modulus measurements of ultrathin polymer films made using a buckling technique [32, 34] and papers showing an increase in mobility at the surface of thin polymer films[41, 42] . However they may be consistent with papers which show a reduced relaxation in polymer glasses at surfaces [20].

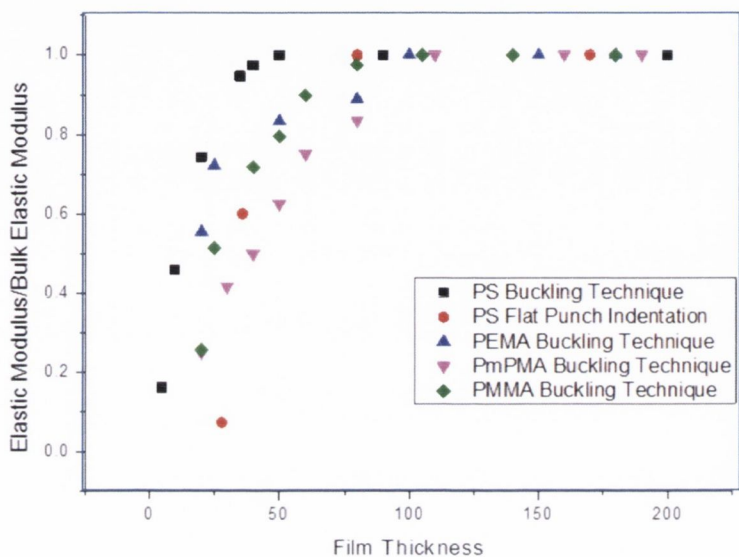


Figure 3.4: EM/bulk EM versus film thickness for various polymers for data from Stafford's buckling technique[34, 43, 44] and CM/Bulk CM data from FP nanoindentation.

Elastic property measurements present in the literature for homopolymer surfaces and thin films tested below their bulk glass transition temperature, compared with data from 10 to 1 aspect ratio FP nanoindentation are compared a little later. From this graph (figure 3.4) it is clear that as film thickness drops below 100 nm a decrease in E is seen, both for Stafford's buckling technique and FP nanoindentation.

Figure 3.5 presents FS over Bulk FS against film thickness for PS and shows how FS decreases as film thickness is decreased below 50 nm. This is all the data available from literature for forming stress (related to the yield stress) for ultra thin films and was adapted from Rowland *et al.*[29] From this one can see there is a scarcity of mechanical data for ultra-thin polymer films that this thesis seeks to remedy.

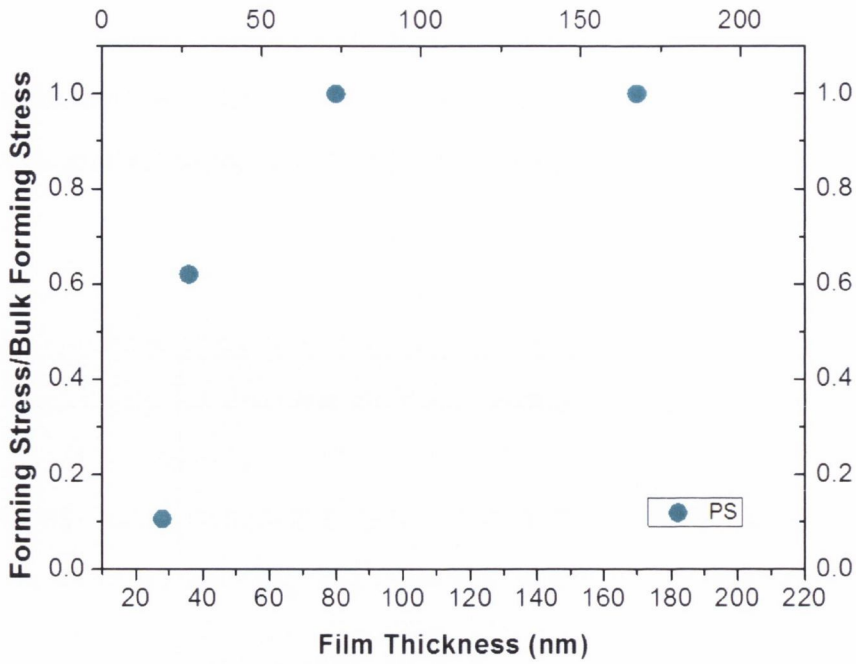


Figure 3.5: presents FS over Bulk FS against film thickness for PS. FS/Bulk FS decreases as film thickness is decreased below 50 nm. This data was adapted from Rowland et al.[29]

3.8 Small Size Effects: Enhanced Surface Relaxation

In addition to these results from NMR and BDS Fakjraai and Forrest show that the motion of polymer chain segments cooled below T_g slows rapidly. [45] With sufficient cooling the large segmental motion became completely arrested. These experiments were carried out by partially embedding and then removing gold nanospheres in a polystyrene surface and measuring the time dependent relaxations of these surface deformations. Temperature was varied between 277 and 369 kelvin. For temperatures near T_g the relaxation time of the surface was similar to that of the bulk. The deviation from the large segmental transitions (similar to α transitions) became more pronounced as the temperature was decreased below the bulk T_g . However, surface relaxation continued to be observed at all temperatures providing strong direct evidence for enhanced surface mobility relative to the bulk. In addition the temperature dependence of the relaxation time became weaker as the temperature decreased while the process exhibited no measureable temperature dependence between 277° K and 307° K. This is contrary to what is expected from the

temperature dependence of glass forming behaviour where below T_g an Arrhenius temperature dependence with constant activation energy is the norm. Therefore as the temperature was reduced below T_g the surface relaxation continued to occur, even while large segmental motions were arrested.

However their results were not sufficient to show whether these segmental motions at the surface were α processes that strongly deviate from the bulk or whether they were a previously unheard of mode relaxation that only occurs at a free surface. Yet what is clear is that some kind of enhanced relaxation occurs in PS at and around room temperature.

In contrast to these results Priestley *et al.* used a fluorescence technique to analyse the glassy state structural relaxation of polymers near the surfaces and interfaces of various film thicknesses at approximately room temperature. [20] Their technique allows them to compare the rate of structural relaxation, associated with β relaxations, at these interfaces compared to the bulk. They found that the rate of relaxation at the surface of PMMA on silica substrate is reduced by a factor of two at the free surface and by a factor of fifteen at the substrate, which is equivalent to a complete arresting of relaxation. The distribution in relaxation rates extends more than one hundred nanometres into the film interior[20].

3.8.1 de Gennes' Tentative Model for Thin Films

In 2000 de Gennes presented a tentative physical model to explain the features of a drop in T_g when Mw is high and the film thickness smaller than the coil size (R_0),[46]

$$R_0 = a\sqrt{N} \quad (\text{Equation 3.5})$$

where N is the polymerisation index and a is the monomer size. He considers a model where two types of motions compete, firstly standard motions controlled by the free volume as described in section 3.9.1 which is independent of chain length and secondly, collective motions along the chain due to free ends of polymers at the free surface. For bulk systems he expects the standard motions to always completely dominate as within the bulk there is always hindrance of the end group of the polymers. However for thin films the dominant process may be the collective motion of a "loop" within the chain which does not involve the chain ends. What becomes most important in this situation is the length of a

typical loop which starts from the surface, as it is a more fluid region and reaches deep into the film.

Later in 2000, de Gennes published a modified version of the “sliding model” where the chain arcs between the two contacts may move if all the barriers along the arc are weaker than a certain threshold. [46, 47] An important advancement of this revised model was that the high limiting chain lengths observed experimentally are accounted for in the model. The same year de Gennes also published a new analysis of data on the reduced glass transitions observed in freely standing films with Dalnoki-Veress, Forrest and Dutcher. They find their analysis is highly suggestive of the existence of this mechanism of mobility in thin freely-standing films that is inhibited in the bulk and distinct from the usual cooperative motion near T_g .

In 2011 Kim and Torkelson [48] published results from a multilayer fluorescence method where they employed a pyrene dye to label the polymers. Their samples consisted of various films with one 14 nm PS sample sandwiched between two 500 nm PS films, one with a free surface on a 500 nm PS layer, one sandwiched between two 21 nm PS films, one on a 42 nm film and lastly a 56 nm PS film. They found that the T_g of a 14 nm PS layer with a free surface matched the T_g of a 14 nm layer sandwiched between two 21 nm films which matched the T_g of a 56 nm film. Since in the 14 nm film sandwiched between the two 21 nm films there can be no chain which forms a loop or bridge reaching the free surface this contrasts with de Gennes’ mechanism whereby T_g reductions only occur at locations where segments are present from chains forming loops or bridges at the surface. In the thicker samples (>500 nm) the 14 nm film on the 500 nm sample had a reduced T_g , while the 14 nm film between the two 500 nm films had a T_g equivalent to the bulk.

3.9 Models for Theory of Elastic to Plastic Transition in Polymer Glasses

To complement the discussion of yield processes in polymers introduced in chapter 2. While yield processes in polymers was introduced in section 2.6 the theory of elastic to plastic transition in polymer glasses will be expanded upon here. One of the earlier models for the elastic to plastic transition in polymer glasses came from Henry Eyring in the mid-

20th century.[49] Eyring assumed that the deformation of a polymer was a thermally activated process involving the motion of segments of chain molecules over potential barriers.[50, 51] He envisaged the flow of the polymer chain as the propagation of kinks in the molecules, or the segments of molecular chains, into available holes. The Eyring model is one of the simplest models and is good for qualitative rationalization and hence worthwhile place to begin.

3.9.1 The Eyring Model

In order for the motion of the kink to result in a plastic flow, it must be raised (energised) into the activated state and pass over the saddle point. This was the earliest molecular theory of yield behaviour in amorphous polymers, and Eyring presented a theoretical framework which formed the basis of many subsequent considerations. The frequency of the plastic deformation depends on the ease with which a chain segment can overcome a potential barrier. When no stress is being applied dynamic equilibrium exists. Therefore an equal number of chain segments can move each direction over the potential energy barrier (ΔH) at a frequency (ν) given by

$$\nu = \nu_0 \exp\left(\frac{-\Delta H}{kT}\right) \quad (\text{Equation 3.6})$$

An applied stress σ (Figure 3.6) is assumed to produce linear shifts $\nu^*\sigma$ of the energy barriers in a symmetrical way, where β has the dimensions of volumes. The flow in the direction of the applied stress is then given by

$$\nu_1 = \nu_0 \exp\left[-\frac{(\Delta H - \nu^*\sigma)}{kT}\right] \quad (\text{Equation 3.7})$$

This is compared with a smaller flow in the backward direction of

$$\nu_2 = \nu_0 \exp\left[-\frac{(\Delta H + \nu^*\sigma)}{kT}\right] \quad (\text{Equation 3.8})$$

The net flow in the forward direction is then given by

$$\nu' = \nu_1 - \nu_2 = \nu_0 \exp\left(-\frac{\Delta H}{kT}\right) \left\{ \exp\left(\frac{(\nu^*\sigma)}{kT}\right) - \exp\left(\frac{(-\nu^*\sigma)}{kT}\right) \right\} \quad (\text{Equation 3.9})$$

If we assume that the net flow in the forward direction is directly related to the rate of change of strain ($\dot{\epsilon}$) we have

$$\frac{de}{dt} = \dot{\epsilon} = \dot{\epsilon}_0 \exp\left(-\frac{(\Delta H)}{kT}\right) \sinh\left(-\frac{v\sigma}{kT}\right) \quad (\text{Equation 3.10})$$

where $\dot{\epsilon}_0$ is a constant pre-exponential factor and v , which replaces v^* , is termed the activation volume for the molecular event. Note that

$$\sinh\left(-\frac{v\sigma}{kT}\right) = \exp\left(\frac{(v\sigma)}{kT}\right) - \exp\left(\frac{(-v\sigma)}{kT}\right) \quad (\text{Equation 3.11})$$

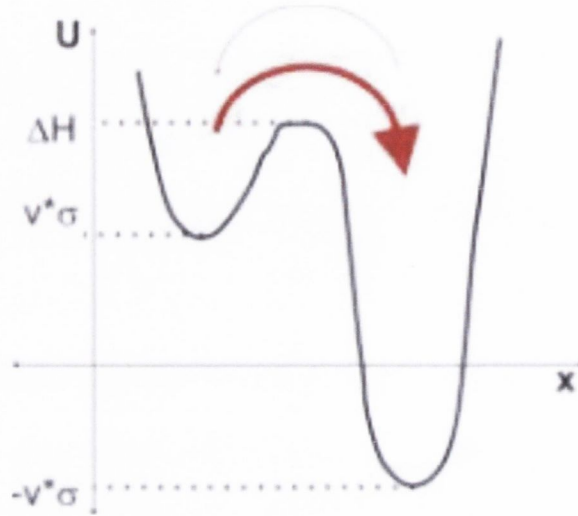


Figure 3.6: Representation of kink in a polymer molecule when shear stress applied. H represents energy.

From equation 3.11 the activation energy required for a plastic event to occur and v^* , the activation volume, is considered to represent the volume of the polymer segment which has to move as a whole in order for plastic deformation to occur, are calculated. For high values of stress $\sinh \chi = \frac{1}{2} \exp \chi$ and

$$\dot{\epsilon} = \frac{\dot{\epsilon}_0}{2} \exp\left(-\frac{(\Delta H - v\sigma)}{kT}\right) \quad (\text{Equation 3.12})$$

This gives the yield stress (σ) in terms of strain rate as

$$\sigma = \frac{RT}{v} \left\{ \frac{\Delta H}{kT} + \ln \frac{2\dot{\epsilon}}{\dot{\epsilon}_0} \right\} \quad (\text{Equation 3.13})$$

These equations are useful as they may give an indication of the underlying molecular mechanisms within the material as it experiences a plastic deformation. We can see from equation 3.13 that as the strain rate ($\dot{\epsilon}$) increases σ increases, and as temperature (T) increases σ decreases.

3.9.2 Recent Models of Polymer Deformation

Over the last 30 years there has been many advances in models for polymer deformation, but to go into these models in great detail here is not the focus of this thesis. To skip ahead approximately 40 years, in 2002 Capaldi, Boyce and Rutledge further developed their model[52, 53] following Loo's *et al.* paper [54] about experimental results showing increased chain mobility in the amorphous region of nylon 6 observed under active uniaxial deformation. Capaldi and Boyce talk about the increased molecular mobility that accompanies plastic deformation of glassy amorphous polymer under applied stress. In their computer simulation they see significant increases in torsional transition rates during active deformation prior to, and just beyond the yield point. The transition rate drops when active deformation stops.

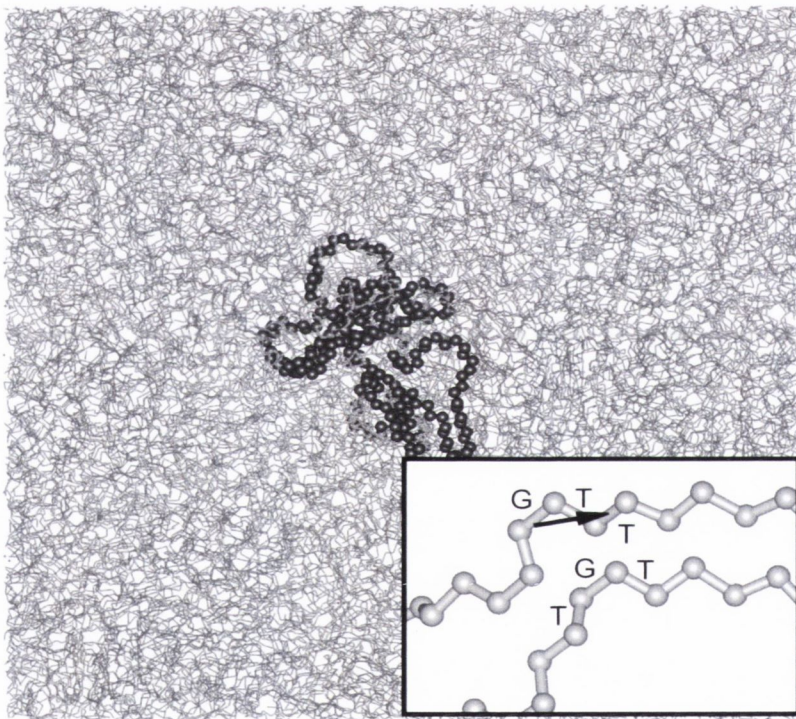


Figure 3.7: Image of molecular dynamics simulations from Capaldi Boyce and Rutledge.[52] A single chain within the simulation cell is highlighted. The inset depicts a subset of this chain and illustrates a transition that occurred along this chain.

Recent studies have challenged the traditional idea that entanglements between polymer chains control strain hardening. There are a number of reasons for this. One is that as T_g is approached the strain hardening (G_r) calculated using the entropic model is 100 times smaller than measured. Also as temperature increases G_r decreases experimentally. This is

the opposite of what one would expect from an entropic model. In addition G_r and σ_0 are treated as separate and independent parameters. This ignores any potential contribution of plastic deformation to strain hardening. As experiments theory and simulations have all shown that σ_0 and G_r are linearly related when temperature, pressure or strain rate are varied this indicates that they should not be treated completely independently from each other.

Recently simulations by Hoy and Robbins have also shown that strain hardening occurs in polymers too short to form entangled networks. Strain hardening in unentangled networks can be mapped to that of entangled chains in macroscopic deformation. Instead they consider the orientation of individual chains to play the dominant role.[55, 56] In addition in the last ten years Chen and Schweizer have developed a microscopic constitutive equation theory for the nonlinear response of polymer glasses. [57-59] The key physics in their model is contained in a deformation dependent elastic modulus and α relaxation time. Using their model they find that the strain rate dependences of yield stress and yield strain for PMMA are roughly logarithmic with upward deviations at high strain rates. Their model also predicts how deformation reduces the segmental relaxation time. The dependences of the yield stress and strain, steady state flow stress and strain softening amplitude on deformation rate, temperature, pre-aging time, and also two distinct thermal history protocols are investigated in detail for PMMA glass. Overall, good agreement between theory and experiment is found.

3.10 Yield processes in Thin Polymer Films

Flat punch nanoindentation in recent years has allowed us to carry out mechanical tests on thin films, yielding load versus displacement graphs which are easily converted to stress vs. strain curves. From these graphs it is possible to access the elastic response of the material as well as being able to clearly pinpoint the yield points. Flat punch nanoindentation demonstrating the results of the Eyring model in 170 nm polystyrene (PS) films adapted from Rowland *et al.* [31, 60] are shown in figure 3.8. These results also demonstrate how the same theory used for conventional macroscopic mechanical testing can be scaled right down to 100's of nanometres. Hence this macroscopic theory for yield point in polymer glasses is still applicable at the nanoscale. Figure 3.8a shows clearly that

as the temperature increases from room temperature to 105 °C the yield point decreases. Figure 3.8b shows that as the loading rates increase from 12.5 MPa/s to 1250 MPa/s the yield point increases.

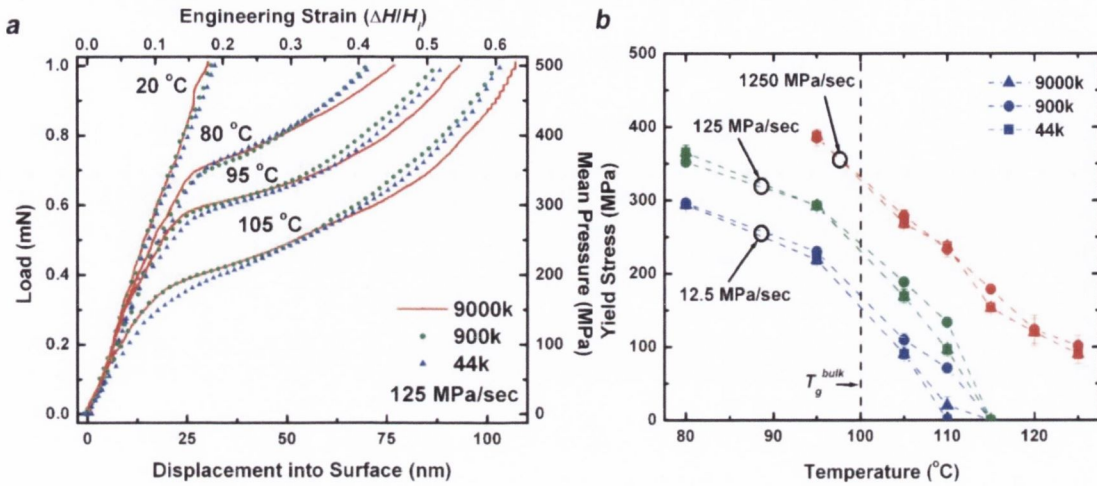


Figure 3.8. Glassy elastic-to-plastic transition behaviour for low polydispersity 9000K, 900K, and 44K Mw polystyrene at 170 nm film thickness. (a) Load versus displacement curves loading at 125 MPa/s to 500 MPa from 20 to 105 °C. A range of over two decades in molecular weight exhibits nearly identical mechanical response during loading. (b) Mean yield stress measurements loading at rates from 12.5 to 1250 MPa/s and temperatures from 20 to 125 °C. Adapted from [31].

3.11 Relevant Length Scales

In summary, there are two types of length scales in this problem that must be considered. Firstly, there are the intrinsic length scales of the polymers themselves, such as the Kuhn length and the radius of gyration R_g . Since R_g is directly dependent on Mw and the Kuhn length (Equation 3.1 and 3.2) they can be amalgamated into one term as presented in Eqn 3.2. In this thesis, several different Mw's of PS are focused on, including 44 K PS, corresponding to a R_g of 5.7 nm, 900K, corresponding to a R_g of 26 nm and 9000 K, corresponding to a R_g of 82.1 nm. For PMMA the Mw is 48 K, corresponding to a R_g of 5.9 nm.

The second important length scale is the polymer film thickness. Depending on the polymer film thickness certain polymer properties begin to change. A reduced E has been measured in both PMMA and PS below 60 nm thicknesses [34, 43], while T_g has been shown to vary when the film thickness is reduced below 100 nm [24]. The cause of this

decrease in EM and T_g is not understood, and indeed is the source of much debate [9, 61]. In this thesis the point at which the material begins to yield is investigated in films above and below the 100 nm and compared and contrasted with what exists in the literature. A second effect, investigated elsewhere, is the effect of confining entangled polymers to films thinner than R_g . This has been shown to have the effect of accelerating large strain deformation the during squeeze flow of nanoimprint forming [29].

3.12 Shear Banding in Polymer Glasses

Shear band nucleation and propagation in nanoscale crystalline material samples has been experimentally probed in crystalline materials [62, 63] and bulk metallic glasses [63] via nanoindentation. Schuh *et al.* [63] reports possible shear band nucleation and propagation in bulk metallic glasses while for platinum he makes measurements of the activation energy (ϵ), activation volume (V) and attempt probability (\dot{n}) for the first plastic event to occur in this material. The Eyring model formed the basis for these calculations whereby they assumed there is a local, kinetically limiting process that takes place under the indenter (for example, the nucleation of a dislocation) that requires an activation energy ϵ . This energy barrier could be reduced through the mechanical work of indentation, or may be overcome by an appropriate thermal fluctuation, or a combination of both. The probability of such an event in a given volume of material is written as

$$\dot{n} = \dot{n}_0 \exp\left(-\frac{\epsilon - \sigma V}{kT}\right) \quad (\text{Equation 3.17})$$

where \dot{n}_0 is the attempt frequency per unit volume. This equation is very similar to equation 3.2, except now instead of an energy barrier H there is an activation energy ϵ , attempt probability (\dot{n}) and activation volume (V) for one single plastic event to occur. As before the mechanical work is equal to a stress σ acting on an activation volume V , and the thermal energy is Boltzmann's constant k multiplied by temperature T . This same type of analysis may be applied to amorphous polymer materials, although amorphous polymer materials have proved to have some additional experimental difficulties.

3.13 References

- [1] M. J. Fasolka and A. M. Mayes, "Block copolymer thin films: Physics and Applications1," *Annual Review of Materials Research*, vol. 31, pp. 323-355, 2001.

- [2] J. Y. Cheng, A. M. Mayes, and C. A. Ross, "Nanostructure engineering by templated self-assembly of block copolymers," *Nat Mater*, vol. 3, pp. 823-828, 2004.
- [3] C. Park, J. Yoon, and E. L. Thomas, "Enabling nanotechnology with self assembled block copolymer patterns," *Polymer*, vol. 44, pp. 6725-6760, 2003.
- [4] M. Park, C. Harrison, P. M. Chaikin, R. A. Register, and D. H. Adamson, "Block Copolymer Lithography: Periodic Arrays of $\sim 10^{11}$ Holes in 1² Square Centimeter," *Science*, vol. 276, pp. 1401-1404, May 30, 1997 1997.
- [5] R. S. McLean and B. B. Sauer, "Tapping-Mode AFM Studies Using Phase Detection for Resolution of Nanophases in Segmented Polyurethanes and Other Block Copolymers," *Macromolecules*, vol. 30, pp. 8314-8317, 1997.
- [6] T. Thurn-Albrecht, R. Steiner, J. DeRouchey, C. M. Stafford, E. Huang, M. Bal, M. Tuominen, C. J. Hawker, and T. P. Russell, "Nanoscopic Templates from Oriented Block Copolymer Films," *Advanced Materials*, vol. 12, pp. 787-791, 2000.
- [7] R. N. Haward and R. J. Young, *The Physics of Glassy Polymers*. London: Chapman And Hall, 1997.
- [8] G. Adam and J. H. Gibbs, "On the Temperature Dependence of Cooperative Relaxation Properties in Glass-Forming Liquids," *J. Chem. Phys.*, vol. 43, p. 139, 1965.
- [9] A. Mataz and G. B. McKenna, "Effects of confinement on material behaviour at the nanometre size scale," *Journal of Physics: Condensed Matter*, p. R461, 2005.
- [10] L. H. Sperling, *Introduction to physical polymer science* 3ed.: Wiley-Interscience, 2001.
- [11] M. Doi and S. F. Edwards, *The theory of polymer dynamics*. Oxford Oxford University Press,, 1986.
- [12] M. Rubinstein and R. H. Colby, *Polymer Physics*. Oxford: Oxford University Press, 2003.
- [13] P. G. De Gennes, "Soft Matter," *Nobel Lecture*, 1991.
- [14] P. G. De Gennes, "Dynamics of Entangled Polymer Solutions. I. The Rouse Model," *Macromolecules*, vol. 9, pp. 587-593, 2012/08/24 1976.
- [15] E. Gacoin, C. Fretigny, A. Chateauminois, A. Perriot, and E. Barthel, "Measurement of the mechanical properties of thin films mechanically confined within contacts," *Tribology Letters*, vol. 21, pp. 245-252, 2006.
- [16] C. A. Tweedie, G. Constantinides, K. E. Lehman, D. J. Brill, G. S. Blackman, and K. J. Van Vliet, "Enhanced stiffness of amorphous polymer surfaces under confinement of localized contact loads," *Adv. Mater.*, vol. 19, p. 2540, 2007.
- [17] W. A. Spitzig and O. Richmond, "Effect of hydrostatic pressure on the deformation behavior of polyethylene and polycarbonate in tension and in compression," *Polymer Engineering & Science*, vol. 19, pp. 1129-1139, 1979.
- [18] R. Quinson, J. Perez, M. Rink, and A. Pavan, "Yield criteria for amorphous glassy polymers," *Journal of Materials Science*, vol. 32, pp. 1371-1379, 1997.
- [19] E. Jones Parry and D. Tabor, "Effect of hydrostatic pressure on the mechanical properties of polymers: a brief review of published data," *Journal of Materials Science*, vol. 8, pp. 1510-1516, 1973.
- [20] R. D. Priestley, C. J. Ellison, L. J. Broadbelt, and J. M. Torkelson, "Structural Relaxation of Polymer Glasses at Surfaces, Interfaces, and In Between," *Science*, vol. 309, pp. 456-459, 2005.
- [21] Boyce MC and H. RN., *The physics of glassy polymers* vol. The post-yield deformation of glassy polymers. London: Chapman & Hall, 1997.
- [22] R. Quinson, J. Perez, Y. Germain, and J. M. Murraciale, "Alpha and beta relaxations in poly(methyl methacrylate) and polycarbonate: non-linear anelasticity studies by antistress relaxation," *Polymer*, vol. 36, pp. 743-752, 1995.
- [23] R. Casalini and C. M. Roland, "Excess wing in the dielectric loss spectra of propylene glycol oligomers at elevated pressure," *Physical Review B*, vol. 69, p. 094202, 2004.

- [24] J. L. Keddie, R. A. L. Jones, and R. A. Cory, "Size-Dependent Depression of the Glass Transition Temperature in Polymer Films," *EPL (Europhysics Letters)*, p. 59, 1994.
- [25] H. Lu, W. Chen, and T. P. Russell, "Relaxation of Thin Films of Polystyrene Floating on Ionic Liquid Surface," *Macromolecules*, vol. 42, pp. 9111-9117, 2011/11/15 2009.
- [26] M. Tress, M. Erber, E. U. Mapesa, H. Huth, J. Müller, A. Serghei, C. Schick, K.-J. Eichhorn, B. Voit, and F. Kremer, "Glassy Dynamics and Glass Transition in Nanometric Thin Layers of Polystyrene," *Macromolecules*, vol. 43, pp. 9937-9944, 2010.
- [27] L. Si, M. V. Massa, K. Dalnoki-Veress, H. R. Brown, and R. A. L. Jones, "Chain Entanglement in Thin Freestanding Polymer Films," *Physical Review Letters*, vol. 94, p. 127801, 2005.
- [28] T. Yves, "Two-dimensional nanometric confinement of entangled polymer melts," *Polymer*, vol. 52, pp. 5193-5196.
- [29] H. D. Rowland, W. P. King, J. B. Pethica, and G. L. W. Cross, "Molecular Confinement Accelerates Deformation of Entangled Polymers During Squeeze Flow," *Science*, vol. 322, pp. 720-724, October 31, 2008 2008.
- [30] C. M. Stafford, B. D. Vogt, C. Harrison, D. Julthongpiput, and R. Huang, *Macromolecules*, vol. 39, p. 5095, 2006.
- [31] H. D. Rowland, W. P. King, G. L. W. Cross, and J. B. Pethica, "Measuring Glassy and Viscoelastic Polymer Flow in Molecular-Scale Gaps Using a Flat Punch Mechanical Probe," *ACS Nano*, vol. 2, pp. 419-428, 2008.
- [32] J. M. Torres, C. Wang, E. B. Coughlin, J. P. Bishop, R. A. Register, R. A. Riggleman, C. M. Stafford, and B. D. Vogt, "Influence of Chain Stiffness on Thermal and Mechanical Properties of Polymer Thin Films," *Macromolecules*, 2011/11/03.
- [33] A. M. Donald and E. J. Kramer, "Effect of molecular entanglements on craze microstructure in glassy polymers," *Journal of Polymer Science: Polymer Physics Edition*, vol. 20, pp. 899-909, 1982.
- [34] C. M. Stafford, C. Harrison, K. L. Beers, A. Karim, E. J. Amis, M. R. VanLandingham, H.-C. Kim, W. Volksen, R. D. Miller, and E. E. Simonyi, "A buckling-based metrology for measuring the elastic moduli of polymeric thin films," *Nat Mater*, vol. 3, pp. 545-550, 2004.
- [35] J. M. Torres, C. M. Stafford, and B. D. Vogt, "Elastic Modulus of Amorphous Polymer Thin Films: Relationship to the Glass Transition Temperature," *ACS Nano*, vol. 3, pp. 2677-2685, 2009.
- [36] G. Reiter, uuml, and nter, "Dewetting of thin polymer films," *Physical Review Letters*, vol. 68, p. 75, 1992.
- [37] G. Reiter, M. Hamieh, P. Damman, S. Slavovs, S. Gabriele, T. Vilmin, and E. Raphael, "Residual stresses in thin polymer films cause rupture and dominate early stages of dewetting," *Nat Mater*, vol. 4, pp. 754-758, 2005.
- [38] H. Bodiguel and C. Fretigny, "Viscoelastic Properties of Ultrathin Polystyrene Films," *Macromolecules*, vol. 40, pp. 7291-7298, 2007.
- [39] F. Dinelli, C. Buenviaje, and R. M. Overney*, "Glass transition measurements on heterogeneous surfaces," *Thin Solid Films* vol. 396, pp. 138-144, 2001.
- [40] S. Sills, R. M. Overney, W. Chau, V. Y. Lee, R. D. Miller, and J. Frommer, "Interfacial glass transition profiles in ultrathin, spin cast polymer films," *The Journal of Chemical Physics*, vol. 120, pp. 5334-5338, 2004.
- [41] K. Paeng, R. Richert, and M. D. Ediger, "Molecular mobility in supported thin films of polystyrene, poly(methyl methacrylate), and poly(2-vinyl pyridine) probed by dye reorientation," *Soft Matter*, vol. 8, pp. 819-826, 2011.
- [42] H.-N. Lee, K. Paeng, S. F. Swallen, and M. D. Ediger, "Direct Measurement of Molecular Mobility in Actively Deformed Polymer Glasses," *Science*, vol. 323, pp. 231-234, January 9 2009.
- [43] C. M. Stafford, B. D. Vogt, C. Harrison, D. Julthongpiput, and R. Huang, "Elastic Moduli of Ultrathin Amorphous Polymer Films," *Macromolecules*, vol. 39, pp. 5095-5099, 2011/11/10 2006.

- [44] J. M. Torres, C. M. Stafford, and B. D. Vogt, "Manipulation of the Elastic Modulus of Polymers at the Nanoscale: Influence of UVâ Ozone Cross-Linking and Plasticizer," *ACS Nano*, pp. null-null.
- [45] Z. Fakhraai and J. A. Forrest, "Measuring the Surface Dynamics of Glassy Polymers," *Science*, vol. 319, pp. 600-604, 2008.
- [46] P. G. de Gennes, "Glass transitions in thin polymer films," *The European Physical Journal E: Soft Matter and Biological Physics*, vol. 2, pp. 201-205, 2000.
- [47] P.-G. d. Gennes, "Glass transitions of freely suspended polymer films," *Comptes Rendus de l'AcadÃ©mie des Sciences - Series IV - Physics*, vol. 1, pp. 1179-1186, 2000.
- [48] S. Kim and J. M. Torkelson, "Distribution of Glass Transition Temperatures in Free-Standing, Nanoconfined Polystyrene Films: A Test of de Genne' Sliding Motion Mechanism," *Macromolecules*, vol. 44, pp. 4546-4553, 2012/01/31 2011.
- [49] K. Dalnoki-Veress, J. A. Forrest, P. G. de Gennes, and J. R. Dutcher, "Glass transition reductions in thin freely-standing polymer films : A scaling analysis of chain confinement effects," *J. Phys. IV France*, vol. 10, pp. Pr7-221-Pr7-226, 2000.
- [50] I. M. Ward and D. W. Hadley, *Mechanical Properties of Solid Polymers*. Chichester, New York, Brisbane, Toronto, Singapore: John Wiley and Sons, 1993.
- [51] Z. H. Stachurski, "Deformation mechanisms and yield strength in amorphous polymers," *Progress in Polymer Science*, vol. 22, pp. 407-474, 1997.
- [52] F. M. Capaldi, M. C. Boyce, and G. C. Rutledge, "Enhanced Mobility Accompanies the Active Deformation of a Glassy Amorphous Polymer," *Physical Review Letters*, vol. 89, p. 175505, 2002.
- [53] F. M. Capaldi, M. C. Boyce, and G. C. Rutledge, "Molecular response of a glassy polymer to active deformation," *Polymer*, vol. 45, pp. 1391-1399, 2004.
- [54] L. S. Loo, R. E. Cohen, and K. K. Gleason, "Chain Mobility in the Amorphous Region of Nylon 6 Observed under Active Uniaxial Deformation," *Science*, vol. 288, pp. 116-119, April 7 2000.
- [55] R. S. Hoy and M. O. Robbins, "Strain hardening of polymer glasses: Effect of entanglement density, temperature, and rate," *Journal of Polymer Science Part B: Polymer Physics*, vol. 44, pp. 3487-3500, 2006.
- [56] R. S. Hoy and M. O. Robbins, "Strain hardening of polymer glasses: Entanglements, energetics, and plasticity," *Physical Review E*, vol. 77, p. 031801, 2008.
- [57] K. Chen and K. S. Schweizer, "Stress-enhanced mobility and dynamic yielding in polymer glasses " *EPL (Europhysics Letters)*, vol. 79, 2007.
- [58] K. Chen and K. S. Schweizer, "Theory of Yielding, Strain Softening, and Steady Plastic Flow in Polymer Glasses under Constant Strain Rate Deformation," *Macromolecules*, vol. 44, pp. 3988-4000, 2012/08/25 2011.
- [59] K. Chen, E. J. Saltzman, and K. S. Schweizer, "Segmental dynamics in polymers: from cold melts to ageing and stressed glasses," *Journal of Physics: Condensed Matter*, vol. 21, p. 503101, 2009.
- [60] G. L. W. Cross, B. S. O'connell, J. B. Pethica, H. Rowland, and W. P. King, "Variable temperature thin film indentation with a flat punch," *Review of Scientific Instruments*, vol. 79, pp. 013904-13, 2008.
- [61] A. Serghei, M. Tress, and F. Kremer, "Confinement Effects on the Relaxation Time Distribution of the Dynamic Glass Transition in Ultrathin Polymer Films," *Macromolecules*, vol. 39, pp. 9385-9387, 2006.
- [62] C. A. Schuh, J. K. Mason, and A. C. Lund, "Quantitative insight into dislocation nucleation from high-temperature nanoindentation experiments," *Nat Mater*, vol. 4, pp. 617-621, 2005.
- [63] C. A. Schuh, T. C. Hufnagel, and U. Ramamurty, "Mechanical behavior of amorphous alloys," *Acta Materialia*, vol. 55, pp. 4067-4109, 2007.

Chapter 4: Experimental Methods

In this thesis the main focus is investigation of thin polymer film mechanical properties using a variant of standard sharp tip nanoindentation. In general, nanoindentation is a technique for measuring mechanical properties including elastic modulus and hardness in small volumes at the surface of a bulk material [1]. Here the testing geometry is altered to that of a flat punch indented into a thin film.

In contrast to all other thin film mechanical techniques, flat punch indentation allows access to a full stress versus strain response of films prepared to thicknesses less than 100 nm. Once well aligned, a principle advantage of the technique over other mechanical contact experiments is the unambiguous determination of contact area (e.g. a constant equivalent to the punch face area) throughout the experiment. A further advantage is the ability to consistently impose a particular thin film testing boundary condition over a large range of strain, strain rate and (isothermal) temperature conditions. This is achieved by use of a well-defined flat punch indented across a thin film sample over a short period of time. The deformation field is then characterized by strongly separated elastic, yield and plastic flow states which are described by contact modulus, forming stress and strain hardening parameters that are otherwise impossible to access in ultrathin films using any of the methods currently available [2-7].

This chapter will first introduce the modified nanoindenter system we use followed by a description of the fabrication of the custom made diamond flat punch tips used in this thesis. Alignment of these flat punch tips in the nanoindentation system is of utmost importance and so the alignment process will also be discussed. Finally sample preparation for homopolymer films and BCP films used in the thesis will be presented.

4.1 Nanoindentation

A nanoindenter is an instrument designed to characterize the small scale mechanical properties of matter using very sensitive measurements of force and displacement. A

typical nanoindenter can measure forces and displacements as small as 0.2 μN and 0.2 nm [8]. Traditionally measurements are carried out by pushing a sharp diamond tip into the material to be characterised and measuring the force and displacement. After sometime the load (F) is removed and the residual area (A_r) of the indentation into the sample is measured. The hardness (H) which is defined as

$$H = \frac{F}{A_r} \quad (\text{Equation 4.1})$$

is then calculated[9]. In principle, if a very sharp tip is used, the contact area between the sample and the tip, and thus the volume of material that is tested, can be made arbitrarily small. However the problem then arose of how to determine the indentation area if the indentation is so small that it becomes extremely difficult to see without a powerful microscope. This led to depth sensing indentation methods been developed and the load and displacement of the indenter being recorded during the indentation process. This data is then analysed to obtain the contact area, and thereby mechanical properties, without having to see the indentations. From this, parameters such as H and E can be found. To accomplish this, results from Sneddon who showed that load displacement relationships for many simple punch geometries can be written as

$$F = \alpha h^m \quad (\text{Equation 4.2})$$

where h is the elastic displacement and α and m are constants related to the geometry of the punch were utilised [10, 11]. For example, $m = 1$ for flat punches. However, including plasticity in a model for indentation contact is a more complex problem as the constitutive equations are non-linear and a number of material parameters such as yield strength and work hardening coefficient must be included. Therefore most of the important findings of plasticity in indenter contact problems has come from experimental work, in particular work by Tabor who studied the indentation of a number of metals deformed by spherical indenters[12].

One very important observation of these studies was that the shape of the hardness impression left after the indenter unloaded and the material had elastically recovered, at least for metals, was the same shape as the indenter while having a slightly larger radius than the original indenter shape. This was also observed for conical indenters with the

shape of the left over impression having a larger included angle than the original conical tip. The importance of this observation was that as elastic contact solutions existed for each of these geometries, the ways in which plasticity affected the interpretation of elastic unloading data could be dealt with by considering the shape of the perturbed surface in the elastic analysis. Tabor used this observation to show that the shape of the entire unloaded curve and the total amount recovered displacement can be accurately related to elastic modulus and size of the contact impression for both spherical and conical indenters. He also found that the diameter of the contact impression in the surface formed by conical indenters does not recover during unloading—only the depth recovers. Finally, the indentation must be loaded and unloaded a few times before the load displacement behaviour becomes perfectly reversible, *i.e.*, a limited amount of plasticity sometimes occurs in each of the first few loading and unloading cycles.

In 1992 Oliver and Pharr published the most widely used method for calculating the elastic modulus from indentation using the unload data[10]. They found that since the unload is rarely linear, even at the beginning of the unload, it is more accurate to use power laws such as equation 4.1 to describe the unloading data, where the exponent varies from 1.2 to 1.6 depending on the tip geometry. As a result of these advances the nanoindenter is now widely used to measure both H and E of materials.

4.1.1 Nanoindentation Set-up

Load control nanoindentation was provided via an indentation die actuated in a direction perpendicular to the sample surface using a modified commercial nanoindentation system (MTS Nano Instruments Nanoindenter XP), figure 4.1 a.

Due to the sensitivity of the measurements the nanoindenter is housed in a chamber to protect it from external sources of vibration, air currents and sound. The machine is set on a floating table inside this housing so that it is better isolated from floor vibration.

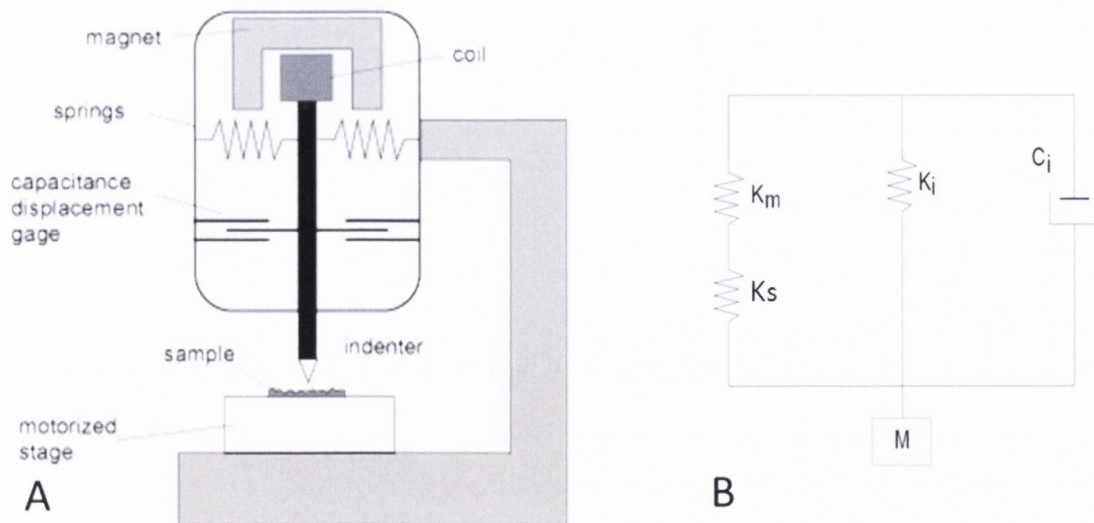


Figure 4.1: A) Simple Schematic of nanoindenter set up.[13] B) Representation of springs (K_m , K_i and K_s) and capacitor (C_i) in the nanoindenter.

The nanoindenter actuates movement of the tip by applying a current to the coil which then generates a magnetic force at the top of the shaft. The applied load is measured by a calibrated operational amplifier which measures the actual coil current, while displacement is measured by calibration of the differential capacitive output. When the tip comes into contact with a sample, these raw data channels are used to calculate the actual load and displacement of the tip at the sample contact point using formulae which take the calibration constants, stiffness of the leaf springs and frame stiffness (support springs) into account. Both the load and displacement calibration constants must be found for each individual nanoindenter head.

The load calibration is performed by balancing the coil force to known weights which are hung from the indenter mountings. The raw load current for each weight in free space is adjusted until the displacement voltage reaches a set value. This is repeated for several different weights. The coil current versus load has a linear relationship and the calibration constant for the load is found from the slope of this line. The displacement calibration uses a Newton's rings interferometry technique. The nanoindenter is set to move a constant velocity while attached to the Newton's rings set-up. The motion of the nanoindenter causes a variation of the position of the interference fringes which in turn are measured with a telescope. The variation of position of the fringes can be related to the displacement

voltage measured by the indenter and from this linear relationship the displacement calibration constant is found.

The system is load instrumented with low noise (100 nN noise floor) force provided by a solenoid apparatus that controls the indenter-terminated shaft which has a mass of 100 g. This shaft is supported by an 80 N/m dual leaf spring arrangement that ensures one-dimensional motion. Forces varying between 0.0001 and 8000 mN can be applied with ~0.0001 mN resolution. The indenter and shaft displacement measures over a range of 2 mm with 0.05 nm resolution using a differential capacitive sensor.

When the indenter contacts a sample it has a S associated with it which is the stiffness of the indenter tip and sample contact. This contact sample stiffness is arranged in parallel with the support springs (K_i) which have a nominal 80 N/m stiffness. The support springs consist of both the leaf springs, which support and guide the mass of the indenter shaft, and the frame of the indenter and are shown in figure 4.1 a. Together, these elements are in series with the overall instrument frame which has a stiffness of six million N/m (K_m). This means that for typical sample contact stiffness of 1000's to 100,000's N/m, the support springs are small, and the frame stiffness is large, giving only small corrections on the measurement for either part (figure 4.1 B).

K_m and S are in parallel to the leaf spring stiffness and also the displacement capacitance, which has a dampening coefficient of C_i . This dampening coefficient is calculated by oscillation of the indenter shaft in free space without any contact to the sample. In addition, the support spring stiffness can also be measured by moving the indenter in free space and measuring the load voltage and corresponding displacement voltage. In order to calibrate the support spring's stiffness indentation experiments are conducted on a material with a known elastic modulus and Poisson ratio.

The compliance of the system is found using total compliance of the system (J) is given by

$$J = \frac{1}{S_i} = J_f + J_c = J_f + \frac{\pi}{2E\sqrt{A}} \quad (\text{Equation 4.3})$$

where S_i is the combined stiffness of the machine and the calibration specimen, J_f is the machine compliance and J_c is the specimen compliance. E is the modulus of the specimen and A is the contact area of the tip with the specimen. A series of indents at different

depths are conducted and from the slope of $1/\sqrt{A}$ versus the measured compliance J , J_f can be found. From this equation the value of the support springs of the nanoindenter used has been calculated to be 80 N/m.

4.1.2 Continuous Stiffness Measurement Mode of Nanoindentation

Traditionally, in the nanoindentation technique, the measurement of S and E is determined from the unloading slope of the quasi-static load-displacement data, and in such calculation, it only allows one to determine S , E and H at the maximum penetration depth [10]. The Continuous Stiffness Measurement (CSM) is a technique which allows continuous calculation of S , and hence E , as the indenter tip carries out the indent.

The CSM imposes a faster, small amplitude dynamic mode of a (typical) 45 Hz sinusoidal load under feedback regulation to provide a constant displacement amplitude motion of the die at all stages of indentation. It can apply either a set load or a set displacement and maintains this throughout the indentation process. The load the CSM applies is called the harmonic load and the displacement called the harmonic displacement, to differentiate the data collected by the CSM from the overall load and displacement recorded by the nanoindenter. Throughout this thesis the CSM is most utilised by setting a harmonic displacement amplitude of 2 nm. Amplitude and phase of the sample displacement signal relative to loading is recorded and from this S and E of the samples can be continuously calculated as the tip indents into the material.

Using the CSM S is calculated by the CSM according to $S = \frac{dF}{d\delta}$ where δ the harmonic displacement and F is the harmonic load. This then allows a continuous measurement of E to be calculated, as S and E are related via Poisson's ratio (ν) and a geometry factor as presented in Yang's model [14] according to

$$E = \frac{(1+\nu)(1-2\nu)}{(1-\nu)} \frac{S}{Area} h \quad (\text{Equation 4.4})$$

where h is the original film thickness. This is utilised and discussed further in Section 5.4.4. and is extremely useful for materials where the mechanical properties may change with surface penetration, such as layered materials.

The basic principle behind AC modulation is to superimpose an oscillatory modulation δP on the quasi-static load P already applied to the indenter, and then monitor the displacement amplitude and phase shift of this modulation. This AC displacement is measured with a lock-in amplifier. A driving force of $F = F_0 \sin \omega t$ is applied where F_0 is the amplitude of the force, ω is the angular frequency and t is the time. This corresponds to the following equation of motion between the nanoindenter and the nanoindenter head

$$m\ddot{x} + C_i\dot{x} + kx = F_0 \sin \omega t \quad (\text{Equation 4.5})$$

The solution to this equation is $x = X \sin(\omega t - \varphi)$. [15] X is the amplitude of the displacement oscillation and φ is the phase difference between the displacement and the driving force. The amplitude of the displacement oscillation can then be found from

$$X = \frac{F_0}{\sqrt{(k-m\omega^2)^2 + (C_i\omega)^2}} \quad (\text{Equation 4.6})$$

and the phase angle can be found from

$$\varphi = \tan^{-1} \frac{\omega C_i}{k-m\omega^2} \quad (\text{Equation 4.7})$$

Where k is the combined spring constant

$$k = K_i + \frac{1}{\frac{1}{K_m} + \frac{1}{S}} \quad (\text{Equation 4.8})$$

For a sample not in contact $S = 0$ the values K_i , m and K_m can all be found from the calibration measurements described previously. Therefore we can find out what the damping coefficient C_i is from the previous equations. Once this is known, the machine can then be calibrated so that S can be found from the CSM when the tip is in contact with a sample. For the CSM the ω value is set and x_0 , ϕ and F_0 are measured. Normally in oscillation experiments the spring constant, K is fixed and the oscillation frequency ω is measured but in nanoindentation experiments the spring constant changes during the test and the oscillation frequency is kept fixed. When the indenter head is moving in free space the spring constant $K = K_i$. The natural frequency of the nanoindenter head used for these measurements is $\sqrt{K_i/m} = 20$ Hz.

Figure 4.2 shows the AC modulation technique schematic. The DC signal is applied to the coil in the indenter head. The outputted load voltage is passed through a high pass filter which is then passed into the lock-in amplifier.

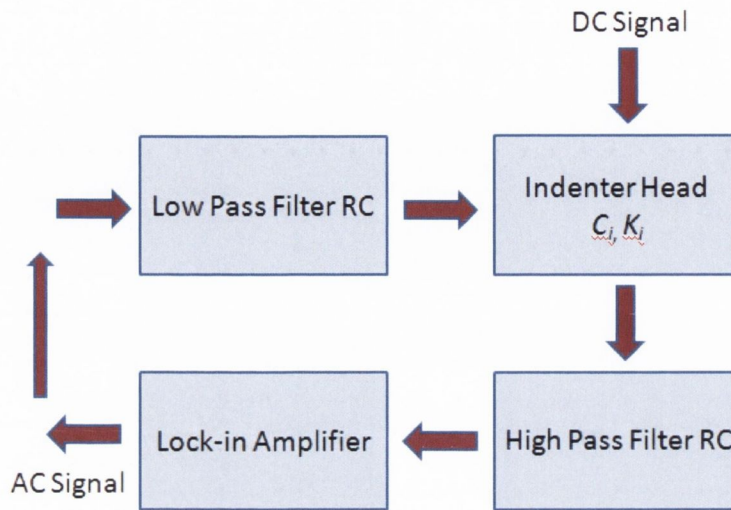


Figure 4.2: Schematic of DC signal which controls the motion of the indenter head (C_i is the capacitor in the nanoindenter and K_i is indenter springs) in conjunction with the configuration of AC modulation[16] the controls the small oscillation that is superimposed on the overall motion of the indenter tip by the CSM.

A sinusoid AC signal with a known frequency and amplitude is produced by the lock-in amplifier. It is then passed through the low pass filter and onto the coil along with the DC signal. The resultant AC signal is then passed through a high pass filter and is passed back into the lock-in amplifier. This measures the amplitude of the AC signal and the phase difference between the excitation from the source and the resultant signal. In free space, the phase shift is due to the filters and to the dampening coefficient, C_i . The dampening in the capacitors is usually due to air in the capacitors and C_i varies depending on the position of the middle plate with respect to the fixed parallel outer plates.

In addition within the nanoindenter set up there is also a 50X optical microscope (50X) which can be used to calibrate the location of indents with areas on the sample undergoing measurement. The nanoindenter is controlled via a software program called Nanosuite which allows different methods of indentation to be programmed. For instance it is possible to control the displacement of the tip and/or the load that the tip applies. This

means it is possible to have a level of control over the loading rate which is extremely important considering the time dependence of polymer samples. The methods can also control how the die approaches the sample and how it recognises when it is contact. The data collected is then analysed via nanosuite, Microsoft Excel and Origin Lab.

4.1.3 Raw data: Nanoindentation

Figure 4.3(a) presents raw data collected from the indentation of an 800 nm diameter diamond flat punch indented into a 150 nm PMMA film. The aim of presenting this data here is to introduce the form of the raw data collected during indentation along with an overview of noise on the system and how the nanoindenter calculates when it is in contact with the sample. Additional analysis is carried out on this raw data to convert it to stress vs. strain curves, which are then used to extract elastic modulus and yield stress. This is expanded upon in the analysis sections of chapters 5, 6 and 7. Firstly, load on sample versus displacement into sample is shown in figure 4.3 a along with a section of data from raw displacement versus raw load of nanoindentation tip when the tip is in free space.

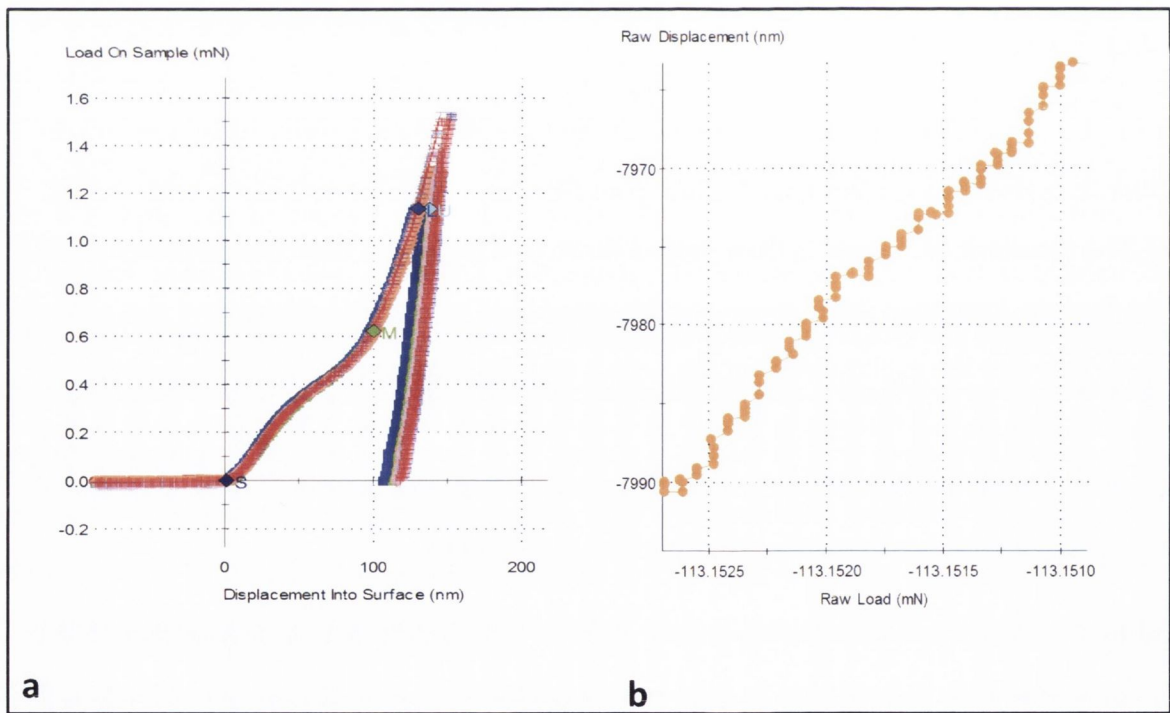


Figure 4.3: a) load on sample versus displacement into sample for 800 nm diamond flat punch into 150 nm 48 K PMMA. b) presents data of raw displacement versus raw load of nanoindenter when the tip is in free space.

This load versus displacement representation is the most fundamental data associated with nanoindentation. At the most basic level the nanoindenter applies a load and measures a displacement, and this is the most basic data from nanoindentation.

When the CSM is switched on a harmonic load or a harmonic displacement is set and maintained via a feedback loop. From the slope of harmonic load versus harmonic displacement the stiffness can be calculated. This can then be converted into an elastic modulus for the initial section of the indent (analysis carried out in chapter 5). In the most commonly used method throughout this thesis a harmonic displacement of 2 nm is chosen for flat punch nanoindentation which corresponds to a 2 nm oscillation on the indenter tip as it moves. Figure 4.3 b shows this harmonic displacement in free space. The nanoindenter uses a feedback loop as described in section 4.1.2 to calculate the load required to maintain the 2 nm displacement. Figure 4.4 presents the data for the harmonic load and harmonic displacement just before and during the actual indentation of the tip into the sample.

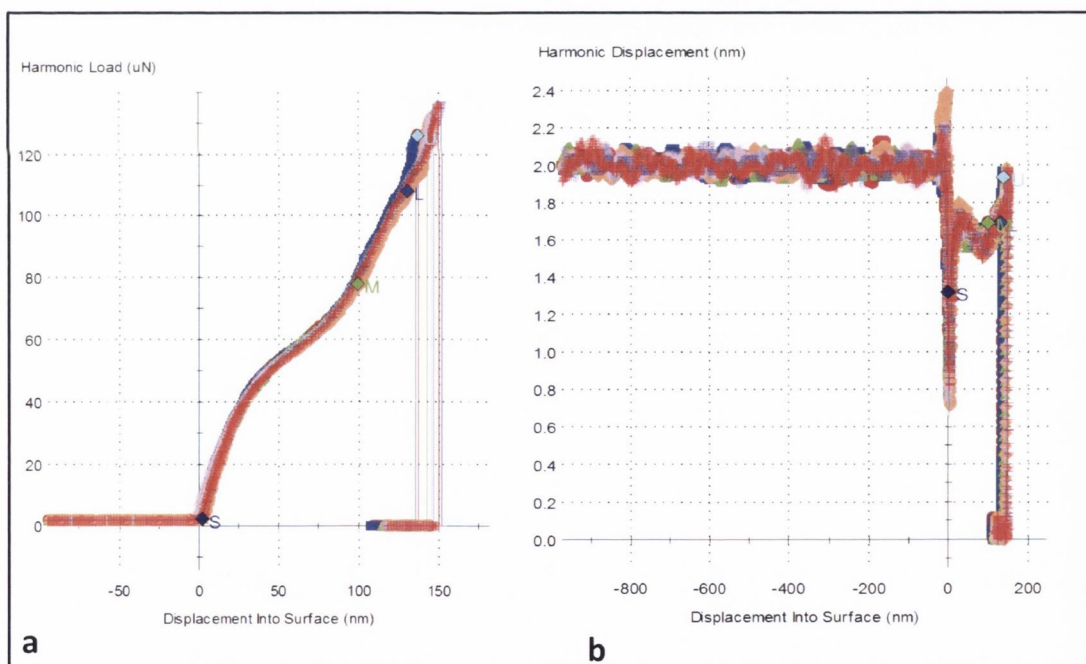


Figure 4.4: a) harmonic load required to maintain a harmonic displacement of 2 nm. b) presents the data for how well the nanoindenter managed to maintain the 2 nm displacement. From this data it is possible to see that before contact the indenter easily maintained a 2 nm harmonic displacement, but when it came in contact with the material it fluctuated to ~1 nm harmonic oscillation. After the system stabilised it then recovered to 1.8 nm oscillation rather than the set point of 2 nm.

Figure 4.4a shows the harmonic load required to maintain a harmonic displacement of 2 nm while figure 4.4b presents the data for how well the nanoindenter managed to maintain the 2 nm displacement. It becomes obvious from this data that before contact the indenter easily maintained a 2 nm harmonic displacement, but when it came in contact with the material it fluctuated around the set point before stabilising to ~ 1.8 nm harmonic displacement oscillation. The reason for this fluctuation is the speed of the feedback loop in the electronics of the nanoindenter which has a maximum frequency of 500 Hz. When the indenter undergoes a large variation it takes the electronics of the nanoindenter a period of time to adjust. One way to lessen the effect of this electronic adjustment time is to insert a small hold segment on the nanoindenter tip just after it comes into contact with the sample. This has the effect of reducing the error in the CSM data as indentation into the actual sample is carried out, although it has not proven possible to completely remove this error from the measurement.[17] However, as the indenter does correctly measure the harmonic displacement it actually achieved, as well as the harmonic load required, it is possible from recalculation of the sample after the test to calculate a reasonable stiffness shortly after the contacting section of the indentation.

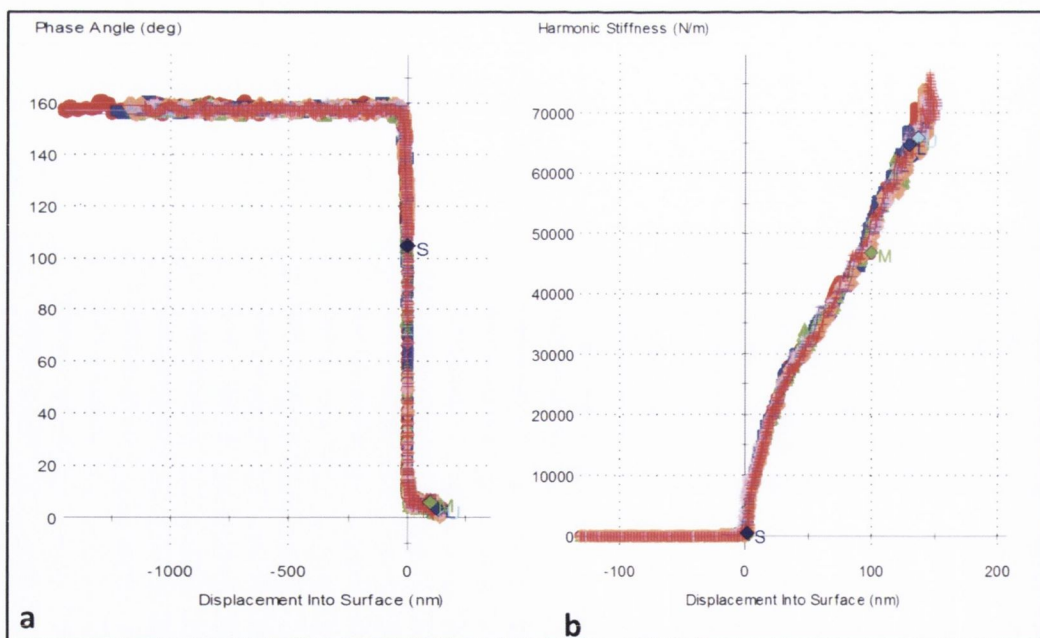


Figure 4.5 a) phase angle for indenter in free space and as it indents into sample. b) corresponding harmonic stiffness internally calculated by the nanoindenter software from harmonic displacement and harmonic load (Figure 4.4).

Figure 4.5 a presents the raw data for the phase angle, described in section 4.1.2. for the indenter just before it contacts the sample and as it indents into the sample. In this thesis this is the main method used to recognise when the indenter contacts the sample surface. In the most widely used set up for nanoindentation when the nanoindenter comes in contact with, what are generally, very hard materials the harmonic stiffness calculated shoots up upon contact with the hard material. Thus normal nanoindentation uses a surface find triggered when the harmonic stiffness (figure 4.5 b) goes above 200 N/m. However for softer materials, such as polymers, where it is possible for the indenter to contact the material but not drive the harmonic stiffness above 200 N/m, it is possible to program the indenter to trigger the surface when the phase angle, which is normally $156^\circ \pm 4^\circ$ drops below a certain value, for example 110° s (figure 4.5 b) in this experiment. The raw data collected is then analysed via Nanosuite, Microsoft Excel and Origin Lab and the results are presented in chapters 5, 6 and 7.

4.2 Custom Tip Manufacturing Process

4.2.1: Initial Alignment and Planarization of Diamond Flat Punches

A good supply of diamond flat punch tips is central to this thesis. As it is not possible to purchase these they must be fabricated internally in the group. The ideal customised flat punch tip is perfectly circular, has very low surface roughness (of the order of 1-2 nm) and sharp edges and sits at the lowest point of the tip, enabling it to cleanly contact the sample when placed in the indenter. Dimensions of the tip are also important, as the tip must be tall enough to offer good clearance when contacting a sample such that any pile-up that occurs does not contact any part of the tip. As most polymer samples used in this thesis were of the order of less than 200 nm thickness this does not present a large issue for this work. Manufacturing these tips involved the use of customised holders, FIB and SEM.

Standard sharp diamond indenter tips were obtained from MTS Nano Instruments and the indenter tip to be customised was mounted at an angle approximately 49 degrees in the FEI Focused Ion Beam (FIB) as in figure 4.6. It was possible for the tilt stage in the FEI FIB to move from -14 to 52 degrees. A tip holder was designed so as to limit the need of the tilt

stage from approximately 0 to +7. This drastically reduced the likelihood of crashing the tip while in the SEM and allowed the indenter tip to be easily aligned with both the FIB beam and the electron beam.

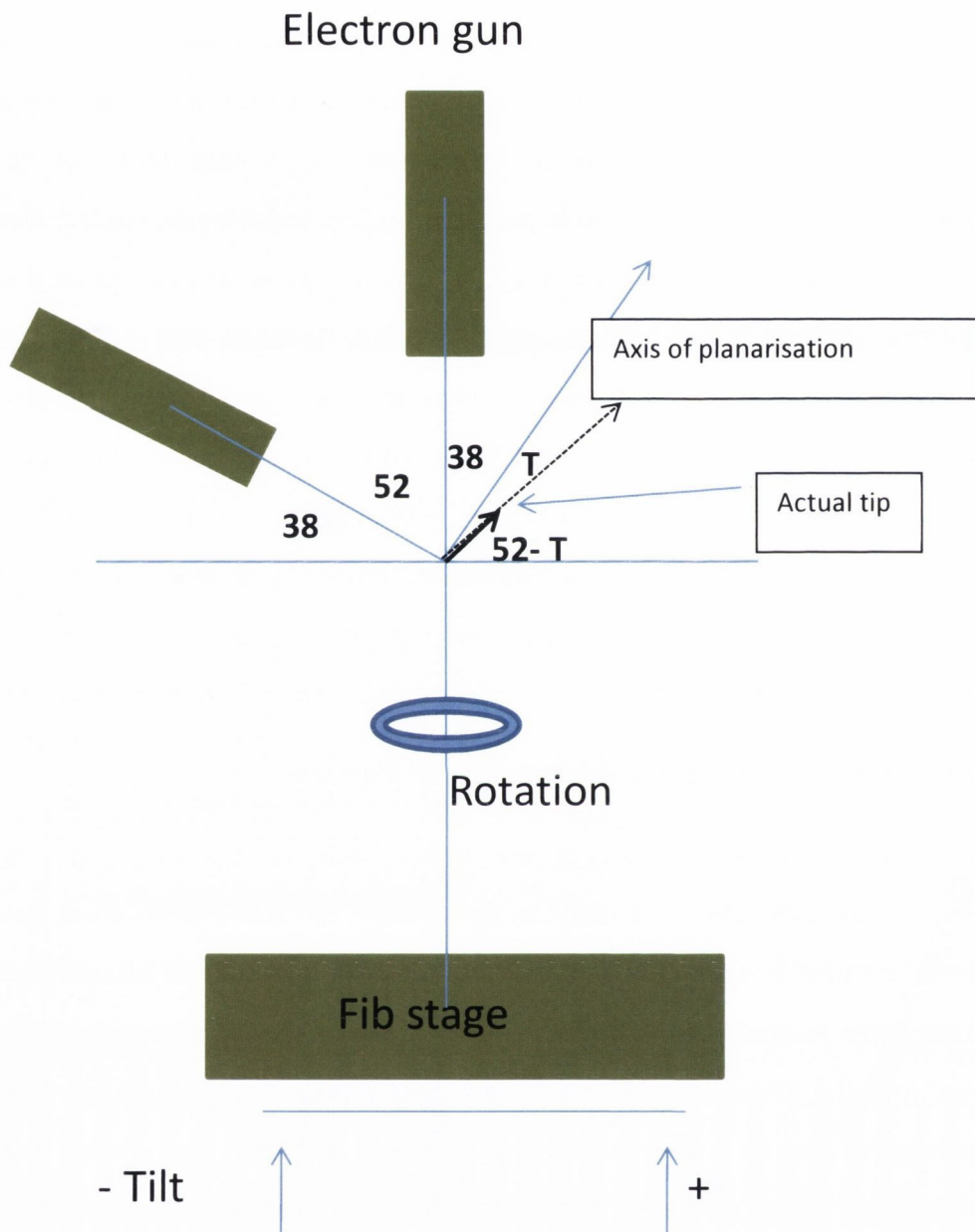


Figure 4.6: Initial FIB set up for manufacturing diamond flat punches.

Next the tip was focused on using the ebeam and FIB. Figure 4.7 shows two ultra high resolution images of a tip about to undergo customisation.

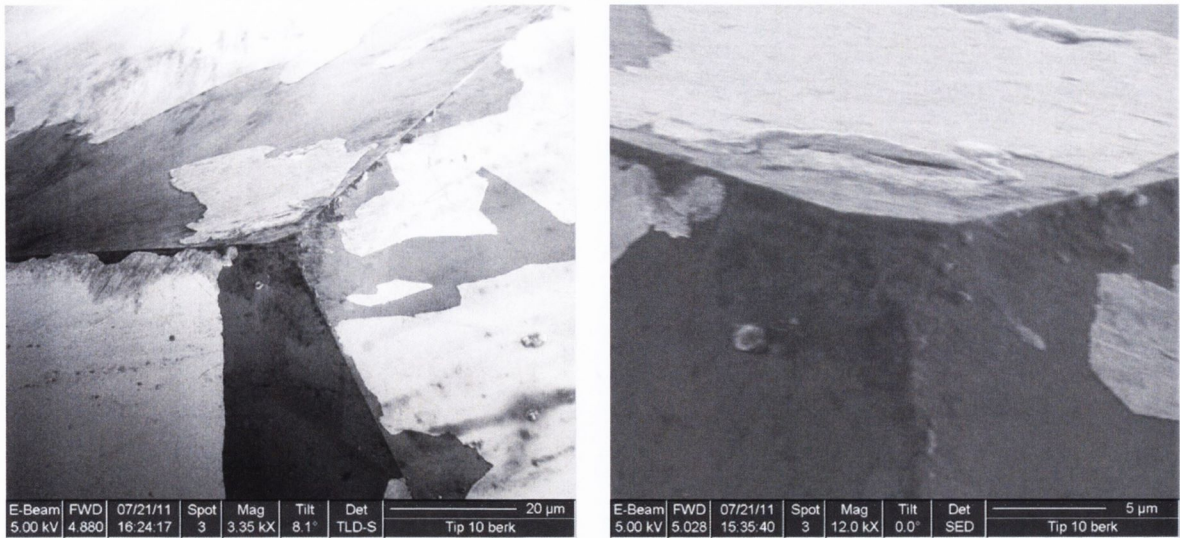


Figure 4.7: Ultra high resolution images of diamond nanoindentation tip about to undergo manufacture into flat punch.

The next step was to position the tip for planarization. The objective of this step is to cut a smooth plane at the top of the nanoindenter tip where the flat punch will be fabricated. This smooth plane should be cut so that when the nanoindenter tip is taken out of the FIB and placed in the nanoindenter, upon indentation it should be close to being aligned when coming into contact with a smooth surface, without using a tilt stage. This means that the planarised area should be parallel to the base of the indenter tip, which is the part that slots into the nanoindenter. To do this the tip must be first tilted, and then rotated about its axes, until any cuts made using the FIB will be close to parallel with the surface of the tip base. To do this one must switch to the FEI FIB to FIB imaging and align the base of the tip at 90 degrees to it. This alignment was done by altering the tilt until it is possible to draw a horizontal line along the tip base. The tilt angle (T) was then recorded.

The rotation (R) of the tip about its axis was next corrected by moving to the edges of the tip base. The tip was then rotated until the tip base, as best as can be seen by eye, was parallel to the ion beam. This was then referred to as position 1. Figure 4.8 shows the base of a well aligned tip.

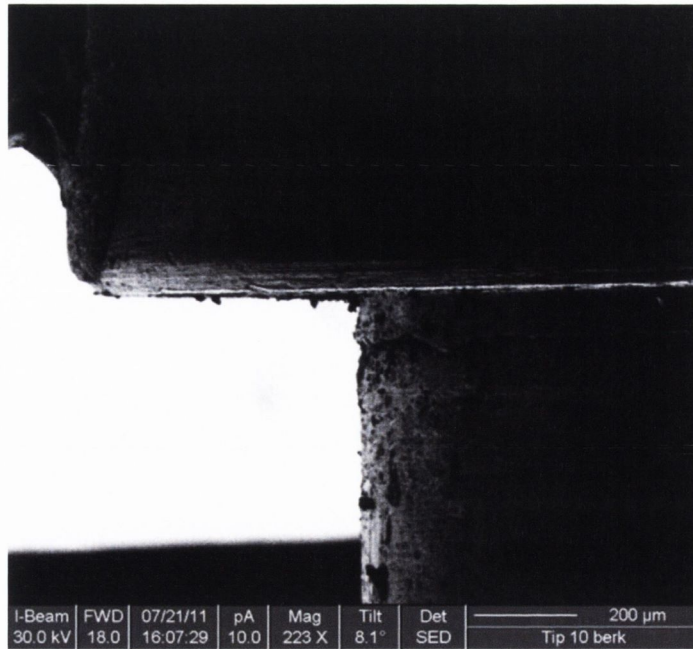


Figure 4.8: FIB image of the base of an aligned inverted nanoindenter tip as described above.

Using the FIB to align the base of the tip at 90° to the FIB beam translates to good alignment in the nanoindenter system. This is because the base of the tip inserts into the nanoindenter system. After alignment the FIB is moved back to the top of the tip and an ion beam of ~ 10 pA used to mill a planarised surface (Figure 4.9).

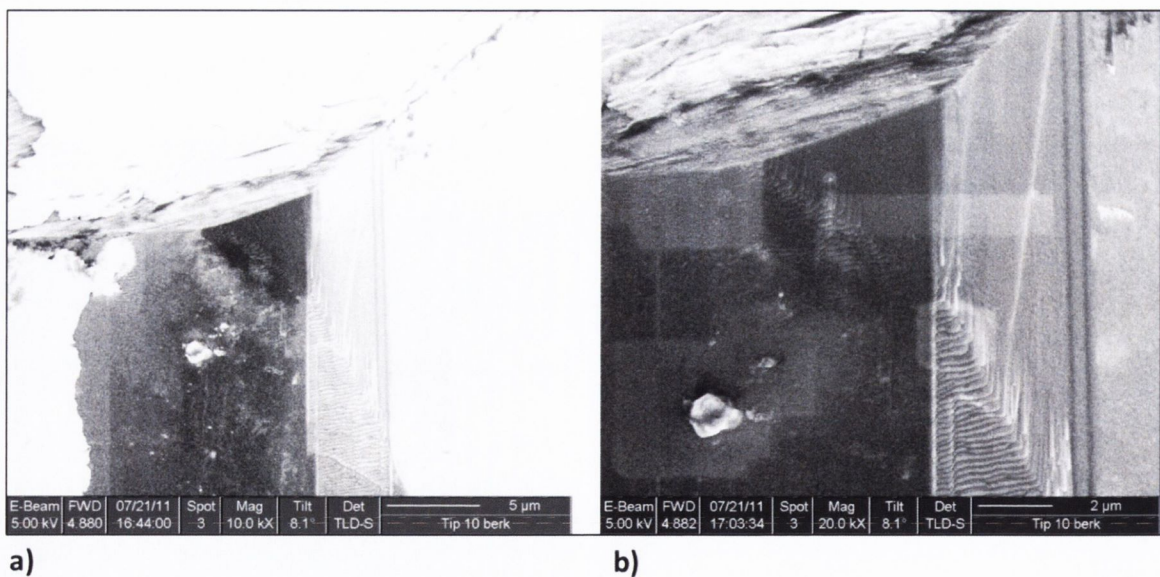


Figure 4.9 a) UHR resolution ebeam view after 240 seconds of milling with a 10 pA FIB current. b) UHR resolution ebeam view after 308 seconds of milling with a 10 pA FIB current.

The next step was top down milling to create the flat punch. For this step it was necessary to have the planarised surface at a right angle to the FIB beam as in figure 4.10. To accomplish this the tilt was zeroed so that absolute tilt (T_a) = 0 degrees. This ensured that when the tip was rotated it rotated with respect to the axis of the electron gun. Next the tip was rotated by 180 degrees. The tip was then at an angle of 38 degrees + T degrees from the electron gun. For top down milling the tip had to be at exactly 52 degrees from the electron gun to ensure planarised section of the tip is at 90 °s to the FIB beam. Therefore the tip holder was tilted by T_a to get it aligned for top down milling where

$$52 - 38 - T = T_a \quad . \quad \text{(Equation 4.9)}$$

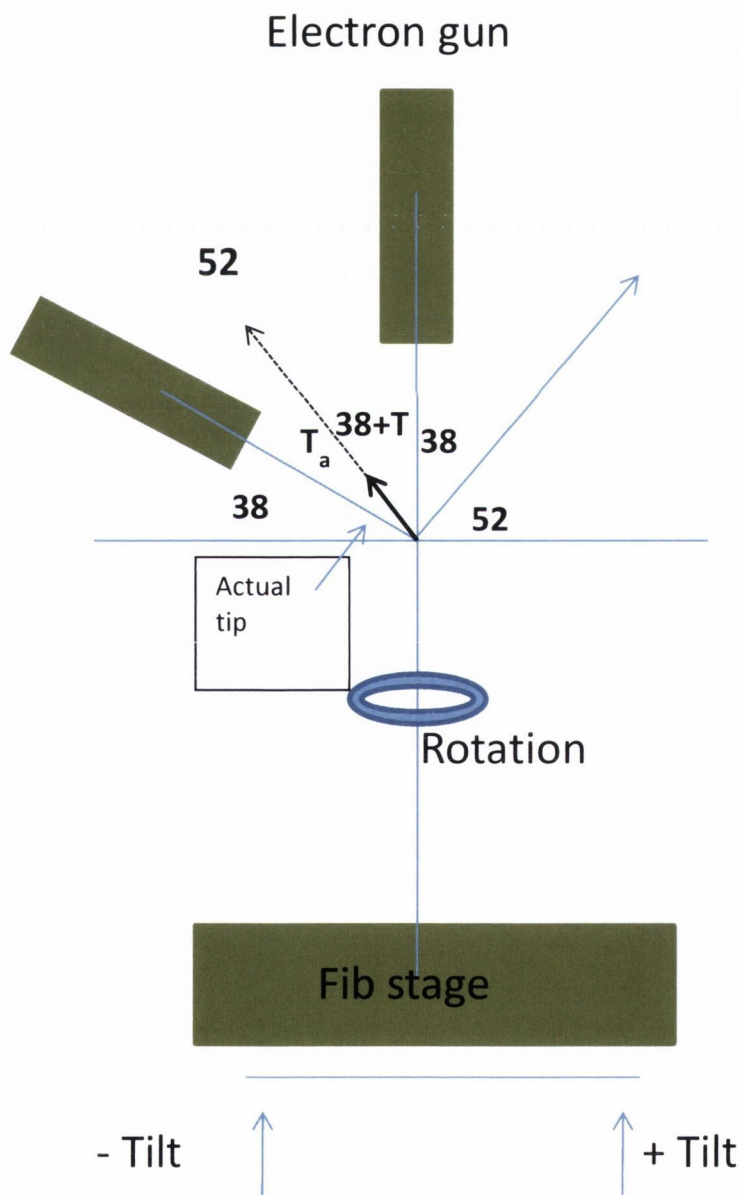


Figure 4.10: FIB set up for top down milling of diamond flat punches.

4.2.2: Direct top-down FIB Milling of Diamond Flat Punches

Following planarization, two methods were used to fabricate punches: Direct milling and gallium implant masking. All but one punch was manufactured using the direct milling technique described in this section. In Section 4.2.3, the implant masking process will be described.

Direct top-down FIB milling of planarised sharp diamond tips was used to produce circular punches of various diameters. For the first cut, a high FIB beam current was chosen depending on the amount of material to be removed. Flat, circular punches similar to that shown in figure 4.11(a), was the desired end result. To obtain a clean, defect free punch with sharp edges, a lower, finer-cutting beam current was employed as the cuts got closer to the final diameter of the flat punch required as shown in figure 4.11(b) and Figure 4.11(c).

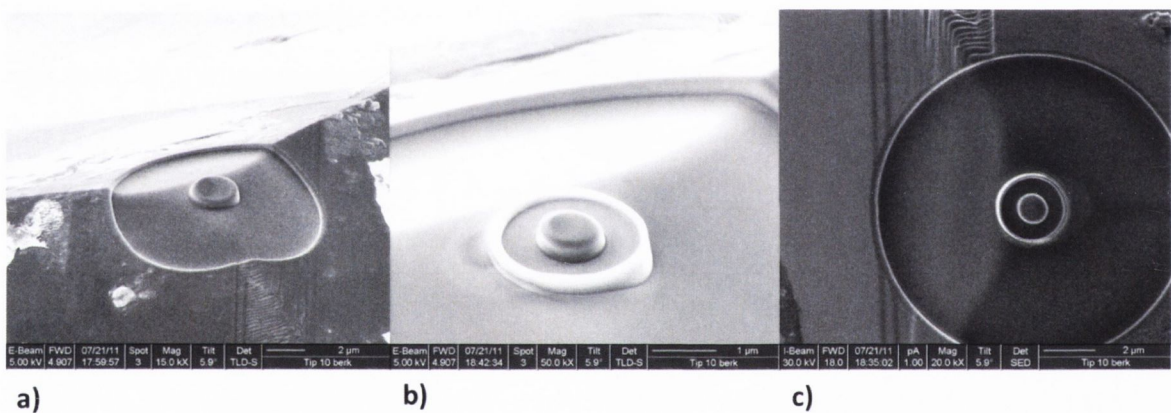


Figure 4.11: a) After top down coarse FIB mil (100 pA). b) after top down fine mil (10 pA). c) Top down view of the punch using the FIB beam at 10 pA.

The final step was to return it to position one and replanarise the flat punch by using a fine mil of 10 pA to clean the surface as in figure 4.12. Note that this punch was used for indentation into 50 - 60 nm films and so very little clearance was required above the circular outer walls of the punch. In addition the outer walls of the punch helped with alignment of the punch in the nanoindenter as described in the next section.

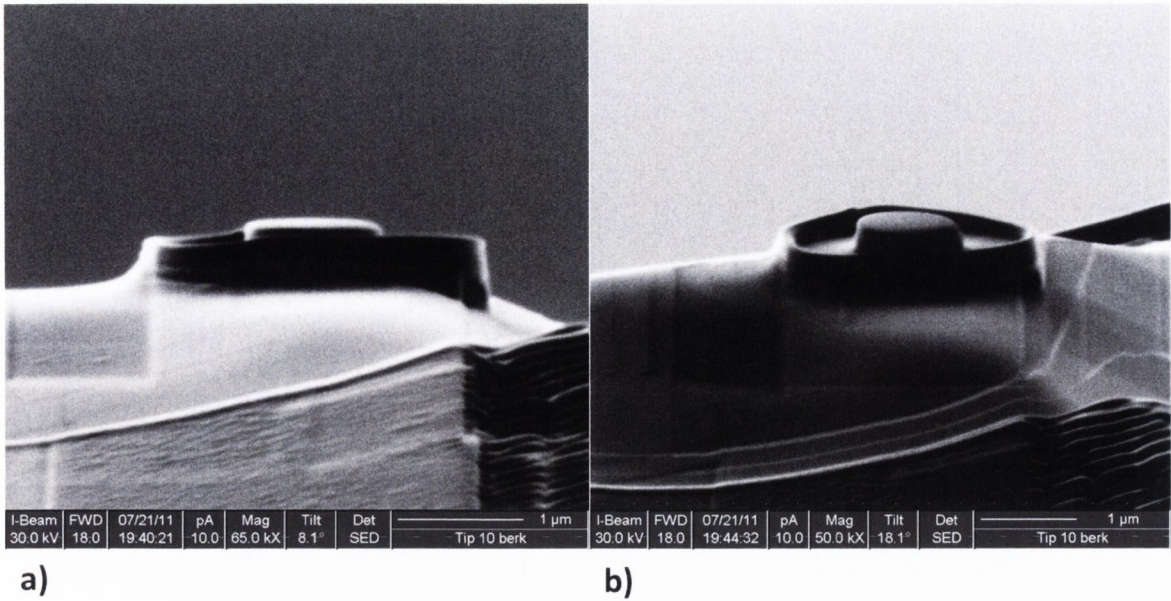


Figure 4.12: a) FIB side view of finished flat punch. b) E beam tilted view of finished flat punch.

4.2.3: FIB Masking and Plasma Etching of Diamond Flat Punches

One 400 nm DFP was manufactured using a different process from described above. Firstly a conductive diamond (or boron doped) tip was ordered from MTS system MTS Nano Instruments. All steps until the beginning of section 4.2.2 were identical. However, at this stage a gallium mask of the required flat punch diameter was created on the planarised surface. The tip was then placed in a plasma etcher and the end results is shown in figure 4.10 This process is described in more detail in McKenzie *et. al.* [18] and Tripathi *et. al.*[19]

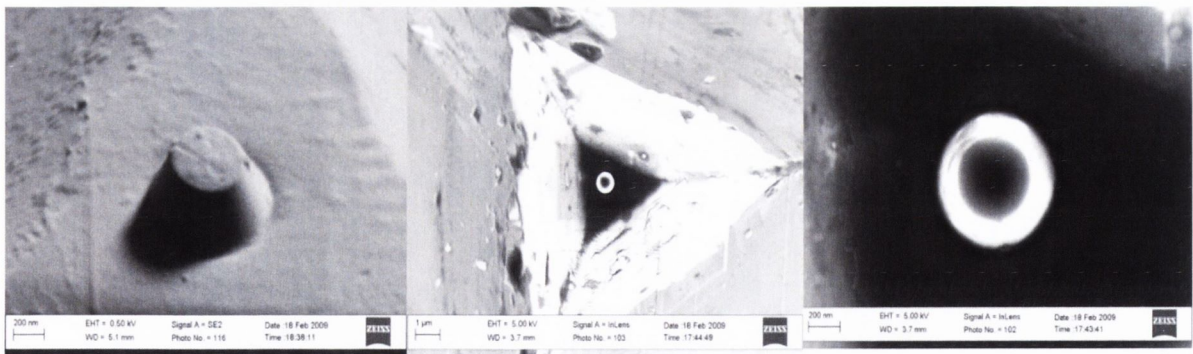


Figure 4.13: 400 nm diamond flat punch. a) is a tilted e-beam ultra high beam resolution image of the finished punch. b) is a zoomed out FIB image of top down view of the punch. c) is a zoomed in FIB image of a top down view of the punch.

4.3 Alignment of a flat punch to the sample surface

Punch face to film surface alignment [20] is a critical aspect of our experimental technique. When well-aligned, the indenter die face comes in contact uniformly with the sample, applying an instantaneous uniform strain across this entire region. We expect a characteristic signature of this kind of indentation into a film of elastic-plastic material (Figure 4.14). For materials like ductile polymer glasses we expect, with increasing strain, successive regimes of elastic deformation, elastic to plastic transition at a specific yield point followed by a post yield elastoplastic flow. As the elastoplastic flow develops to large strain, we see an additional effect of substrate elastic relaxation due to the difficulty in extruding a highly thinned film. In a typical load program, the loading is followed by a hold period where creep is observed. After creep is allowed to occur, the indenter is unloaded. Figure 4.14 shows this characteristic graph for a 52 nm thin film of polystyrene glass. The punch used was a 350 nm diamond flat punch with a punch face roughness of 2-3 nm. Excessive face roughness and misalignment of the flat punch leads can alter this signature. The strain at yield point appears to be high due to these contacting defects.

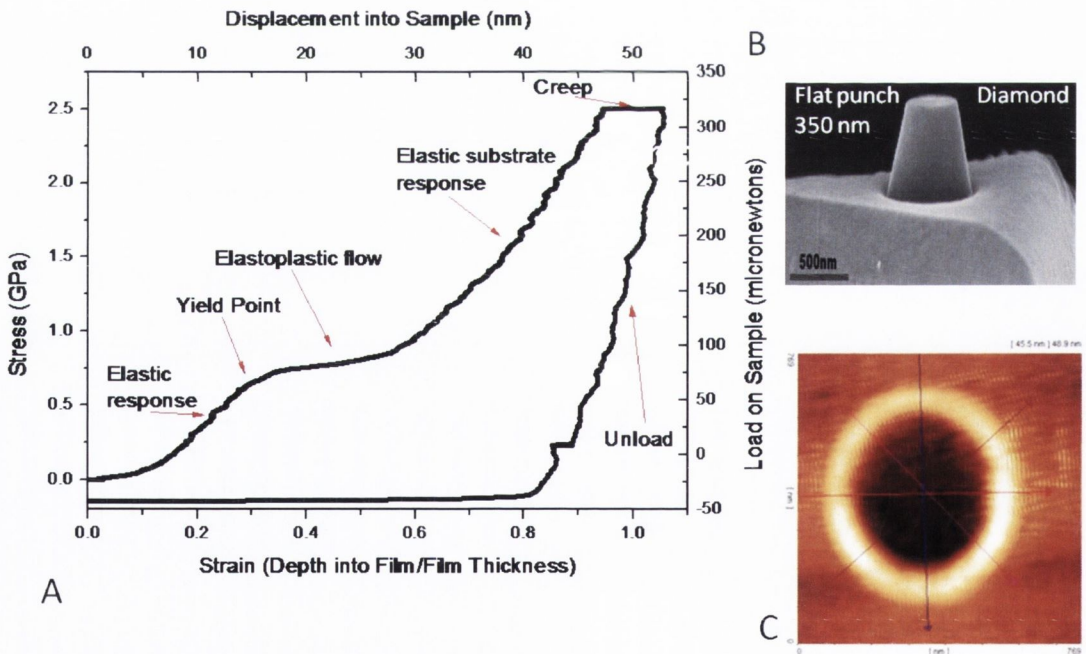


Figure 4.14: a) Characteristic measurement of ultra-thin polymer film taken using a 350 nm DFP. b) DFP used in indentation and c) shows an AFM of the remaining deformation.

4.3.1 Method of Alignment of Flat punch in Nanoindenter

It is of utmost importance during flat punch nanoindentation to be well aligned to the plane of the substrate. The direction of indentation must be perpendicular to the sample as shown in figure 4.15. A badly aligned punch shown in figure 4.16 will have larger error values associated with it.

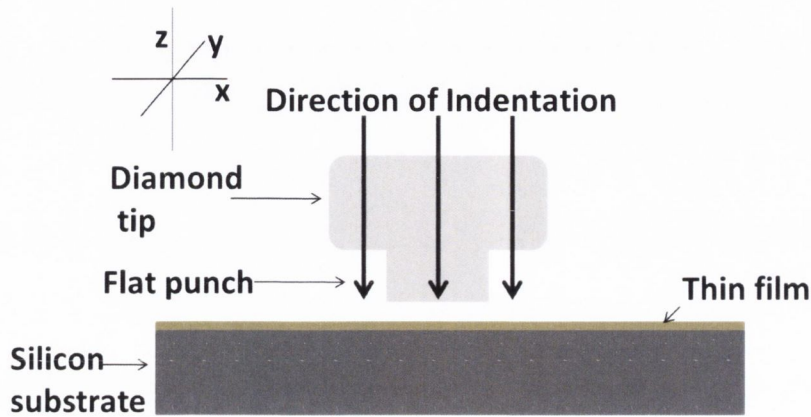


Figure 4.15: Schematic of aligned flat punch indentation.

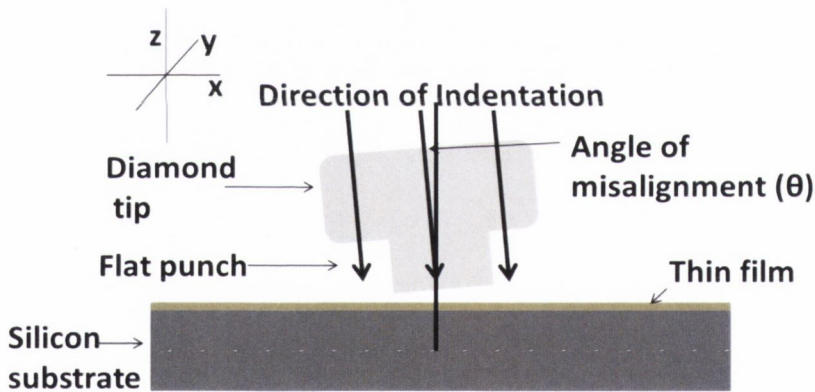


Figure 4.16: Schematic of misaligned flat punch indentation.

In the misaligned schematic (Figure 4.16) the flat punch does not contact the sample smoothly, and it will be $2r \sin \theta$ before the punch is fully in contact with the sample, where r is the radius of the circular punch face and θ is the angle of misalignment. This will lead to error in our measurement which can result in an increased contact modulus and forming stress.

To reduce this error in measurement a precision tilt stage (Physik Instrumente) is used that allows the sample to be rotated independently about two orthogonal directions in the

plane of the sample. This capability is used in conjunction with an *in situ* Atomic Force Microscope (AFM, Danish Micro Engineering (DME)) that verifies the planarity of shallow contact impressions. To achieve good alignment, a series of indents are carried out using the flat punch and thin film sample. The depths of indentations are varied, generally from 10 nm indent depth to 100% of the film thickness. AFM images of the indents are taken and then profiles of the images analysed. The AFM image and nanoindenter optics are out of phase by 2.8 degrees (figure 4.17). This can be accounted for simply by rotating the image by 2.8 degrees in the clockwise direction and then carrying out the x and y axis profile analysis. If this misalignment is not accounted for Where it may cause an issue is in additional movement rotation of the tilt stage if any estimates of the position of the x and y axis are off significantly.

Nanoindenter X-Y plane (top down)

AFM X-Y Plane alignment (top down)

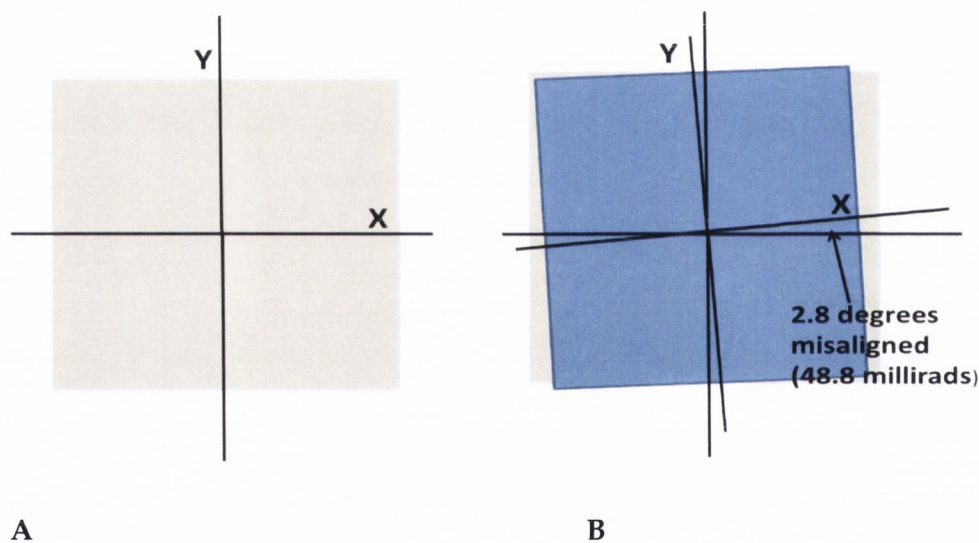


Figure 4.17: Nanoindenter x and y plane, top down alignment with AFM.

Using AFM image of a flat punch indent a depth profile along the x and y axis of the indent is calculated. As these are orthogonal planes they are linearly independent and so varying the angle of one in the z direction does not affect the other. When an angle of misalignment is calculated (shown in figure 4.16) the tilt stage is then moved so as to move the indenter tip in the x plane perpendicular to the sample x axis (or the flat surface of the punch along the x axis is parallel to the sample's x axis). The tilt stage has a resolution of 0.003 millirads. Once this is corrected for in the x axis it is repeated along the sample y axis.

When the base of the indent and the sample are parallel in the two orthogonal directions then we can be confident that the sample is aligned. Any apparent misalignment error in alignment is then due to any features on the flat punch surface.

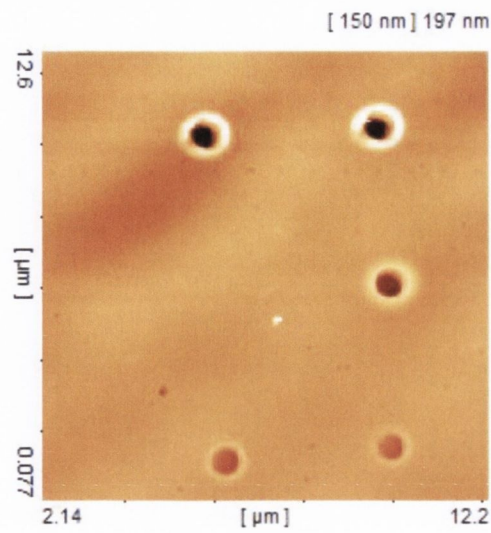


Figure 4.18: 700 nm DFP indents to 20, 50 and 150 nm into 150 nm film of PMMA.

Indenting to various depths (figure 4.18) give an overall impression of alignment within the sample. Here it can be seen that the indent to 20 nm (figure 4.19) leaves a definite circular indent.

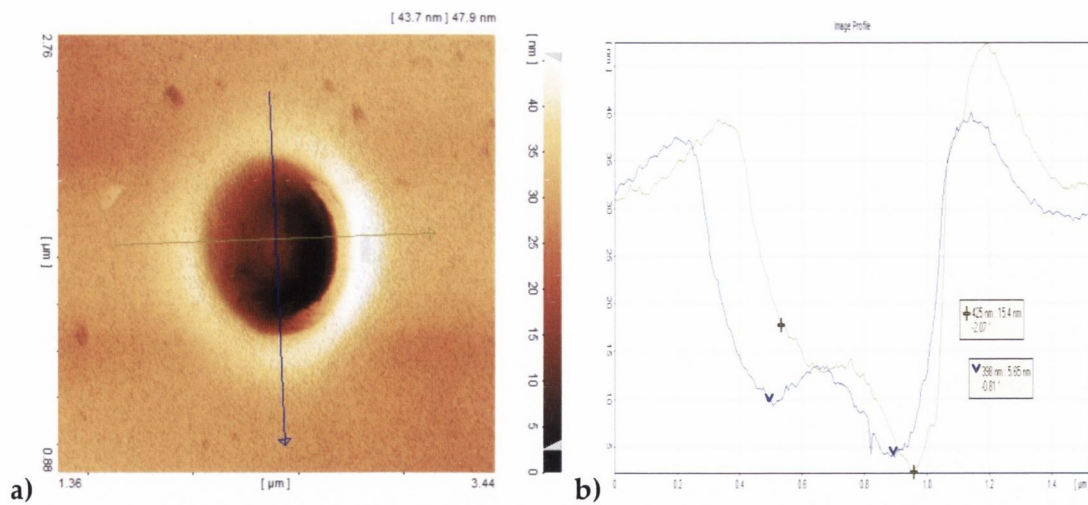


Figure 4.19: a) AFM image focused in on indent to 20 nm depth. b) Profiles corresponding to figure 4.19 a.

From figure 4.20 we see that the x axis must be rotated $2.07 \times 17.4 \times 3184$ steps to accommodate this tilt and $0.81 \times 17.4 \times 3184$ steps in y to accommodate the y misalignment.

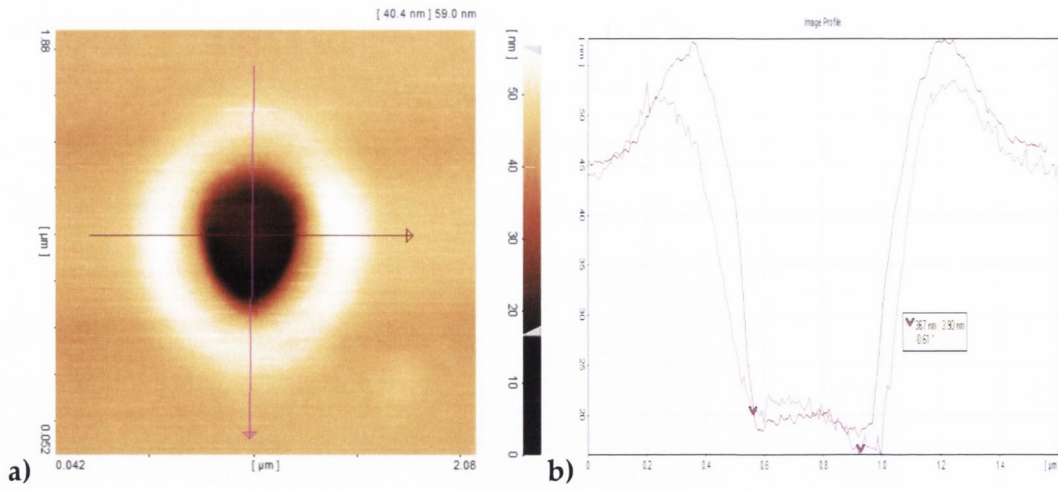


Figure 4.20: AFM and profile image after adjusting x and y plane by 110000 steps in x and 40000 in y.

At this stage the x axis is well aligned, however the y axis still needs to be rotated the equivalent of 0.61 degrees. Figure 4.21 shows an example of well aligned 400 nm punch

after all adjustments have been carried out.

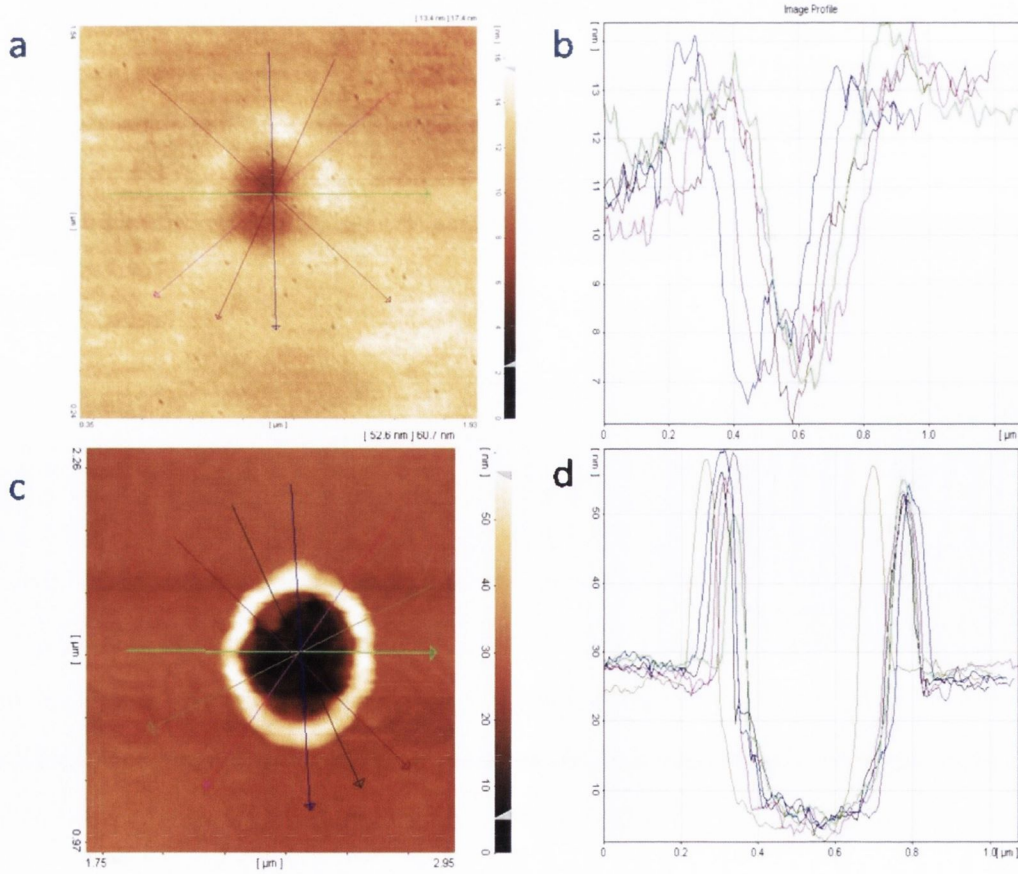


Figure 4.21: 400 nm punch into 30 nm film aligned. Indent was to a) 5 nm and c) 50 nm with b) and d) been the respective profiles of the flat punch indent.

4.3.2: Mounting and Alignment of Multiple Polymer Samples on Same Test Stub

Alignment of individual samples with DFP tips is a time consuming and costly process. Therefore if several samples are mounted on one stub and this alignment can be quantified it reduces the time required to move between samples. Therefore, several samples were mounted on one aluminium stub by heating the stub to 90 ° C and depositing a thin layer of crystal bond upon it.

Crystal bond is a heat based wafer mounting adhesive. Advantages of this material is that when cooled, there is a very high stiffness associated with it which means we can discount it as a source of any unwanted mechanical compliance during the test. Additionally it dissolves in acetone meaning that for most samples it is reversible. When the crystal bond is in an extremely liquid state the sample to be tested is placed on top of it and pressed into place. The stub is then cooled quickly by placing the base of it in cold water and the crystal bond solidifies.

To test the difference in alignment between several samples on the same stub a simple nanoindentation test was carried out. After careful alignment of the first sample as described in section 4.3.2, the same tip was brought in contact with each sample and the height of sample, and position in the horizontal plane recorded. Here is important to note that during the alignment process the goal was to have the flat of the DFP at a 90° angle to the sample. This is illustrated in figure 4.2. To do this a tilt stage was employed until the sample was aligned at a right angle to the flat of the DFP.

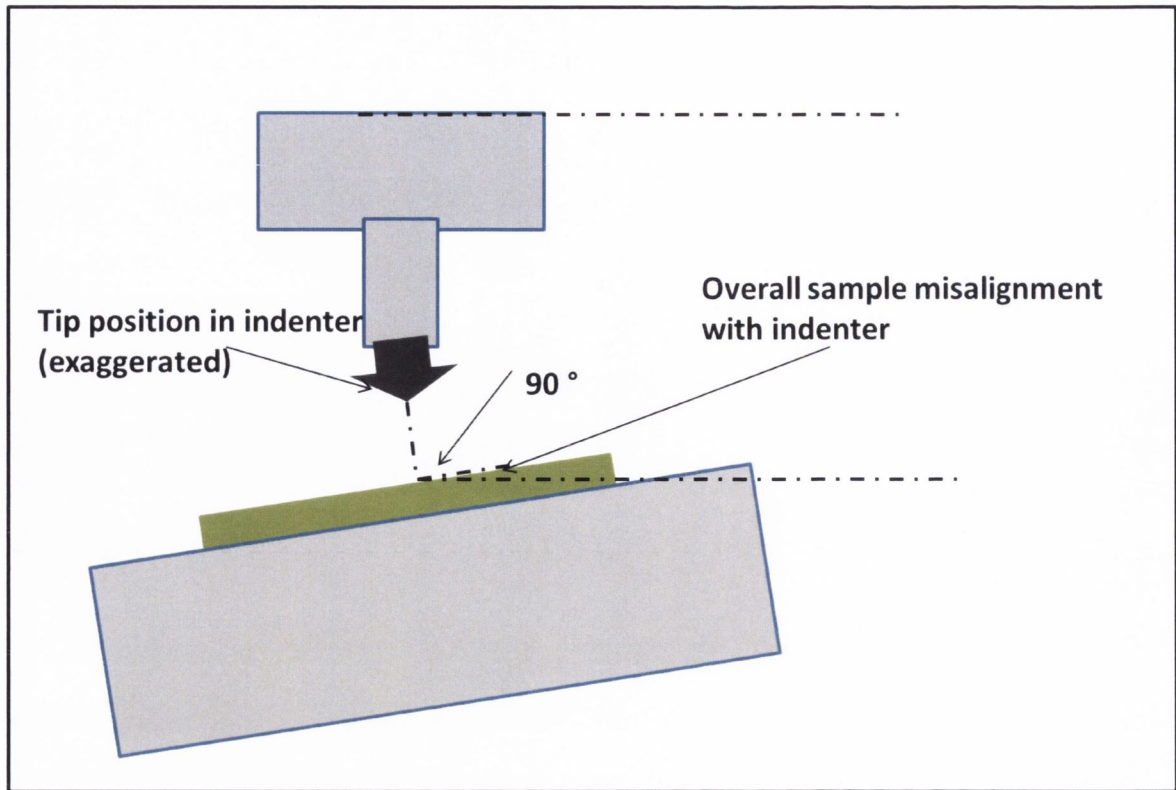


Figure 4.22: Schematic to illustrate the alignment process in indenter and affect that has on alignment in several samples.

Using Pythagoras's theorem, the overall sample misalignment with indenter was calculated by measuring the x, y and z position of several points on one sample. This was then compared with several different samples mounted on the same stub and repeated for several stubs. The overall angle of misalignment was found to have an error of 0.02° or 3.5 millirads when samples were carefully prepared in this manner. This is a reasonable error [20] which correspond to less than 1% error in measured forming stress and forming strain. Hence, once one sample on a stub is aligned, all samples can be assumed to be aligned within this error.

4.4 Sample Preparation

4.4.1 Homopolymer Preparation

Homopolymer films were prepared by cleaning silicon substrates in acetone, methanol, and deionized water rinses, followed by a 20 min dehydration bake at 120°C . In these

experiments, thin films of PS 384 K M_w (purchased from polymersource.com) were prepared to various thicknesses by spin-casting polymers of different % wt. in toluene at various spin speeds, following closely the experimental method described in Hall et al's paper on spincoating ultra-thin films [21] of both PS and PMMA. Samples were annealed at 150 °C for 120 min in air to reduce spin-casting-induced internal stresses [22] with heating and cooling ramps of 2 °C/min to 150 °C and holding the temperature for 2 hours at 150 °C. Samples were aged for at least three months at 20 °C prior to testing and showed no signs of large-scale dewetting.

All film thicknesses were measuring using a Veeco DekTak surface profilometer which has an accuracy of ± 0.5 nm. To carry out this measurement it was necessary to scratch away a small section of the polymer film in several areas of the film and record a minimum of five profiles per scratch. From this an average film thickness and error in film thickness was calculated.

4.4.2 Block Copolymer Preparation

Thin films of 37-37 K PS-PMMA block copolymers were prepared using the following steps by Richard Farrell and Dipu Borah of Professor Mike Morris's group in Tyndall, Cork. 8" silicon wafers were cleaned using fresh piranha solution. A random PS-PMMA copolymer brush layer of approximately 2-3 nm was then prepared on the surface. This brush layer acts as a method for precise control of the relative surface affinities of PS and PMMA and is discussed in more detail by Mansky et al [23]. A polymer solution of 1.0 wt.% was prepared in chromatographic grade toluene. The admixture was stirred at 1000 rpm for 24 h at room temperature (~ 15 °C) to ensure complete dissolution of the polymer. This solution was spin coated onto substrates at 3000 rpm for 30 s followed by an annealing step in a vacuum oven at 170 °C. Half the samples with annealed for 1 h, the rest for 6 h. When the samples were removed from the vacuum oven they were quenched to room temperature. The polymer brush anchored silicon substrates were cleaned prior to spin coating the lamellar diblock copolymer. Cleaning is necessary to remove the unanchored polymer from the substrate. Substrates were sonicated in fresh chromatographic grade toluene for 5 min (repeated thrice) and then ringed in fresh chromatographic grade toluene (repeated thrice). Finally, they were oven dried at 60 °C for 1 h.

The diblock copolymer used is a Poly(styrene)-*b*-poly(methyl methacrylate), P(S-*b*-MMA) with molecular weights (M_n) of 37,000 g mol⁻¹ for poly(styrene) and 37,000 g mol⁻¹ for poly(methyl methacrylate) blocks respectively with a poly-dispersity index of 1.07. Solution of 1.0 wt.% was prepared in chromatographic grade toluene. The admixture was stirred at 1000 rpm for 24 h at room temperature (~15 °C) to ensure complete dissolution of the polymer. The solution was spin coated onto the substrates at 3000 rpm for 30 s before half of the samples were annealed in a vacuum oven at 170 degrees for 1 hour and the second half annealed for 6 hours. Annealing for just one hour ensures that the toluene has been removed from the BCP sample but is not sufficient time for the sample to have undergone phase separation. The substrates were removed from the vacuum oven after annealing and quenched to room temperature. They were subsequently imaged using AFM (figure 4.23) to confirm the state of microphase separation from weakly to strongly segregated.

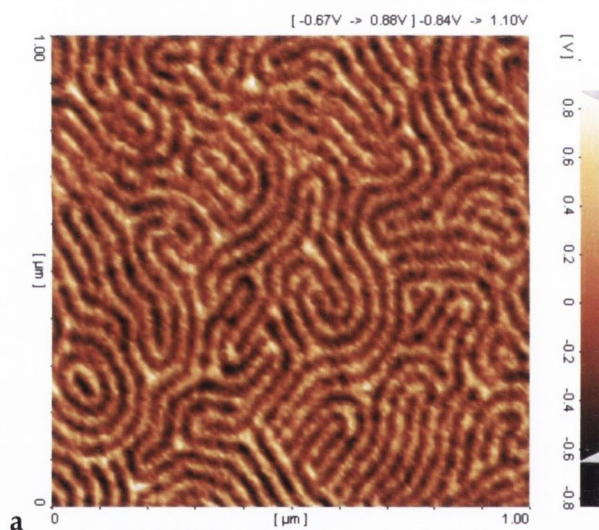


Figure 4.23 : a) shows an AFM phase image of 37-37 K block copolymers phase separated into PS and PMMA domains under strong segregation.

4.5 References

- [1] W. C. Oliver and G. M. Pharr, "Measurement of hardness and elastic modulus by instrumented indentation: Advances in understanding and refinements to methodology," *Journal of Materials Research*, vol. 19, pp. 3-20, 2004.

- [2] G. Reiter, M. Hamieh, P. Damman, S. Sclavons, S. Gabriele, T. Vilmin, and E. Raphael, "Residual stresses in thin polymer films cause rupture and dominate early stages of dewetting," *Nat Mater*, vol. 4, pp. 754-758, 2005.
- [3] C. M. Stafford, C. Harrison, K. L. Beers, A. Karim, E. J. Amis, M. R. VanLandingham, H.-C. Kim, W. Volksen, R. D. Miller, and E. E. Simonyi, "A buckling-based metrology for measuring the elastic moduli of polymeric thin films," *Nat Mater*, vol. 3, pp. 545-550, 2004.
- [4] E. P. Chan, K. A. Page, S. H. Im, D. L. Patton, R. Huang, and C. M. Stafford, "Viscoelastic properties of confined polymer films measured via thermal wrinkling," *Soft Matter*, vol. 5, pp. 4638-4641, 2009.
- [5] H.-N. Lee, K. Paeng, S. F. Swallen, and M. D. Ediger, "Direct Measurement of Molecular Mobility in Actively Deformed Polymer Glasses," *Science*, vol. 323, pp. 231-234, January 9 2009.
- [6] J. A. Forrest, "A decade of dynamics in thin films of polystyrene: Where are we now?," *The European Physical Journal E: Soft Matter and Biological Physics*, vol. 8, pp. 261-266, 2002.
- [7] A. Mataz and G. B. McKenna, "Effects of confinement on material behaviour at the nanometre size scale," *Journal of Physics: Condensed Matter*, p. R461, 2005.
- [8] J. B. Pethica, R. Hutchings, and W. C. Oliver, "Hardness measurement at penetration depths as small as 20 nm," *Philosophical Magazine A*, vol. 48, pp. 593 - 606, 1983.
- [9] A. C. Fischer-Cripps, *Nanoindentation*, 2nd Edition ed. New York Springer-Verlag, 2004.
- [10] W. C. Oliver and G. M. Pharr, "An improved technique for determining hardness and elastic modulus using load and displacement sensing indentation experiments," *Journal of Material Research*, vol. 7, 1992.
- [11] K. L. Johnson, *Contact Mechanics*, 1 ed. Cambridge: Cambridge University Press, 1985.
- [12] I. M. Hutchings, "The contributions of David Tabor to the science of indentation hardness," *Journal of Materials Research*, vol. Vol. 24, 98.
- [13] http://www.nanoindentation.cornell.edu/Machine/commercial_machine.htm.
- [14] F. Yang, "Asymptotic solution to axisymmetric indentation of a compressible elastic thin film," *Thin Solid Films*, vol. 515, pp. 2274-2283, 2006.
- [15] J. B. Pethica and W. C. Oliver, "Tip Surface Interactions in STM and AFM," *Physica Scripta*, vol. 1987, p. 61, 1987.
- [16] E. Doherty, in *Physics*. vol. PhD Dublin: Trinity College, 2012.
- [17] A. J. Moseson, S. Basu, and M. W. Barsoum, "Determination of the effective zero point of contact for spherical nanoindentation," *J. Mater. Res.*, vol. 23, 2008.
- [18] W. McKenzie, J. B. Pethica, and G. L. W. Cross, "A direct-write, resistless hard mask for rapid nanoscale patterning of diamond," *Diamond and Related Materials*, vol. 20, 2011.
- [19] S. K. Tripathi, D. Scanlan, N. O'Hara, A. Nadzeyka, S. Bauerdick, L. Peto, and G. L. W. Cross, "Resolution, masking capability and throughput for direct-write, ion implant mask patterning of diamond surfaces using Ion Beam Lithography," *Journal of Micromechanics and Microengineering*, vol. 22, 2012.
- [20] G. L. W. Cross, B. S. O'connell, J. B. Pethica, H. Rowland, and W. P. King, "Variable temperature thin film indentation with a flat punch," *Review of Scientific Instruments*, vol. 79, pp. 013904-13, 2008.
- [21] D. B. Hall, P. Underhill, and J. M. Torkelson, "Spin coating of thin and ultrathin polymer films," *Polymer Engineering & Science*, vol. 38, pp. 2039-2045, 1998.
- [22] T. Miyazaki, K. Nishida, and T. Kanaya, "Thermal expansion behavior of ultrathin polymer films supported on silicon substrate," *Physical Review E*, vol. 69, p. 061803, 2004.
- [23] P. Mansky, Y. Liu, E. Huang, T. P. Russell, and C. Hawker, "Controlling Polymer-Surface Interactions with Random Copolymer Brushes," *Science*, vol. 275, pp. 1458-1460, March 7, 1997.

Chapter 5 Flat punch Nanoindentation as a Method to Investigate Mechanical Properties of and Size Effects in Polymer Thin Films

5.1 Introduction

Flat punch nanoindentation has been introduced in chapter 2 and chapter 4 along with best practice for aligning the flat punch in contact with the polymer materials. However there are additional factors that must be taken into consideration. Firstly, the aspect ratio between the flat punch radius and the film thickness has a significant effect. Secondly the effect of contact geometry in TFFPN set up must be verified. Hydrostatic pressure under the punch, as discussed in chapter 2 must also be considered. While deformation of metals is generally independent of hydrostatic pressure this is certainly not the case for polymers and so this hydrostatic pressure does affect the deformation behaviour of the polymer samples and so must be taken into account. Additionally, the effect of sharp edges in flat punch nanoindentation must also be considered.

Thin film flat punch indentation specifically allows the measurement of mean stress vs. engineering strain signals in an experiment. The question is, for instance in a simple picture where one assumes behaviour can be adequately captured by an elastic-plastic constitutive law, how well can these curves can be used to extract E and Y_S material parameters. The first goal of this chapter is demonstrate to what extent it possible to extract values of elastic modulus and yield stress directly from flat punch nanoindentation curves, independent of the flat punch tip used.

Additionally, a highly non trivial section of the mechanics of materials is to understand the relationship between mechanics and the nanoscale structure. This has been examined in detail for metals and ceramics, but polymers have remained virtually untouched. While micron scale polymer physics has been probed, real size effects and changes in polymer behaviour have not. This chapter aims to highlight scalable mechanical size effects in polymer materials. To accomplish this, measurements were be made on ultra-thin polymers below 100 nm in thickness. Results presented here show that as film thickness of

PS and PMMA is reduced below approximately 50 nm the forming stress drops to much lower values. While this has been seen in FP nanoindentation for PS [1] it has never been seen before in PMMA. Also, as long as there is no issue of confinement of the molecule into a film thickness of less than R_g this effect appears to be independent of M_w in PS. In addition, for films below a thickness of 80 nm, E also drops for both materials.

5.2 Experimental Set-up

The premise here is to indent the same circular flat punch into various thicknesses of the two polymer material. The exact stress and flow field history of the deforming material will change depending on the starting geometry, evolving with film thickness. This measurement will allow us to plot FS against aspect ratio and examine the effect aspect ratio has on TFFPN.

Diamond flat punches of diameters 320 nm, 400 nm, 650 nm, 800 nm and 900 nm were fabricated using the focused ion beam method presented in chapter 4 (Figure 5.1)

The 400 nm punch (Figure 5.1 e) was manufactured using a different process from all the other punches. For this punch an etch process was used where a conductive diamond tip was planarised as described in section 4.2.1 but then the 400 nm circular mask was doped with gallium. This punch was then plasma etched and the 400 nm DFP was the result. This process is also discussed in section 4.2.2. What becomes apparent from Figure 5.1e(i), unlike the other punches which appear quite smooth, the 400 nm etched DFP appears to have significantly more surface roughness associated with this tip when compared with those in Figures 5.1 a-d. Also, its edges are notably sharper than the other punches, a fact which was discussed in chapter 2. Furthermore, the etched 400 DFP is chemically different from the other punches. This tip was manufactured using a gallium mask, and it was originally a conductive diamond tip. The different chemistry of this flat punch may cause it to interact with the polymers in a different way.[2] PMMA films and PS films were prepared as described in section 4.4.

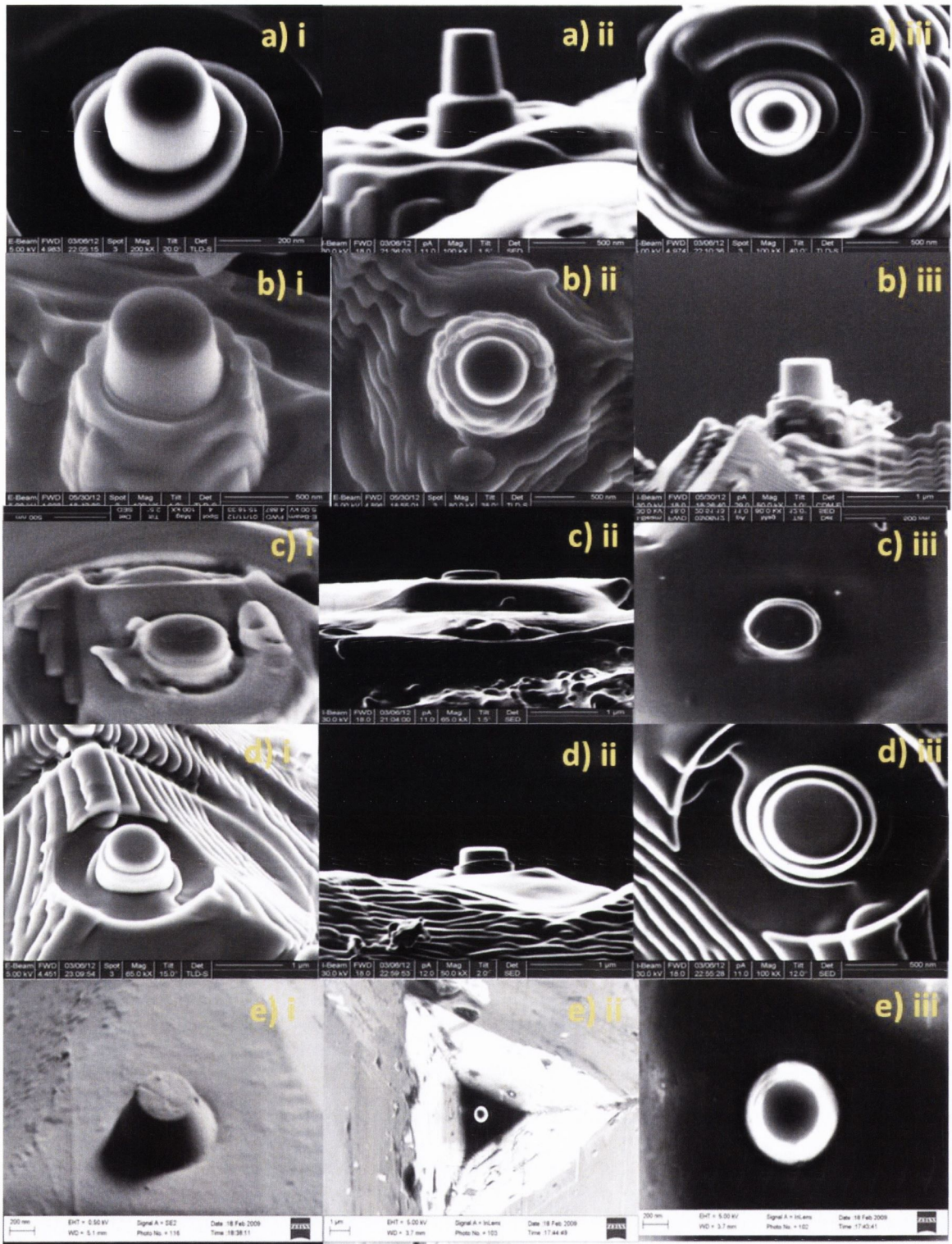


Figure 5.1 a: 320 nm DFP a i) is a tilted e-beam ultra high beam (uhb) resolution image of the punch. a ii) is a FIB image of a side on view of the punch. a iii) is a FIB image of a top down view of the punch. b: 900 nm DFP b i) is a tilted e-beam uhb resolution image of the finished punch. b ii) FIB image of top down view of the punch. b iii) FIB side view image of the punch. c) 650 nm DFP c i) is a tilted e-beam uhb resolution image c ii) is a zoomed out FIB image of top down view of the

punch. c) is a zoomed in FIB image of a top down view of the punch. d) 800 nm DFP d i) is a tilted e-beam uhb resolution image d ii) is a FIB image of a side on view of the punch. d iii) is a FIB image of a top down view of the punch. e) 400 nm DFP e i) is a tilted e-beam uhb resolution image of the finished punch e ii) is a zoomed out FIB image of top down view of the punch. e iii) is a zoomed in FIB image of a top down view of the punch.

	PS 44K	PS 900K	PS 9000K	PMMA 48K
Polydispersity	1.05	1.18	1.22	1.3
Film Thickness	50 ± 2 nm	26 ± 1.5 nm	31 ± 1.5 nm	26 ± 1.5 nm
Film Thickness	60 ± 2 nm	42 ± 2 nm	42 ± 2 nm	39 ± 1.5 nm
Film Thickness	84 ± 2 nm	52 ± 2 nm	63 ± 2 nm	60 ± 2 nm
Film Thickness	100 ± 3 nm	66 ± 2 nm	84 ± 2 nm	80 ± 2 nm
Film Thickness	168 ± 3 nm	168 ± 3 nm	168 ± 3 nm	150 ± 3 nm
Ageing State	6 months +	48 months +	48 months +	6 months +

Table 5.1: Polymer thin films prepared and tested in aspect ratio study.

5.3 Results and Discussion

The effect of aspect ratio and contact geometry will be analysed using a simple linear model. A sample of the data collected is presented in Figures 5.2 and 5.3. For each graph between ten and thirty indents were carried out. The results were then averaged and interpolated. The data was then fitted in a similar manner as used by van Melick *et. al.*[3] and by Rowland *et. al.* [4, 5]; whereby a linear fit was made to the low strain data, taking into consideration an offset that encapsulates any error in alignment of contact in addition to any features on the flat punch surface which might introduce apparent error in the contact. The slope of this line corresponds to a rough calculation of contact modulus (CM), however this is strictly true only for the case of zero strain. A second linear fit was made with the mid strain data, after the “knee” point in the data, and it is the intersection of the two linear fits that is taken here as the forming stress. The offset in error is subtracted from the strain at FS and it is this value that is considered to be the actual strain at FS, or the forming strain. One important note on FS, and in YS in other measurements made, is that it tends to occur at the approximately the same percentage strain of 7-8 % in tensile

experiments.[6] In TFFPN the knee in the stress strain curve generally corresponds to approximately 25%, with the reason for the increase in percentage strain thought to be due to both the compressive nature of the testing, geometrical factors and also any error in alignment. It is expected that this trend continues as film thickness is reduced, although hydrostatic pressure in the experiment does have the effect of blurring the exact point where the knee occurs.

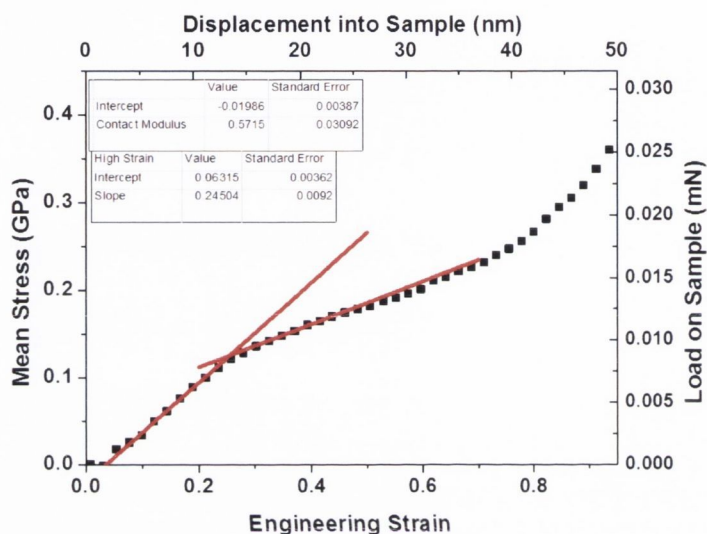


Figure 5.2: 320 nm DFP into 52 nm 9000 K PS. FS is found at the intersection of the two linear fits and is $0.12 \text{ GPa} \pm 0.02 \text{ GPa}$ and CM is calculated from the slope of the lower linear fit to be $0.57 \pm 0.03 \text{ GPa}$. Here error in misalignment and due to erroneous features on DFP is equivalent to 4% error in strain. Thus strain at FS is 0.24 ± 0.02 .

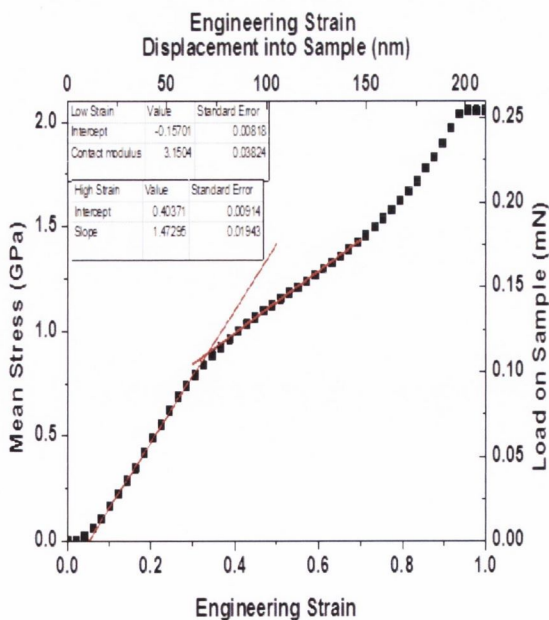
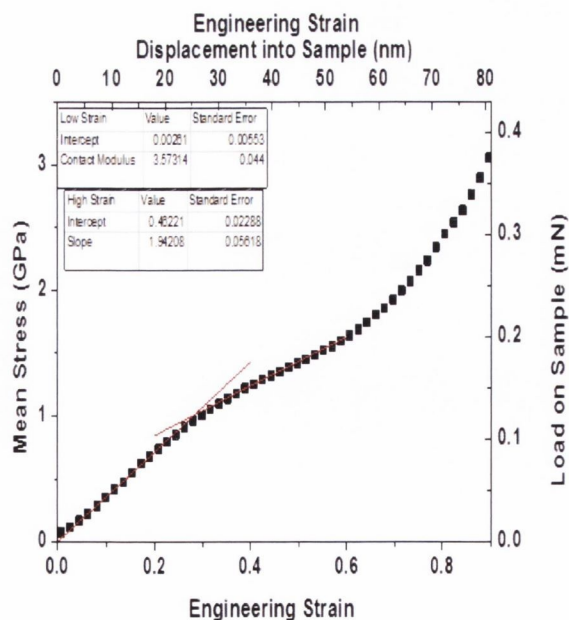
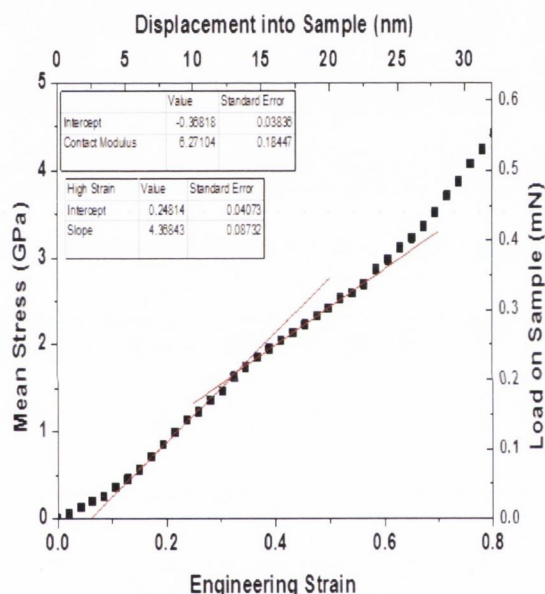
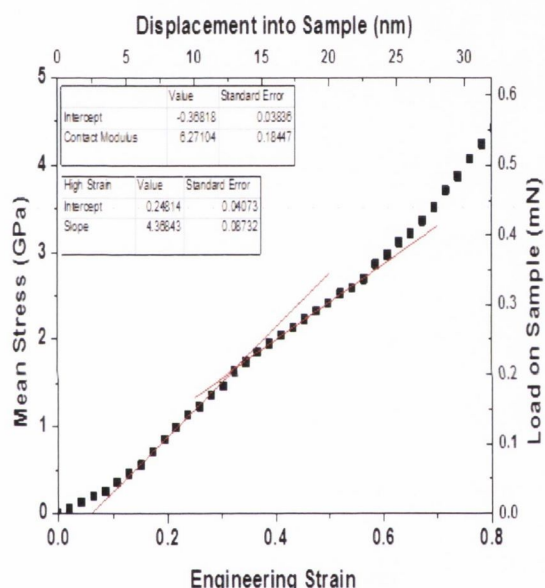
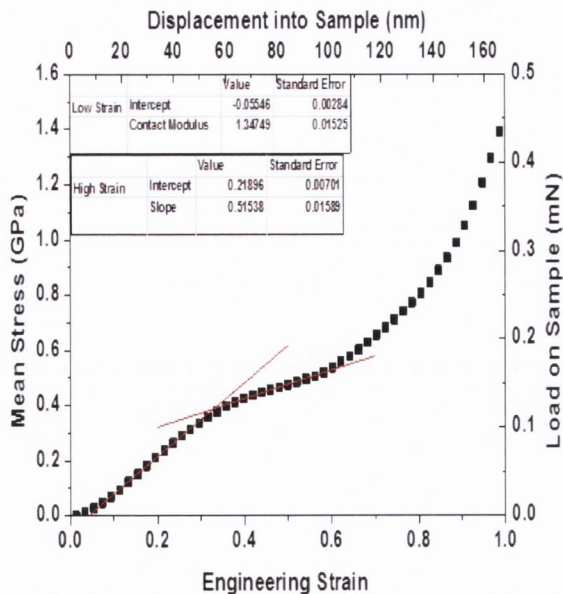
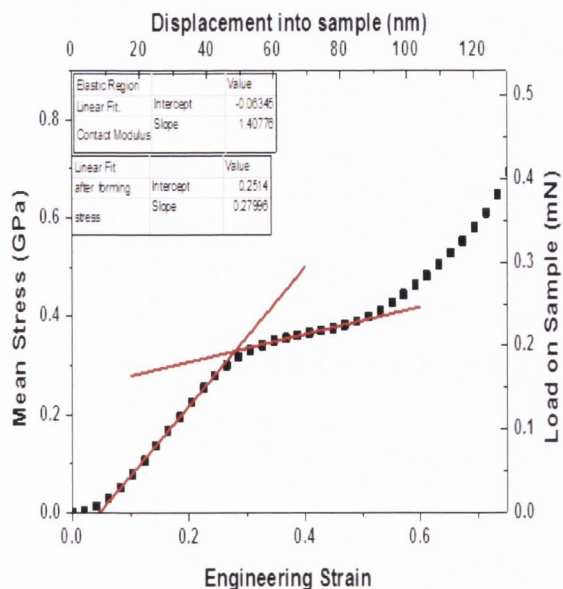


Figure 5.3: a) 900 nm into 168 nm 44 K PS. FS is $0.31 \text{ GPa} \pm 0.02 \text{ GPa}$ and CM is $1.4 \text{ GPa} \pm 0.1 \text{ GPa}$. Here error in misalignment and due to erroneous features on DFP is equivalent to 5% error in strain. Thus strain is at FS is 0.18 ± 0.01 . b) 650 nm into 160 nm 900K PS is $0.39 \text{ GPa} \pm 0.01 \text{ GPa}$ and CM is calculated to be $1.35 \text{ GPa} \pm 0.01 \text{ GPa}$. Here error in misalignment and due to erroneous features on DFP is equivalent to 2.5% error in strain. Strain at FS is 0.3 ± 0.05 c) 400 nm into 40 nm 48 K PMMA. FS is $1.7 \text{ GPa} \pm 0.03 \text{ GPa}$ and CM is $6.2 \text{ GPa} \pm 0.2 \text{ GPa}$. Here error in misalignment and due to erroneous features on DFP is equivalent to 6% error in strain. Strain at FS is 0.26 ± 0.03 . d) 400 nm into 65 nm 48 K PMMA. FS is $1.25 \text{ GPa} \pm 0.05 \text{ GPa}$ and CM is calculated to be $4.2 \pm 0.05 \text{ GPa}$. Here error in misalignment and due to erroneous features on DFP is equivalent to 6% error in strain. Strain at FS is 0.28 ± 0.05 . e) 400 nm into 90 nm 48 K PMMA. FS is $1.1 \text{ GPa} \pm 0.05 \text{ GPa}$ and CM is calculated to be $3.57 \pm 0.04 \text{ GPa}$. Here error in misalignment and due to erroneous features on DFP is equivalent to 0% error in strain. Strain at FS is 0.28 ± 0.01 . e) 400 nm into 200 nm 48 K PMMA. FS is $0.8 \text{ GPa} \pm 0.05 \text{ GPa}$ and CM is calculated to be $3.15 \pm 0.04 \text{ GPa}$. Here error in misalignment and due to erroneous features on DFP is equivalent to 4% error in strain. Strain at FS is 0.2 ± 0.01 .

5.3.1 Analysis of Forming Stress and Contact Geometry

Figure 5.4 shows forming stresses, extracted from raw data presented in the appendix, plotted against film thickness. One can see that, for both PMMA and PS, as the film thickness increases the FS decreases.

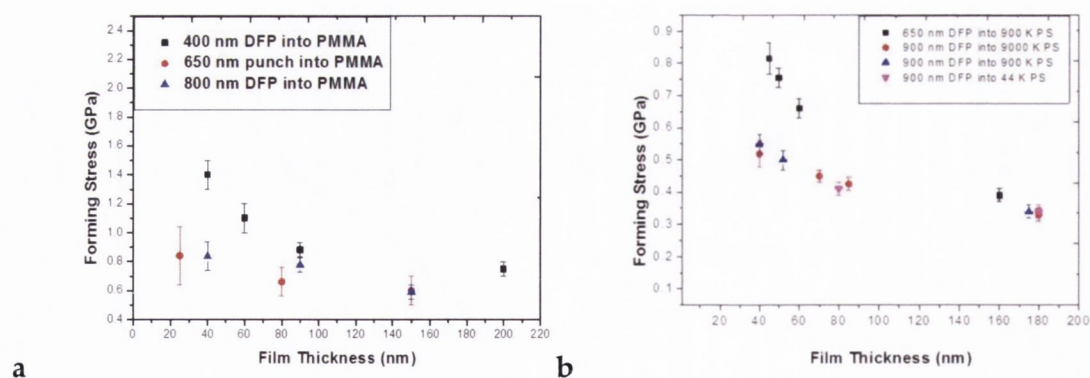


Figure 5.4: a) FS against film thickness plotted for 400 nm, 650 nm and 800 nm DFP into PMMA and b) for 650 nm and 900 nm DFP into PS.

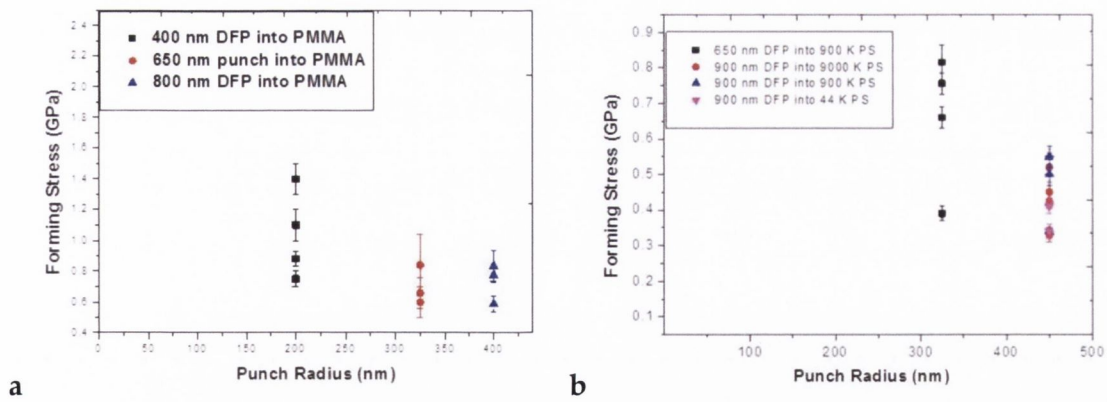


Figure 5.5: a) FS against punch radius (a) plotted for 400 nm, 650 nm and 800 nm DFP into PMMA and b) for 650 nm and 900 nm DFP into PS.

Figure 5.5 shows the forming stresses against punch radius. One can see again that for both PMMA and PS that, as the punch radius increases, the FS decreases.

However there are not enough punches used for this trend to be confirmed. In figure 5.4 there appears to be an overall drop in FS for film thicknesses about 100 nms. Below 100 nms the FS appears to be a little higher. In figure 5.5, for PMMA, the 650 nm punch and 800 nm punch appear to have a very similar range of values for FS. Overall, it is difficult to find any conclusive trends from these graphs, especially as the same 650 nm punch in PS and PMMA appears to behave differently.

To summarize these geometric trends, another way to plot this data, is to plot the forming stress plotted against a/h for various aspect ratios of punches and films (figure 5.6 and 5.7). This allows us to see if the aspect ratio has an influence on forming stress. For PMMA a 900 nm DFP, 800 nm DFP, 650 nm DFP and 400 nm DFP are used into various films. The data is fit linearly and extrapolated until it crosses the y axis using a very simple linear model where α is FS extrapolated back to a case of zero aspect ratio, m is simple the slope of the line and (a/h) is the aspect ratio.

$$FS = \alpha + m \left(\frac{a}{h} \right) \quad (\text{Equation 5.1})$$

What quickly becomes apparent is that this very simple model does fit the data for 4 separate punches with a value for α of 635 MPa \pm 50 MPa falling out of the data. Similar values for m of 0.026 for the 650 nm DFP, 0.018 for 800 nm DFP and 0.028 for 900 nm DFP

are found. However, for the 400 nm DFP a value approximately 10 times greater of 0.22 is found.

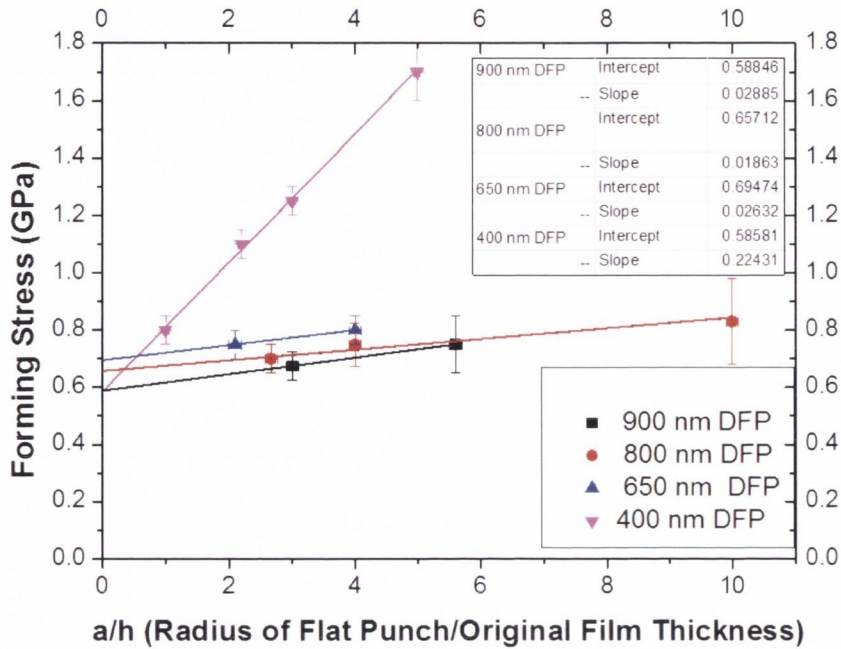


Figure 5.6: Forming stresses for 400 nm DFP, 650 nm DFP and 800 nm DFP against aspect ratio for various film thicknesses of PMMA.

To understand the anomalous result of the 400 nm punch we consider this punch itself in more detail. The fabrication of this 400 nm punch (Figure 5.1 e) was described in section 4.2.2. As this punch was fabricated using a gallium mask and an etch process on a conductive diamond tip the chemistry of this punch, and so its surface interaction with the polymers, may be very different from the other punches. Results similar to this have been seen in one paper, where Tweedie et. al.[2] used a spherical nanoindenter to carry out load limited indents corresponding to depths between 5 nm and 100 nm into 1 micron samples of PS, PMMA and PC. Their results showed an unexpected, but consistent, increase in the elastic modulus of up to 200% at depths < 50 nm into the polymers. The main cause of the increased E in the case of Tweedie et al[2] was considered to be an attraction toward and repulsion from the probe material which could restrict molecular mobility in the confined region of mechanical contact adjacent to the probe. As, chemically, the gallium doped conductive diamond flat punch is very different from the FIB manufactured diamond flat tips a difference in how they interact with the polymers is very likely. This may be one

piece of very important evidence for how the effect of the flat punch surface affects these measurements.

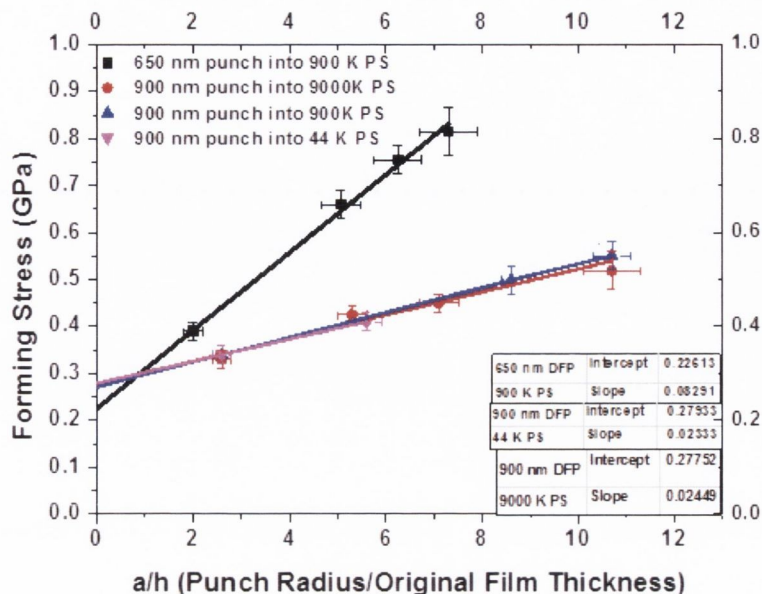


Figure 5.7: Forming Stress against a/h in PS for 900 nm DFP and 650 nm DFP.

For PS, using a 650 nm DFP and 900 nm DFP into three different M_w films, the four lines intersect the y axis at $210 \text{ MPa} \pm 20 \text{ MPa}$ (Figure 5.7). The m values for the punches are, for 650 nm DFP $m = 0.08$ and for the 900 nm DFP $m = 0.02$. The same 650 nm DFP and 900 nm DFP were used to indent into PS and PMMA. There is a large difference in how the 650 nm DFP acts while indenting into the PS compared with indenting into PMMA. This appears to be an anomaly and indicates a fundamental change in either the chemical or physical make-up of the punch. These experiments were carried out first into PMMA and then PS, and it is likely that this erroneous result is due to structural a change in the punch cause by either damage to the 650 nm tip or the tip picking up material.

Additionally the 900 nm DFP was indented into similar film thicknesses of 3 different M_w PS films (Figure 5.7). When the data is plotted with FS against a/h the three lines fall on each other within error showing an independence of M_w .

However before any more findings are concluded from this very simple model the fact that polymers are a hydrostatic pressure dependent material must be considered.

5.3.2 Analysis and Discussion: Effect of Hydrostatic Pressure on Deformation in Polymers

The problem of a flat punch indenting a supported layer has been examined in rigid-plastic slip field analysis[7], soil foundation mechanics[8], polymer film debonding[9] and numerous other elastic [10-15] and inelastic[16-19] material treatments. The geometry is different from constant area squeeze flow of rheometry[20-22], coupon upsetting tests of solid mechanics[23, 24] and finite volume tests of adhesive elastomer tack[25] (which may be referred to as “poker chip” geometries) by the surrounding film constraint and pileup of extruded material at the punch edges. The small ϵ behaviour of this system is well studied in the context of the adhesive tack test on soft elastic and other thin coatings[25-27]. To use these results, mirror symmetry for small strain compressive and tensile behaviour is assumed. At high Poisson ratio (ν) and no slip for incompressible materials including Newtonian fluids and high ν rubbers, the lubrication approximation holds and the stress distribution is found[15] to be parabolic in the radial direction r and constant in the film thickness direction z . However this varies with ν and this is discussed here.

Slight compressibility ($\nu < 0.49$) dramatically flattens the radial distribution, leaving the only stress variation concentrated near the punch edge[26, 27]. The combined effect of finite ν , compressibility, and slip at the die interface on the contact mechanics has been studied in detail by Lin *et al* [27] that as $\frac{a}{h} \rightarrow \infty$ in regions under the punch away from the edge where the stress is uniform, directly comparing the relative contribution of hydrostatic to the von Mises’s deviatoric stress.

$$\frac{P}{\sigma_{vm}} = \frac{\sqrt{2}(\nu+1)}{3\sqrt{27\nu^2+4(1-2\nu)}} \quad (\text{Equation 5.2})$$

That is, the nature of the state of deformation is governed only by the Poisson ratio ν (Figure 5.2).

From figure 5.8 it is possible to extract a ratio of hydrostatic stress over normal stress, which for a ν of 0.3, the approximate ν for PMMA and PS, is 0.8. Therefore in the elastic regime, for a total stress of 635 MPa \pm 50 MPa for PMMA, 508 MPa \pm 40 MPa is hydrostatic pressure. For a stress of 210 MPa \pm 20 MPa in PS 168 MPa \pm 16MPa is hydrostatic pressure. These values for stress correspond to the extrapolated values for FS at 0 aspect ratio in

figures 5.6 and 5.7. From chapter 2, it is expected that hydrostatic pressure will have the effect of increasing the yielding stress in polymers which was quantified by Quinson et al [28] to be 0.23 MPa/ MPa for PMMA and 0.19 MPa/MPa for PS. This correlates to a contribution towards forming stress from hydrostatic pressure of ≈ 117 MPa for PMMA and ≈ 32 MPa for PS.[29]

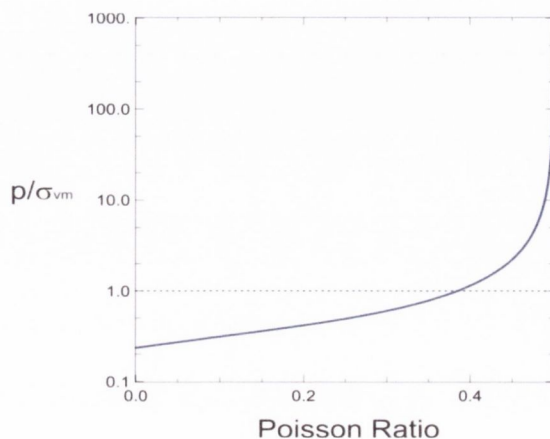


Figure 5.8: Hydrostatic pressure divided by von Mises stress vs. Poisson ratio in thin film flat punch contact.

Therefore, for PMMA a FS of $520 \text{ MPa} \pm 40 \text{ MPa}$ is calculated and for PS $178 \text{ MPa} \pm 16 \text{ MPa}$. This is very high when compared with literature values for yield stress of PMMA which, at room temperature has been measured using compressive techniques and high strain rates to vary from 200 MPa [30, 31] up to 400 MPa [31]. For PS, values between 30 MPa [32] and up to ~ 100 MPa in thin films [33] has been measured for yield. Generally scatter is always seen in these results, and this may be due to different sample preparation, ageing states [34] or the sample's dimensions. However, the values calculated here for FS in PMMA and PS are for TFFPN, and are thus influenced by the confining presence of the surrounding material. As discussed in chapter 2 using the analysis of Johnson and Kudo [35], this geometric confinement results in a multiplying factor of 2.5 for the pressure required to cause plastic flow compared with cylindrical billet compression with no confinement. This confinement factor has been calculated for plane strain deformation of rigid plastic material, however the results predicted by this form of analysis have been shown to predict closely, for example, the Tabor indentation confinement factor of 3 found empirically for metals. While we cannot make a precise prediction of the corresponding factor for our TFFPN of polymer systems, as we noted in Chapter 2 the Tabor parameter for polymers

ranges from 1.5 to 2. Thus, applying a similar scaling to the 2.5 factor, this gives us a polymer scaling factor of 1.25 to 1.7. Applying this to our results, we find an equivalent yielding value under billet compression for PMMA ranging from 300 MPa to 420 MPa and for PS of 100 MPa to 140 MPa. These values are excellent agreement for PS while remaining slightly high for literature values reported for lubricated compression yield in PMMA.

Additionally, this may also explain the linear aspect ratio scaling effect in figures 5.6 and 5.7. As the aspect ratio increases, this causes the stress field to change and the relative component of hydrostatic pressure to increase. This causes the stress required for yield to increase and so may explain the linear non-zero slopes seen in figure 5.6 and 5.7. For example in PMMA, one would expect, for a forming stress of 800 MPa for the 900 nm punch, that 147 MPa of that pressure required to cause yield is as a result of hydrostatic pressure. Similarly, for PS it will cause a rise of 90 MPa for the 900 nm DFP at the higher aspect ratios. Therefore the reason for the non-zero values of m can be explained, within error on figure 5.6 (PMMA). It may be a result of an aspect ratio (geometrical) effect which drives up hydrostatic pressure causing a higher yielding value due to the hydrostatic pressure dependence of PMMA. For PS it does not explain the entire reason for the higher forming stresses at high aspect ratio; hence this does require further investigation.

5.3.3 Analysis and Discussion: Effect of Contact Geometry, Aspect Ratio and Pressure on Modulus

The effect of aspect ratio, pressure and contact geometry on elastic modulus E is not straight forward, and indeed appears to be interdependent. As the effect of aspect ratio on TFFPN is to drive up the FS it follows that this nominally leads to an increase in the E measured. This is seen by Spitzig and Richmond [36] who carried out a thorough analysis of the effect of hydrostatic pressure on the yielding in PC and PE. They found that as the hydrostatic pressure increased, E also increased. Parry and Tabor also published a review article in 1973 of the effect of hydrostatic pressure on E and yield, where they reviewed many experiments which had shown an increase in elastic modulus and yield in polymers with increasing hydrostatic pressure.[37] The aim of this section is analyse and discuss the calculated E in polymers using flat punch indentation. For this the continuous stiffness

measurement (CSM) data is used as this provides a continuous measurement of displacement and load of an oscillation imposed on the indenter shaft as it makes its absolute movement in and out of contact with the sample.

The conversion of S data to E data is carried out using the theory presented by Yang in 2006.[38] Certain assumptions are made in this analysis including that this work is carried out on a thin compressible elastic film bonded to a rigid substrate where a rigid, cylindrical flat punch is in sliding contact with the thin film and indentation depths are small relative to the film thickness. These assumptions are relatively accurate when considering TFFPN, especially for the initial stages of indentation. In addition all analysis in this section is focused on the first twenty percent of the indent so indentation depths are small when compared to the film thickness.

$$E = \frac{(1+\nu)(1-2\nu)}{(1-\nu)} \frac{S}{Area} h \quad (\text{Equation 5.3})$$

Where E is the elastic modulus and S is the stiffness calculated by the CSM according to

$$S = \frac{dF}{d\delta} \quad (\text{Equation 5.4})$$

where δ the harmonic displacement and F is the harmonic load. Using this model E is calculated for the 800 nm and 650 nm DFP's into 48 K 150 nm, 150 nm, 100 nm and 80 nm PMMA (Figure 5.9). These results show clearly that E increases with hydrostatic pressure, as expected. Also, the value of E for PMMA measured using the CSM is calculated to be approximately $2.75 \text{ GPa} \pm 0.25 \text{ GPa}$ at 0.15 GPa hydrostatic pressure. Here we discount the 80 nm PMMA film from this approximation as it appears that a size effect may be beginning to have some influence on the E of the film. This is discussed in more detail, along with results for 40 nm PMMA films in the next section. This value of $2.75 \text{ GPa} \pm 0.25 \text{ GPa}$ for E for bulk films of PMMA is comparable to the E measured by other techniques including bulk compression testing, spherical testing [25, 58] and Stafford's buckling technique.[39]

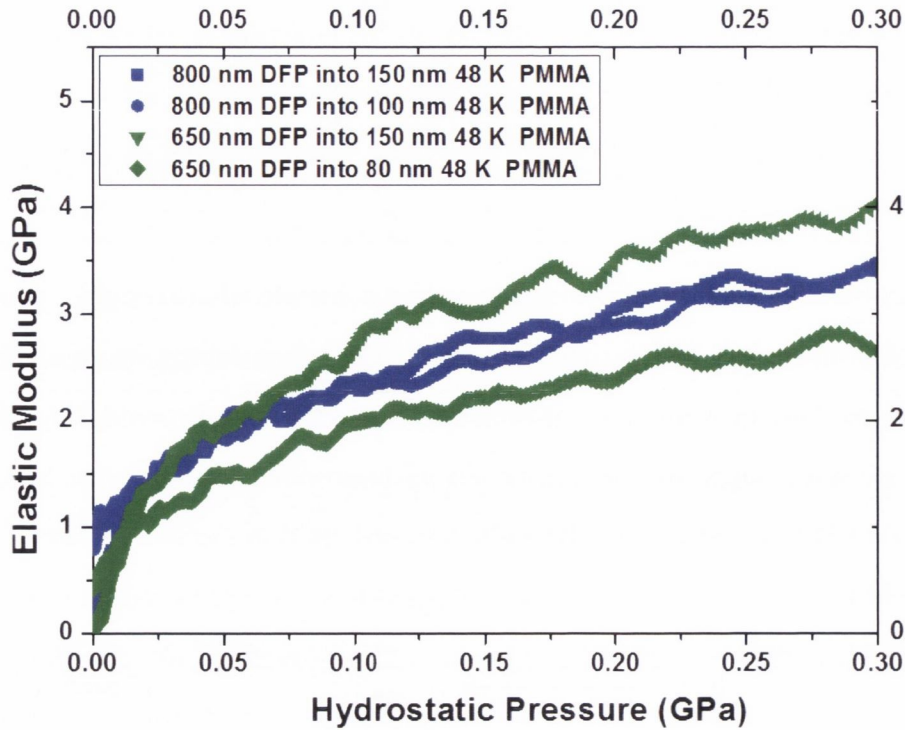


Figure 5.9: Elastic modulus versus hydrostatic pressure of an 800 nm DFP and 650 nm DFP into 150nm, 100 nm and 80 nm film thicknesses of 48 K PMMA. Elastic modulus is seen to increase with hydrostatic pressure.

E is also calculated for the 900 nm and 650 nm DFP's into 100 nm and 150 nm film thicknesses of 9000 K, 900K and 44K PS (Figure 5.10). These results show clearly that E once again increases with hydrostatic pressure. The value of E for PS measured using the CSM is calculated to be approximately $2.5 \text{ GPa} \pm 0.25 \text{ GPa}$ at 0.15 GPa hydrostatic pressure which is once again comparable to measurements by other techniques including bulk compression testing, spherical testing [25, 58] and Stafford's buckling technique.[39] Additionally this results show that E is independent of M_w for film thicknesses greater or equal to 100 nm.

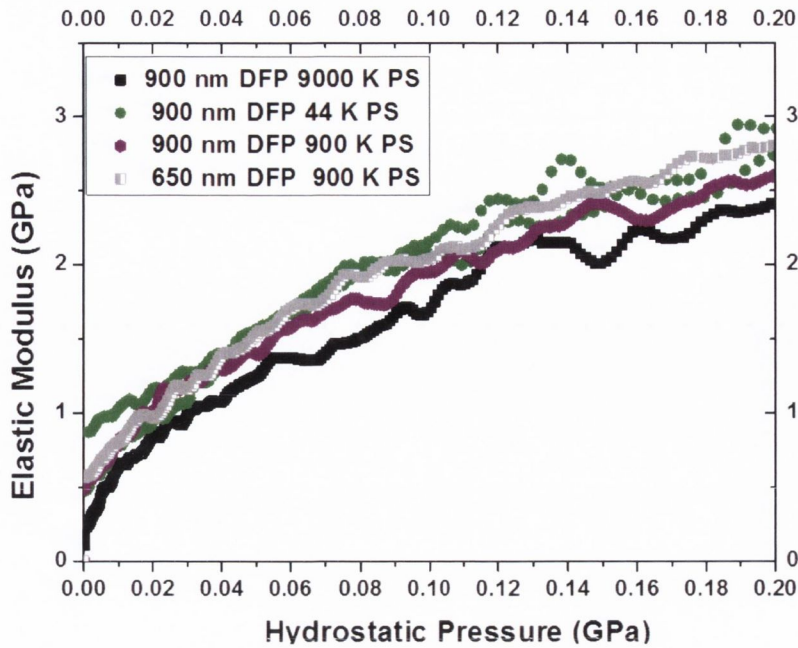


Figure 5.10: Elastic modulus versus hydrostatic pressure of an 800 nm DFP and 650 nm DFP into 150nm and 100 nm film thicknesses of various molecular weights of PS. Elastic modulus is seen to increase with hydrostatic pressure.

Another way to consider E is to plot it against strain (Figure 5.11 and 5.12). When plotted this way a similar trend becomes evident, as E increases, so too does strain for both PS and PMMA. Strain is plotted up to 0.3 as the model used to calculate E is valid only at low strains. At the initial stage of the graph (<0.025 strain) the data is a little unreliable. This is related to a stabilisation period for the CSM as it contacts the sample, and in context of very thin film relates to only a few nms depth into sample. Above this a small jump can be seen in E for PMMA and PS, particularly in the thicker films, before a slow increase in E with strain is seen. It then levels off at approximately 0.15 strain. This increase with strain into the sample may be related to a surface effect in the polymers which result in a graduated E . For the thinner films (<100 nm) the jump is smaller and overall E measured is lower than in the thicker films, with less of an increase seen with strain. This is similar to the reduced modulus measured in thin films reported by Stafford et al.[39, 40]

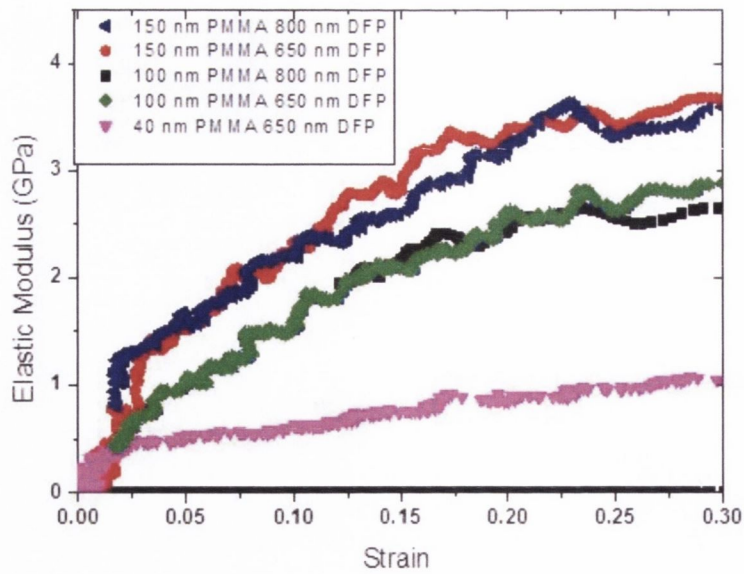


Figure 5.11: Elastic Modulus versus strain for an 800 nm DFP and 650 nm DFP into various film thicknesses of PMMA. Elastic modulus is seen to increase with increasing strain, while an overall decrease is seen as film thickness is reduced.

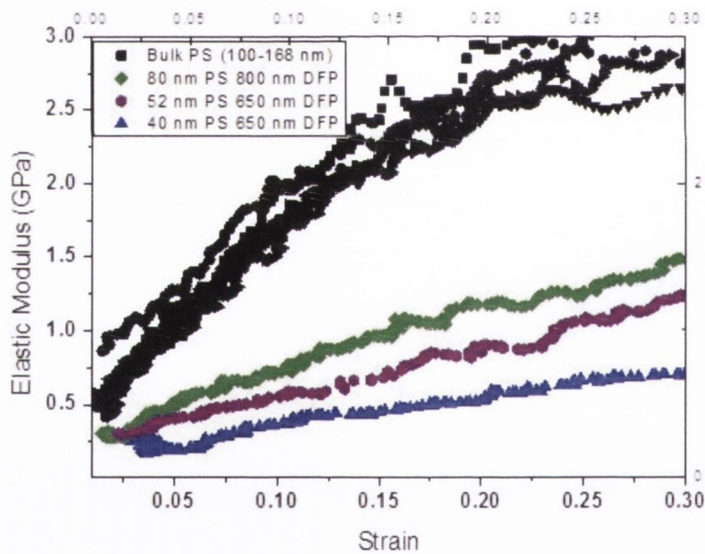


Figure 5.12: Elastic modulus versus strain for an 800 nm DFP and 650 nm DFP into various film thicknesses of PS. Elastic modulus is seen to increase with increasing strain, although for films < 100 nm a large drop is seen in E.

Contact Modulus (CM) is different approach to looking at the elastic response of the samples calculated directly from the lower region of the stress strain curve (Figure 5.13).

CM is physically related to E , but will differ due to the geometry factors, aspect ratio factors and also due to the two different timescales that they are measured over. CM is a quasistatic measurement as opposed to E which is measured at 45 Hz. To put this in perspective, the loading section of the curve for FP nanoindentation takes approximately 20 s. CM is directly measured from this curve. However as E is measured from the CSM which is at 45 HZ, this corresponds to a time length for each oscillation of 0.022 s. As these polymers do have a weak viscoelastic response, even in the glassy state, this will result in a much lower measurement of CM . Nevertheless CM is a useful measurement as it allows one to compare flat punch stress strain curves quickly, with a minimum of analyses, and yet still see any changes in CM which are then reflected in any advanced analysis involving E .

An example of determining CM for two different aspect ratios and thus hydrostatic pressure conditions by calculation directly from the stress strain curve is shown in figure 5.13. One can see here that as aspect ratio increases the strain at the “knee” section of the curve becomes more difficult to clearly define. This corresponds to results from Spitzig and Richmond [36] who found that as hydrostatic pressure was increased a clear yielding point became more difficult to define, but the yielding strain appeared to increase and moved to the right in the stress strain curve. In flat punch nanoindentation as aspect ratio increases, hydrostatic pressure which is related to the load on the sample increases. Therefore as aspect ratio increases one expects there to be an increase in hydrostatic pressure throughout the stress strain curve. This increase in hydrostatic pressure makes clearly defining the end of the lower linear section of the curve more difficult to do.

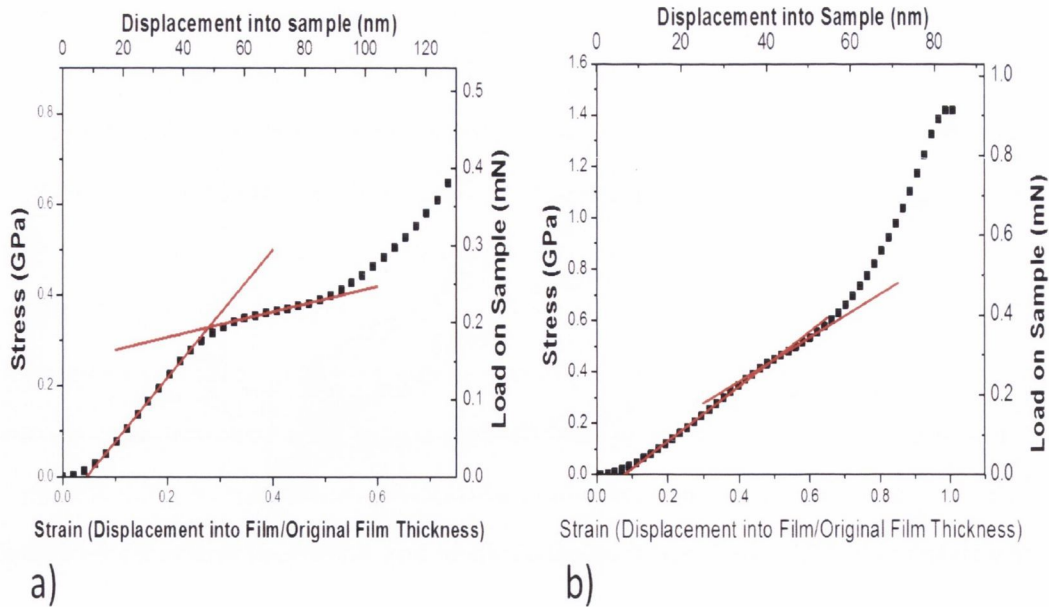
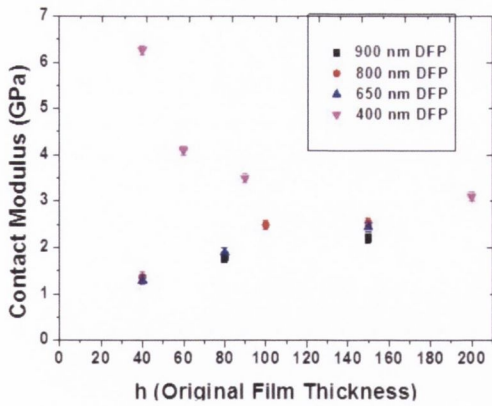
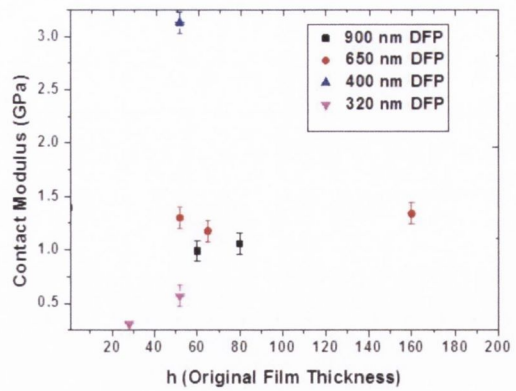


Figure 5.13 : 900 nm DFP into a) 168 nm film of 9000 K PS and b) 84 nm film of 9000 K PS. Note that the intersection of the lines corresponding to forming stress become less obvious as the film thickness is reduced and also right shifts, similar to the results seen in Spitzig and Richmond[36].

Figure 5.14 a and b shows CM plotted against film thickness for various aspect ratios of PMMA using a 900 nm DFP, 800 nm DFP, 650 nm DFP and 400 nm DFP and for PS for 900 nm DFP and 650 nm DFP, 400 nm DFP and 320 nm DFP respectively. In general there appears to be a trend that as film thickness (h) increases CM increases. This corresponds well to a decrease in modulus seen as h is reduced below ~ 80 nm. This trend is broken by two punches. Firstly the 400 nm punch has the opposite trend, CM decreases as h increases. This is the same punch that showed the anomalous results when looking at the effect of aspect ratio on FS and once again this is possible due to an unknown surface interaction. Additionally, there is one point for the 400 nm DFP indented into PS. This point is much higher than other points for CM in PS and the reason for this is seen as also due to an unknown surface interaction. The 650 nm DFP indenting into PS is also seen to go against this trend, while for PMMA it behaves in the same way as the other punches. Therefore it is likely that any surface contaminant that has affected the punch when indenting into PS is causing this unusual response.



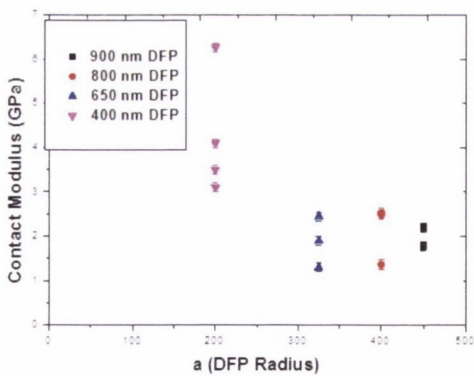
a) PMMA



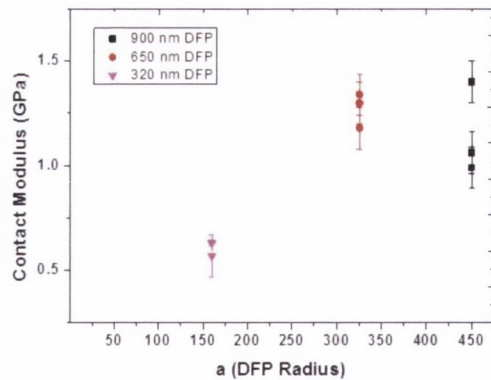
b) PS

Figure 5.14: Contact Modulus plotted against original film thickness for several punches indenting into a) PMMA and b) PS.

Additionally, *CM* was plotted against flat punch radius (Figure 5.15). In PMMA, if one disregards the 400 nm punch, one sees that the values for *CM* are similar for the 900, 800 and 650 nm punches. For PS, a large drop in *CM* is seen for the 320 nm DFP, but this is likely to be related to a size effect as the film thickness is reduced below 60 nm rather than any other factor. There is some more scatter for the 900 nm DFP than for the 650 nm punch in PS, but there is not enough punches used here to make any conclusive findings.



a) PMMA



b) PS

Figure 5.15: Contact Modulus plotted against radius of diamond flat punch for several punches indenting into a) PMMA and b) PS.

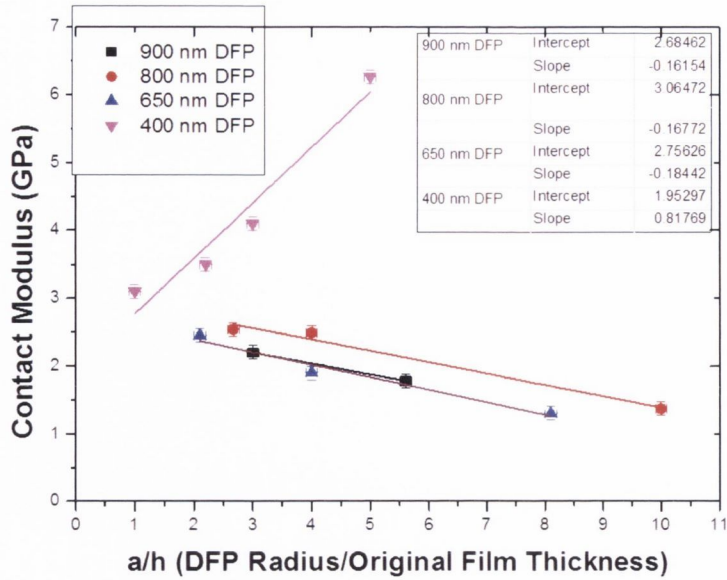


Figure 5.16: 400 nm DFP, 650 nm DFP and 800 nm DFP into various film thicknesses of PMMA.

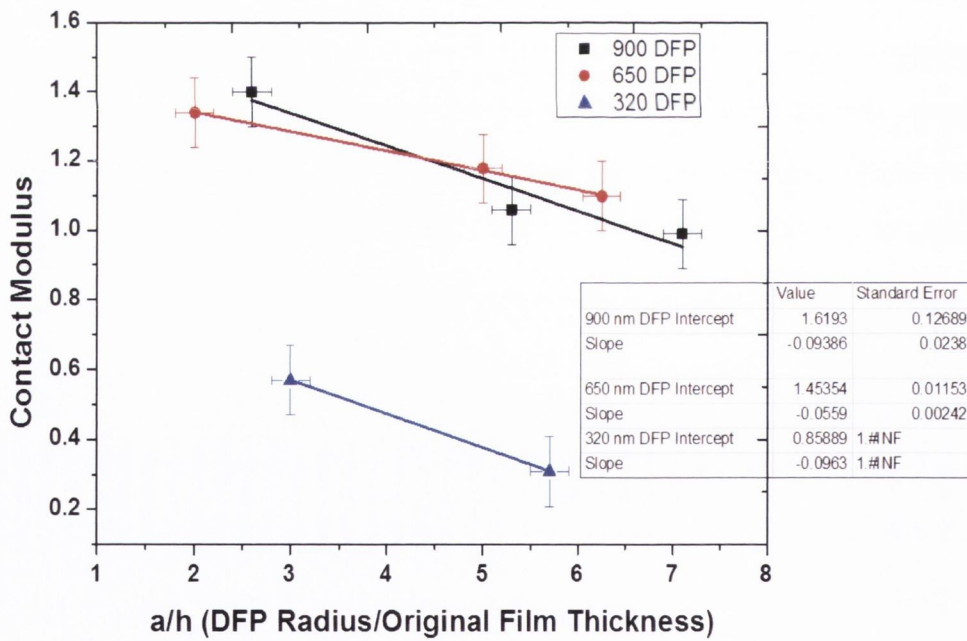


Figure 5.17: Contact modulus against a/h in PS for 900 nm DFP, 650 nm DFP and 320 nm DFP.

Once again, an additional way to consider CM is to plot it against aspect ratio. This allows any dependency on geometry to be clearly seen. From Figure 5.16 and Figure 5.17 we see a downward trend in contact modulus against aspect ratio for all punches except the 400 nm punch which is discussed in the next paragraph. This downward trend with aspect ratio is

the opposite of what is seen in the CSM data. The downward trend can be explained by figure 5.13 where one can see that the yield strain increases with increasing aspect ratio and also that it becomes more difficult to clearly identify the forming stress. This has the effect of causing the slope of the linear section of the curve to decrease with increasing aspect ratio and is responsible for the downward trend in CM with aspect ratio.

In addition, the values of CM are 50 % lower than the values of E calculated using the CSM. CM is physically related to E , but will differ due to the geometry factors and also due to the two different timescales that they are measured over. As has been mentioned earlier CM is a quasistatic measurement as opposed to E which is measured at 45 Hz. The loading section of the curve for FP nanoindentation takes approximately 20 s while E is measured from the CSM which has a time length for each oscillation of 0.022 s. As these polymers do have a weak viscoelastic response, even in the glassy state, this will result in a much lower measurement of CM compared to E . The main reason for the increase in stiffness values for the CSM is that it measures at 3 orders of magnitude faster rate than the quasistatic loading rate, and the polymer glasses are weakly viscoelastic. In general for my work the quasistatic loading rates are similar enough that this is a minor effect when comparing CM across different experiments, but when comparing CM with E , measured from CSM this difference becomes evident.

However, there is the anomalous case of the increase in CM against aspect ratio for the 400 nm DFP as it indents into PMMA. This is clearly contrary to the downward trend seen from all the other flat punches. This anomaly echoes the strange behaviour that was seen in throughout these graphs for the same punch and is likely to have the same root cause. Also, what is very noticeable about the stress strain curves for the 400 nm DFP into PMMA is that as the aspect ratio increases the forming strain remains around 0.24 ± 0.04 (Figure 5.3). Therefore as the FS increases, but the forming strain remains constant with aspect ratio, the CM increases. This is further evidence for the conjecture that attraction toward and repulsion from the gallium doped probe material could result in restricted molecular mobility in the confined region of mechanical contact adjacent to the probe. This may be one piece of very important evidence for how the effect of the flat punch surface affects these measurements.

5.3.4 Results and Analysis: FP Nanoindentation into sub 100 nm Films of PS and PMMA

Figure 5.18 shows 4 curves of approximately 10 to 1 aspect ratio of PS and PMMA indents, where each curve represents at least 12 separate indents averaged and interpolated. These indents correspond to a 6200 nm DFP into 700 nm 44K PS film, 320 nm DFP into 28 nm 44 K PS film, 800 nm DFP into 160 nm of 48 K PMMA and 320 nm DFP into 26 nm 48 K PMMA. Both PS and PMMA homopolymer supported films show dramatic mechanical weakening under indentation at reduced film thickness, of order five-fold for PS and four-fold for PMMA as can be seen in Figure 5.18. For PS, the observed weakening with film thickness is consistent with previous findings [1] which also confirmed M_w independence of the entire stress vs. strain glassy PS response for film thickness greater than the bulk radius of gyration.[5] For PMMA, the results are new. However, a reduced flat punch indentation contact modulus is consistent with a reduced modulus found under thin film buckling experiments of PMMA supported on a rubbery (PDMS) substrate with a free surface.[39]

Figure 5.19 displays FS against aspect ratio for the 400 nm DFP indented into 200 nm, 90 nm, 60 nm, 40 nm and 28 nm films of PMMA. This is similar to the results shown in earlier this chapter but with an additional film thickness of 28 nm included. From earlier results one would expect the reduced aspect ratio to result in an increase in the FS. However what is remarkable here is that for the 28 nm film there is a large drop in the FS. Although one may have expected a drop on the FS for the 40 nm film, and possibly the 60 nm film, this did not occur as the effect of the increasing aspect ratio appears to dominate the FS value. However the 28 nm film has experienced such a reduction in FS due to the size effect, which now begins to dominate the calculated FS value.

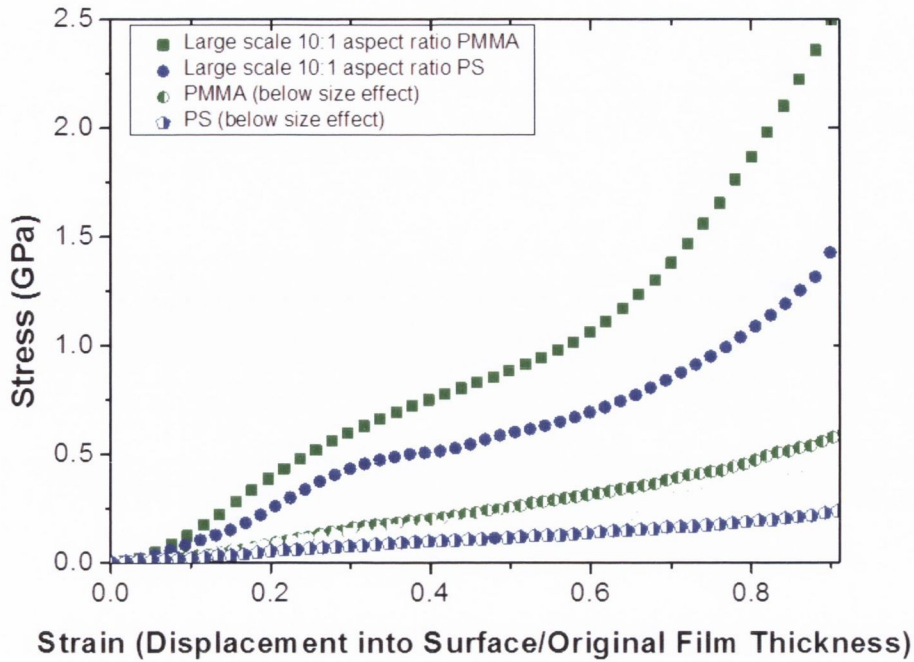


Figure 5.18: Stress versus strain for large scale 10 to 1 aspect ratio indentation of PS and PMMA compared with small scale 10 to 1 aspect ratio indentation of PS and PMMA. Each curve is at least 12 separate indents averaged and interpolated from 0 to 0.9 engineering strain

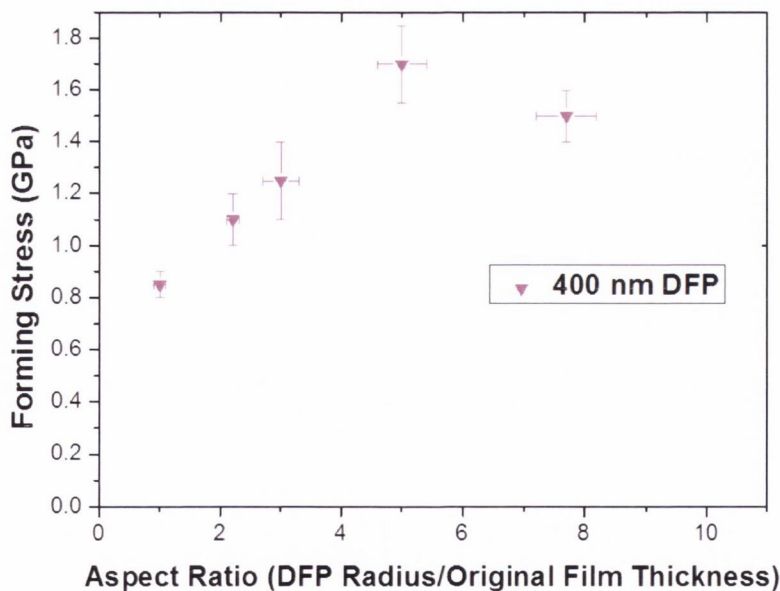


Figure 5.19: FS against aspect ratio for 400 nm plasma etched DFP indented into film thicknesses of PMMA varying from 28 nm to 200 nm. The point here corresponding approximately to aspect ratio 8 is a thin film case, as the film here is 26 nm in thickness.

5.3.5 Results and Analysis: Elastic Modulus for sub-100 nm Films of PS and PMMA

A 900 nm DFP was indented into various film thicknesses from 168 nm to 40 nm (Figure 5.20) of 9000 K, 900 K and 44 K PS. In addition a 650 nm DFP was also indented into the various film thicknesses. E was calculated using the same method adapted from Yang[38] presented earlier, but this time for films down to thicknesses of 40 nm. What quickly becomes apparent from these indents is that as the film thickness is reduced below 100 nm the E modulus reduces from approximately 2.5 ± 0.25 GPa at 0.15 GPa hydrostatic pressure to 0.4 GPa ± 0.1 GPa. Neither M_w , nor aspect ratio, appears to affect this trend. This is consistent with the findings of the Stafford et al.'s buckling technique [39-41]. Figure 5.21 shows E against hydrostatic pressure for 800 nm and 650 nm DFP indented 48 k PMMA films varying in thickness from 150 nm to 40 nm. Once again as the film thickness decreased below 100 nm there was a drop in E , in this case from approximately 2.8 ± 0.25 GPa at 0.15 GPa hydrostatic pressures to 0.8 GPa ± 0.1 GPa.

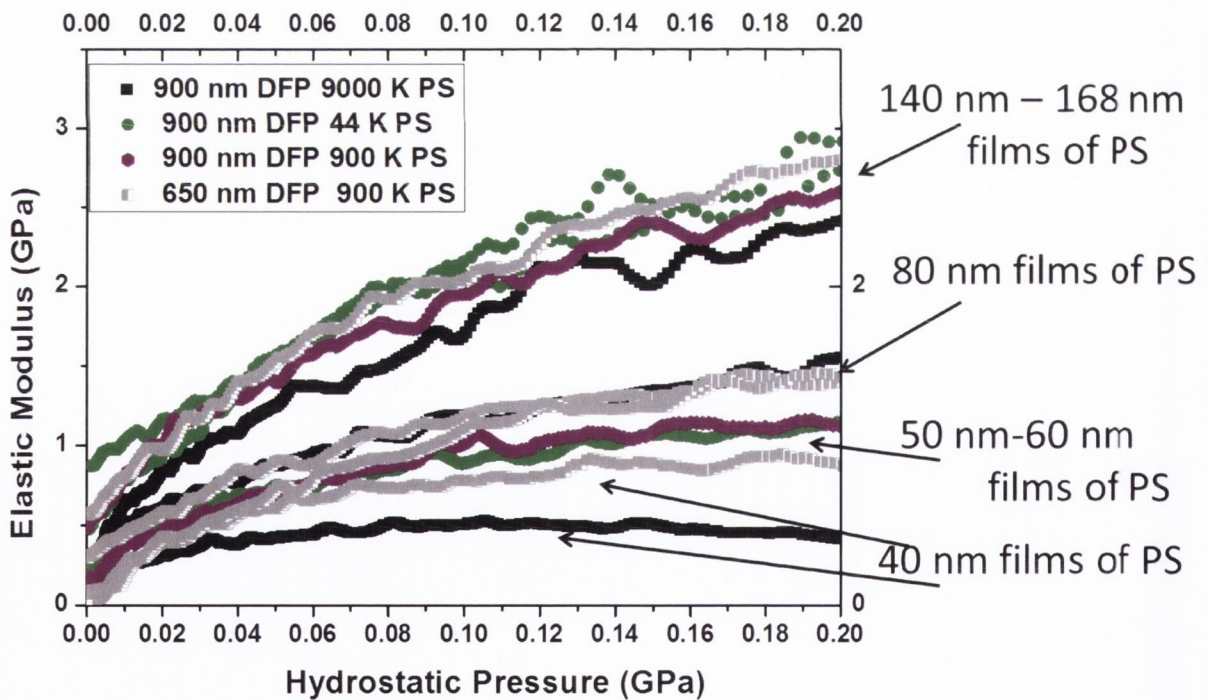


Figure 5.20: Elastic modulus versus hydrostatic pressure for 900 nm DFP and 650 nm DFP into film thicknesses of PS 9000 K, 900 K and 44 K varying from 168 nm to 40 nm. As film thickness is reduced E decreases from ~ 2.5 GPa to ~ 0.4 GPa at 0.15 GPa hydrostatic pressure, regardless of M_w .

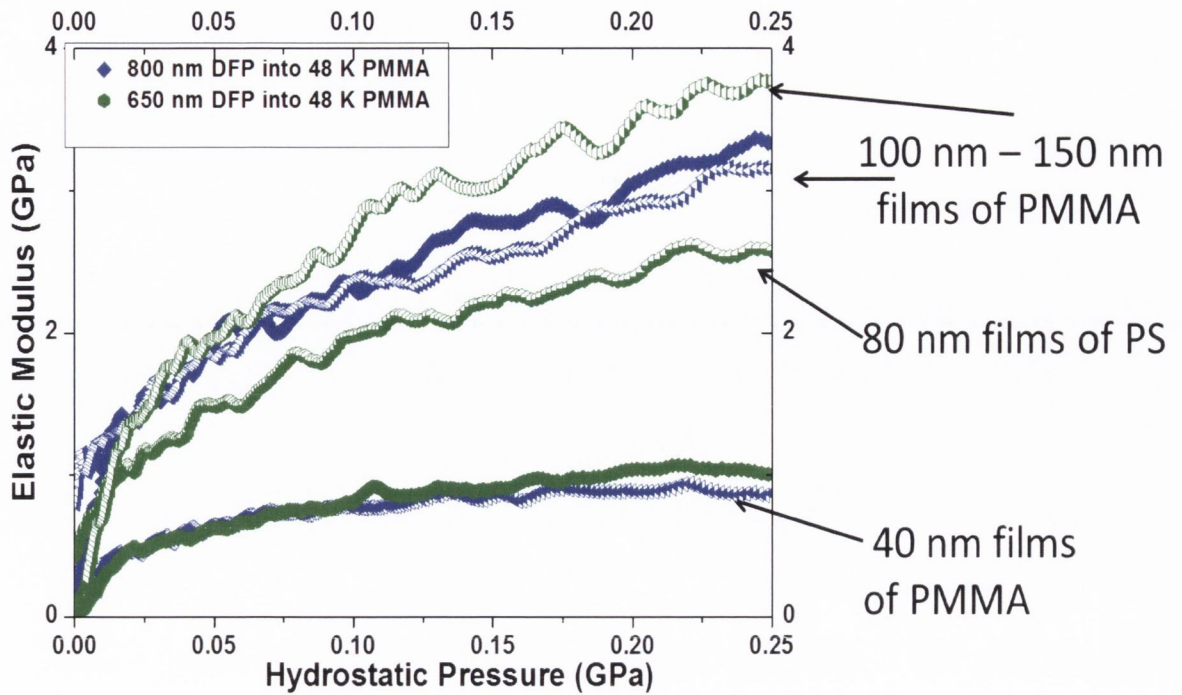


Figure 5.21: Elastic modulus versus hydrostatic pressure for 800 nm DFP and 650 nm DFP into film thicknesses of 48 K PMMA varying from 150 nm to 40 nm. As film thickness is reduced E decreases from ~ 2.8 GPa to ~ 0.8 GPa at 0.15 GPa hydrostatic pressure.

5.3.6 Results and Analysis: Stress Normalised by FS for Films Above and Below Size Effect

Figure 5.22 shows the PS homopolymer stress vs. strain curves normalized by their own forming stress value for 10 to 1 aspect ratio of FP diameter to film thickness. A strong congruence appears under this transformation for each curve, particularly for the low strain section, regardless of the film thickness used. This is not expected. As the film thickness dropped below 50 nm the FS, and the entire stress versus strain curve, dropped severely (Figure 5.18). However, the shape of the curves of Stress/FS appear to be very similar implying one only needs to have knowledge of the forming stress for each film thickness, and from this, in particular, low strain data can be estimated as long as similar aspect ratios are maintained.

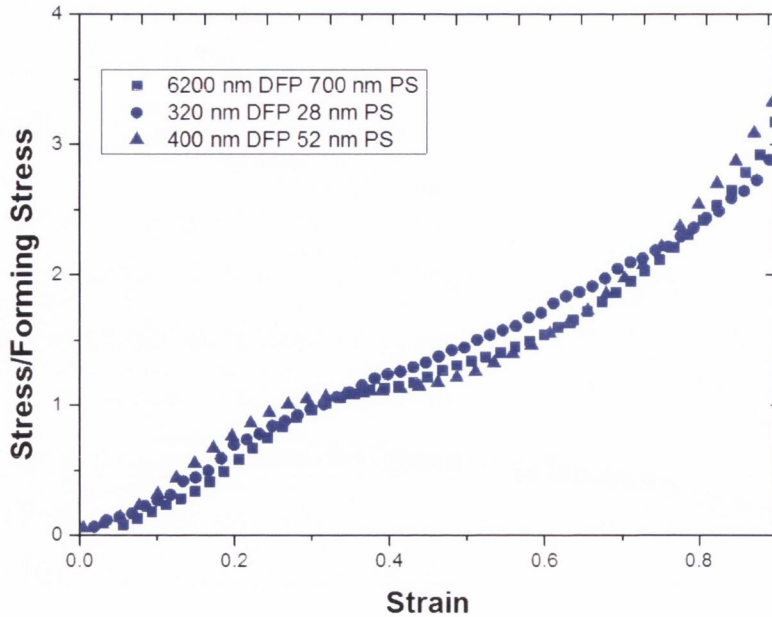


Figure 5.22: PS homopolymer stress vs. strain curves normalized by their own forming stress value for 10 to 1 aspect ratio.

Figure 5.23 shows the PMMA homopolymer stress vs. strain curves normalized by their own forming stress value. Once again a remarkable congruence appears under this transformation for each curve along with the same implications as for PS.

Figure 5.24 compares both the PS and PMMA homopolymer stress vs. strain curves normalized by their own forming stress value. This time a strong congruence appears under this transformation for each polymer species, while an increased stress at high strain is apparent for PMMA vs. PS, consistent with expected increased strain hardening in PMMA.[42]

This is quite a remarkable result. In these experiments FP indentation has been carried out into large and small scale polymer films. In doing this a fivefold decrease in FS of PMMA was seen and a fourfold decrease in FS of PS (Figure 5.16). Upon normalising the stress using the FS the 10 to 1 aspect ratio curves all fall on each other from low to high strains. In PMMA the effect is noticeable to the extent that a strain hardening effect, which one expects in PMMA, is clearly visible. This implies that regardless of the scale of the experiment, if a FS is calculated for any of these thin films then CM and high strain results can be extracted.

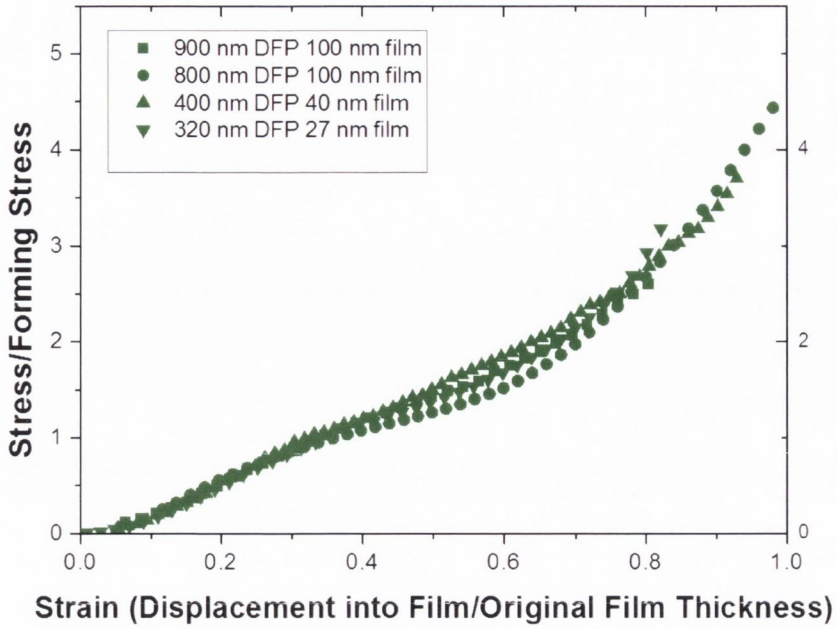


Figure 5.23: PMMA homopolymer stress vs. strain curves normalized by their own forming stress value for 10 to 1 aspect ratio.

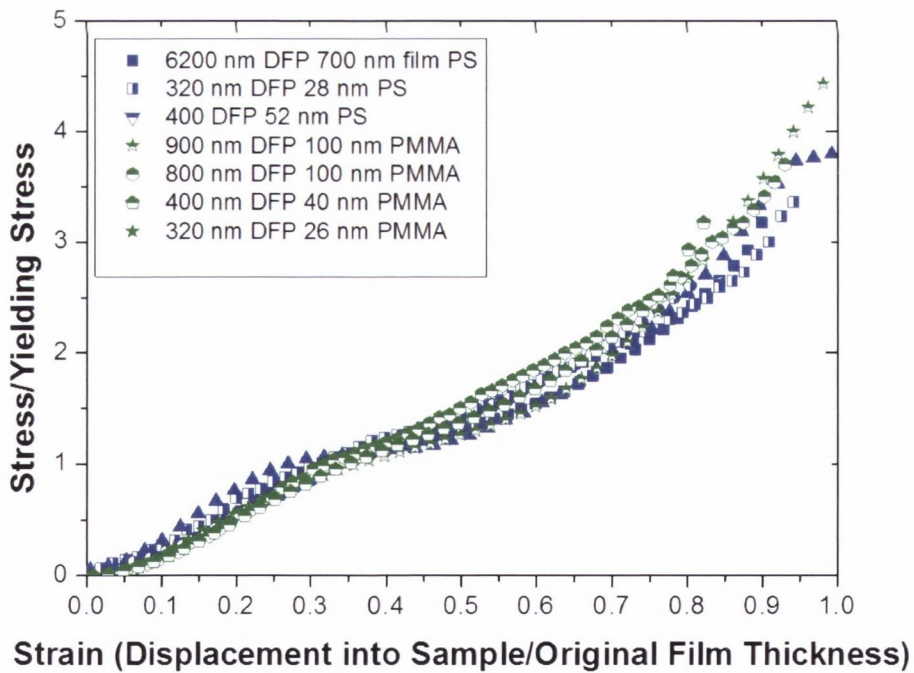


Figure 5.24: PS and PMMA homopolymer stress vs. strain curves normalized by their own forming stress value for 10 to 1 aspect ratio.

5.4 Conclusion

The pressure required for yielding a polymer thin film using FP nanoindentation was found to be lightly dependent on aspect ratio. The effect of hydrostatic pressure on FS was also discussed using results from Quinson *et al*[32] and Spitzig and Richmond[36]. Their results, in conjunction with Lin *et al.*'s theory for the amount of hydrostatic pressure that occurs under a flat punch at various Poisson's ratio, was used to estimate the contribution of hydrostatic pressure towards forming stress. For PMMA it was found to be ≈ 117 MPa which reduces the value of the forming stress found via flat punch nanoindentation to $518 \text{ MPa} \pm 55 \text{ MPa}$. For PS it was found to correlate to a reduced FS from flat punch nanoindentation of $178 \text{ MPa} \pm 20 \text{ MPa}$. Additionally, when a confining geometry correction was made for TFFPN, using the analysis of Johnson and Kudo [35] yielding values for PMMA of $350 \text{ MPa} \pm 50 \text{ MPa}$ and for PS of $120 \text{ MPa} \pm 20 \text{ MPa}$ were calculated. These values are in excellent agreement with literature values for lubricated compression yield in PS, while remain about twice that expected for PMMA. .

It may be a result of an aspect ratio (geometrical) effect which drives up hydrostatic pressure causing a higher yielding value due to the hydrostatic pressure dependence of these polymers. In PMMA and PS, as they are both hydrostatic pressure dependent materials, and changing aspect ratio does result in a change in hydrostatic pressure, one would thus expect to see a change in the pressure required to cause deformation. This results in $m > 0$ for both PS and PMMA. For PMMA, this agrees within error for the 900 nm DFP at high aspect ratio, where every MPa of hydrostatic pressure results in a required 0.23 MPa of additional pressure to cause deformation. However for PS it does not explain the entire reason for the higher forming stresses at high aspect ratio so this must be investigated further.

E was also calculated using the CSM in conjunction with Yang's model [13] and a CM directly measuring from the stress strain curve. This calculation of E was found to be superior to the direct method of measuring CM . CM should be extrapolated from 0 and this is where direct measurements of the slope of the linear section of the curve is not precise enough. Additionally from the CSM results it is clear that E increases with hydrostatic pressure for both PS and PMMA. The value of E for bulk films of PMMA was calculated to

be approximately $2.75 \text{ GPa} \pm 0.25 \text{ GPa}$ at 0.15 GPa hydrostatic pressure. The value of E for PS is calculated to be approximately $2.5 \text{ GPa} \pm 0.25 \text{ GPa}$ at 0.15 GPa hydrostatic pressure. These values are comparable to the E measured by other techniques including bulk compression testing, spherical testing [25, 58] and Stafford's buckling technique.[39]

The 400 nm DFP indenting does appear to have attributes very different from all other punches. As the aspect ratio increases the forming strain remains around 0.24 ± 0.04 . Therefore as the FS increases, the forming strain remains constant with aspect ratio and the calculated CM increases. The root cause of this may be attributed to the existence of a different surface interaction between the 400 nm DFP and all the flat punches due to differences in the initial punch (conductive diamond versus diamond) and the plasma etch process versus the FIB process that was used to fabricate the punch.

Size effects in PS and PMMA have also been investigated. This was carried out by using various DFPs to indent into film thicknesses varying from 700 nm to 26 nm . For the overall curve of stress versus strain for these materials maintaining a 10 to 1 aspect ratio, a large decrease in FS was clear. While this has been seen before in PS it has never been presented in PMMA. Additionally, using the 400 nm plasma etched DFP a large drop off in FS was seen for the 28 nm film of PMMA when compared with a $200, 90, 60$ and 40 nm films. This was regardless of the aspect ratio variation which apparently dominated FS down to the 40 nm film before the size effect came to dominate in the 28 nm film.

Elastic Modulus versus hydrostatic data was also presented for $900, 800$ and 650 DFP into films thicknesses from 168 nm to 40 nm . Below 100 nm film thickness there was a clear decrease in E with an 8 fold decrease for the PS and a 3.5 decrease for the PMMA. This was independent of M_w in PS, and independent of aspect ratio in PS and PMMA.

Finally stresses vs. strain curves normalized by their own forming stress value for 10 to 1 aspect ratio of FP diameter to film thickness were presented for PS and PMMA. An unexpected strong congruence appears under this transformation for each curve, even as the film dropped below 50 nm thickness. This is quite an unexpected, yet remarkable, result. FP indentation has been carried out into large and small scale polymer films. In doing this a fivefold decrease in FS of PMMA was seen and a fourfold decrease in FS of PS was seen. Upon normalising the stress using the FS the 10 to 1 aspect ratio curves all fall on

each other from low to high strains. In PMMA the effect is noticeable to the extent that a strain hardening effect, which one expects in PMMA, is visible. This congruency for Stress/FS versus strain appears to be strongly implying that one needs only to have knowledge of the FS each film thickness and one stress strain curve, and from this a CM and high strain results can be extracted. Therefore this highly non trivial section of mechanics of materials, which is to understand the relationship of the mechanics to the nanoscale structure, has been investigated here.

5.6 References

- [1] H. D. Rowland, W. P. King, J. B. Pethica, and G. L. W. Cross, "Molecular Confinement Accelerates Deformation of Entangled Polymers During Squeeze Flow," *Science*, vol. 322, pp. 720-724, October 31, 2008 2008.
- [2] C. A. Tweedie, G. Constantinides, K. E. Lehman, D. J. Brill, G. S. Blackman, and K. J. Van Vliet, "Enhanced stiffness of amorphous polymer surfaces under confinement of localized contact loads," *Adv. Mater.*, vol. 19, p. 2540, 2007.
- [3] H. G. H. van Melick, O. F. J. T. Bressers, J. M. J. den Toonder, L. E. Govaert, and H. E. H. Meijer, "A micro-indentation method for probing the craze-initiation stress in glassy polymers," *Polymer*, vol. 44, pp. 2481-2491, 2003.
- [4] G. L. W. Cross, B. S. O'connell, J. B. Pethica, H. Rowland, and W. P. King, "Variable temperature thin film indentation with a flat punch," *Review of Scientific Instruments*, vol. 79, pp. 013904-13, 2008.
- [5] H. D. Rowland, W. P. King, G. L. W. Cross, and J. B. Pethica, "Measuring Glassy and Viscoelastic Polymer Flow in Molecular-Scale Gaps Using a Flat Punch Mechanical Probe," *ACS Nano*, vol. 2, pp. 419-428, 2008.
- [6] Boyce MC and H. RN., *The physics of glassy polymers vol. The post-yield deformation of glassy polymers*. London: Chapman & Hall, 1997.
- [7] W. Johnson and H. Kudo, "The compression of rigid-perfectly-plastic materials between rough parallel dies of unequal width," *International Journal of Mechanical Science*, vol. 1, pp. 336-341, 1960.
- [8] J. Mandel and J. Salencon, "Bearing Capacity of Soil on Rigid Layer (Theoretical Study)," *Geotechnique*, vol. 22, pp. 79-&, 1972.
- [9] Y. Lu and D. M. Shinozaki, "Microindentation induced debonding of polymer thin films from rigid substrates," *Journal of Materials Science*, vol. 37, pp. 1283 – 1293, 2002.
- [10] H. T. Xu and G. M. Pharr, "An improved relation for the effective elastic compliance of a film/substrate system during indentation by a flat cylindrical punch," *Scripta Materialia*, vol. 55, pp. 315-318, Aug 2006.
- [11] R. B. King, "Elastic analysis of some punch problems for a layered medium," *International Journal of Solids and Structures*, vol. 23, pp. 1657-1664, 1987.
- [12] F. Q. Yang, "Thickness effect on the indentation of an elastic layer," *Materials Science and Engineering a-Structural Materials Properties Microstructure and Processing*, vol. 358, pp. 226-232, Oct 2003.
- [13] F. Q. Yang, "Asymptotic solution to axisymmetric indentation of a compressible elastic thin film," *Thin Solid Films*, vol. 515, pp. 2274-2283, Dec 2006.

- [14] F. Q. Yang, "Axisymmetric indentation of an incompressible elastic thin film," *Journal of Physics D-Applied Physics*, vol. 36, pp. 50-55, Jan 2003.
- [15] A. N. Gent, "Compression of Rubber Blocks," *Rubber Chemistry and Technology*, vol. 67, pp. 549-558, Jul-Aug 1994.
- [16] S. N. G. Chu and J. C. M. Li, "Impression Creep - New Creep Test," *Journal of Materials Science*, vol. 12, pp. 2200-2208, 1977.
- [17] F. Q. Yang, X. Y. He, M. Dembo, and J. C. M. Li, "Impression creep of a viscous fluid," *Journal of Applied Physics*, vol. 81, pp. 7751-7756, Jun 1997.
- [18] F. Q. Yang and J. C. M. Li, "Impression Creep of a Thin-Film by Vacancy Diffusion .1. Straight Punch," *Journal of Applied Physics*, vol. 74, pp. 4382-4389, Oct 1993.
- [19] F. Q. Yang and J. C. M. Li, "Impression Creep of a Thin-Film by Vacancy Diffusion .2. Cylindrical Punch," *Journal of Applied Physics*, vol. 74, pp. 4390-4397, Oct 1993.
- [20] J. Engmann, C. Servais, and A. S. Burbidge, "Squeeze flow theory and applications to rheometry: A review," *Journal of Non-Newtonian Fluid Mechanics*, vol. 132, pp. 1-27, 2005.
- [21] C. W. Macosko, *Rheology Principles, Measurements, and Applications*. New York: Wiley-VCH, 1994.
- [22] H. M. Laun, M. Rady, and O. Hassager, "Analytical solutions for squeeze flow with partial wall slip," *Journal of Non-Newtonian Fluid Mechanics*, vol. 81, pp. 1-15, 1999.
- [23] G. E. Dieter, *Mechanical Metallurgy*, 3 ed. London: McGraw-Hill, 1988.
- [24] J. J. Wu and C. P. Buckley, "Plastic deformation of glassy polystyrene: A unified model of yield and the role of chain length," *Journal of Polymer Science Part B-Polymer Physics*, vol. 42, pp. 2027-2040, Jun 2004.
- [25] K. R. Shull and C. Creton, "Deformation behavior of thin, compliant layers under tensile loading conditions," *Journal of Polymer Science Part B-Polymer Physics*, vol. 42, pp. 4023-4043, Nov 2004.
- [26] C. Creton and H. Lakrout, "Micromechanics of flat-probe adhesion tests of soft viscoelastic polymer films," *Journal of Polymer Science Part B-Polymer Physics*, vol. 38, pp. 965-979, Apr 2000.
- [27] Y. Y. Lin, C. Y. Hui, and H. D. Conway, "A detailed elastic analysis of the flat punch (Tack) test for pressure-sensitive adhesives," *Journal of Polymer Science Part B-Polymer Physics*, vol. 38, pp. 2769-2784, Nov 2000.
- [28] R. Quinson, J. Perez, Y. Germain, and J. M. Murraciale, "Alpha and beta relaxations in poly(methyl methacrylate) and polycarbonate: non-linear anelasticity studies by antistress relaxation," *Polymer*, vol. 36, pp. 743-752, 1995.
- [29] G. M. Swallowe and S. F. Lee, "Quasi-static and dynamic compressive behaviour of poly(methyl methacrylate) and polystyrene at temperatures from 293 K to 363 K," *Journal of Materials Science*, vol. 41, pp. 6280-6289, 2006.
- [30] J. Richeton, S. Ahzi, K. S. Vecchio, F. C. Jiang, and R. R. Adharapurapu, "Influence of temperature and strain rate on the mechanical behavior of three amorphous polymers: Characterization and modeling of the compressive yield stress," *International Journal of Solids and Structures*, vol. 43, pp. 2318-2335, 2006.
- [31] M. Nasraoui, P. Forquin, L. Siad, A. Rusinek, and E. Dossou, "Mechanical behaviour of PMMA: Influence of temperature and confining pressure," vol. 2, pp. 1103-1108, 2009.
- [32] R. Quinson, J. Perez, M. Rink, and A. Pavan, "Yield criteria for amorphous glassy polymers," *Journal of Materials Science*, vol. 32, pp. 1371-1379, 1997.
- [33] B. Du, O. K. C. Tsui, Q. Zhang, and T. He, "Study of Elastic Modulus and Yield Strength of Polymer Thin Films Using Atomic Force Microscopy," *Langmuir*, vol. 17, pp. 3286-3291, 2013/02/20 2001.
- [34] E. J. Kramer, "Open questions in the physics of deformation of polymer glasses," *Journal of Polymer Science Part B: Polymer Physics*, vol. 43, pp. 3369-3371, 2005.

- [35] W. Johnson and H. Kudo, "The compression of rigid-perfectly-plastic material between rough parallel dies of unequal width," *International Journal of Mechanical Sciences*, vol. 1, pp. 336-341, 1960.
- [36] W. A. Spitzig and O. Richmond, "Effect of hydrostatic pressure on the deformation behavior of polyethylene and polycarbonate in tension and in compression," *Polymer Engineering & Science*, vol. 19, pp. 1129-1139, 1979.
- [37] E. Jones Parry and D. Tabor, "Effect of hydrostatic pressure on the mechanical properties of polymers: a brief review of published data," *Journal of Materials Science*, vol. 8, pp. 1510-1516, 1973.
- [38] F. Yang, "Asymptotic solution to axisymmetric indentation of a compressible elastic thin film," *Thin Solid Films*, vol. 515, pp. 2274-2283, 2006.
- [39] C. M. Stafford, C. Harrison, K. L. Beers, A. Karim, E. J. Amis, M. R. VanLandingham, H.-C. Kim, W. Volksen, R. D. Miller, and E. E. Simonyi, "A buckling-based metrology for measuring the elastic moduli of polymeric thin films," *Nat Mater*, vol. 3, pp. 545-550, 2004.
- [40] C. M. Stafford, B. D. Vogt, C. Harrison, D. Julthongpiput, and R. Huang, "Elastic Moduli of Ultrathin Amorphous Polymer Films," *Macromolecules*, vol. 39, pp. 5095-5099, 2011/11/10 2006.
- [41] J. M. Torres, C. M. Stafford, and B. D. Vogt, "Elastic Modulus of Amorphous Polymer Thin Films: Relationship to the Glass Transition Temperature," *ACS Nano*, vol. 3, pp. 2677-2685, 2009.
- [42] van Melick H.G.H. , Govaert L.E. *, and M. H.E.H., "On the origin of strain hardening in glassy polymers," *Polymer*, vol. 44, pp. 2493-2502, 2003.

Chapter 6: The effect of microphase separation on the mechanical stress vs. strain curve of an ultrathin block copolymer film

6.1 Introduction

While ultra-thin polymer films are of both technological and fundamental scientific interest, ordered BCP nanocomposites in thin film form are anticipated to play an important role in nanofabrication of semiconductor, storage and biomedical devices. This means there an interesting material to utilise the technique of TFFPN. Indentation stress vs. strain curves for 30 nm symmetric PS-PMMA diblock copolymer supported films at room temperature are focused on in this chapter. Atomic force and scanning electron microscopy analysis were used to confirm mechanical testing of the weakly segregated and strongly segregated states of the block copolymer system, deforming a region equivalent to about 15 domains (~320 nm) in size was carried out. Results from the TFFPN into BCP's are presented in this chapter.

The use of pre and post phase separated block co polymer films also allow the investigation of additional questions that have arisen in the literature. Firstly, questions have been asked as to whether lack of sufficient annealing is responsible for the size effects measured in thin films of polymers. At small dimensions, both interfaces and confining volumes have been shown to have a significant effect on polymer thermal and mechanical properties[1], with the most familiar example being the change in glass transition temperature T_g at small thickness for thin films[2]. Debate has ensued as to whether measurement of anomalous T_g values may be a result of film preparation history and/or boundary conditions, with some researchers finding under sufficient annealing the apparent film thickness dependency of T_g disappears[3, 4] and others finding the presence of free surfaces modulates T_g reduction[5]. Annealing leading to microphase separation implies diffusive relaxation of the polymer chain blocks by displacement on order of the bulk radius of gyration. This leaves the anomalous thin film mechanical weakening effects observed here and elsewhere in spin-cast supported thin films difficult to attribute to sample preparation history effects such as residual stress, local structural gradients and unreleased solvent.

The second question that investigating BCPs allow to be addressed is the effect of the microphase separation of the polymers into separate domains and whether the addition of lateral interfaces within the block co polymer film has any effect on the mechanical properties of the ultra-thin film. Here it is found that the effect of reducing the film thickness, as seen in chapter 5, appears to be dominant. The introduction of lateral confinement at the 20 nm scale by creating glassy block copolymer segregation walls has a limited influence on the overall mechanics, manifesting only at high strain. For polymer nanostructures formed by block copolymer lithograph, a significant loss in mechanical strength (compared to bulk polymer) occurs by the initial creation of the supported thin film, but no further penalty is incurred by in-film structuring.

6.2 Review of BCP Phase Separation and Mechanical Studies

BCP systems consist of two or more distinct polymer chains covalently bonded together to form a more complex macromolecule. Compared to homopolymer systems, fewer mechanical studies have been carried out on bulk block copolymer systems, often because mechanical testing requires a volume of material that is available only for a few selected microstructures and chemistries. In addition, assumptions as to the nature and uniformity of phase separated structure must be considered carefully due to thermal gradients present during heating or cooling of bulk sample low thermal conductivity materials. In strongly segregated states, it has been shown that the nature (glassy or rubbery) and the type of organization (*eg.* lamellae, cylinders, gyroid, spheres) of the immiscible blocks have a profound effect on the macroscopic mechanical behaviour[6]. In the weakly segregated state, mechanical properties of bulk BCP systems have also been carried out via tensile tests. It was shown that the tensile strength for poly(styrene-*b*-butyl methacrylate) diblock copolymers (PS-*b*-PBMA) in the composition range between 70% and 80% PS exceeds markedly the value of pure PS. It was also observed for a block copolymer with 74% PS that both the tensile strength and the strain at break was higher than that of pure PS[7]. The role of specific phase separated architecture in the mechanical failure of BCP systems has also been investigated in some detail[8-11], but results are generally reported for multi-

block copolymers which tend to show greatest changes in mechanical properties, especially for the elastic modulus.

Films of diblock PS-b-PMMA copolymers are used as adhesive joints between the otherwise immiscible homopolymers with the result that the BCP layer increases the toughness of the joint by a factor of up to 50, going from very weak to sufficiently strong to be close to the cohesive strength of the homopolymers[12]. The adhesion layer between the two homopolymers has been investigated with most tests been carried out with the thin BCP film sandwiched between the two homopolymers [13, 14]. If the constituent polymers are sufficiently immiscible, phase separation on the scale of the copolymer chains can be induced leading to thin films characterised by a single layer of nanoscale domains[15]. While these films can be imaged by AFM [16, 17] or SEM [18], mechanical deformation studies have so far been limited to post-tensile strain inspection of craze or shear deformation in films with 100's nm thickness consisting of multiple domains in all directions. In recent work [19, 20]using a copper grid extension technique [Kramer] [21]have shown the role of top-layer domain island decoration on craze initiation, growth and failure in all-glassy PS-b-P2VP films containing several layers of well aligned horizontal lamellar domains. Additional work on 500 nm thick PS-b-PMMA samples, where the molar fraction of each copolymer were varied, have shown that when the percentage of PMMA increases there is an increase in strain for crazing and fibril breakdown attributed to increased entanglements in PMMA[22].

At a sub-domain scale, AFM has been used to reveal surface topography variations between domains, as well as localised nanomechanical measurements of Young's modulus of individual domains[23] using a JKR analysis[24]. For the surface of thick films of phase separated SEBS block copolymers, the modulus for PS domains was found to be far lower than bulk PS, while the PEB domain modulus remained close to bulk. This would indicate that the PS has become much softer, most likely, due to the microstructure affect that the soft PEB blocks surrounding and supporting the PS blocks underneath may have. Here, it is important to bear in mind that in this method an AFM tip is used to calculate the mechanical properties within individual domains and so all results are from highly localised sections of the thin film.

BCP's are also of interest to the nanocomposites community who are mixing polymers and nanoparticles to engineer flexible composites that may exhibit improved electrical, optical and mechanical properties.[25] When a polymer is doped with nanoparticles, as in the case of functionalised CdSe dispersed in PS by Lee et al, nanoparticles were found to segregate to the tip of a crack via entropic interactions.[20] As the nanoparticles are solids the polymer chains must stretch around them causing a loss of conformational entropy that increases with particle radius. Due to the lack of certain interactions larger nanoparticles can then be expelled from the bulk of the polymers. When this is carried out in BCPs certain sized particles can be more compatible with one or other of the copolymers. Therefore certain particles will localise at the centre of one copolymer while other particles may disperse throughout another copolymer.[26] In this case the nanoparticles have also been found to alter the orientation of the BCP domains. These outcomes can be extremely advantageous as, for example, the optical performances of composites are highly sensitive to the specific location of the particles within the domains. However mechanically characterising these systems is extremely tough and so there is much need for a technique, such as flat punch indentation, to help exploit the possible mechanical advantages of these nanocomposites.

In this chapter, BCP thin film mechanical properties are investigated by flat punch nanoindentation using a 320 nm DFP. In contrast to all other thin film mechanical techniques, flat punch indentation allows access to a full stress versus strain response of films prepared to a thickness of one phase separated lamellar domain, or about 30 nm.

In the case of the BCP films tested here, the 320 nm diameter cylindrical punch employed integrates the mechanical response over a region of ~15 domains, effectively testing the nanocomposite nature of the material. Flat punch nanoindentation was carried out into 26 nm neat PMMA film, 28 nm neat PS film and 33 nm films of PS-b-PMMA in a weakly segregated (*ie.* pre-phase separation) and strongly segregated (post phase separation) states. Measurement of both PMMA and PS homopolymer thin films of similar molecular weight show that the PMMA-b-PS system consistently interpolates the stress-strain

response of the homogeneous systems, whether phase separated or not. Overall, all systems tested showed a marked reduction in mechanical stiffness and strength from the bulk, demonstrated by thick PS and PMMA film flat punch indentation using a geometrically congruent deformation geometry.

6.3 Experimental Set-Up

Thin films of 37-37 K PS-PMMA block copolymers and PS and PMMA homopolymers were prepared as described in chapter 4. The same 320 nm diameter diamond flat punch was used for all experiments which were carried out using the nanoindenter described in chapter 4. Measurements were performing using static load control at 19 ° C, at a linear loading rate of 0.01 mN per second. Flat punch was held on the surface for 5 seconds via a displacement feedback loop before loading began. After reaching maximum load the load was held for 10 seconds before unloading to 90% of load. Drift was then determined over a duration of 100 seconds before unload completed.

Using the CSM amplitude and phase of the sample displacement signal relative to this loading were recorded. A process of careful alignment of the flat punch to the sample surface was carried out, as described once again in chapter 4.

To examine the mechanical properties of BCPs the flat punch method was used to carry out nanoindentation on a 28 nm thin film of PS homopolymer, a 26 nm PMMA homopolymer thin film and prephase separated (a mixed system) and phase separated BCP 33 nm thin films. All indents have the same characteristic graph expected from flat punch nanoindentation of a film of glassy elastic-plastic material. AFM images of the BCP films before indentation are presented (Figure 6.1) and also an SEM image of an indent carried out by the 300 nm diamond flat punch (Figure 6.2). No metal coating was used in these SEM images and all imaging was done using a Zeiss Ultra SEM at 2 kV accelerating voltage. The thin darker grey lines correspond to PMMA while the larger lighter grey areas correspond to PS. In the SEM image they do not appear to be the same size due to beam damage.

6.4 Results and Discussion

All films were characterized by intermittent contact mode AFM immediately prior to indentation. In figure 6.1, AFM dynamic phase contrast images of the weakly segregated (a) and strongly segregated (b) PS-*b*-PMMA samples are shown. 2D fast Fourier transforms of each surface are provided as insets in each panel to show in particular the clear emergence of the single phase block length scale post segregation. The flat punch indentation technique establishes mechanical response in a volume containing about 200 chains, with up to 15 domains across the diameter of the punch in the strongly segregated state.

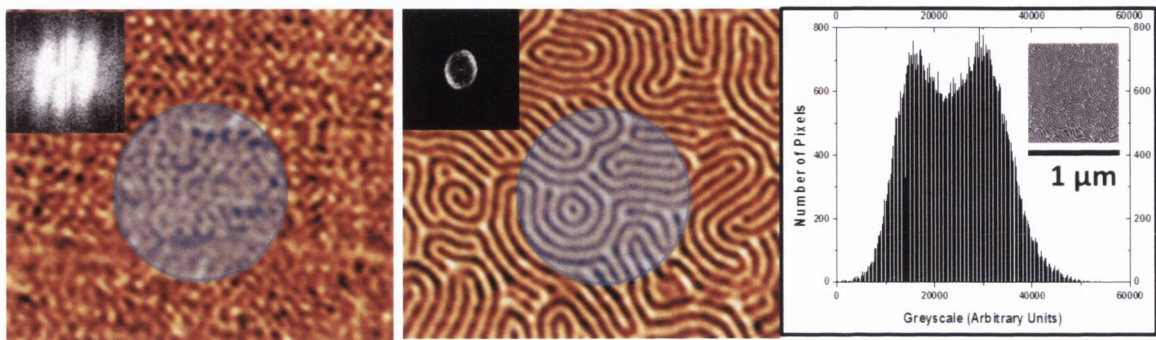


Figure 6.1: Analysis of phase segregation state of 37k-37k PS-*b*-PMMA block copolymer films of 32 nm thickness. Mechanical phase contrast in intermittent contact AFM shows the weakly (a) and strongly (b) segregated states with the distinct 20 nm microphase separation length scale evident in the fast Fourier transform (FFT) of (b) shown in inset, with no distinct length scale in the FFT inset of (a). In (c) a larger area AFM image of the strongly segregated state shown in greyscale shows two distinct and identical height peaks in a pixel value histogram (d) indicating a symmetric lamellar domain formation.

Figure 6.2 shows an SEM image of a flat punch indentation into the phase separated PS-*b*-PMMA thin film. The thin dark grey lines correspond to the PMMA phase, with the asymmetry in apparent phase size an artefact due to the secondary electron imaging mechanism used to make this SEM image. This asymmetry is not reflected in the phase contrast AFM images of Fig. 6.1 (b). The pile-up region surrounding the 320 nm diameter crater formed is approximately 40 nm in width, consistent with predicted large strain plastic flow pattern in this geometry.[27] Evidence of BCP phase domains on the surface of the pileup is present, and seems to follow on from the surrounding (undisturbed) domain

pattern. By optimizing the contrast of SEM secondary electron imaging, a pattern is revealed across the floor of the indentation crater. This pattern is again reminiscent of the surrounding domain fingerprint pattern, and it is possible to trace the domain path from outside to inside and back again as shown in Fig. 6.2.

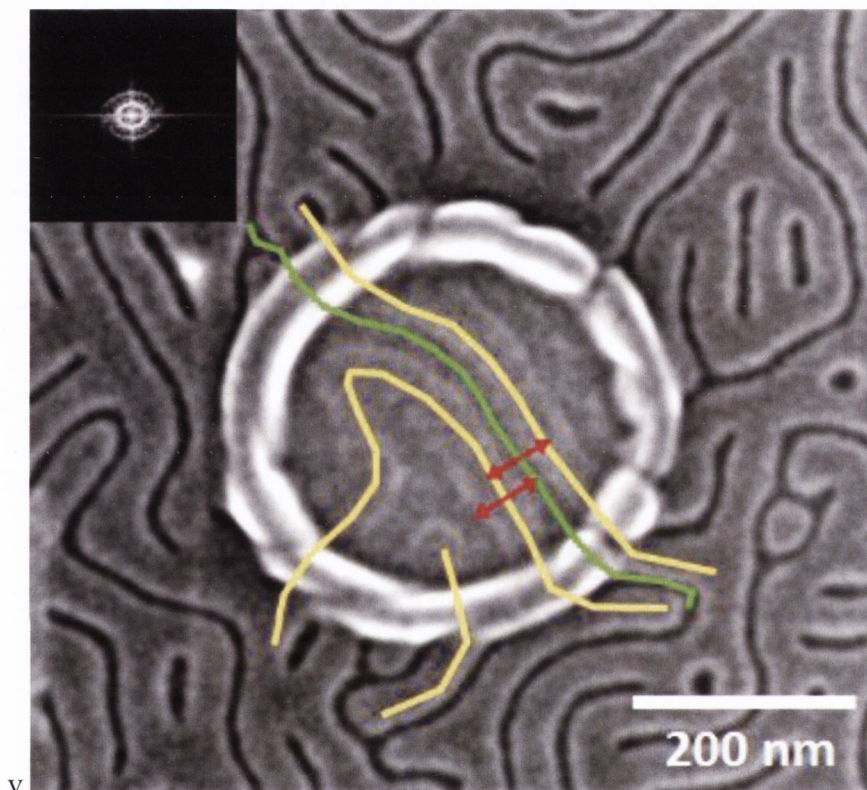


Figure 6.2: Secondary electron SEM image of the strongly segregated state of the PS-*b*-PMMA 33 nm film, showing an indentation by the 320 nm diamond flat punch to high strain. The fingerprint lamellar structure is clearly evident around the indent, while from the indent it is also clear that the BCP remains phase separated on the surface even after it went plastic deformation. The thin darker grey lines correspond to PS while the larger lighter grey areas correspond to PMMA. In the SEM image they do not appear to be the same size due to beam imaging effects. Coloured lines trace domains meanders from undeformed region to corresponding residual deformation pattern. A 50% domain pitch spreading (red arrows) is observed due to the indentation. Note it is possible to trace the domain path from outside to inside and back again as shown

If simple biaxial extensional deformation (eg. uniaxial compression) with affine radial deformation of lamellar domains occurred, one would expect to see little or no remains of

the original fingerprint pattern, with only material corresponding the centre domain remaining due to the large plastic compressive strain. The opposite of this, complete pinning at both upper and lower boundaries, would give a barrelling squeeze flow [28] and might be expected to leave a nearly undistorted residual pattern behind. Instead, in In figure 6.2 residual fingerprint pattern at the bottom of the indentation crate is apparent. Under careful analysis the pattern shows a ~40% broadening of domain pitch. Any further spatially modulated distortion is not perceptible at present. This is interpreted as a condition of partial slip, possibly at both boundaries but most likely at the upper boundary with the observed residual pattern due to BCP chains trapped in the random copolymer brush. It is postulated that an extremely thin region adjacent to the substrate that forms a mechanically distinct region due to covalent brush anchoring and additional entanglements. This region suffers the observed 40% deformation only at the last stages of indentation once softer material above is squeezed out.

6.4.1 Small strain discussion – interfacial influence on relaxation

Polymer thin films have time-dependent mechanical properties in both the melt and glassy state[29]. At the continuum level, the deformation of glassy amorphous polymers can be described by an viscoelastic-elasto viscoplastic behaviour[30, 31] with time-dependent viscoelastic features of creep and stress relaxation at low stress, as well as rate-dependent yield, strain softening and strain hardening at high stress. These properties are affected by the thermomechanical processing history of the glass, including effects of ageing and mechanical rejuvenation. In this analysis, time-dependent aspects are ignored as all tests were carried out under the same preparation process and indentation load program, and refer to apparent elastic and elasto-plastic characteristics of the stress vs. strain curves as revealed over the characteristic time-scale of the experiments.

Figure 6.3 shows raw data for a 320 nm DFP carrying out several indents into a 33 nm film of 37 K-37 K PS-PMMA BCP , 26 nm 48 K PMMA and 28 nm 44 K PS. To within experimental uncertainty, small strain elastic and elastic-plastic yield properties of the block copolymer were found to be unaffected by phase separation.

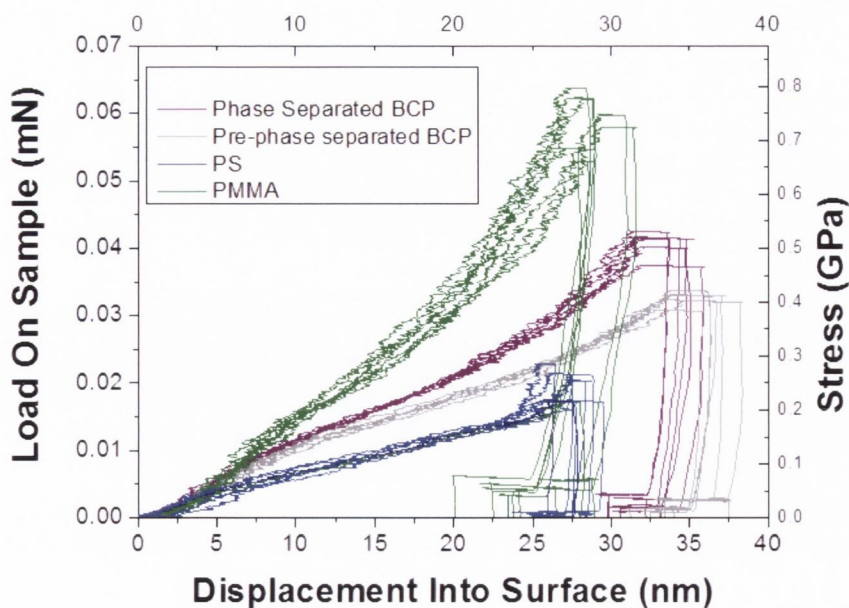


Figure 6.3: Load on sample versus displacement into surface response for a 320 nm diamond flat punch indenting into 28 nm thin film PS, 26 nm thin film PMMA and 33 nm BCP film, both prephase separated and post phase separated, is shown. Note the low scatter between individual curves.

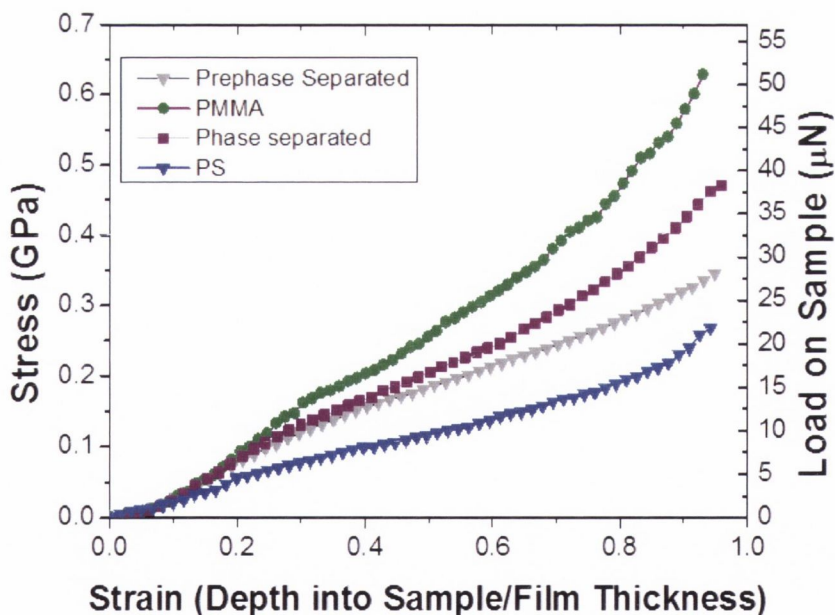


Figure 6.4: Average stress versus strain response for thin film systems of 28 nm thin film PS, 26 nm thin film PMMA and 33 nm BCP film, both prephase separated and post phase separated.

Figure 6.4 shows the raw data from figure 6.3 averaged and converted into stress versus strain for the loading section of the indent. Once again it is very obvious that at small strain both elastic and elastic-plastic yield properties of the block copolymer were found to be unaffected by phase separation.

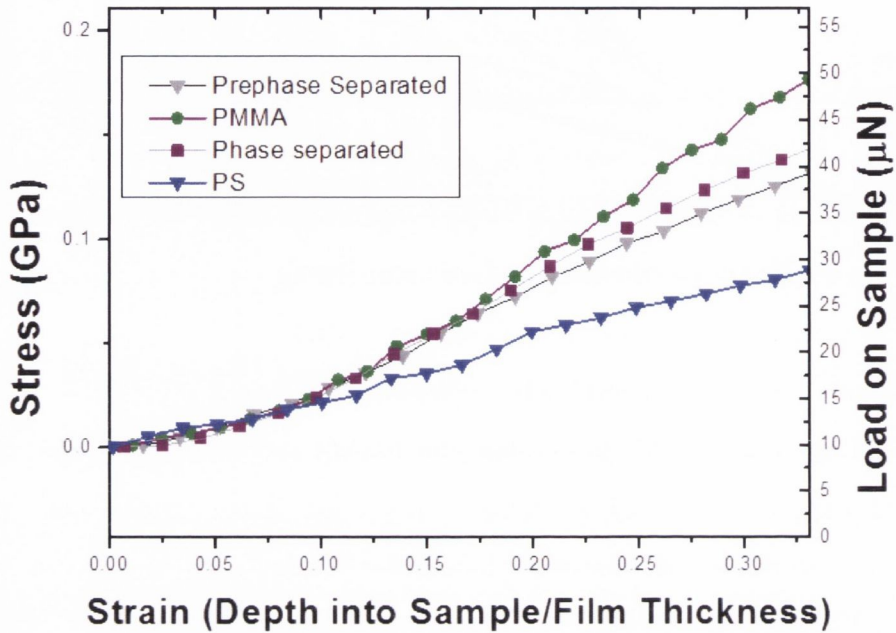


Figure 6.5 : Low strain zoom of average stress versus strain response for thin film systems of 28 nm thin film PS ,26 nm thin film PMMA and 33 nm BCP film, both prephase separated and post phase separated.

Figure 6.5 shows the low strain response of the thin films. Here it is possible to see the very small difference in the low strain behaviour of the phase separated BCP versus the pre phase separated BCP. From analysis of the raw data ,figure 6.4, and the stress vs. strain curves ,figure 6.4 and 6.5, a CM of 470 ± 20 MPa in the weakly segregated state is calculated. This becomes 530 ± 20 MPa under phase separation. Similarly, the forming stress is found to slightly increase from 110 ± 20 MPa to 130 ± 20 MPa. The mechanical parameters for the homopolymer films with similar but slightly lower thickness are contact modulus 280 ± 10 MPa and 660 ± 90 MPa and forming stress 80 ± 10 MPa and 160 ± 10 MPa for PS and PMMA respectively.

The homopolymer response of indenting into thin films is discussed in detail in chapter 5. The as-measured contact modulus and forming stress of the thin film block copolymer system is found to be broadly consistent with a simple law of mixtures (~50-50 wt%) of the measured thin film homopolymer values. This is shown in figure 6.6.

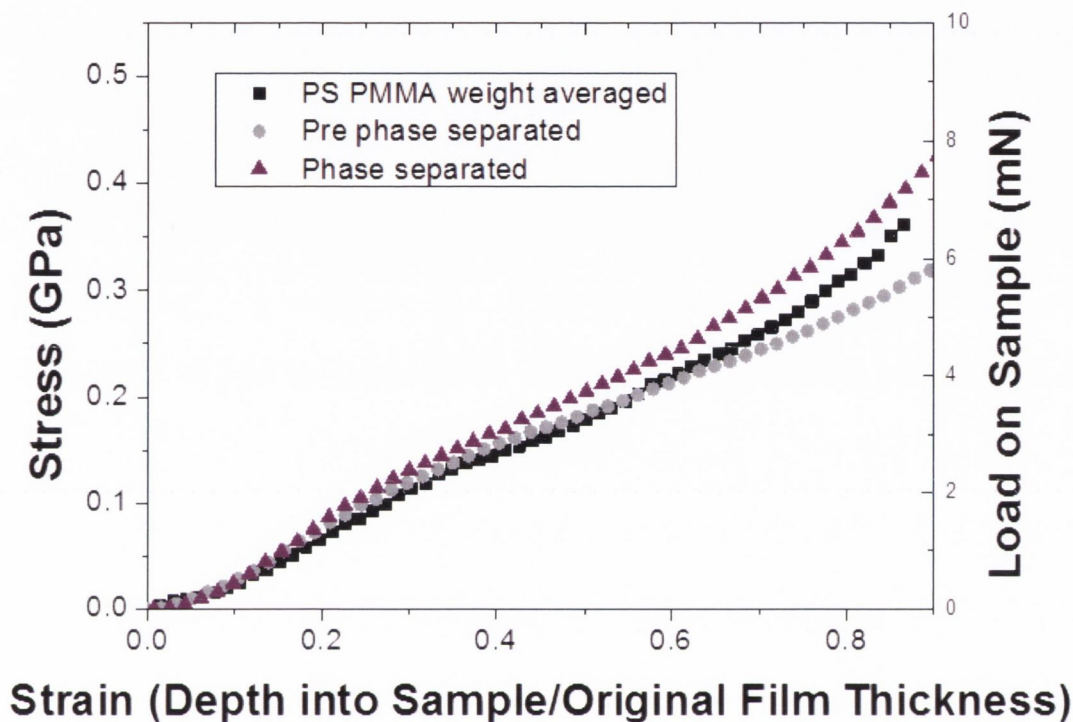


Figure 6.6: Weight average homopolymer response compared to the BCP pre and post phase separated response.

From the empirical model fitting, the contact modulus of the segregated BCP system, 530 ± 20 MPa is slightly higher than the weight average 430 ± 10 MPa value, while the forming stress of the strongly (weakly) segregated BCP system, 130 ± 10 MPa (110 ± 10 MPa) is slightly lower than the weight average 140 ± 10 MPa measurement. In figure 6.6 the full weight averaged homopolymer stress vs. strain response is compared to the BCP curves. There remain several notable differences between the homopolymer and BCP systems tested: (i) the M_w of each homopolymer chain (~37k) is half that of the block copolymer (~74k), (ii) the film thickness of each homopolymer (PMMA 28 nm, PS 26 nm) is about 6 nm (20%) less than the BCP (33 nm), and (iii) the supporting (lower) interface for the homopolymers is

the native oxide of the Si wafer while the BCP system is supported on the random brush on native Si oxide. Above the M_w threshold for entanglement, bulk polymer glass small-strain properties including modulus and yield are not expected to depend on M_w . This has recently been confirmed for supported PS thin films (M_w 44k to 9000k) under Si/SiO_x flat punch indentation prepared under spin casting, anneal and ageing regimens[32] and also in chapter 5 of this thesis. From these measurements and the elastic buckling measurements of Stafford *et. al.* [33], it is estimated that there will be a drop of ~10-15 MPa/nm in E in this thickness region for PMMA and PS, or potentially up a 60-90 MPa effect for the 6 nm difference in film thickness between the homopolymer and BCP system. This is consistent with the findings of an average 70 MPa lower contact modulus.

The presence of the PS-PMMA random copolymer brush for the BCP system may change both the lower interface influence on the prepared thin film state and the mechanics of squeeze flow by changing the frictional state. Nevertheless good agreement of the BCP system with the weight averaged homopolymer curve is maintained throughout, suggesting a marginal influence of brush-altered mechanical constitutive properties or interfacial flow shear on the mechanics

6.4.2 The Effect of Phase Separation

With the effect of the supporting and contacted upper boundary considered, the effect on the mechanics of the film of BCP microphase separation was considered, while holding all other factors constant. Several effects of phase separation in the thin film BCP system is expected. As confirmed by AFM results here, a symmetric, 20 nm wide, lamellar homopolymer domains separated by a new, discrete interface of strongly segregated PS and PMMA phases with an estimated boundary width of <2 nm is introduced. This process maintains (average) film density and hence thickness. On average, the total area of the PS-PMMA strong segregation interface within the 320 nm diameter film deformation volume under the punch was estimated. As the height to width aspect ratio of each lamellar domain is approximately 3:2, the formation of a BCP interface with about 2/3 the area of the contacting punch surface, *i.e.* of the order of the same dimension is expected.

A second effect of microphase separation is the diffusive motion of chains a distance on the order of the radius of gyration. The final, strongly segregated domain size of ~20 nm is approximately twice the bulk radius of gyration of 37k PS or PMMA homopolymers. Neutron scattering experiments of bulk PS-PMMA phase separated systems have shown elongation from a normally spherical polymer chain distribution along an axis normal to the domain wall together with density conserving, concomitant shrinkage in the orthogonal direction[34-36]. It has further been predicted that there is a change in the distribution of entanglements in strongly segregated block copolymer domains compared to homopolymer systems[37].

For PMMA and PS materials tested at room temperature, a glass-like elastic to plastic stress-strain response, as observed in both the thick (bulk) and thin homopolymer films, is expected. For the BCP system this transition is clearly maintained under phase separation despite the formation of 20 nm homopolymer domains. The continued presence of dynamic yielding in the strongly segregated state indicates that at least one phase domain remains in a glass like state. When passing through the glass transition, both PS and PMMA are known suffer drastic reduction in shear strength and milder but significant (three fold) [38] reduction in bulk modulus. Thus, the precise quantitative stress-strain agreement at small strain for all states of BCP film segregation which is observed, which also agrees with the weight-averaged homopolymer response, strongly suggests that both phases remain in a glassy state mechanically similar to the homopolymer films. This means that the phase separation boundary tested here is a “hard” interface between glassy phases [39]. These mechanical observations are consistent with T_g related studies in BCP phase separation [40] and other polymer nanocomposite materials which see no alteration of T_g despite the presence of a large polymer-polymer interface giving a significant area to volume ratio in bulk samples.

Despite the small strain congruence, at large strains under conditions dominated by plastic flow, the phase separated condition shows a distinct increase in stress with strain (40% at 0.9 compressive strain) in figure 6.4 compared to the mixed system. This may be attributed to additional strain hardening [41-43] arising from altered chain network morphology of the strongly segregated state, altered friction of lamellar homopolymer domains sliding

past one or both boundaries, or a combination of both these effects. The extended annealing conditions of phase separation may lead to this change in the chain network as the number of entanglements in the phase separated BCP may differ from the number in the prephase separated state. Despite the topological constraints and possible “smectic” character of block chains that could lead to entanglement depletion in the middle of a domain[37], this result of apparent strain hardening is interpreted as a net increase in overall entanglement development, most likely in a region close to the domain walls (Figure 6.7). Whether effective entanglement density is significantly modulated at the domain wall itself presently cannot be addressed by this measurement.

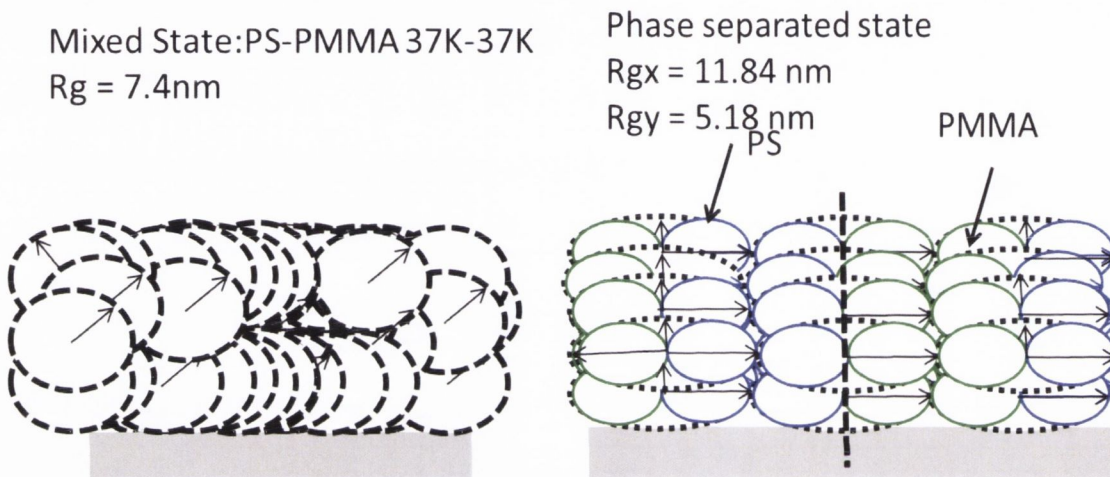


Figure 6.7: Expected BCP system chain packing and entanglement state pre and post phase separation. Pre phase separation the R_g is considered to be represented by R_g of a 74 K generic molecule which has the average properties of PS and PMMA. After phase separation occurs the generic molecule separated into 2 sections of PS and PMMA which each have an R_{gy} of 5.4 nm and an R_{gx} of 11.8nm.

6.5 Implications for BCP Lithography

Finally, a comment on thin film BCP applications such as BCP lithography. These results have obvious implications for the structural behaviour of polymer nanostructures as exemplified by the EUV resist collapse problem.[44] For failure by elastic buckling[45] or plastic yield, the severe reduction in mechanical stiffness and strength already apparent in the phase separated BCP system will likely represent an upper bound for final state nanostructure mechanical integrity when one phase is removed by further etch processing.

6.6 Conclusions

Flat punch nanoindentation was used to measure the effect of microphase separation on mechanical deformation of single-lamellar domain thickness block copolymer films. When compared to PS and PMMA homopolymer thin films of similar thickness and molecular weight, a strict interpolation of the room temperature stress vs. strain curve was found to high strain. This was true for PS-*b*-PMMA films in both the as-prepared spin-cast state and following microphase separation into 20 nm lamellar fingerprint domains induced by thermal annealing. Overall, the thin film stress-versus-strain envelope as defined by neat PS and PMMA showed a pronounced softening compared to measured thick (>100 nm) film response, consistent with previous reports. The BCP pre and post phase separated states had identical small strain elastic and yield response; while the phase separated state demonstrated an effective strain hardening effect above 0.5 strain, to a value of 40% excess stress at 0.9 strain. These results have implications for both thin film polymer mechanics and block copolymer lithography. Annealing leading to microphase separation implies diffusive relaxation of the polymer chain blocks by displacement on order of the bulk radius of gyration. This leaves the thin film mechanical weakening effects observed here and elsewhere in spin-cast supported thin films difficult to attribute to sample preparation history effects such as residual stress, local structural gradients and unreleased solvent. Instead, the nature of confining interfaces seems to be dominant. Confinement during testing provided here by a lower silicon substrate and an upper (hard) punch surface with 30 nm separation has a profound softening effect on the entire stress vs. strain curve, while the introduction of a further lateral confinement at the 20 nm scale by creating glassy BCP segregation walls has a limited influence on the overall mechanics, manifesting only at high strain. For polymer nanostructures formed by block copolymer lithograph, a significant loss in mechanical strength (compared to bulk polymer) occurs by the initial creation of the supported thin film, but no further penalty is incurred by in-film structuring.

6.7 References

- [1] A. Mataz and G. B. McKenna, "Effects of confinement on material behaviour at the nanometre size scale," *Journal of Physics: Condensed Matter*, p. R461, 2005.
- [2] J. L. Keddie, R. A. L. Jones, and R. A. Cory, "Size-Dependent Depression of the Glass Transition Temperature in Polymer Films," *EPL (Europhysics Letters)*, p. 59, 1994.
- [3] H. Lu, W. Chen, and T. P. Russell, "Relaxation of Thin Films of Polystyrene Floating on Ionic Liquid Surface," *Macromolecules*, vol. 42, pp. 9111-9117, 2011/11/15 2009.
- [4] M. Tress, M. Erber, E. U. Mapesa, H. Huth, J. Müller, A. Serghei, C. Schick, K.-J. Eichhorn, B. Voit, and F. Kremer, "Glassy Dynamics and Glass Transition in Nanometric Thin Layers of Polystyrene," *Macromolecules*, vol. 43, pp. 9937-9944, 2010.
- [5] O. Baumchen, J. D. McGraw, J. A. Forrest, and K. Dalnoki-Veress, "Reduced Glass Transition Temperatures in Thin Polymer Films: Surface Effect or Artifact?," *Physical Review Letters*, vol. 109, Aug 2012.
- [6] C. Creton, G. Hu, F. Deplace, L. Morgret, and K. R. Shull, "Large-Strain Mechanical Behavior of Model Block Copolymer Adhesives," *Macromolecules*, vol. 42, pp. 7605-7615, 2009.
- [7] R. Weidisch, M. Stamm, G. H. Michler, H. Fischer, and R. Jerome, "Mechanical Properties of Weakly Segregated Block Copolymers. 3. Influence of Strain Rate and Temperature on Tensile Properties of Poly(styrene-*b*-butyl methacrylate) Diblock Copolymers with Different Morphologies," *Macromolecules*, vol. 32, pp. 742-750, 1999.
- [8] C. M. Koo, L. Wu, L. S. Lim, M. K. Mahanthappa, M. A. Hillmyer, and F. S. Bates, "Microstructure and Mechanical Properties of Semicrystalline¹ Rubbery² Semicrystalline Triblock Copolymers," *Macromolecules*, vol. 38, pp. 6090-6098, 2011/11/16 2005.
- [9] T. J. Hermel, S. F. Hahn, K. A. Chaffin, W. W. Gerberich, and F. S. Bates, "Role of Molecular Architecture in Mechanical Failure of Glassy/Semicrystalline Block Copolymers: CEC vs CECEC Lamellae," *Macromolecules*, vol. 36, pp. 2190-2193, 2011/11/16 2003.
- [10] X. Zhu, L. Wang, and J. Lin, "Distinct Elastic Response to Hierarchical Nanostructures," *Macromolecules*, vol. 44, pp. 8314-8323, 2011/11/16.
- [11] A. J. Meuler, M. A. Hillmyer, and F. S. Bates, "Ordered Network Mesostructures in Block Polymer Materials," *Macromolecules*, vol. 42, p. 7221, 2009.
- [12] H. R. Brown, "Effect of a diblock copolymer on the adhesion between incompatible polymers," *Macromolecules*, vol. 22, pp. 2859-2860, 1989.
- [13] R. Schnell, M. Stamm, and C. Creton, "Mechanical Properties of Homopolymer Interfaces: Transition from Simple Pullout To Crazing with Increasing Interfacial Width," *Macromolecules*, vol. 32, pp. 3420-3425, 1999.
- [14] S. Horiuchi, A. Nakagawa, Y. Liao, and T. Ougizawa, "Interfacial Entanglements between Glassy Polymers Investigated by Nanofractography with High-Resolution Scanning Electron Microscopy," *Macromolecules*, vol. 41, pp. 8063-8071, 2008.
- [15] M. J. Fasolka and A. M. Mayes, "Block copolymer thin films: Physics and Applications¹," *Annual Review of Materials Research*, vol. 31, pp. 323-355, 2001.
- [16] R. S. McLean and B. B. Sauer, "Tapping-Mode AFM Studies Using Phase Detection for Resolution of Nanophases in Segmented Polyurethanes and Other Block Copolymers," *Macromolecules*, vol. 30, pp. 8314-8317, 1997.
- [17] T. Thurn-Albrecht, R. Steiner, J. DeRouchey, C. M. Stafford, E. Huang, M. Bal, M. Tuominen, C. J. Hawker, and T. P. Russell, "Nanosopic Templates from Oriented Block Copolymer Films," *Advanced Materials*, vol. 12, pp. 787-791, 2000.
- [18] M. Park, C. Harrison, P. M. Chaikin, R. A. Register, and D. H. Adamson, "Block Copolymer Lithography: Periodic Arrays of $\sim 10^{11}$ Holes in 1² Square Centimeter," *Science*, vol. 276, pp. 1401-1404, May 30, 1997 1997.
- [19] A. J. Crosby and J. Y. Lee, "Polymer nanocomposites: The "nano" effect on mechanical properties," *Polymer Reviews*, vol. 47, pp. 217-229, 2007.

- [20] J.-Y. Lee, Q. Zhang, T. Emrick, and A. J. Crosby, "Nanoparticle Alignment and Repulsion during Failure of Glassy Polymer Nanocomposites," *Macromolecules*, vol. 39, pp. 7392-7396, 2012/08/25 2006.
- [21] A. M. Donald and E. J. Kramer, "Effect of molecular entanglements on craze microstructure in glassy polymers," *Journal of Polymer Science: Polymer Physics Edition*, vol. 20, pp. 899-909, 1982.
- [22] W. Kim, J. Han, C. Y. Ryu, and H. Yang, "Chemical composition effects on the fracture of polystyrene-block-poly(methyl methacrylate)block copolymers," *Journal of Polymer Science Part B: Polymer Physics*, vol. 44, pp. 3612-3620, 2006.
- [23] D. Wang, S. Fujinami, K. Nakajima, and T. Nishi, "True Surface Topography and Nanomechanical Mapping Measurements on Block Copolymers with Atomic Force Microscopy," *Macromolecules*, vol. 43, pp. 3169-3172.
- [24] O. K. C. Tsui, X. P. Wang, J. Y. L. Ho, T. K. Ng, and X. Xiao, "Studying Surface Glass-to-Rubber Transition Using Atomic Force Microscopic Adhesion Measurements," *Macromolecules*, vol. 33, pp. 4198-4204, 2012/10/25 2000.
- [25] A. C. Balazs, T. Emrick, and T. P. Russell, "Nanoparticle Polymer Composites: Where Two Small Worlds Meet," *Science*, vol. 314, 2006.
- [26] R. B. Thompson, V. V. Ginzburg, M. W. Matsen, and A. C. Balazs, "Predicting the Mesophases of Copolymer-Nanoparticle Composites," *Science*, pp. 2469-2472, 2001.
- [27] W. Johnson and H. Kudo, "The compression of rigid-perfectly-plastic material between rough parallel dies of unequal width," *International Journal of Mechanical Sciences*, vol. 1, pp. 336-341, 1960.
- [28] M. M. Denn, "Extrusion Instabilities and Wall Slip," *Annual Review of Fluid Mechanics*, vol. 33, pp. 265-287, 2001.
- [29] H. D. Rowland, W. P. King, G. L. W. Cross, and J. B. Pethica, "Measuring Glassy and Viscoelastic Polymer Flow in Molecular-Scale Gaps Using a Flat Punch Mechanical Probe," *ACS Nano*, vol. 2, pp. 419-428, 2008.
- [30] J. J. Wu and C. P. Buckley, "Plastic deformation of glassy polystyrene: A unified model of yield and the role of chain length," *Journal of Polymer Science Part B: Polymer Physics*, vol. 42, pp. 2027-2040, 2004.
- [31] H. E. H. Meijer and L. E. Govaert, "Mechanical performance of polymer systems: The relation between structure and properties," *Progress in Polymer Science*, vol. 30, pp. 915-938, 2005.
- [32] H. D. Rowland, W. P. King, J. B. Pethica, and G. L. W. Cross, "Molecular Confinement Accelerates Deformation of Entangled Polymers During Squeeze Flow," *Science*, vol. 322, pp. 720-724, October 31, 2008 2008.
- [33] J. M. Torres, C. M. Stafford, and B. D. Vogt, "Elastic Modulus of Amorphous Polymer Thin Films: Relationship to the Glass Transition Temperature," *ACS Nano*, vol. 3, pp. 2677-2685, 2009.
- [34] Y. Matsushita, K. Mori, R. Saguchi, Y. Nakao, I. Noda, and M. Nagasawa, "Molecular weight dependence of lamellar domain spacing of diblock copolymers in bulk," *Macromolecules*, vol. 23, pp. 4313-4316, 1990.
- [35] Y. Matsushita, K. Mori, R. Saguchi, I. Noda, M. Nagasawa, T. Chang, C. J. Glinka, and C. C. Han, "Chain conformations and locations of parts of a block polymer in a lamellar structure," *Macromolecules*, vol. 23, pp. 4387-4391, 1990.
- [36] Y. Matsushita, N. Torikai, Y. Mogi, I. Noda, and C. C. Han, "Chain Conformations of Homopolymers Dissolved in a Microdomain of Diblock Copolymer," *Macromolecules*, vol. 27, pp. 4566-4569, 1994.
- [37] M. Murat, G. S. Grest, and K. Kremer, "Lamellar block copolymers: Diffusion and reduction of entanglement effects," *Europhys. Lett.*, vol. 44, pp. 401-406, 1998.

- [38] P. H. Mott, J. R. Dorgan, and C. M. Roland, "The bulk modulus and Poisson's ratio of incompressible materials," *Journal of Sound and Vibration*, vol. 312, pp. 572-575, 2008.
- [39] A. Sanz, A. Nogales, and T. A. Ezquerra, "From hard to soft confinement in a symmetric block copolymer: local and segmental dynamics," *Soft Matter*, vol. 7, pp. 6477-6483.
- [40] C. G. Robertson, T. E. Hogan, M. Rackaitis, J. E. Puskas, and X. Wang, "Effect of nanoscale confinement on glass transition of polystyrene domains from self-assembly of block copolymers," *Journal of Chemical Physics*, vol. 132, p. 104904.
- [41] E. G. Leon, A. P. E. Tom, W. Michael, A. T. Theo, and W. S. Ulrich, "Does the strain hardening modulus of glassy polymers scale with the flow stress?," *Journal of Polymer Science Part B: Polymer Physics*, vol. 46, pp. 2475-2481, 2008.
- [42] R. S. Hoy and M. O. Robbins, "Strain hardening of polymer glasses: Effect of entanglement density, temperature, and rate," *Journal of Polymer Science Part B: Polymer Physics*, vol. 44, pp. 3487-3500, 2006.
- [43] R. S. Hoy and M. O. Robbins, "Strain hardening of polymer glasses: Entanglements, energetics, and plasticity," *Physical Review E*, vol. 77, p. 031801, 2008.
- [44] S. Ouk Kim, H. H. Solak, M. P. Stoykovich, N. J. Ferrier, J. J. de Pablo, and P. F. Nealey, "Epitaxial self-assembly of block copolymers on lithographically defined nanopatterned substrates," *Nature*, vol. 424, pp. 411-414, 2003.
- [45] C. M. Stafford, C. Harrison, K. L. Beers, A. Karim, E. J. Amis, M. R. VanLandingham, H.-C. Kim, W. Volksen, R. D. Miller, and E. E. Simonyi, "A buckling-based metrology for measuring the elastic moduli of polymeric thin films," *Nat Mater*, vol. 3, pp. 545-550, 2004.

Chapter 7 Displacement Controlled Indentation into Polymer Films

7.1 Introduction

Nanoindentation of increasingly smaller volumes of material has allowed us to dramatically advance understanding of plastic yielding in polymer glasses. It has already been shown by Rowland *et al* [1] that some important qualitative properties of bulk materials scale down to the nanoscale, including increasing temperature causing the yield stress to decrease while increased strain rate causing an increase in the yield stress. However the study of incipient plasticity, or the point where the plastic deformation is just beginning to form, has not been addressed in glassy polymers. In clean crystalline surfaces incipient plasticity is studied through the examination of indentation load-displacement curves acquired by a load controlled nanoindenter or atomistic simulations for indentation of perfect metals. Schuh *et al* [2] has published a pioneering experimental paper dealing with the statistics of observed discrete nucleation of dislocations on the crystalline surface of (110) oriented platinum. The authors calculated the activation volume (V), the activation energy (ϵ) and the attempt probability of nucleation (\dot{n}) using rate activation Eyring model as their basis. Here the aim was to observe this incipient plasticity, for the first time, in polymer glasses, which is hypothesised, will correspond to the nucleation and propagation dynamics of individual shear bands in the material.

Their approach to the incipient plasticity problem was based upon an observation that had been documented previously [3, 4] the initiation of the first displacement burst in crystalline materials is stochastic. A series of nominally 'identical' nanoindentations on the same clean surface gave a significant spread of plastic yield points. By performing large numbers of these experiments, in which the temperature was varied over several temperatures, these authors calculated the V , ϵ and \dot{n} .

In this chapter results are presented which may correspond to the emergence of the shear bands at the surface of thin films of PS. The pile-up region around indents was imaged via AFM and thus the emergence of circumferential cracks has been observed. However these

results only appear when the nanoindenter is been ran via a displacement control method, and has never been observed previously. All present generation nanoindenters are controlled via load control. This means that indenter actuation is provided only by load histories and data such as displacement, elastic modulus, and time on sample are collected as a response to those load time series. However this means that there is always an uncontrolled response from the nanoindenter. This tends to mask important deformations effects such as strain softening – particularly characteristic of complex soft matter systems such as polymers. Strain softening takes place in such materials after the yield point has been reached, when the deformation continues to occur at a lower load than the yield point occurred at. When the nanoindenter is ran in load control mode it continues to indent using a given load and so the load is always exerting a force on the material and thus does not reduce unless the user specifically programs the nanoindenter to do so. This means it cannot react to a material property such as strain softening when running in load control.

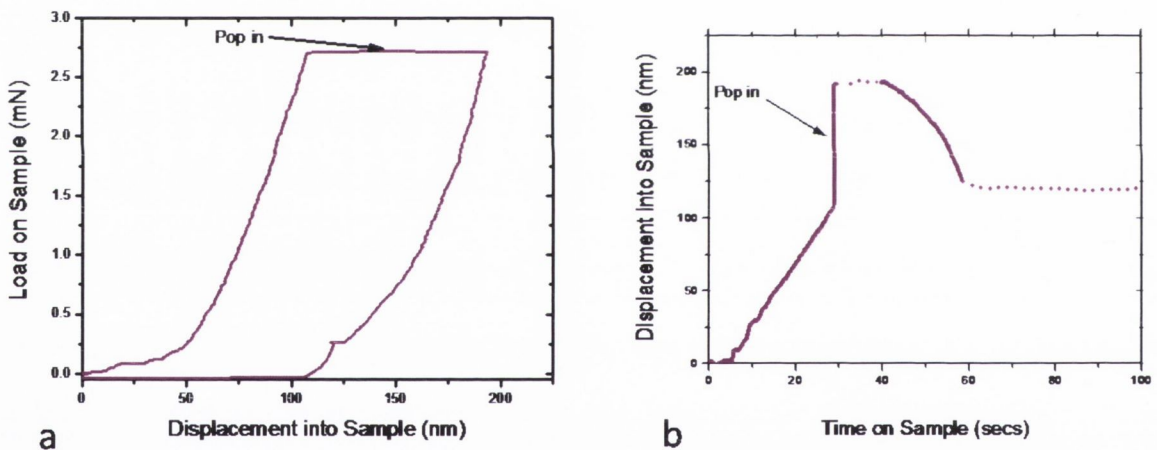


Figure 7.1: A “pop in” event occurring in silicon. A 400 nm diamond flat punch into silicon was used to carry out the indentation. a) shows the load versus displacement graph for the indent. The large jump in displacement of ~100 nm at a constant load is an indicator for the pop in event. b) shows the displacement into sample against the time on sample. This shows that there is a jump in displacement of 100 nm happening very suddenly at around the 28th second.

However, it is possible to gain information on some material properties which happen instantaneously, for example “pop in”s. A “pop in” is when a dislocation propagates instantaneously in a sample, although it appears to act over a few milliseconds due to the

electronic and dynamical response of the nanoindenter. What is seen in the load versus displacement graph is a large jump in displacement occurring at a constant load (Figure 7.1). It is also possible to plot time on sample against displacement into sample in which case you will see a large jump in displacement over a few milliseconds. The data collected during this jump is generally characteristic of the instrument mechanics such as the stiffness and inertia of the indenter shaft, and not the sample material contact. At the end of the jump, uncontrolled kinetic energy is often transferred to the sample, modifying the indented load program.

Schuh et al published graphs (Figure 7.2) displaying a staircase of “pop ins” in bulk metallic glass which they proposed correspond to the nucleation of individual shear bands. They propose that the “knee” of each step corresponds to the nucleation of a shear band, while the “pop in” section corresponds to the propagation of the shear band.

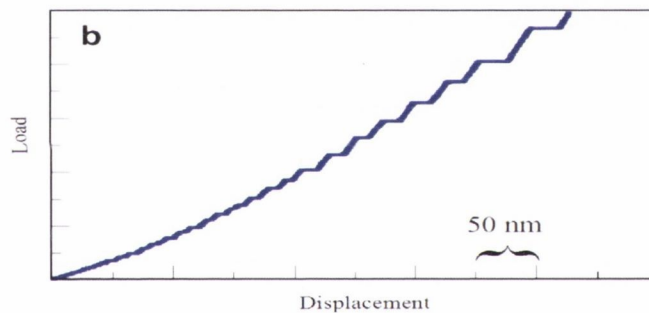


Figure 7.2: Figure adapted from reference [4] showing “staircase” response of indenting under load control into bulk metallic glass.

7.2 Experimental Set up

Here preliminary results which exhibit an unusual step like response upon indenting into a thin film using a flat punch under displacement control are presented. A 6200 nm and 400 nm DFP were used to indent into a 700 nm of 384 K PS ($R_g = 16.7$ nm) thin film and a 52 nm 9000 K PS thin film respectively.

Load control indentation into polymers yields the characteristic graph displayed in figure 7.2. In order to access more information a displacement controlled method was designed. It was believed that this would allow better measurement of softening phenomena in

materials and limit the uncontrolled exchange of energy between instrument and sample as it is attempted to run the nanoindenter in a pseudo displacement control regime. This means that an attempt is made to couple the load and displacement response by means of a feedback loop with proportional, integral and derivative (PID) gain. This allows a method to control the displacement of the indenter, allowing the load to increase or decrease to give us a prescribed velocity, strain rate, etc. However the bandwidth of the PID loop is limited by the electronics of the nanoindenter, limiting the range of effectiveness of this form of control. Experiments must be carefully designed to fall within the controllability window of the instrument.

7.3 Results and Analysis

The velocity was set to 5 nm/s. Upon indentation a remarkable phenomenon of a series of step like features was discovered. Figure 7.3 shows 8 indents to different depths in the 800 nm PS film. The effect is clearly reproducible, with the steps appearing at approximately the same point each time. By stopping the indents at different depths it enables AFMs of different sized indents. The series of step like features is very similar to indenting under load control bulk metallic glasses (Figure 7.2), but has never before been reported for indenting into polymers.

Figure 7.3 a shows 2 6200 nm DFP indents to 600 nm into an 700 nm film of Polystyrene, one under load control and the other under displacement control. It can be seen from the graph that the load control indent has the characteristic graph have is expected from flat punch indentation (chapter 4). The main difference between load control and displacement control is the additional two steps that occurred in figure 7.4a under displacement control. The punch used here has a surface roughness of the order of 20 nm. This punch face roughness and any misalignment of the flat punch leads to contacting defects in the contacting zone. Full contact is established at ~40 nm depth into the film. The displacement at yield point appears to be high due to these contacting defects.

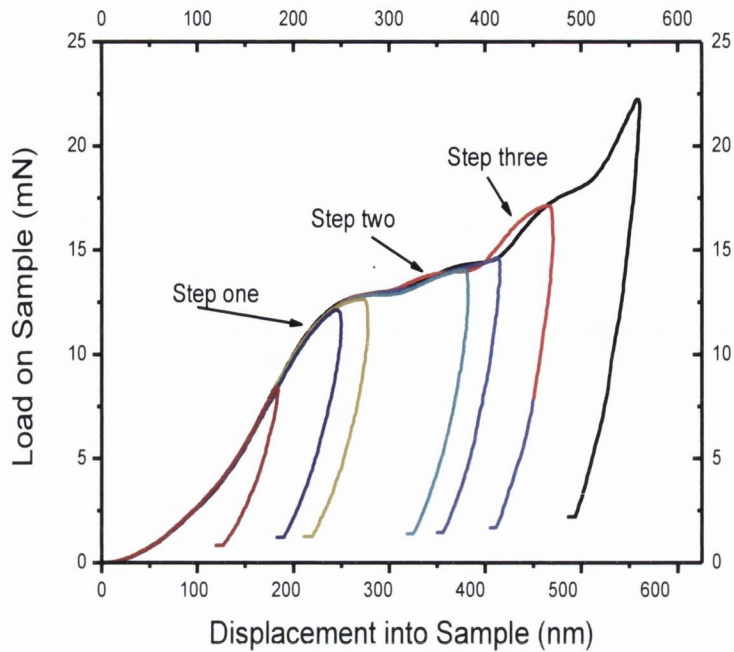


Figure 7.3: shows 8 indents to different depths in the 700 nm PS film. The indents were carried out to different depths. The effect is clearly reproducible, with the steps appearing at approximately the same point in separate traces.

Figure 7.4 b shows the displacement slope (velocity) against the displacement into sample for the control methods. Here the displacement control starts to work at about 20 nm displacement into surface and then succeeds in keeping the velocity at $\sim 5 \pm 5$ nm/s. This is clearly a huge error on the velocity channel but nevertheless does yield some valuable information. The velocity of the flat punch when controlled via load control drops to 5 nm/s after 100 nm into the sample, and stay there for about 200 nm. However at this point the yield stress is reached and the velocity of the indenter shoots up to 30-40 nm/s for the next 250 nm indenting into the sample. It is in this region of 250 nm that the additional 2 steps occur in the velocity control indent, implying that these steps are rate dependent phenomena, and only occur when the indentation happens at low, constant, strain rates. This is the reason that only one step is observed using load control. Since these steps appear to be a rate dependent effect, and occur at the stage in the indent where strain softening is expected to occur, the increase in load at this point means the material deforms plastically in a different manner. There is also an issue as to why the load on sample does

not reduce after crossing over a step. At this point it was suspected that it was related to poor PID control of the system, and this is an area to improve on.

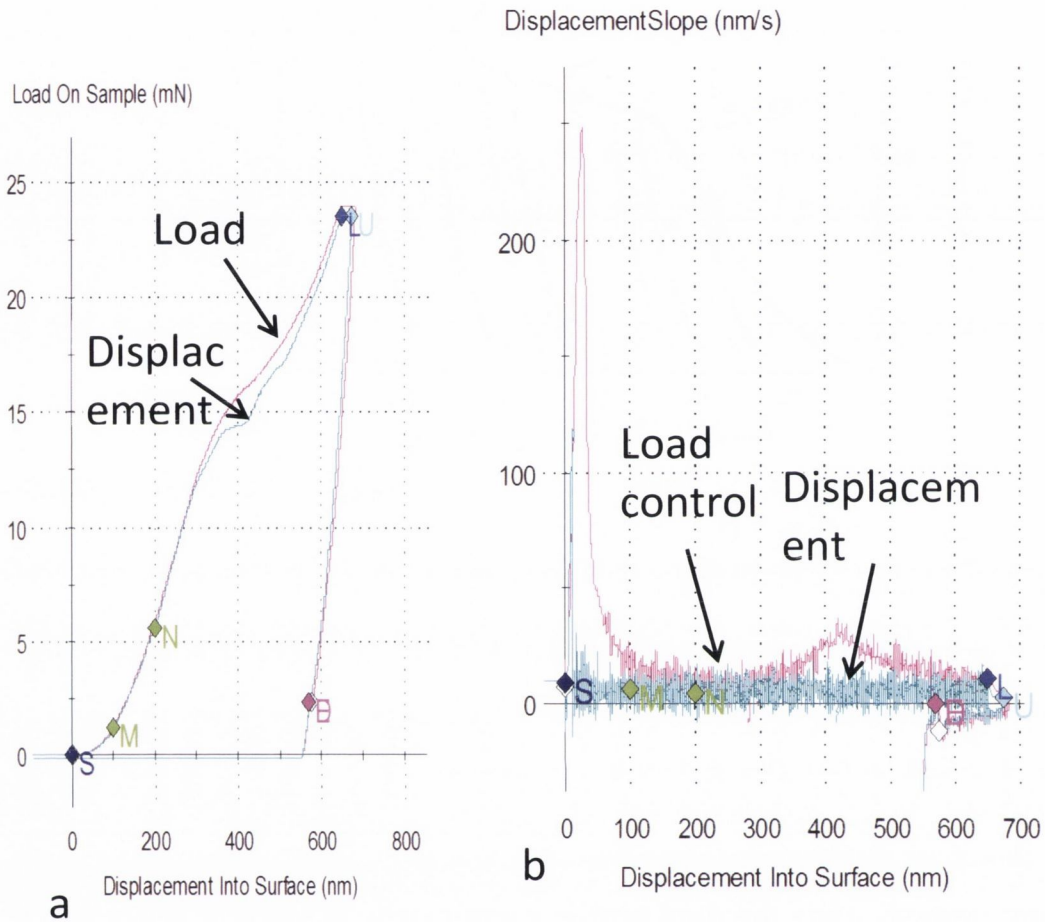


Figure 7.4: a) Graph showing 2 6200 nm DFP indents to 600 nm into an 800 nm film of Polystyrene, one under load control and the other under displacement control. It can be seen from this graph that the load control has one main step, while the velocity control shows 2-3 steps. Full contact was established at ~150 nm and the yield point appears to be high due to contacting defects. b) shows the corresponding displacement slope (velocity) versus displacement data for the same indents. It can be seen from this graph the difference in the velocities of the indents when carried out using displacement control and load control.

Several experiments were designed to further investigate this effect. First of all the velocity with which these experiments were carried out was varied from 50 nm/s down to 1 nm/s

(Figure 7.5). For 50 nm/s only one step occurred, while for 1 nm/s five steps occurred. Therefore it is concluded that if this is a material property then it is a time dependent one.

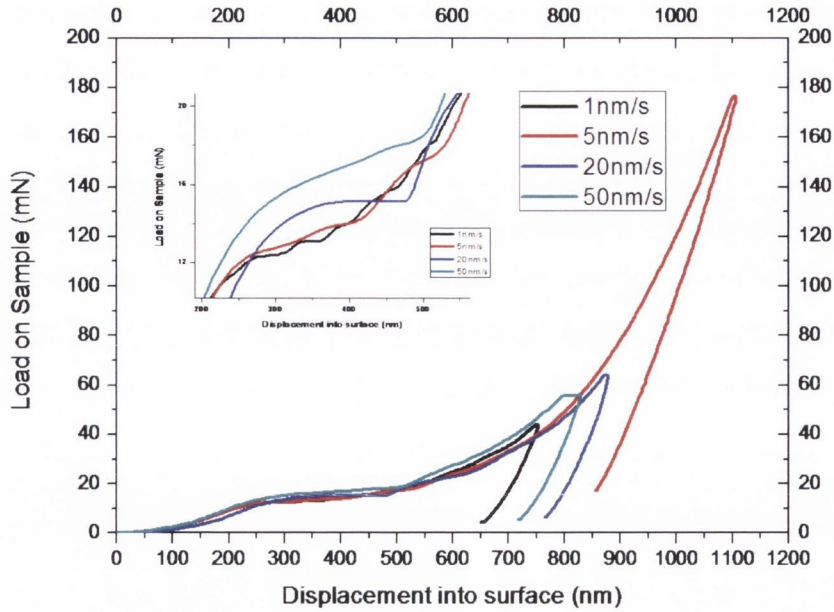


Figure 7.5: Displacement controlled indentation carried out by 6200 nm DFP into 800 nm PS. These indentations were carried out at 1, 5, 20 and 50 nm/s. An increased number of steps of smaller size (ie. increased “staircasing”) occurred as the velocity of the nanoindenter decreased.

As further evidence for the existence of shear band phenomena in these indentations and their correlation to stress vs. strain “staircasing”, the pile-up region around the indents was imaged using AFM. It was attempted to correlate the circumferential cracks that are seen to the number of steps, with the interpretation that they may correspond to the emergence of the shear bands at the surface (Figure 7.6).

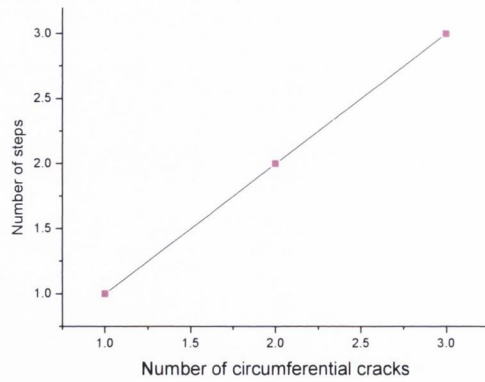


Figure 7.6: Graph of circumferential cracks versus number of steps for 6200 nm DFP indenting under displacement control into 800 nm PS.

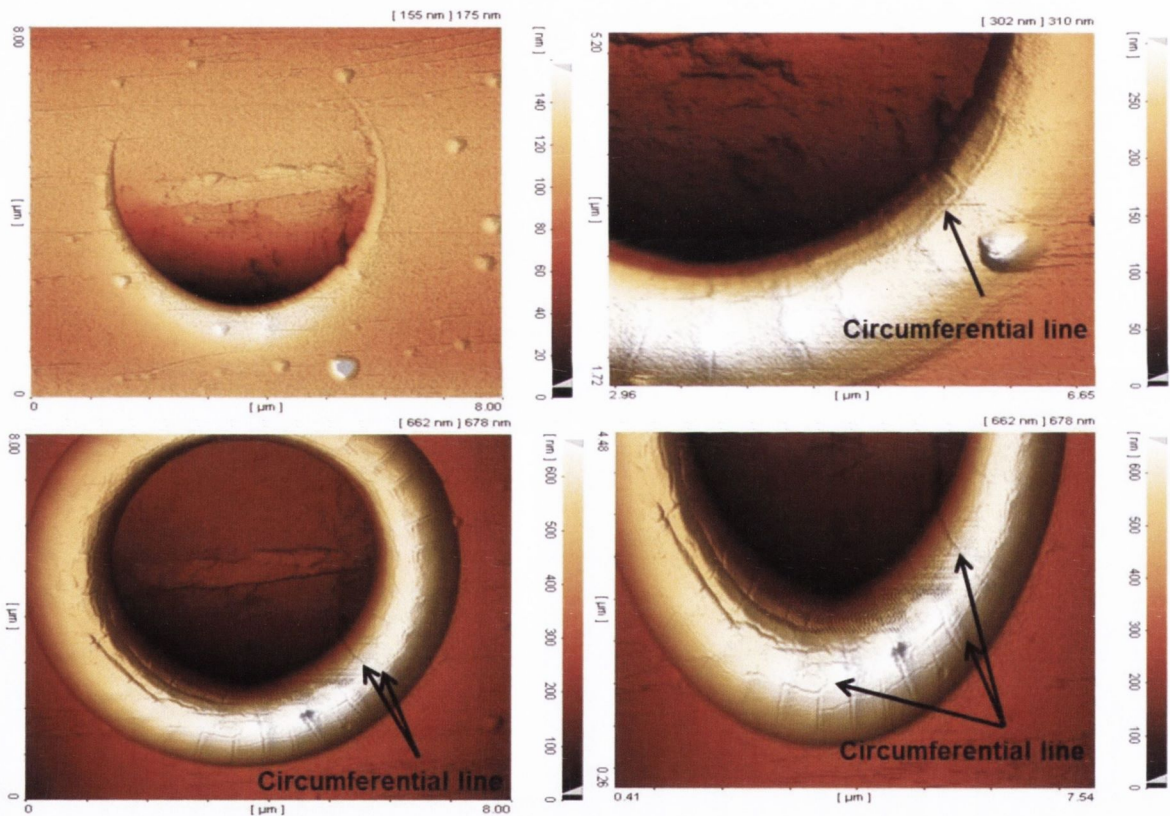


Figure 7.7: AFM image's corresponding to 3 of the indents shown in figure 7.3 .a) shows first indent to 90 nm This image shows the very initial state of plastic deformation occurring before even any pile up has occurred. b) shows the 250 nm indent. In this indent three features are evident, 1) pile up has begun to occur, 2) there are crazes in the pile up perpendicular to the flat punch and 3) a line appears in the pile up circumferential to the flat punch. c) and d) shows the 390 nm indent. Here it is possible to make out 2 lines parallel to the flat punch and the beginning of a third line.

Shear bands with dimensions down to several tens of nm have been observed in annealed polystyrene glass compression tests [7] since the 1970's using Transmission Electron Microscopy (TEM). The conjecture here is that this may be the first time they have been nucleated and imaged on a one to one basis. Images were taken of the indents and are shown in figure 7.7. These images correspond to 3 of the indents shown in Figure 7.3. The first indent was made to 90 nm which corresponds on the graph to just before the first step can be seen, and an AFM image taken.

This image shows the very initial state of plastic deformation occurring before even any pile up has occurred. The next indent image included here was the 250 nm indent (Figure 7.7 b). In this indent three features are evident, 1) pile up has begun to occur, 2) there are crazes in the pile up perpendicular to the flat punch and 3) a line appears in the pile up parallel to the flat punch. The second feature, the crazes, have been reported before by van Melick et al[5] where they carried out flat punch indentation into polymer glasses via a load control method. However the third feature of the line in the pile up has not been reported in literature and only occurs under velocity control. The 390 nm indents is also shown here (Figure 7.7 c). Here it is possible to make out 2 lines parallel to the flat punch and the beginning of a third line. The 390 nm indent corresponds to the beginning of the third step in figure 7.7 d [6] This is compared with figure 7.8 which shows both the load versus displacement curve and an AFM of the remaining indent using the same punch under load control. It is noticeable in the load displacement curve that there is just one step, corresponding to the FS in the material, and in the AFM there is a lack of the circumferential lines seen in figure 7.8.

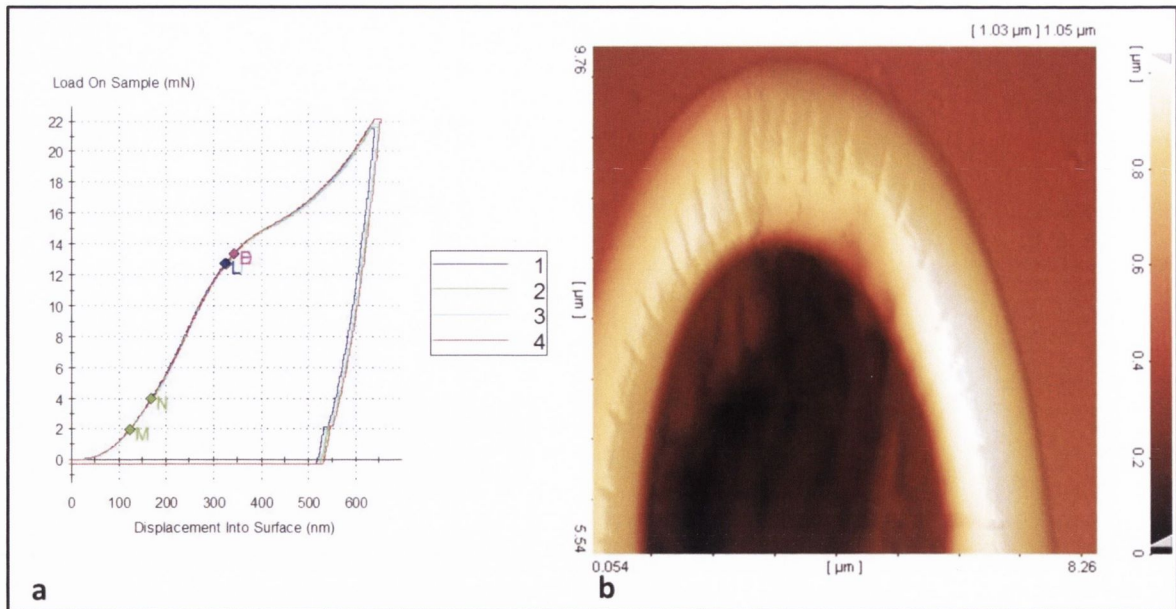


Figure 7.8: a shows a load versus displacement curve for the 6200 nm DFP into 800 nm 382 K PS. b shows the corresponding image for the indent. Note the lack of continuous circumferential lines in the pile up.

7.4 Discussion and Conclusion

A displacement controlled method for nanoindentation is a valuable technique for accessing strain softening phenomena which may be ubiquitous on the nanoscale where the discrete nature of plasticity may begin to be accessed. Here preliminary results which indicate a step like response upon indenting into a thin film using a flat punch under velocity control are presented. This step like behaviour has been reported before for load controlled indentation into bulk metallic glasses. Each step in the bulk metallic glasses was thought to correspond to the nucleation and propagation of a shear band in the bulk metallic glass. However it has never been reported in the literature for indentation carried out in polymer glasses. It was found from Atomic Force Imaging Microscopy that cracks circumferential to the punch appear in the pile up around the indent seemingly corresponding in a one to one manner to the steps in the load versus displacement graph. Whether these cracks are surface effects, or the result of the nucleation and propagation of some kind of singular event, possible shear bands, has yet to be understood.

Therefore, while initial experimentation to design a feedback controlled method to carry out velocity controlled indentation was carried out here this work was limited by the 500 Hz limit of the CSM. This frequency is several kHz short of been able to maintain a velocity control indentation method and thus severely restricts the abilities of the Agilent nanoindenter from measuring strain softening in the polymeric materials which is required if the root cause of the multiple steps in chapter 8 are to be fully understood. However, Hysitron have developed a nanoindenter which can carry out displacement controlled indenting in situ in a SEM[8]. This is done using a differential capacitance half bridge method with a 150 kHz signal on one fixed outer plate of the displacement sensor core and a second signal of the same frequency but phase shifted by 180 degrees on the other fixed outer plate of the same core. These signals are high enough in frequency relative to the mechanical bandwidth of the transducer to not actuate it. Fabricating a DFP indenter tip and carrying out indentation into polymer materials with this increased feedback frequency in situ in SEM could yield very exciting results building on the ones presented here.

7.5 References

- [1] H. D. Rowland, W. P. King, G. L. W. Cross, and J. B. Pethica, "Measuring Glassy and Viscoelastic Polymer Flow in Molecular-Scale Gaps Using a Flat Punch Mechanical Probe," *ACS Nano*, vol. 2, pp. 419-428, 2008.
- [2] C. A. Schuh, J. K. Mason, and A. C. Lund, "Quantitative insight into dislocation nucleation from high-temperature nanoindentation experiments," *Nat Mater*, vol. 4, pp. 617-621, 2005.
- [3] Y. L. Chiu and A. H. W. Ngan, "Time-dependent characteristics of incipient plasticity in nanoindentation" *Acta Materialia*, vol. 50, pp. 1599-1611, 2002.
- [4] C. A. Schuh, A. C. L. A. o. n. t. t. r. d. o. incipient, and plasticity during nanoindentation. *J. Mater. Res.* 19, "Application of nucleation theory to the rate dependence of incipient plasticity during nanoindentation," *Journal of Material Research*, vol. 19, pp. 2152-2158, 2004.
- [5] H. G. H. van Melick, O. F. J. T. Bressers, J. M. J. den Toonder, L. E. Govaert, and H. E. H. Meijer, "A micro-indentation method for probing the craze-initiation stress in glassy polymers," *Polymer*, vol. 44, pp. 2481-2491, 2003.
- [6] C. M. Stafford, C. Harrison, K. L. Beers, A. Karim, E. J. Amis, M. R. VanLandingham, H.-C. Kim, W. Volksen, R. D. Miller, and E. E. Simonyi, "A buckling-based metrology for measuring the elastic moduli of polymeric thin films," *Nat Mater*, vol. 3, pp. 545-550, 2004.

- [7] J.C.M. Li and J. B. C. Wu, "Pressure and normal stress effects in shear yielding," *Journal of Materials Science*, vol. 11, pp. 445-457, 1976.
- [8] K.A. Rzepiejewska-Malyska, G. Buerki, J. Michler, R.C. Major, E. Cyrankowski, S. A. S. Asif, and O. L. Warren, "In situ mechanical observations during nanoindentation inside a high-resolution scanning electron microscope," *Journal of Materials Research*, vol. 23, pp. 1973-1979, 2008.

Chapter 8 Conclusions and Future Work

In summary, a body of work has been presented here that encapsulates a thorough investigation of flat punch nanoindentation and the advantages and disadvantages of the technique. Experiments were carried out from large to small scale in polymer materials in and the first results for scalable size effects analysed and discussed in chapter 5. Application of flat punch nanoindentation to extract mechanical properties of ultra-thin films of a highly technologically relevant material interesting to the nanocomposites community, namely BCPs were discussed in chapter 6. In addition a new form of deformation that is only accessible via a velocity controlled experiment utilising flat punch nanoindentation was presented in chapter 7.

8.1 Conclusions

A core section of mechanics of materials is to understand the relationship of the mechanics to the nanoscale structure. This has been looked at in metals, ceramics, but in polymers has been virtually untouched. While micron scale polymer physics has been probed, real size effects and changes in polymer behaviour have not. This thesis attempts to remedy this by using diamond flat punch nanoindentation to probe size effects in polymer materials, in particular PS and PMMA.

Understanding the mechanics of polymer glass is of practical importance due to its uses as an industrial structural material and adhesive, as well as its role as a functional biological [1]material. Fundamental understanding and prediction of polymer glass mechanics remains challenging, due largely to non-linear coupling of relaxation modes over wide ranges of energy, time and space. [2-7] This leads to a history dependent, non-linear nature of deformation[8-10] for these materials which can be resistant to standard equilibrium-based theoretical analysis. At small scales such as thin film and other confining environments, additional complication arises from interfacial interactions and confining volumes present at small scales.[11] This is of increasing importance for advanced technology manufacturing where EUV lithography block copolymer lithography and

nanoimprint form polymer nanostructures and altered mechanics can influence the geometric integrity of pattern transfer masks.[12] Understanding the small scale mechanics of polymer based materials and composites is also important for next applications in areas such as pressure sensitive adhesives[13], lubricants and interlayer dielectrics in microelectronics[12, 14, 15].

In order to be able to carry out small scale measurements it was necessary to start at large scale effects in these polymers and optimise the technique of flat punch nanoindentation for these materials. As nanoindentation is generally used for extremely hard materials optimising this technique for indenting into soft polymeric materials was the first challenge. In addition, designing and fabricating diamond flat punch, using focused ion beam and a scanning electron microscope, to work in the nanoindenter was another issue. Bringing the flat punch into contact with the sample in an aligned manner is also a non-trivial problem and requires careful use of a tilt stage and atomic force microscopy. These issues are all addressed in chapter four, the experimental method chapter.

Chapter five deals with effects of contact geometry on the small strain measurements obtained by flat punch nanoindentation. We report the effects of film thickness, punch radius, and aspect ratio on elastic and yielding behaviour, where aspect ratio is the ratio of the diameter of the flat punch to the film thickness. In this section we attempted to demonstrate the extent to which it is possible to extract a yield stress and an elastic modulus, taken into consideration aspect ratio and geometry, from the forming stress and contact modulus calculated for the material by the nanoindenter. For this it was necessary to stay in a regime where size effects in polymers have not been measured in the literature. A simple linear model in addition with analysis by Johnson and Kudo[17], for homogeneous compression of a disc yields very good results when adapted for flat punch nanoindentation and this is the central model used to extract yield stress from forming stress. Additionally, the effect of hydrostatic pressure on FS was also discussed using results from Quinson *et al*[18] and Spitzig and Richmond[19]. Their results, in conjunction with Lin *et al.*'s theory for the amount of hydrostatic pressure that occurs under a flat punch at various Poisson's ratio, was used to estimate the contribution of hydrostatic pressure towards forming stress. For PMMA the effect of hydrostatic pressure was found

to be ≈ 117 MPa which, which reduces the value of the forming stress found via flat punch nanoindentation to $518 \text{ MPa} \pm 55 \text{ MPa}$. For PS it was found to correlate to a reduced FS from flat punch nanoindentation of $178 \text{ MPa} \pm 20 \text{ MPa}$. Additionally, when a confining geometry correction was made for TFFPN, using the analysis of Johnson and Kudo [34] yielding values for PMMA of $350 \text{ MPa} \pm 50 \text{ MPa}$ and for PS of $120 \text{ MPa} \pm 20 \text{ MPa}$ were calculated. These values are in excellent agreement with literature values for lubricated compression yield in PS, while remain about twice that expected for PMMA.

E was also calculated using both the CSM in conjunction with Fuquin Yang's model [22] and from direct calculation from the stress versus strain curve. From the CSM results it is clear that E increases with hydrostatic pressure for both PS and PMMA. The value of E for greater than 100 nm films of PMMA was calculated to be approximately $2.75 \text{ GPa} \pm 0.25 \text{ GPa}$ at 0.15 GPa hydrostatic pressure and approximately $2.5 \text{ GPa} \pm 0.25 \text{ GPa}$ at 0.15 GPa hydrostatic pressure for PS. These values are comparable to the E measured by other techniques including bulk compression testing, spherical testing [25, 58] and Stafford's buckling technique.[23] Chapter 5 also probes mechanical size effects in PS and PMMA. Both PS and PMMA homopolymer supported films were found to show a dramatic mechanical weakening under indentation at reduced film thickness, of order five-fold for PS and four-fold for PMMA. For polystyrene the observed weakening with film thickness is consistent with previous results. For PMMA, the results confirm this mechanical size effect. Additionally, for PS this effect was shown to be independent of M_w 's greater than the entanglement threshold. Below 100 nm film thickness there was also a clear decrease in elastic modulus with an eightfold decrease for PS and a 3.5 fold decrease for PMMA. This was independent of M_w in PS, and independent of aspect ratio in PS and PMMA.

Finally, stresses vs. strain curves of thick and ultra-thin polymer films were linked together by normalized by their own forming stress value for 10 to 1 aspect ratio experiments of FP indentation. An unexpected strong congruence appears under this transformation for each curve, even as the film dropped below 50 nm thickness. This is quite an unexpected, yet remarkable, result. While FP indentation has been carried out into large and small scale polymer films a large fivefold decrease in FS of PMMA was seen and a fourfold decrease in FS of PS was measured. Upon normalising the stress using the FS the 10 to 1 aspect ratio curves all fall on each other from low to high strains. In PMMA the effect is noticeable to

the extent that a strain hardening effect, which one expects in PMMA. This congruency for Stress/FS versus strain appears to be strongly implying that one needs only to have knowledge of the FS each film thickness and one stress strain curve, and from this a *CM* and high strain results can be extracted.

Chapter 6 uses the work from chapter 5 and the theory of flat punch nanoindentation to probe the mechanical properties of ultra-thin films of a highly technologically relevant polymer material, namely block copolymers. Here PS-PMMA diblock copolymers were chosen for investigation due to the body of knowledge that had already been built up for these polymers using flat punch nanoindentation. Additionally, the structure of the phase separated block copolymers (BCPs) was chosen to be in a lamellae phase of equal sized domains of PS and PMMA. Flat punch nanoindentation was used to measure the effect of microphase separation on mechanical deformation of single-lamellar domain thickness BCP films. When compared to PS and PMMA homopolymer thin films of similar thickness and molecular weight, a strict interpolation of the room temperature stress vs. strain curve was found to high strain. This was true for PS - PMMA films in both the as-prepared spin-cast state and following microphase separation into 20 nm lamellar fingerprint domains induced by thermal annealing. Overall, the thin film stress versus strain curves for the pre and post phase separated BCP showed a pronounced softening compared to measured >100 nm film response, consistent with results from chapter 6. The BCP pre and post phase separated states had identical small strain elastic and yield response; while the phase separated state demonstrated an effective strain hardening effect above 0.5 strain, to a value of 40% excess stress at 0.9 strain.

Using pre and post phase separated block co polymer films also allowed us to investigate to additional questions that have arisen in the literature. Firstly, questions have been raised as to whether lack of sufficient annealing is responsible for the size effects measured in thin films of polymers. Annealing leading to microphase separation implies diffusive relaxation of the polymer chain blocks by displacement on order of the bulk radius of gyration. This leaves the anomalous thin film mechanical weakening effects observed here and elsewhere

in spin-cast supported thin films difficult to attribute to sample preparation history effects such as residual stress, local structural gradients and unreleased solvent.

Additionally chapter 6 describes a study of the effect of microphase separation of ultrathin symmetric diblock copolymer films on the full stress vs. strain response of the material including the elastic, yield and plastic flow regimes. The single-domain thickness films considered here are used in block copolymer lithography [12, 14] as templates for pattern transfer or for seeding growth and otherwise containing and organizing nano-objects[15, 24]. The results are compared with results for ultrathin homopolymer films of PS and PMMA. Measuring the mechanical properties of diblock films and comparing with homopolymer films allow us to approach the issue of whether the reduction in elastic modulus in ultra-thin films, which has been reported, is purely due to the material not being fully relaxed.

For structural mechanical properties, it has been found that when polymers are confined to film thickness approximately equal to the molecular chain radius of gyration R_g , complex behaviour arises, often related to processing conditions[25]. The material can soften[26] and enhanced inelastic strain is observed for a given stress[27]. Even for thin film dimensions greater than molecular size, a thickness dependent reduction in modulus[28, 29] and simultaneously in modulus and yield[28] has been found below around 50 nm. The modulus effect may not be universal, but instead depend on chain flexibility[30]. Studies of dewetting front geometries in spin-coated, supported PS films indicate residual stress left from non-equilibrium chain conformations produced during vitrification by solvent removal[31]. Thin PS film relaxation experiments have been interpreted through an enhanced free surface mobility[32, 33], but this may also be due to through-film residual stress[34]. Loaded contact experiments can also perform mechanical characterization of thin films and regions near the surface. Lateral Force Microscopy (LFM) experiments have been carried out to determine the T_g of polymer surfaces[35, 36]. Vertical modulation in T_g for thin, homogeneous polystyrene films where values drop at the surface and then rise has been reported using shear-modulated scanning force microscopy[37]. Nanoparticle sinking under capillary action [38, 39] has shown softening in a near surface layer, while indentation based techniques of Tweedie et. al.[1] show an increase in the elastic modulus for PS of up to 200% at depths < 50 nm over a range of processing conditions.

The second question that using BCPs allowed to be addressed was the effect of the microphase separation of the polymers into separate domains and whether the addition of lateral interfaces within the block co polymer film has any effect on the mechanical properties of the ultra-thin film. It is found that the effect of reducing the film thickness, as seen in chapter 6, seems to be dominant. The introduction of lateral confinement at the 20 nm scale by creating glassy block copolymer segregation walls has a limited influence on the overall mechanics, manifesting only at high strain. For polymer nanostructures formed by block copolymer lithograph, a significant loss in mechanical strength (compared to bulk polymer) occurs by the initial creation of the supported thin film, but no further penalty is incurred by in-film structuring.

Chapter 7 attempts to push the boundaries of what nanoindentation can currently accomplish. In clean crystalline surfaces incipient plasticity is studied through the examination of indentation load-displacement curves acquired by a load controlled nanoindenter or atomistic simulations for indentation of perfect metals. However the study of incipient plasticity, or the point where the plastic deformation is just beginning to form, has not been addressed in glassy polymers. The main reason for this is the time dependency of deformation in polymer materials. One property of this time dependency can be seen in nanoindentation by increasing the strain rate which results in an increase in the yield stress. However, so far it has not been possible to measure strain softening in polymer material, which is key to being able to access incipient plasticity in polymers. With this in mind, a controlled displacement rate method of indentation was designed for use in the nanoindenter with flat punch nanoindentation. Using this method, clear steps became obvious in the stress strain indentation curve which it is hypothesised may correspond to the nucleation and propagation dynamics of individual shear bands in the material. However, limitations with feedback frequency the nanoindenter can attain restricted the control with which displacement control could be carried out. Furthermore, definitive identification of remnant shear band activity, as has been possible for indented metallic glass systems was not possible due to the lack of an effective means to perform subsurface imaging of polymer material. Therefore these displacement controlled are preliminary

results for what may be nucleation and propagation of individual shear bands in polymer materials.

8.2 Future work

It would be very useful for this technique if the effect of the sharp edges of the flat punch tip which was addressed in chapter 5 were investigated further. I would suggest a series of experiments where a flat punch tip of area approximately 1500 nm in diameter is fabricated and a series of indents carried out into various film thicknesses of PS and PMMA thin films to quantify the effect the sharp edges. The reason to maintain a large diameter of 1500 nm is to avoid size effects as reported in chapter 6 and 7 while measuring a 10 to aspect ratio into 150 nm PS and PMMA. Very high quality AFMs of the indents must be carried out using ultra sharp AFM tips, as fabricated by the ADAMA company located in CRANN. The corner of the punch should be returned to the FIB where careful rounding of the side edges of the punch will be carried out before a second series of indents carried out. The punch should then undergo this rounding process again and the indentations and AFM process repeated. This should allow a better understanding of the effect of the sharp edges of the punch due to the flat punch sharp edges on FS and CM and allow for design of an ideal flat punch tip.

An important experiment to be proposed here is related to the energy landscape of the flat punch, as discussed once again in chapter 5. DFP's should be manufactured using the plasma etch technique laid out in chapter 4, indentation into various film thicknesses of PS and PMMA carried out and high quality AFMs imaged. DFP diameter should once again be approximately 1500 nm. In addition silicon oxide flat punches, as used in earlier flat punch nanoindentation work [27, 40-42] should be manufactured and the same indentation and AFM imaging carried out. What would be expected from experiment upon plotting FS against aspect ratio and extrapolating to zero aspect ratio is a similar value of FS, within error, at zero aspect ratio to be calculated for all three punches, as was seen in figure 5.18 for a plasma etched punch and FIB manufactured punch. If the value for m is still reasonable, i.e. between 0 and 1, and a linear relationship is found for FS against aspect ratio the Dieter model used in chapter 5 will further be confirmed. If results obtained contrast with this expected result it implies there is an additional effect at work, which may

be a surface repulsive or attractive forces as speculated upon by Tweedie *et al.* [1] and Napolitano *et al.* [43], which will certainly require additional experimentation.

Additionally, while initial experimentation to design a feedback controlled method to carry out velocity controlled indentation was carried out this work was limited by the 500 Hz limit of the CSM. This frequency is several kHz short of been able to maintain a velocity control indentation method and thus severely restricts the abilities of the Agilent nanoindenter from measuring strain softening in the polymeric materials which is required if the root cause of the multiple steps in chapter 6B are to be fully understood. However, Hysitron have developed a nanoindenter which can carry out displacement controlled indenting in situ in a SEM[44]. This is done using a differential capacitance half bridge method with a 150 kHz signal on one fixed outer plate of the displacement sensor core and a second signal of the same frequency but phase shifted by 180 degrees on the other fixed outer plate of the same core. These signals are high enough in frequency relative to the mechanical bandwidth of the transducer to not actuate it. Fabricating a DFP indenter tip and carrying out indentation into polymer materials with this increased feedback frequency in situ in SEM could yield very exciting results building on the ones presented here.

8.3 References

- [1] C. A. Tweedie, G. Constantinides, K. E. Lehman, D. J. Brill, G. S. Blackman, and K. J. Van Vliet, "Enhanced stiffness of amorphous polymer surfaces under confinement of localized contact loads," *Adv. Mater.*, vol. 19, p. 2540, 2007.
- [2] R. S. Hoy and M. O. Robbins, "Strain hardening of polymer glasses: Effect of entanglement density, temperature, and rate," *Journal of Polymer Science Part B: Polymer Physics*, vol. 44, pp. 3487-3500, 2006.
- [3] R. S. Hoy and M. O. Robbins, "Strain hardening of polymer glasses: Entanglements, energetics, and plasticity," *Physical Review E*, vol. 77, p. 031801, 2008.
- [4] E. G. Leon, A. P. E. Tom, W. Michael, A. T. Theo, and W. S. Ulrich, "Does the strain hardening modulus of glassy polymers scale with the flow stress?," *Journal of Polymer Science Part B: Polymer Physics*, vol. 46, pp. 2475-2481, 2008.
- [5] K. Chen, E. J. Saltzman, and K. S. Schweizer, "Segmental dynamics in polymers: from cold melts to ageing and stressed glasses," *Journal of Physics: Condensed Matter*, vol. 21, p. 503101, 2009.
- [6] K. Chen and K. S. Schweizer, "Stress-enhanced mobility and dynamic yielding in polymer glasses" *EPL (Europhysics Letters)*, vol. 79, 2007.
- [7] K. Chen and K. S. Schweizer, "Theory of Yielding, Strain Softening, and Steady Plastic Flow in Polymer Glasses under Constant Strain Rate Deformation," *Macromolecules*, vol. 44, pp. 3988-4000, 2012/08/25 2011.
- [8] L. C. E. Struik, "PHYSICAL AGING IN AMORPHOUS GLASSY POLYMERS*," *Annals of the New York Academy of Sciences*, vol. 279, pp. 78-85, 1976.
- [9] H. E. H. Meijer and L. E. Govaert, "Mechanical performance of polymer systems: The relation between structure and properties," *Progress in Polymer Science*, vol. 30, pp. 915-938, 2005.
- [10] H. G. H. van Melick, O. F. J. T. Bressers, J. M. J. den Toonder, L. E. Govaert, and H. E. H. Meijer, "A micro-indentation method for probing the craze-initiation stress in glassy polymers," *Polymer*, vol. 44, pp. 2481-2491, 2003.
- [11] A. Mataz and G. B. McKenna, "Effects of confinement on material behaviour at the nanometre size scale," *Journal of Physics: Condensed Matter*, p. R461, 2005.
- [12] R. Ruiz, H. Kang, F. A. Detcheverry, E. Dobisz, D. S. Kercher, T. R. Albrecht, J. J. de Pablo, and P. F. Nealey, "Density Multiplication and Improved Lithography by Directed Block Copolymer Assembly," *Science*, vol. 321, pp. 936-939, August 15, 2008 2008.
- [13] H. R. Brown, "Effect of a diblock copolymer on the adhesion between incompatible polymers," *Macromolecules*, vol. 22, pp. 2859-2860, 1989.
- [14] V. Gowrishankar, N. Miller, M. D. McGehee, M. J. Misner, D. Y. Ryu, T. P. Russell, E. Drockenmuller, and C. J. Hawker, "Fabrication of densely packed, well-ordered, high-aspect-ratio silicon nanopillars over large areas using block copolymer lithography," *Thin Solid Films*, vol. 513, pp. 289-294, 2006.
- [15] H. W. Li and W. T. S. Huck, "Ordered Block-Copolymer Assembly Using Nanoimprint Lithography," *Nano Lett.*, vol. 4, pp. 1633-1636, 2004.
- [16] G. E. Dieter, *Mechanical Metallurgy*: McGraw-Hill Book Company, 1988.
- [17] W. Johnson and H. Kudo, "The compression of rigid-perfectly-plastic material between rough parallel dies of unequal width," *International Journal of Mechanical Sciences*, vol. 1, pp. 336-341, 1960.

- [18] R. Quinson, J. Perez, M. Rink, and A. Pavan, "Yield criteria for amorphous glassy polymers," *Journal of Materials Science*, vol. 32, pp. 1371-1379, 1997.
- [19] W. A. Spitzig and O. Richmond, "Effect of hydrostatic pressure on the deformation behavior of polyethylene and polycarbonate in tension and in compression," *Polymer Engineering & Science*, vol. 19, pp. 1129-1139, 1979.
- [20] Thomas F. Juliano, Mark R. VanLandingham, Tusit Weerasooriya, and P. Moy, "Extracting Stress-Strain and Compressive Yield Stress Information From Spherical Indentation," *Army Research Laboratory*, 2007.
- [21] A. C. Balazs, T. Emrick, and T. P. Russell, "Nanoparticle Polymer Composites: Where Two Small Worlds Meet," *Science*, vol. 314, 2006.
- [22] F. Q. Yang, "Asymptotic solution to axisymmetric indentation of a compressible elastic thin film," *Thin Solid Films*, vol. 515, pp. 2274-2283, Dec 2006.
- [23] C. M. Stafford, C. Harrison, K. L. Beers, A. Karim, E. J. Amis, M. R. VanLandingham, H.-C. Kim, W. Volksen, R. D. Miller, and E. E. Simonyi, "A buckling-based metrology for measuring the elastic moduli of polymeric thin films," *Nat Mater*, vol. 3, pp. 545-550, 2004.
- [24] C. Tang, E. M. Lennon, G. H. Fredrickson, E. J. Kramer, and C. J. Hawker, "Evolution of Block Copolymer Lithography to Highly Ordered Square Arrays," *Science*, vol. 322, pp. 429-432, October 17, 2008 2008.
- [25] G. Reiter and P. G. de Gennes, "Spin-cast, thin, glassy polymer films: Highly metastable forms of matter," *European Physical Journal E*, vol. 6, pp. 25-28, Sep 2001.
- [26] L. Si, M. V. Massa, K. Dalnoki-Veress, H. R. Brown, and R. A. L. Jones, "Chain Entanglement in Thin Freestanding Polymer Films," *Physical Review Letters*, vol. 94, p. 127801, 2005.
- [27] H. D. Rowland, W. P. King, J. B. Pethica, and G. L. W. Cross, "Molecular Confinement Accelerates Deformation of Entangled Polymers During Squeeze Flow," *Science*, vol. 322, pp. 720-724, October 31, 2008 2008.
- [28] H. D. Rowland, W. P. King, J. B. Pethica, and G. L. W. Cross, "Molecular Confinement Accelerates Deformation of Entangled Polymers During Squeeze Flow," *Science*, vol. 322, p. 720, October 2, 2008 2008.
- [29] C. M. Stafford, B. D. Vogt, C. Harrison, D. Julthongpiput, and R. Huang, *Macromolecules*, vol. 39, p. 5095, 2006.
- [30] J. M. Torres, C. Wang, E. B. Coughlin, J. P. Bishop, R. A. Register, R. A. Riggelman, C. M. Stafford, and B. D. Vogt, "Influence of Chain Stiffness on Thermal and Mechanical Properties of Polymer Thin Films," *Macromolecules*, 2011/11/03.
- [31] P. Damman, S. Gabriele, S. Coppee, S. Desprez, D. Villers, T. Vilmin, E. Raphael, M. Hamieh, S. Al Akhrass, and G. Reiter, "Relaxation of residual stress and reentanglement of polymers in spin-coated films," *Physical Review Letters*, vol. 99, Jul 2007.
- [32] Z. H. Yang, Y. Fujii, F. K. Lee, C. H. Lam, and O. K. C. Tsui, "Glass Transition Dynamics and Surface Layer Mobility in Unentangled Polystyrene Films," *Science*, vol. 328, pp. 1676-1679, Jun 2010.
- [33] Z. Fakhraai and J. A. Forrest, "Measuring the surface dynamics of glassy polymers," *Science*, vol. 319, pp. 600-604, Feb 2008.
- [34] M. Chowdhury, P. Freyberg, F. Ziebert, A. C. M. Yang, U. Steiner, and G. Reiter, "Segmental Relaxations have Macroscopic Consequences in Glassy Polymer Films," *Physical Review Letters*, vol. 109, p. 136102, 2012.
- [35] S. Sills, R. M. Overney, W. Chau, V. Y. Lee, R. D. Miller, and J. Frommer, "Interfacial glass transition profiles in ultrathin, spin cast polymer films," *Journal of Chemical Physics*, vol. 120, pp. 5334-5338, 2004.
- [36] F. Dinelli, C. Buenviaje, and R. M. Overney*, "Glass transition measurements on heterogeneous surfaces," *Thin Solid Films*, vol. 396, pp. 138-144, 2001.
- [37] S. Sills, R. M. Overney, W. Chau, V. Y. Lee, R. D. Miller, and J. Frommer, "Interfacial glass transition profiles in ultrathin, spin cast polymer films," *The Journal of Chemical Physics*, vol. 120, pp. 5334-5338, 2004.

- [38] J. H. Teichroeb and J. A. Forrest, "Direct imaging of nanoparticle embedding to probe viscoelasticity of polymer surfaces," *Physical Review Letters*, vol. 91, Jul 2003.
- [39] T. B. Karim and G. B. McKenna, "Evidence of surface softening in polymers and their nanocomposites as determined by spontaneous particle embedment," *Polymer*, vol. 52, pp. 6134-6145, Dec 2011.
- [40] G. L. W. Cross, B. S. O'Connell, J. B. Pethica, and W. C. Oliver, "Some Issues in the Mechanical Forming of Nanoimprint Structures," *Journal of Photopolymer Science and Technology*, vol. 18, pp. 559-562, 2005.
- [41] G. L. W. Cross, B. S. O'Connell, J. B. Pethica, H. Rowland, and W. P. King, "Variable temperature thin film indentation with a flat punch," *Review of Scientific Instruments*, vol. 79, pp. 013904-13, 2008.
- [42] H. D. Rowland, W. P. King, G. L. W. Cross, and J. B. Pethica, "Measuring Glassy and Viscoelastic Polymer Flow in Molecular-Scale Gaps Using a Flat Punch Mechanical Probe," *ACS Nano*, vol. 2, pp. 419-428, 2008.
- [43] S. Napolitano and M. Wã¼bberhorst, "Deviation from bulk behaviour in the cold crystallization kinetics of ultrathin films of poly(3-hydroxybutyrate)," *Journal of Physics: Condensed Matter*, vol. 19, p. 205121, 2007.
- [44] K.A. Rzepiejewska-Malyska, G. Buerki, J. Michler, R.C. Major, E. Cyrankowski, S. A. S. Asif, and O. L. Warren, "In situ mechanical observations during nanoindentation inside a high-resolution scanning electron microscope," *Journal of Materials Research*, vol. 23, pp. 1973-1979, 2008.